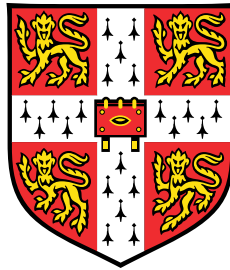


# Numerical Construction of Gravitational Solutions in Asymptotically Anti-de Sitter Spacetimes

JULIJA MARKEVIČIŪTĖ



Under the supervision of J. E. Santos

Department of Applied Mathematics and Theoretical Physics  
University of Cambridge

Fitzwilliam College

*This dissertation is submitted for the degree of  
Doctor of Philosophy  
April 2019*



# Numerical Construction of Gravitational Solutions in Asymptotically Anti-de Sitter Spacetimes

Juliya Markevičiūtė

Asymptotically anti-de Sitter (AdS) spacetimes display intriguing phenomena which have recently sparked increasing interest in the research of gravitational solutions in these spaces. Considerable motivation stems from gauge/gravity duality, which is a conjecture relating classical gravity with a negative cosmological constant to strongly coupled quantum field theories. In this dissertation, we present novel stationary, asymptotically AdS black hole and soliton solutions, which we construct numerically. We employ numerical techniques which have been successfully used to tackle the complexities of the Einstein equations, and allow us to study the fully non-linear systems in unparalleled detail.

We present a numerical study of rotating and charged hairy black hole solutions in five-dimensional AdS, which originate from a consistent truncation of  $\mathcal{N} = 8$  supergravity, and can be uplifted to the type IIB supergravity with  $\text{AdS}_5 \times \text{S}^5$  asymptotics. The hairy black holes have one scalar field charged under a  $U(1)$  gauge field, and branch from the near-extremal black holes due to the superradiant instability. We give numerical evidence that the hairy solutions exist arbitrarily close to the BPS bound for all charges, which is saturated in the zero and infinite temperature limits. We compute the phase diagram, and analyse the thermodynamics across different ensembles. Finally, we conjecture the existence of a one-parameter hairy solution extension of the known supersymmetric black hole in this theory. Our work demonstrates the importance and complexity of black hole solutions with scalar condensate in supergravity. It also opens new possibilities to resolve a long-standing problem in Maldacena's original AdS/CFT correspondence, namely the understanding of the Bekenstein-Hawking entropy of supersymmetric black holes in terms of microstate counting.

The study of gravitational solutions in AdS also provides valuable insights into classical phenomena in general relativity. In particular, superradiance has been important in the context of the weak cosmic censorship hypothesis. In order to study this relationship, we constructed novel four-dimensional asymptotically global AdS solutions by turning on a dipolar differential rotation at the conformal boundary. At fixed energy and boundary profile, we find two different geometries: a horizonless AdS soliton, and a deformed black hole. Both solutions develop an ergoregion attached to the boundary, and are superradiantly unstable. We discuss the intricate phase diagram which exhibits up to six-fold degeneracy, and the implications of our results for weak cosmic censorship and the corresponding dual field theory at strong coupling.



## Declaration

I hereby declare that except where specific reference is made to the work of others, the contents of this dissertation are original and have not been submitted in whole or in part for consideration for any other degree or qualification in this, or any other university. This dissertation is my own work and contains nothing which is the outcome of work done in collaboration with others, except as specified in the text and acknowledgments.

April 2019

Julija Markevičiūtė



## Acknowledgements

First and foremost, I would like to thank my supervisor Jorge Santos, for his guidance and support throughout my PhD studies. Without his ideas and advice, this thesis would not have been possible. I am grateful to my fellow PhD students in DAMTP, who have made my experience here enjoyable, and with whom I have shared many stimulating conversations. I would also like to thank my family and friends, for their continuous love and support, and for always keeping my spirits up. My special thanks goes to Charles.

# Table of contents

<b>List of figures</b>	<b>xi</b>
<b>1 Introduction</b>	<b>1</b>
1.1 Overview . . . . .	1
1.2 The gauge/gravity duality . . . . .	3
1.3 The dictionary . . . . .	6
1.4 Hairy black holes in AdS . . . . .	10
<b>2 Numerical Construction of Stationary Solutions in AdS</b>	<b>13</b>
2.1 The Einstein equation . . . . .	13
2.2 The Einstein-DeTurck equation . . . . .	14
2.2.1 Ellipticity . . . . .	14
2.2.2 Stationarity . . . . .	17
2.2.3 Ricci solitons . . . . .	19
2.3 The Newton-Raphson method . . . . .	19
2.4 Numerical approach . . . . .	20
<b>3 Hairy Black Holes in <math>\text{AdS}_5 \times \text{S}^5</math></b>	<b>23</b>
3.1 Introduction . . . . .	23
3.2 Setup . . . . .	27
3.2.1 The action and equations of motion . . . . .	27
3.3 The BPS solitons . . . . .	30
3.4 Numerical construction of hairy black holes . . . . .	32
3.5 Static Hairy Black Holes . . . . .	34
3.5.1 Phase diagram . . . . .	34
3.5.2 The planar limit . . . . .	39
3.5.3 Thermodynamics . . . . .	41
3.5.3.1 Grand-canonical ensemble . . . . .	41

3.5.3.2	Canonical ensemble . . . . .	42
3.5.3.3	Microcanonical ensemble . . . . .	44
3.5.3.4	Planar limit . . . . .	45
3.6	Comparison with perturbative results . . . . .	46
3.7	Summary and discussion . . . . .	47
3.A	Numerical validity . . . . .	49
<b>4</b>	<b>Rotating Hairy Black Holes in <math>\text{AdS}_5 \times \text{S}^5</math></b>	<b>51</b>
4.1	Introduction . . . . .	51
4.2	Summary of the phase diagram . . . . .	53
4.3	Setup . . . . .	55
4.3.1	The field equations for the stationary ansatz . . . . .	55
4.3.2	Charged, equally-rotating black holes . . . . .	59
4.4	Hairy Black holes . . . . .	61
4.4.1	Numerical setup . . . . .	61
4.4.2	Thermodynamic quantities . . . . .	64
4.5	Phase diagram of hairy black holes . . . . .	66
4.5.1	Linear instability and the onset plane . . . . .	66
4.5.2	Constant $J$ planes . . . . .	68
4.5.2.1	The extremal limit and the entropy . . . . .	69
4.5.2.2	Isotherms . . . . .	73
4.5.3	Constant $Q$ planes . . . . .	75
4.5.4	Constant $\Omega_H$ planes . . . . .	77
4.6	Tidal forces . . . . .	79
4.7	Thermodynamics . . . . .	83
4.8	Rotating black branes . . . . .	86
4.8.1	Ansatz . . . . .	86
4.8.2	Solution space and thermodynamics . . . . .	89
4.8.3	The Abelian-Higgs model . . . . .	90
4.9	The non-interacting thermodynamic model . . . . .	91
4.10	Discussion and future directions . . . . .	94
4.A.1	Numerical convergence . . . . .	98
<b>5</b>	<b>Stirring a Black Hole</b>	<b>101</b>
5.1	Introduction . . . . .	101
5.2	Setup . . . . .	103

5.3	Numerical Construction . . . . .	104
5.3.1	Soliton . . . . .	104
5.3.2	Black Holes . . . . .	105
5.4	Numerical Results . . . . .	107
5.4.1	Soliton . . . . .	107
5.4.2	Black Holes . . . . .	108
5.4.2.1	The horizon geometry . . . . .	108
5.4.2.2	Curvature invariants . . . . .	111
5.4.2.3	Entropy . . . . .	112
5.4.3	Stress-Energy tensor . . . . .	114
5.4.3.1	Soliton . . . . .	116
5.4.3.2	Black Holes . . . . .	118
5.4.4	Thermodynamics . . . . .	119
5.4.4.1	Energy . . . . .	119
5.4.4.2	Grand-canonical ensemble . . . . .	121
5.5	Stability . . . . .	123
5.5.1	Quasinormal modes . . . . .	123
5.5.1.1	Soliton . . . . .	124
5.5.1.2	Black hole . . . . .	126
5.6	Field Theory . . . . .	128
5.7	Equilibrium of spinning test particles . . . . .	130
5.7.1	Equilibrium of non-spinning test particles . . . . .	133
5.8	No Ergoregions . . . . .	135
5.9	Conclusions . . . . .	136
5.A	Numerical validity . . . . .	138
5.B	Additional figures . . . . .	140
5.C	Perturbative expansion . . . . .	141
<b>6</b>	<b>Summary and Future Outlook</b>	<b>147</b>
	<b>References</b>	<b>149</b>

# List of figures

- 3.1 The proposed microcanonical phase diagram by Bhattacharyya *et al* (taken from [62], not drawn to scale). The lower solid line is the BPS bound on which the supersymmetric soliton resides. The straight red segment represents smooth branch and the wiggly black part represents singular soliton. Hairy black holes were proposed to exist between the curve indicating the onset of the superradiant instability (solid blue) and the BPS bound. The dotted black curve is the extremal RNAdS black holes. The grey solid line shows a possible phase transition between two different types of hairy black holes, with different zero size limits. . . . 25
- 3.2 *Left:* Charge of the solitonic solutions  $Q$  versus the vacuum expectation value of the dual operator  $\langle \mathcal{O}_\phi \rangle$ . The black solid line from above is the singular soliton and the red line from below is the smooth solution. The dotted gridlines show coordinates of the special solution with  $\alpha = 2/3$ . *Right:* The  $\alpha = 2$  soliton solutions. The wedges are for constant  $h_2$  which decreases from 1. These solution curves appear to extend to  $|Q| \rightarrow +\infty$ . We also did not find any limiting value for  $\langle \mathcal{O}_\phi \rangle$ . . . . 31
- 3.3 *Left:* Phase diagram for the hairy black holes. The merger curve (solid black) indicates the onset of the superradiant instability. The line of extremal RNAdS solutions is shown as a dashed gray line. The BPS bound is given by  $M_{\text{BPS}}(Q) = 3Q$  (dashed black). The gray dotted gridlines indicate the position of the special soliton with  $\alpha = 2/3$ . *Right:* For clarity, we plot the mass difference  $\Delta M = M - M_{\text{ext}}$ , where  $M_{\text{ext}}$  is the mass of an extremal RNAdS black hole with the same charge  $Q$ . . . 35
- 3.4 *Left:* Zooming in around  $Q = Q_c$ , and observing the transition between  $T < T_2$  and  $T > T_2$ . The color legend is the same as in Fig. 3.3. *Right:* An even closer look for  $Q$  near  $Q_c = 0.261$ . The hairy black hole isotherms terminate at charges above the special singular soliton. . . . 35

- 
- 3.5 *Left:* The hairy black hole charge  $Q$  versus  $\langle \mathcal{O}_\phi \rangle$  for constant central scalar field density  $\epsilon_0$  curves. Red line is the smooth soliton and the green line is the singular soliton. *Right:* Mass difference versus charge  $Q$ . The constant parameter  $\epsilon_0$  curves extend down to  $T = 0.055$ . The inset is a zoomed in plot around  $Q = Q_c$  for some value of  $\epsilon_0$ . . . . . 36
- 3.6 *Left:* Charge versus the vacuum expectation value of the operator dual to the scalar field for constant temperature hairy black hole solutions. The black and red data points are singular and smooth solitons respectively. Dotted gridlines show the point where these two merge. *Right:* The charge of the hairy solutions as we approach the singular soliton with  $\alpha = 1$ , exhibits damped oscillations. This data was collected with  $n = 1000$  grid points. . . . . 37
- 3.7 *Left:* Curvature invariants at the origin for a range of temperatures for constant  $\epsilon_0$ . The Kretschmann scalar remains finite. For lower values of  $\epsilon_0$  it takes longer for the hairy black holes to approach the BPS bound, hence for larger values of the parameter the curves flatten out quicker. *Right:* Kretschmann invariant  $K^2$  for the range of temperatures scaled by the  $K^2$  of the corresponding RNAdS black hole in the grand-canonical ensemble. As  $\epsilon_0$  increases the invariant increases without a bound. . . . . 38
- 3.8 Gauge invariant quantities  $\phi g_{xx}$  and  $\phi g_{rr}$  for the hairy planar solutions, versus the compact coordinate  $y$ . According to the exact solution, both these curves should approach the same constant value when  $\tilde{T} \rightarrow +\infty$ . 39
- 3.9 *Left:* The difference between the Gibbs free energies of hairy and RNAdS solutions with the same chemical potential and temperature. *Right:* Difference of the Helmholtz free energies of the Reissner-Nortström and the hairy solution with the same temperature and charge. . . . . 40

- 3.10 *Left*: Canonical ensemble: RNAdS black holes exist below the extremality curve (the curve separating orange (top left) and light-orange (middle) regions) and the hairy black holes exist above the merger curve (purple data points) and for  $\mu > 1$ . RNAdS dominate over pure AdS only in the yellow region (bottom right). The hairy black holes have a higher free energy than thermal AdS and thus are not the preferred phase in the ensemble. *Right*: Grand-canonical ensemble: when both solutions coexist (again above the merger curve), the hairy black holes have a higher free energy than the corresponding RNAdS with the same  $\mu$  and  $T$ . The yellow region (middle) shows the parameter space in which the RNAdS dominates over thermal AdS. The orange region (top left) is the extremal RNAdS and light-orange region (bottom left) is the sector in which pure AdS is preferred over the RNAdS black holes. . . . . 42
- 3.11 *Top row*: Entropy versus mass for the hairy solutions for three different temperatures. Red diamonds correspond to the RNAdS black hole with the same charge. *Middle row*: Canonical free energy versus charge for the hairy solutions for three different temperatures. Red solid line is the corresponding RNAdS solution. For  $T < T_1$ , (left panel) the hairy solutions dominate over the RNAdS black hole. For  $T_1 < T < T_2$ , the three solutions coexist: two hairy black holes and RNAdS. One of the hairy solutions dominates over the RNAdS, while the other is subdominant (middle panel). For  $T > T_2$ , the RNAdS black hole is always dominant in the canonical ensemble. *Bottom row*: Gibbs free energy versus chemical potential for the hairy global black holes. Red solid line is the corresponding RNAdS solution. . . . . 43
- 3.12 The entropy difference  $S - S_{\text{RN}}$  of the hairy black holes and the corresponding RNAdS with the same values of  $Q$  and  $M$ , as a function of the scaled mass  $M/M_{\text{merger}}$  plotted for a range of temperatures. Here  $M_{\text{merger}}$  is the mass at the onset of the superradiant instability, where by definition  $S - S_{\text{RN}} = 0$ . . . . . 44

---

3.13	Scaled thermodynamic potentials for the planar hairy black holes. The red line in each figure is the RNAdS solution in the corresponding ensemble (microcanonical in <i>top left</i> , canonical in <i>top right</i> , grand-canonical in <i>bottom left</i> ). The hairy black branes are only dominant in the microcanonical ensemble. <i>Bottom right</i> : Planar hairy black hole masss against charge, in terms of the scale invariant quantities. Red line shows the RNAdS black holes, and black data points are the hairy counterparts. . . . .	45
3.14	Comparison of the data to the small charge perturbative expansion for the four main thermodynamic quantities. The black disks are the numerical data for the hairy black holes (with $\varepsilon = 0.1$ ) and the red solid line shows the prediction of [62]. As expected, we observe larger deviations in the temperature and chemical potential. . . . .	46
3.15	The infinity norm of the DeTurck vector across a range temperatures with the number of gridpoints $n = 600$ . Lower temperature hairy global solutions have the highest norm. . . . .	49
3.16	Comparison of the two <i>ansatz</i> . $M_1$ is the (3.12) <i>ansatz</i> , $M_2$ is the (3.14) <i>ansatz</i> . <i>Left</i> : $n = 400$ data. <i>Right</i> : $n = 600$ data. The highest temperature solutions agree the best and the agreement gets worse as we lower the temperature. . . . .	49
3.17	Convergence for the hairy global solutions for different values of the central scalar field density $\epsilon_0$ for one particular temperature. Convergence for the first <i>ansatz</i> is at least few orders of magnitude worse. <i>Left</i> : The norm of the DeTurck vector versus the grid size. <i>Right</i> : Hairy black hole mass error versus the grid size. As the mass involves second derivatives other thermodynamical quantities have at least two order of magnitude better convergence. For $\epsilon_0 > 20$ convergence falls rapidly. . . . .	50
3.18	Convergence for the hairy planar solutions for different values of the central scalar field density $\epsilon_0$ . As expected it is much better than for the hairy solutions. . . . .	50

- 4.1 *Left:* Microcanonical phase diagram of charged, non-rotating hairy black holes [62, 92]. The Reissner-Nordström black holes exist above their extremal limit (black dashed line), and the hairy black holes exist below the bold orange line, which shows the onset of the superradiant instability. These solutions extend down to the BPS bound, where they reduce to the smooth soliton (the purple wavy line) in the limit  $T \rightarrow 0$ , while keeping the value of the scalar field at the horizon  $\varepsilon_H$  fixed. *Right:* Microcanonical phase diagram of charged, rotating hairy black holes at a constant angular momentum  $J$ . The hairy black holes exist between the merger line (orange) and the BPS bound (dashed red), in the region shaded in light red. The black disk is the supersymmetric Gutowski-Reall black hole [117], which lies at the intersection of the extremal and the BPS planes. The purple wavy line shows a line of the conjectured supersymmetric hairy black holes, which terminates at a finite charge  $Q_{\max}(J)$ , where the black holes become singular. . . . . 56
- 4.3 Thermodynamic quantities against the temperature  $T$ , for black holes with fixed angular momentum  $J = 0.05$  and horizon scalar field  $\varepsilon_H = 10^{-4}$  (black data points). The dashed gridlines show the values for the supersymmetric black hole with the same  $J$ . . . . . 65
- 4.4 *Left:* The line of solutions showing the onset of the superradiance for the CLP black holes at constant charge  $Q = 0.1315$  (black points). These solutions extend arbitrarily close to the supersymmetric black holes (red square), with the temperature asymptotically approaching  $T = 0$ . The grey dashed line shows the extremality, and the red bold line shows the BPS bound  $M = 3Q + 2J$ . *Right:* The difference  $M - M_{\text{ext}}$  against the charge  $Q$ , for black holes with fixed  $J = 0.05$  and  $\varepsilon_H = 10^{-4}$  (black data points), where  $M_{\text{ext}}$  is mass of the extremal CLP black hole with the same  $Q$ . Red solid line is the BPS bound, and the red star shows the Gutowski-Reall solution. . . . . 67

- 4.5 *Left*: The mass difference  $M - M_{\text{ext}}$  against the charge  $Q$  for fixed angular momentum  $J = 0.05$  and different values of the horizon scalar  $\varepsilon_H$  (coloured disks; the lower curves have higher  $\varepsilon_H$ ), where  $M_{\text{ext}}$  is the mass of the corresponding extremal CLP black hole with the same  $J$  and  $Q$ . The black disk shows the supersymmetric black hole, the black solid line shows the BPS bound (the lowest curve), the orange solid line (the top curve) shows the onset of the instability. *Right*: The charge  $Q$  against the expectation value of the operator dual to the scalar field, for families of hairy black holes with constant  $J = 0.05$  and various values of the horizon scalar  $\varepsilon_H$ . . . . . 68
- 4.6 Log-linear plot of the entropy (*left*) and the horizon angular velocity (*right*, the legend is the same as for  $S$ ) of the hairy solutions with fixed angular momentum  $J = 0.05$  against the temperature, for several values of the horizon scalar  $\varepsilon_H$ . The horizontal dashed gridline shows the values for the supersymmetric black hole with the same  $J$ . . . . . 69
- 4.7 Log-linear plot of the mass (*left*) and the charge (*right*) of the hairy solutions with angular momentum  $J = 0.05$  versus  $T$ , for several values of  $\varepsilon_H$ . The horizontal dashed gridline shows the values for the supersymmetric black hole with the same  $J$ . The legend is the same as in Fig. 4.6. . . . . 70
- 4.8 Extrapolated zero temperature entropy of the hairy black holes with constant  $J = 0.02$  (orange disks),  $J = 0.05$  (red squares) and  $J = 0.08$  (black diamonds) against the central scalar field  $\varepsilon_H$ . The variation in the entropy as we lower the temperature further gives error less than 0.1%. 71
- 4.9 The value of  $q_1$  at the horizon  $y = 0$  against the temperature, for a black hole family with  $J = 0.05$  and  $\varepsilon_H = 1$ . *Middle*: The value of  $q_1''$  against  $T$ , for several values of  $\varepsilon_H$ . *Right*: the value of  $2q_5q_7 - q_6$  at the horizon against the temperature, for several values of the horizon scalar field. . . 72

- 4.10 *Left*: The log-log plot of the Kretschmann curvature scalar  $K = R_{abcd}R^{abcd}$  against the temperature, for fixed angular momentum  $J = 0.05$  and horizon scalar field  $\varepsilon_H = 1$ . *Right*: Kretschmann curvature invariant at the horizon  $y = 0$  for the hairy black hole with constant horizon values  $\varepsilon_H$  and  $\Omega_H$ , scaled by the  $K$  value of a corresponding CLP black hole in the grand-canonical ensemble, *i.e.* with the same  $\mu$ ,  $T$  and  $\Omega_H$ . The ratio remains finite as we approach the BPS bound, and the black hole family shrinks to a smooth solitonic solution. . . . . 73
- 4.11 Rotating hairy black holes at fixed temperature, for different fixed angular momenta  $J = 0, 0.001, 0.01, 0.05$ , while varying the horizon scalar field  $\varepsilon_H$ . We plot the mass difference  $M - M_{\text{ext}}$  against the charge  $Q$ , where  $M_{\text{ext}}$  is the mass of the corresponding extremal CLP black hole. The solid black line is the scalar instability curve, dashed black line (or red line in the insets) is the BPS bound, black star is the Gutowski-Reall black hole. The vertical dotted line shows the special soliton  $Q_{\text{max}}(J = 0) = Q_c$ . Insets zoom around interesting isotherm behaviour. . . . . 74
- 4.12 Constant angular momentum  $J$  and charge  $Q$  solutions, with the parameter  $y_+$  being varied. We present the horizon scalar field  $\varepsilon_H$  (*left*), the entropy (*middle*), and the expectation value of the dual operator  $\langle \mathcal{O}_\phi \rangle$  (*right*), for three different charges  $Q = 0.0748$  (*bottom row*),  $Q = 0.279$  (*middle row*),  $Q = 0.649$  (*top row*). . . . . 76
- 4.13 Thermodynamic quantities for the hairy black hole families with fixed horizon velocity  $\Omega_H = 0.4$  (*top row*) and  $\Omega_H = 0.9$  (*bottom row*), and a constant horizon scalar  $\varepsilon_H$ . As the temperature  $T \rightarrow 0$ , angular momentum  $J \rightarrow 0$  (*left*), entropy  $S \rightarrow 0$  (*middle*), and chemical potential  $\mu \rightarrow 1$  (*right*). For large horizon velocity, there exists a maximum temperature for the hairy black holes. . . . . 78
- 4.14 Black hole charge  $Q$  against the vacuum expectation value  $\langle \mathcal{O}_\phi \rangle$  of the operator dual to the scalar field  $\phi$ , at fixed horizon scalar charge  $\varepsilon_H$ , and fixed horizon angular velocity  $\Omega_H = 0.4$  (*left*), and  $\Omega_H = 0.9$  (*right*), in the non-rotating frame at infinity. In black are the corresponding values for the non-rotating solutions  $\Omega_H = 0, J = 0$ . The smooth BPS soliton family is shown in gray. . . . . 79

- 4.15 A 3D solution space of the hairy black holes. The CLP black holes exist above the dark gray plane, and intersect the BPS limit  $M = 3Q + 2J$  (the white plane below) at the Gutowski-Reall family (red bold line). The orange plane is the CLP solutions with  $\Omega_H = 1$ , below which the solutions have  $\Omega_H > 1$ . The solid bold lines in rainbow are the hairy solutions with fixed horizon velocity  $\Omega_H = 0.4$ , and fixed horizon scalar value  $\varepsilon_H$ . The first line in blue is the merger line for the constant  $\Omega_H = 0.4$ , and exists just above the extremal plane. The dotted black gridlines on the front right face show the special soliton with  $Q_c \simeq 0.26$ . 80
- 4.16 *Left*: The measure of tidal forces, as felt by a unit energy particle infalling along a radial geodesic,  $T_{ab}\dot{X}^a\dot{X}^b$  at the hairy black hole horizon against the temperature. The quantity shown is for a black hole family with fixed  $j = 0.05$  and  $\varepsilon_H = 1$ , and the plot is in a log-log scale. *Right*: The log-log plot of the Tipler integral, for hairy black hole family with constant angular momentum  $j = 0.05$  and horizon scalar  $\varepsilon_H = 1$ . The integral was computed using the  $R^t_{\psi t \psi}$  component found in a PPNON frame. Different components have similar qualitative behaviour. . . . . 82
- 4.17 *Left*: The entropy difference  $\Delta S = S - S_{\text{CLP}}$  against the mass  $M$ , for black holes with fixed  $J = 0.05$  and  $\varepsilon_H = 0.2$  (black data points), where  $S_{\text{CLP}}$  is the entropy of the CLP black hole with the same charge  $Q$  and angular momentum  $J$ . *Right*: The difference in Gibbs free energy  $\Delta G = G - G_{\text{CLP}}$ , where  $G_{\text{CLP}}$  is the free energy for the corresponding CLP solution with the same temperature  $T$ , and thermodynamic angular velocity  $\Omega_H$ . We find that for all hairy solutions have  $G < 0$ , hence at fixed chemical potential  $\mu$ ,  $\Delta G > 0$  indicates that the phase without hair dominates the ensemble. . . . . 84
- 4.18 Difference in the Helmholtz free energy  $\Delta F = F - F_{\text{CLP}}$ , where  $F_{\text{CLP}}$  is the free energy for the corresponding CLP black hole with the same angular momentum  $J$ , temperature  $T$  and charge  $Q$ . Here  $\varepsilon_H \leq 15$ , and the dashed vertical gridline for  $J = 0$  correspond to the critical charge  $Q_c \simeq 0.26$ . In general the isotherms demonstrate a complicated behaviour, exhibiting cusp and swallowtail type phase transitions. For all hairy black holes  $F > 0$  with respect to the thermal AdS. . . . . 85

- 4.19 *Left*: Condensate against the temperature, for families of rotating hairy black branes with different values of  $\Omega_H$ . The critical temperature  $T_c$ , at which the hairy solutions first appear, decreases with  $\Omega_H$ . *Right*: Expectation value of the dual operator as a function of temperature for a phenomenological Abelian-Higgs model, as a scale invariant quantity, for various values of the horizon velocity  $\Omega_H$ . . . . . 87
- 4.20 *Left*: Rotating hairy brane entropy density as a function of the mass density in the microcanonical ensemble, for different values of  $\Omega_H$  (data points in rainbow). Solid black line shows the onset of the instability, and solid rainbow lines are the corresponding solutions without hair. The black data points show two hairy black hole families, one of constant  $\varepsilon_H = 3.5$ , and one of constant  $\Omega_H = 0.72$ . *Middle*: Hairy black brane free energy density as a function of temperature in canonical ensemble, for different values of  $\Omega_H$  (see the inset legend). The solid lines show the corresponding solutions without hair. *Right*: The free energy density in the grand-canonical ensemble, against the temperature. . . . . 89
- 4.21 *First line*: The comparison with the approximation of [62] for the same charge, mass, and angular momentum  $J = 0.001$ . Black disks are numerical results, and orange triangles are the predicted curves. We expect the model to be valid for small  $Q$ , small  $J$ , and near extremality. For small horizon scalar  $\varepsilon_H$ , the hairy black holes are just above the extremality and coexist with CLP solutions. As  $T \rightarrow 0$ , they approach the Gutowski-Reall solution. For small charge the participating soliton contributes  $Q_s/Q \simeq 0.5\%$  of the total charge. Here the lowest  $T = 0.00633$ , and  $S = 0.0228$ . The error of the approximation to  $S$  close to the BPS bound is less than 1%. *Second line*: The constant  $\varepsilon_H = 0.4$  curve crosses the extremality line. The red rhombi are the corresponding CLPs where they coexist in micro-canonical ensemble. For small charge,  $Q_s/Q \simeq 20\%$ . Here lowest  $T = 0.00597$ , and  $S = 0.0224$ . The error of the approximation to  $S$  close to the BPS bound is 2 – 4%. . . . . 92

- 4.22 *First line:* The comparison with the approximation of [62] for the same charge, mass, and angular momentum  $J = 0.05$ . Black disks are numerical results, and orange triangles are the predicted curves. For small charge,  $Q_s/Q \simeq 0.5\%$ . Here the lowest  $T = 0.00127$ , and  $S = 0.405$ . The error in  $S$  close to the BPS bound is 2 – 4%. Note that in particular as  $T \rightarrow 0$ ,  $\Omega_H \rightarrow 1$ . *Second line:* Red rhombi show the coexisting CLP black holes. For small charge,  $Q_s/Q \simeq 0.6\%$ . Here lowest  $T = 0.00164$ , and  $S = 0.401$ . The error in  $S$  close to the BPS bound is 5%. . . . . 93
- 4.23 Convergence of fractional error in black hole energy  $\Delta M_n = |1 - M_{n+1}/M_n|$  against the grid size  $n$ . *Left:* Hairy black hole solution in DeTurck gauge. The scale is log-log, and the convergence is a power law. *Right:* Convergence in radial gauge, for the same hairy black hole. The scale now is log-linear, exhibiting an exponential decay. . . . . 99
- 4.24 *Left:* Convergence of the energy for a few coldest  $J = 0.05$ ,  $\varepsilon_H = 1$  hairy black holes considered in the paper, with  $T = 0.00052$  (black rhombi),  $T = 0.00031$  (blue squares) and  $T = 0.00016$  (gray triangles). Here we plot the fractional error  $\Delta$  against the grid size  $n$ . *Right:* Low temperature ( $T = 10^{-2} \pm 10^{-3}$ ) hairy black hole energy convergence for a few different horizon scalar values  $\varepsilon_H$ . Black rhombi are for  $\varepsilon_H = 1$ , blue squares for  $\varepsilon_H = 8.5$ , and gray triangles for  $\varepsilon_H = 14.5$ . Here we show the fractional error against the grid size in a log scale. . . . . 99
- 5.1 Illustration of the novel AdS<sub>4</sub> geometries. *Left:* Solitonic solutions with a differentially rotating boundary. *Right:* Black hole solutions. The rotational pull force is maximal at  $\theta = \pi/4$ , deforming the black hole horizon into an hourglass shape. . . . . 102
- 5.2 The log-linear plot of the maximum of the Kretschmann scalar across the whole spacetime against the rotation parameter for the soliton solutions. The dashed gridline marks  $\varepsilon_c$ , and the dotted line shows the  $\max K = 24/L^4$  for pure AdS<sub>4</sub>. . . . . 107
- 5.3 Hyperbolic embedding of the cross section of the black hole horizons, for several values of the parameter  $\varepsilon$  and a fixed temperature  $T = 1/\pi$ . As we increase  $\varepsilon$ , the arms of the horizon cross section get stretched further apart. This picture is qualitatively the same for  $T \geq 1/\pi$ . . . . 108

- 5.4 Hyperbolic embedding of the cross section of the black hole solution horizons, for several values of the parameter  $\varepsilon$  and a fixed low temperature  $T = 0.2506$ . In this regime, there is a four-fold black hole non-uniqueness. *Left*: Embeddings for the upper, thermodynamically dominant branch of solutions with  $\varepsilon \in (1.520, 2.059)$ , and the largest entropy branch (two outer curves in red,  $\varepsilon = 2.055, 2.05$ ). The black circle is the  $T = 1/\pi$ ,  $\varepsilon = 0$  black hole. *Right*: Embeddings for the two small black hole branches. The higher entropy branch has  $\varepsilon \in (1.520, 2.557)$ , and the two inner circles in dark blue represent the lowest branch ( $\varepsilon = 2.55, 2.53$ ). The embeddings are qualitatively similar for the low  $T$  regime. . . . . 109
- 5.5 Log-linear plot of the curvature scalar maximum against  $\varepsilon$ , for a large black hole with  $T = 1/\pi$ . The dashed gridline marks the critical value of  $\varepsilon$ , and the dotted gridline shows  $K_{\max} = 72$  for a Schwarzschild-AdS<sub>4</sub> black hole. The inset is a log-log plot for high values of the rotation amplitude. . . . . 111
- 5.6 *Left*: Entropy against the rotation parameter  $\varepsilon$  for the large branch of black holes with  $T = 1/\pi$ . The inset zooms around the limit, demonstrating the asymptotic behavior. Red dashed gridlines mark the  $\varepsilon = 2$  limit. *Middle*: Logarithmic derivative of  $S$  for the large black hole with  $T = 1/\pi$ . As  $\varepsilon \rightarrow 2$ , the entropy of the large black hole blows up as an inverse power law. *Right*: Entropy of the small branch of black holes with the same temperature. Red dashed gridlines show where  $\varepsilon = 2$  and  $S = 0$ . . . . . 112
- 5.7 *Left*: Entropy against the boundary parameter for low temperature black holes with  $T < T_{\min}^{\text{Schw}} \simeq 0.2757$ . The orange disks show black holes with  $T \simeq T_{\min}^{\text{Schw}}$ . The brown squares show the (hot) small black holes with  $T = 1/\pi$  for reference. As we lower the temperature, the large black holes begin to exist for  $\varepsilon > 2$ . *Right*: The asymptotic behavior of isothermal entropy curves. Both solution branches approach  $\varepsilon = 2$ , with the large branch having a steeply increasing  $S$ , and the small branch having  $S \rightarrow 0$ . The red gridlines show  $\varepsilon = 2$  and  $\varepsilon = \varepsilon_c$ . . . . . 113
- 5.8 The stress-energy tensor component  $\langle T_t^t \rangle$  (*left*), component  $\langle T_\phi^t \rangle$  (*middle*), and component  $\langle T_\theta^\theta \rangle$  (*right*) for solitonic solutions as a function of  $\theta$ , the angle on the  $\mathbb{S}^2$ . Colours represent different values of the parameter  $\varepsilon$ , with larger values corresponding to larger amplitudes. . . 115

- 5.9 Independent stress-energy tensor components of the dual to the large black holes against  $\theta$ , for several values of the parameter  $\varepsilon$ . Colouring codes black hole temperature with darker colours representing temperatures closer to  $T_{\min}(\varepsilon)$ . . . . . 117
- 5.10 *Left*: Soliton solution boundary energy against rotation parameter. The dashed vertical gridline marks the critical amplitude  $\varepsilon = 2$ , and the bold orange line is the perturbative result. *Right*: Log-linear plot of the energy for the black hole solutions against  $\varepsilon$ , for several values of  $T$ . . . 119
- 5.11 *Left*: Black hole entropy against temperature for several values of the boundary rotation parameter  $\varepsilon$ , for  $\varepsilon < 2$ . The upper branches correspond to the large solutions and the lower branches to the small solutions. *Right*: Black hole energy as a function of temperature. Colouring codes the value of the boundary amplitude. The bold black curve is the Schwarzschild-AdS<sub>4</sub> solution with  $\varepsilon = 0$ . . . . . 120
- 5.12 *Left*: Gibbs free energy for the black holes against temperature for a fixed boundary rotation parameter  $\varepsilon = 1$  (red data points). The orange gridline shows the value for the corresponding AdS<sub>4</sub> soliton with the same  $\varepsilon$ . The grey solid curve traces the values of Schwarzschild-AdS<sub>4</sub>, and the grey-dashed gridline shows  $G_{\text{AdS}} = 0$ . *Middle*: Similar plot for  $\varepsilon = 1.5$ , with the horizontal gridline marking the intersection temperature  $T_{\text{HP}}(\varepsilon)$ . To the right of this line the large black holes will be the dominant solutions, whilst solitons dominate to the left. *Right*: As we approach the critical value of  $\varepsilon$ , the phase transition temperature decreases. . . . . 121
- 5.13 Gibbs free energy against the boundary parameter for low temperature black holes. It exhibits a swallowtail phase transition between the inelastic black hole phase and the soliton (brown stars). . . . . 122
- 5.14 Phase diagram for the rotationally polarised solutions. For  $\varepsilon < 2$ , black holes exist above  $T_{\min}(\varepsilon)$  (black data points) and are the dominant phase above the  $T_{\text{HP}}(\varepsilon)$  curve (red area) which marks the corresponding Hawking-Page transition. Below the transition line (red data points), the dominant phase is the soliton. For  $\varepsilon > 2$ , there is a cold inelastic black hole phase (red wedge). The elsewhere subdominant black holes exist up to some maximum  $\varepsilon_{\max}(T)$ , but are hidden by the soliton phase. 123

- 5.15 *Left:* Normal mode frequencies  $\omega$  with  $\ell = m$  vs the boundary rotation parameter  $\varepsilon$  for the soliton metric. At  $\varepsilon = 0$  these reduce to the usual AdS<sub>4</sub> frequencies  $L\omega = 3 + \ell$ . Dashed gridlines show where  $\varepsilon = 2$  (vertical) and  $\text{Re}\omega = 0$  (horizontal). *Right:* Rotation amplitude  $\varepsilon_\times$ , where  $\omega$  becomes negative, against  $m$ . The inset shows the logarithmic derivative of  $\varepsilon_\times$ . We expect that in the limit  $m \rightarrow \infty$ ,  $\varepsilon_\times \rightarrow 2$ . . . . . 125
- 5.16 *Left:* Real part of quasinormal mode frequency with  $\ell = m$  against the boundary rotation parameter  $\varepsilon$ , for small black holes with  $T = 1/\pi$ . At  $\varepsilon = 0$ , these reduce to the Schwarzschild-AdS<sub>4</sub> values. The bold dashed gridline shows the critical  $\varepsilon = 2$  value. *Right:* Rotation amplitude where the zero-mode is for a given  $m$ , against  $m$ . The inset shows the logarithmic derivative of  $\varepsilon_\times$ . We expect that in the limit  $m \rightarrow \infty$ ,  $\varepsilon_\times \rightarrow 2$ . 126
- 5.17 *Left:* Lowest lying mode eigenvalue of the boundary hamiltonian as a function of the boundary rotation parameter  $\varepsilon$ . At  $\varepsilon = 0$  these reduce to  $\ell + 1/2$ . *Right:*  $\varepsilon$  above which  $\lambda_{m,0}$  becomes negative, plotted as a function of  $m$ . The solid line represents our analytic approximation (5.38) valid at large  $m$ . . . . . 129
- 5.18 *Left:* Spin to mass ratio for a spinning test particle in the soliton background with boundary parameter  $\varepsilon = 0.1, 0.4, 1, 2, 2.5$  (corresponding colours vary from dark to light). Dashed black lines show analytic perturbative approximations (53) (pictured for  $\varepsilon \leq 2$ ) which, for small  $\varepsilon$ , are in a very good agreement with numerical solutions. *Right:* Spin to mass ratio for large black holes with  $T = 1/\pi$ , for  $\varepsilon = 0.1, 0.5, 1, 1.5, 1.93, 1.99$  (corresponding colours vary from dark to light). . . . . 132
- 5.19 *Left:* Minima of static potential,  $-g_{tt}$ , for the soliton against the boundary parameter. For  $\varepsilon < 2$ , there is a global minima at  $y = 0$ . For  $\varepsilon > 2$ , the minima is only local, owing to the fact that there is an ergoregion attached to the boundary. For the second branch, the local minima is on the  $x = 0$  axis, and for  $\varepsilon \gtrsim 2.43$ , the minima is no longer local. *Right:* Contour plot for  $-g_{tt}$  for the second branch soliton, at  $\varepsilon = 2.39$ . Black lines mark the contours, with the orange area around  $\theta = \pi/4$  (black dashed gridline) showing the ergoregion, and the fainter orange being the positive areas, where the function increases rapidly. Overplotted in blue are the zero contours of the Kretschmann scalar,  $K$ , whilst the shaded areas are the two minima with a steep maxima between them. . 133

- 
- 5.20 Entropy vs the boundary rotation parameter, when the metric is adjusted so that there is no ergoregion on the boundary. We observe two branches of black hole solutions which join up at some maximum value of  $\varepsilon$ . . . . 135
- 21 *Top left*: Log-linear plot of the DeTurck norm squared for the dominating soliton branch, at  $\varepsilon = 2.5$ . Straight line indicates exponential convergence. *Top right*: Log-linear plot of the relative error in the free energy  $G$  vs the grid size  $n$ , for the same data set as top left. *Bottom left*: Log-linear plot of the DeTurck norm squared vs grid size for a large black hole with  $T = 1/\pi$  and  $\varepsilon = 1.9875$ . *Bottom right*: Log-linear plot of  $\Delta_N G$  against  $n$ , for a cold ( $T = 0.2506$ ), small black hole, upper small branch ( $\varepsilon = 2.5$ ). . . . . 139
- 22 *Left*: Kretschmann scalar  $K$  for the dominant soliton branch,  $\varepsilon = 2.564$ . *Right*:  $K$  for a large black hole with  $\varepsilon = 1.9$ . . . . . 140
- 23 *Left*: Gibbs free energy against the boundary profile for black holes with a fixed temperature  $T = 1/\pi$  (black disks), and soliton (brown squares). The dashed gridline marks the  $\varepsilon \rightarrow 2$  limit. *Right*: Maximum of the Kretschmann invariant against  $\varepsilon$  for the small black hole with a fixed temperature. As  $\max K$  increases, the  $K$  looks very similar to that of the soliton. . . . . 141
- 24 Boundary energy-stress tensor components for a fixed low temperature ( $T = 0.2506$ ), where there are four possible black hole phases: lowest entropy black hole branch (brown squares), small black hole branch (yellow diamonds), thermodynamically dominant middle branch (faint blue triangles) and largest entropy large black holes (blue upside-down triangles). . . . . 142

# Chapter 1

## Introduction

### 1.1 Overview

General relativity is a remarkably rich theory. Black holes are deeply fascinating objects that contain spacetime singularities, and which are crucial for the study of strong field gravity wherein new phenomena arise. In four-dimensional flat space, the most general vacuum stationary solution is the Kerr black hole [1]. However, the presence of a negative cosmological constant allows for a considerably more exotic solution landscape.

The primary motivation for studying stationary black holes in these spaces stems from the anti-de Sitter/conformal field theory (AdS/CFT) correspondence, also known as the gauge/gravity duality [2]. Due to its far reaching implications, it has attracted a great deal of interest from a wide variety of researchers. The correspondence relates two seemingly distinct theories, namely gravity in asymptotically AdS spacetimes and certain quantum field theories. In particular, by studying stationary black hole solutions in classical supergravity, we can understand thermal states in the dual strongly coupled field theory at high energies, where direct calculations are largely inaccessible.

The AdS/CFT correspondence often requires both non-trivial, symmetry-breaking boundary conditions, and higher dimensions. Black hole uniqueness theorems do not necessarily hold in higher dimensions, and even asymptotically flat vacuum black holes can have non-spherical horizon topology. For instance, asymptotically flat solutions were constructed which have ring topology in  $d = 5$  [3], and also the remarkable black saturn

solution was found [4, 5]. Higher dimensional relativity was pioneered by Kaluza [6] and Klein [7], and emerged from attempts to unify gravity and electromagnetism. It marked a significant step in the quest to unify the fundamental forces of nature, which remains the overarching goal of theoretical physics. In modern times, it is anticipated that string theory will play a major role in the full theory of *quantum gravity*, as it naturally contains gravity, as well as provides an explanation of the microscopic origin of the entropy of certain black holes. String theory comes endowed with a number of extra dimensions in order to ensure consistency, which makes studying black hole solutions highly non-trivial, even in the low-energy limit, *supergravity*.

Due to the complexity, the construction of stationary solutions in asymptotically AdS spaces beyond the perturbative regime often requires the use of numerical methods. In this thesis we present various applications of contemporary numerical methods to construct novel stationary geometries in four and five dimensional asymptotically AdS spacetimes. In this chapter we briefly outline black hole instability in AdS, which aids the understanding of the non-uniqueness of the solution space. Next, we give a brief overview of the AdS/CFT correspondence, and the way in which it emerges from the dual description of the coincident D3-brane system in string theory. We also outline the dictionary between the gravitational theory and the corresponding field theory observables.

The remainder of this thesis is organised as follows. The second chapter 2 is dedicated to the numerical methods used to solve the Einstein equation in terms of the boundary value formulation. In chapters 3, 4 and 5 we investigate gravitational systems which, via the gauge/gravity duality, are used to study strongly coupled field theories. Chapters 3 and 4 are dedicated to analysing stationary hairy black holes in a consistent truncation of type IIB supergravity with  $\text{AdS}_5 \times \text{S}^5$  asymptotics, which is dual to strongly coupled  $\mathcal{N} = 4$  super Yang-Mills. Chapter 5 presents a study of a four-dimensional system with a rotating conformal boundary, and models CFTs on rotating backgrounds. This thesis concludes with a discussion and future prospects in chapter 6.

## 1.2 The gauge/gravity duality

The gauge/gravity duality maps a class of  $d$ -dimensional string theories with asymptotically anti de-Sitter boundary conditions, to certain conformal quantum field theories formulated in fewer dimensions. First proposed by Maldacena in the late '90s [2], it was further developed by [8, 9], and has since proven to be one of the most prominent achievements of contemporary theoretical physics<sup>1</sup>. While it remains a conjecture, since its discovery the duality has been supported by immense amount of evidence and a variety of non-trivial, robust tests. Much of its usefulness stems from the fact that is a strong-weak duality, meaning that when one of the sides of the correspondence is in principle solvable, the other is in a regime which is generically inaccessible with current analytic techniques. In particular, in the low energy limit in which the string theory in AdS is approximated by classical supergravity, the duality allows us to study strongly coupled field theories, and therefore explore novel, enticing phenomena.

In its original form, it is a conjecture of an equivalence between four-dimensional  $\mathcal{N} = 4$  Super-Yang-Mills (SYM) with gauge group  $SU(N)$  and coupling constant  $g_{\text{YM}}$  and ten-dimensional type IIB string theory with  $\text{AdS}_5 \times S^5$  asymptotics, string coupling  $g_s$  and string length  $\ell_s = \sqrt{\alpha'}$  [2]. The radius of curvature of both  $\text{AdS}_5$  and  $S^5$  is  $L$ . Furthermore, the field theory lives on the conformal boundary of  $\text{AdS}_5$ , which in global coordinates is the Einstein static Universe  $\mathbb{R}_t \times S^3$ . The two free parameters on the field theory side  $g_{\text{YM}}^2$  and  $N$  are identified with the free parameters  $g_s$  and  $L/\sqrt{\alpha'}$  on the string theory side via

$$g_{\text{YM}}^2 = 4\pi g_s \quad \text{and} \quad \lambda = L^4/\alpha'^2, \quad (1.1)$$

where the 't Hooft coupling is defined as  $\lambda = g_{\text{YM}}^2 N$ . The strongest form of the duality is valid for any value of  $N$  and 't Hooft coupling, in which the gravitational side is a quantum string theory. A weaker form of the correspondence is in the 't Hooft limit [11], where  $N \rightarrow +\infty$ , and  $\lambda$  is arbitrary but fixed, in which the dual theory contains classical strings. The conformal field theory is strongly coupled in the large 't Hooft limit when  $N \gg \lambda \gg 1$ , and corresponds to the low energy limit of the string theory, which is described by classical type IIB supergravity. In this limit the string length  $\ell_s$

---

<sup>1</sup>Due to the prominence and far reaching impact of the theory, there exists a plethora of pedagogical material on the AdS/CFT correspondence. In particular, the author enjoyed a recent review by Hubeny [10].

is small compared to radius of curvature, and any quantum corrections are suppressed. There are many nontrivial tests of the correspondence in this limit, some of which have been reviewed in [12].

The AdS/CFT correspondence can be motivated by considering D3-branes<sup>2</sup> from the open and the closed string perspective. In the weakest form of the correspondence, comparing these two complementary low energy descriptions leads us to identifying the gauge and the gravity theories. Consider a stack of  $N$  parallel D3-branes in 10-dimensional type IIB string theory in the limit where they become coincident. The vibrating open strings satisfy Dirichlet boundary conditions on D3-branes, and describe excitations of the branes, while closed strings propagate in the bulk. At sufficiently weak string coupling  $g_s N \ll 1$  and fixed  $N$ , the gravitational backreaction of the D3-branes is negligible. Taking the low energy limit  $\ell_s \rightarrow 0$ , only the massless string states are excited. The open string sector decouples, and gives modes localized on the branes which are governed by the four-dimensional  $\mathcal{N} = 4$  super Yang-Mills Lagrangian. The other set of massless modes is the closed bulk excitations described by 10-dimensional supergravity.

At strong coupling  $g_s N \gg 1$ , the branes backreact on the spacetime, and result in the extremal, asymptotically  $\mathbb{R}^{9,1}$  black 3-brane geometry

$$ds^2 = f(r)^{-1/2} \eta_{\mu\nu} dx^\mu dx^\nu + f(r)^{1/2} (dr^2 + r^2 d\Omega_5^2), \quad f(r) = 1 + \frac{4\pi g_s N \ell_s^4}{r^4}, \quad (1.2)$$

where  $x^\mu$  are the coordinates of the D3-brane worldvolume, and  $d\Omega_5^2$  is the metric on the unit  $S^5$ . Identifying  $L = (4\pi g_s N)^{1/4} \ell_s$ , the near horizon limit  $r \ll L$  gives

$$ds^2 = \frac{L^2}{r^2} dr^2 + \frac{r^2}{L^2} \eta_{\mu\nu} dx^\mu dx^\nu + L^2 d\Omega_5^2, \quad (1.3)$$

which has an enhanced symmetry and simplifies to a direct product  $\text{AdS}_5 \times S^5$ . Note that this solution has infinite proper distance along spacelike geodesics, and therefore the horizon is connected to the asymptotic region through an infinite *throat*. In the low energy limit, the near-horizon closed string sector is described by supergravity in  $\text{AdS}_5 \times S^5$ , and there is also a decoupled bulk string sector described by 10-dimensional supergravity. These two different descriptions leads us to identify the decoupled systems, and in particular, the strongly coupled  $\mathcal{N} = 4$  super Yang-Mills in  $3 + 1$  dimensions

---

<sup>2</sup>Recall that D-branes are solitonic solutions in the string theory, and can be regarded as Dirichlet boundary conditions of open strings. A flat  $Dp$ -brane is a  $\mathbb{R}^{p,1}$  submanifold.

corresponds to the near horizon region of the black brane with  $\text{AdS}_5 \times \text{S}^5$  geometry. These two low energy descriptions of the D3-brane system are valid in different regimes for the coupling constants, however, the fact that the gauge theory is well defined at any coupling lends support to the strongest form of the duality, which was conjectured by Maldacena.

An immediate test for these ideas can be performed by matching the global symmetries of the two theories.  $\text{AdS}_5$  has isometry group  $SO(4, 2)$ , and  $\text{S}^5$  has isometry group  $SO(6)$ , so the full bosonic symmetry is  $SO(4, 2) \times SO(6)$ . On the field theory side, the maximal bosonic subgroup of the four-dimensional conformal group is  $SU(2, 2) \simeq SO(4, 2)$ , which regards the Poincaré and special conformal transformations, and the global R-symmetry that rotates the six scalar fields and the four fermions is  $SU(4) \simeq SO(6)$ , hence the bosonic subgroup of  $\mathcal{N} = 4$  SYM is  $SO(4, 2) \times SO(6)_R$ . Both sides have 32 supersymmetries, which are Killing spinors on the gravity side, and a superconformal algebra on the CFT side.

The radial bulk direction  $r = L^2/z$  is associated with the energy scale in the gauge theory. In particular, the conformal boundary of AdS  $z = 0$  is naturally identified with the UV/the short distance/high energy gauge theory, leading to a *holographic* notion of the correspondence. In this sense, it is commonly said that the field theory *lives on the boundary* of AdS.

Black holes provide a fundamental probe for quantum gravity. These solutions of classical general relativity are accompanied by curvature singularities, in the vicinity of which the gravity description is commonly thought to break down, and new exotic physics should appear. Further, black hole horizon area and surface gravity are related to thermodynamic quantities such as the classical Bekenstein-Hawking entropy and the black hole temperature. Hawking [13] showed semi-classically that temperature can be understood in terms of quantum particle creation. Thermodynamic entropy should be equal to the statistical entropy, as it gives an account of the number of microscopic degrees of freedom of a system, which should be a universal constraint. It emerges that black hole entropy can be understood in terms of microstates, which are quantum mechanical objects.

The first statistical black hole entropy counting in string theory was accomplished by Strominger and Vafa [14], for a class of asymptotically flat five-dimensional supersymmetric Reissner-Nordström black holes, which can be obtained as a consistent

Kaluza-Klein reduction of the higher dimensional supergravity. The work by Strominger and Vafa launched an active enterprise of reproducing the microscopic entropy of a variety of black hole solutions. However, an analogous calculation for asymptotically AdS black holes has been done only recently, even though AdS/CFT provides a natural framework to analyse the microscopic description of black holes by studying well-defined quantum field theories. However, even in the low energy limit, when the string theory side reduces to a classical supergravity calculation, the duality is hard to study, since the field theory side is strongly coupled. Generally, to obtain the entropy of the semi-classical black holes in the strong coupling regime, we rely on supersymmetry which allows us to perform weak coupling string calculations. The supersymmetric AdS black holes are dual to CFT states which are in Bogomolnyi–Prasad–Sommerfield (BPS) representations and hence weak coupling calculations do not receive quantum corrections.

The entropy counting was successfully performed for the AdS<sub>3</sub> BTZ black holes in [15], and very recently for supersymmetric AdS<sub>4</sub> black holes dual to certain phases of topologically twisted deformation of ABJM theory [16, 17] (for a recent review see *e.g.* [18]). Achieving this calculation for Maldacena’s original correspondence, *i.e.* for a class of five-dimensional rotating AdS black holes in terms of states of the dual  $\mathcal{N} = 4$  SYM, remains a major open problem, due to the immense complexity of the dual CFT. We will discuss this problem in more detail in chapter 4, and attempt to shed some light from the gravitational point of view.

### 1.3 The dictionary

The framework of [8, 9] was developed alongside a dictionary identifying the observables in CFT with quantities in AdS, enabling us to perform concrete holographic calculations. The gauge/gravity duality equates the string partition function to the generating functional of the field theory correlators

$$Z[\Phi] = \int_{\phi} D\Phi \exp iS[\Phi] = W_{\text{CFT}}[\phi], \quad (1.4)$$

where  $\Phi$  denotes all fields and  $\phi$  is a field parametrizing the boundary condition of  $\Phi$  at infinity. Boundary conditions for the bulk fields serve as sources that couple to dual operators. In the large  $N$  limit, one can compute correlation functions of the

CFT operators by differentiating the supergravity on-shell action with respect to the sources.

The on-shell classical supergravity action exhibits infinite volume divergences due to the cosmological constant. These IR (long distance) divergences in supergravity are related to UV divergences of the correlation functions in the dual CFT [19]. In order to make this prescription well-defined, a suitable renormalization must be performed. On the gravitational side, this is achieved by the procedure of *holographic normalization* [20–22] (for an extensive review see [23] and references therein). For instance, given a classical action  $S[\phi, A_\mu, g_{\mu\nu}]$  with the corresponding renormalized on-shell action  $S_{\text{ren}}$ , the bulk fields  $\phi, A_{\mu\nu}, g_{\mu\nu}$  couple to the respective renormalised one-point functions

$$\begin{aligned}\langle \mathcal{O}(x) \rangle &= -\frac{1}{\sqrt{\det g_{(0)}}} \frac{\delta S_{\text{ren}}}{\delta \phi_{(0)}(x)}, \\ \langle J_\mu(x) \rangle &= \frac{1}{\sqrt{\det g_{(0)}}} \frac{\delta S_{\text{ren}}}{\delta A_{(0)}^\mu(x)}, \\ \langle T_{\mu\nu}(x) \rangle &= \frac{2}{\sqrt{\det g_{(0)}}} \frac{\delta S_{\text{ren}}}{\delta g_{(0)}^{\mu\nu}(x)}.\end{aligned}\tag{1.5}$$

Here  $J_\mu$  is the boundary symmetry current,  $T_{\mu\nu}$  is the boundary stress-energy tensor,  $\mathcal{O}(x)$  is the dual operator to the scalar field, and the functional differentiation is with respect to the corresponding source on the boundary. These renormalised one-point functions are related to certain coefficients in the asymptotic expansion of the bulk fields, and in practice can be read off once the gravity solution is constructed.

Any asymptotically AdS spacetime in  $d$  dimensions can be expressed in Fefferman-Graham (FG) coordinates [24, 25] about the conformal boundary  $z = 0$  as

$$ds^2 = \frac{L^2}{z^2} \left( dz^2 + g_{\mu\nu}(x, z) dx^\mu dx^\nu \right),\tag{1.6}$$

where  $g_{\mu\nu}$  admits an expansion in terms of the coordinate  $z$

$$g_{\mu\nu}(x, z) = g_{\mu\nu}^{(0)}(x) + \dots + z^{(d-1)} g_{\mu\nu}^{(d-1)}(x) + \mathcal{O}(z^d).\tag{1.7}$$

Here  $L$  is the AdS radius and is related to the cosmological constant via  $\Lambda = -(d-1)(d-2)/2L^2$ , and  $x^\mu$  are the boundary coordinates. The free coefficient of the expansion is  $g_{\mu\nu}^{(0)}(x)$ , which represents the boundary metric that typically is fixed by the

required boundary conditions. The coefficient  $g_{\mu\nu}^{(d-1)}(x)$  is related to the stress-energy tensor and is fixed by the regularity in the bulk. The exponents in the expansion will depend on the exact contents of the gravitational theory. The Fefferman-Graham expansion makes a direct link with the dual field theory, which lives on the boundary  $z = 0$  with the  $d - 1$ -dimensional metric  $g_{\mu\nu}|_{z=0}$ .

Once the desired form of the metric is obtained, the expectation value of the holographic stress-energy tensor can be extracted as

$$\langle T_{\mu\nu}(x) \rangle = \frac{(d-1)L^{d-2}}{16\pi G_N} g_{\mu\nu}^{(d-1)}(x), \quad (1.8)$$

where  $d$  is even, and  $G_N = g_s^2 l_s^{d-3}$  is Newton's constant. In odd dimensions an extra additive logarithmic term is present in the FG expansion (1.7),  $z^{d-1} \log z^2 \tilde{g}_{\mu\nu}^{(d-1)}$ , and the dual CFT stress tensor (1.8) has an additional,  $d$  dependent, contribution due to the conformal anomalies of the boundary CFT. The prescription of holographic normalization provides a method to compute finite conserved asymptotic charges of the gravitational theory, such as energy and angular momentum, via the holographic stress tensor (1.8).

Let us consider a toy example in a form of a minimally coupled scalar field  $\phi(x, z)$  with mass  $m_\phi$  in  $AdS_{d+1}$ , for which Poincaré coordinates can be recovered by taking  $g_{\mu\nu}(x, z) = \eta_{\mu\nu}$ . The conformal dimension of the dual operator  $\mathcal{O}_\phi$  is given by the relation  $m_\phi^2 L^2 = \Delta(\Delta - d)$ . The bulk action for the scalar reads

$$S[\phi] = -\frac{1}{2} \int dz d^d x \sqrt{-\det g} (g^{\mu\nu} \partial_\mu \phi \partial_\nu \phi + m_\phi^2 \phi^2), \quad (1.9)$$

and the equation of motion is the Klein-Gordon equation

$$(\square_g - m_\phi^2)\phi = 0. \quad (1.10)$$

It is straightforward to check that this equation admits two independent solutions scaling near the boundary  $z = 0$  as  $z^{\Delta_\pm}$ , so that asymptotically

$$\phi(z, x) = A_+(x)z^{\Delta_+} + A_-(x)z^{\Delta_-} + \dots, \quad \text{with} \quad \Delta_\pm = \frac{d}{2} \pm \sqrt{\frac{d^2}{4} + m_\phi^2 L^2}. \quad (1.11)$$

The stability of AdS requires  $\Delta_{\pm}$  to be real, which demands that the scalar field satisfies the Breitenlöhner-Freedman (BF) bound [26]

$$m_{\phi}^2 L^2 \geq -\frac{d^2}{4}, \quad (1.12)$$

which means that  $m_{\phi}^2 < 0$  is allowed, and the field can be tachyonic. Another important bound is the unitarity bound on scaling dimensions of operators in the CFT,  $m_{\text{u}}^2 = m_{\text{BF}}^2 + 1/L^2$ . Scalars with masses  $m_{\phi}^2 \geq m_{\text{u}}^2$  have the normalisable mode  $A_+$ , and the non-normalisable mode  $A_-$ . Typically the non-normalisable mode  $A_-$  sources the boundary operator with conformal dimension  $\Delta_-$ , and its one-point function (vev)  $\langle \mathcal{O}_{\phi} \rangle$  is given by the coefficient  $A_+$  of the normalisable mode. Scalars with  $m_{\text{BF}}^2 < m_{\phi}^2 < m_{\text{u}}^2$  have two normalisable modes. In this case there are various boundary conditions possible which determine the physics of the dual field theory, and whether the field theory is deformed by relevant, irrelevant or marginal operators (for a summary see *e.g.* [27]).

In particular, for  $m_{\phi}^2 = m_{\text{BF}}^2$ , the asymptotic expansion is

$$\phi(z, x) = z^{\Delta_{\text{BF}}} (A_+(x) + A_-(x) \log z) + \dots, \quad (1.13)$$

where the logarithmic term represents a non-normalizable mode that renders AdS unstable [28], and we impose  $A_- = 0$ .

More broadly, at large  $N$  and strong coupling, AdS black holes are high-energy thermal states in the dual field theory. In particular, they are typically the dominant saddle points in the high temperature regime of the canonical ensemble. By studying the black hole solution space in the supergravity limit we can learn about the thermal states of the strongly coupled dual CFT at energies of order  $N^2$  [29]. For instance, the Hawking-Page transition [30] between thermal AdS and large black holes corresponds to the confinement-deconfinement transition on a sphere of the dual CFT [31].

## 1.4 Hairy black holes in AdS

Black hole instability can be instigated by the existence of a marginal, or zero, mode<sup>3</sup> of linear scalar or gravitational perturbations. This often indicates that a new branch of stationary solutions is present, which can significantly enrich the phase diagram. In this section we discuss a few examples of such instabilities, which are relevant to the construction of solutions presented in this thesis.

The canonical example which demonstrates the link between black hole non-uniqueness, instabilities and the appearance of zero frequency modes is the Gregory-Laflamme instability, which affects black strings and black branes in higher dimensions [32]. These objects are unstable to gravitational perturbations along their extended directions, and the solutions branching from the onset of the instability are non-uniform black strings and localized black holes. The nonlinear evolution of five-dimensional black string has been simulated numerically in [33], where the formation of a fractal structure of the horizon was observed. It was shown that the string breaks in finite asymptotic time, thereby leading to the violation of cosmic censorship due to the topological change of the horizon. This instability affects sufficiently small Schwarzschild black holes in global  $\text{AdS}_5 \times \text{S}^5$  [34–36], which were recently constructed in [37].

Another crucial instability which yields new stationary solutions is *superradiance*, the study of which was pioneered by [38–45] in the asymptotically flat context (for an extensive review see [46]). The first quantitative study involving rotating black holes in AdS featured in [47–50]. The rotating black holes in AdS with sufficient angular velocity,  $\Omega_H$ , can have ergoregions, which act as reservoirs for negative energy for scattering waves with azimuthal quantum number  $m$  and frequency<sup>4</sup>  $0 < \omega < m\Omega_H$ . If a rotating black hole with an ergoregion is surrounded by a confining potential resulting from AdS, or by a mass term [43, 51] in asymptotically flat spacetimes, such a process will be recurrent, eventually leading to an instability. The superradiant instability is connected to the appearance of asymptotically AdS hairy black hole branches with neutral scalar hair [48], or gravitational hair [52]. However, these solutions have  $\Omega_H L > 1$ , where  $L$  is the radius of AdS, and are themselves superradiantly unstable to higher azimuthal modes [53]. The endpoint of this instability seems to be outside

<sup>3</sup>The imaginary part of the mode frequency  $\omega$  determines the stability under the perturbation. Modes with  $\text{Im}(\omega) = 0$  are marginal, and zero frequency modes in addition have  $\text{Re}(\omega) = 0$ .

<sup>4</sup>For simplicity, here we consider black holes which are not charged.

the reach of current numerical methods in AdS, however, in [48, 52, 54] it has been argued that the instability is likely to lead to a pointwise violation of the weak cosmic censorship conjecture in AdS.

There are at least two instabilities affecting the Reissner-Nordström type solutions in AdS-Maxwell-Scalar theories whereby the charged black hole acquires scalar field hair. On the one hand, instability of RNAdS black holes can be driven by *charged superradiance*. The sufficiently charged scalar field scattering off the charged black hole becomes amplified *ad infinitum* due to the reflective nature of the conformal boundary of AdS, leading to the instability [55–58, 53]. The condition for the scattering now is  $\omega < \mu e$ , where the scalar field has frequency  $\omega$  and charge  $e$ , and the black hole has chemical potential  $\mu$ . Unlike the rotating case, the endpoint of the superradiant instability is understood better, and it has recently been shown that the four-dimensional RNAdS indeed evolves towards the hairy solution [59]. Charged black holes with charged scalar hair were constructed in [60–64].

On the other hand, the near extremal black holes are unstable against the tachyonic condensation of a scalar field, if the effective mass of the scalar field due to the coupling of the scalar to the Maxwell field violates the effective near horizon Breitenlöhner-Freedman (BF) bound [26]. The BF bound governs the perturbative stability of scalar fields in the  $\text{AdS}_d$  spacetime, and is given by  $m_{\text{BF}}^2 = -(d-1)^2/4L_d^2$ , where  $L_d$  is the radius of curvature of the spacetime. In fact neither the scalar field nor the black hole need be charged [65–67], but the charge exacerbates the instability. This process was shown to occur dynamically by [68] with the endpoint being the hairy black holes of [66, 69]. For example, consider a four-dimensional extremal Reissner-Nordström black hole with AdS asymptotics and a horizon with planar topology. The near-horizon geometry in this case is  $\text{AdS}_2 \times \mathbb{R}^2$ , and it turns out that the BF bound for the  $\text{AdS}_2$  factor is greater than that of the asymptotic  $\text{AdS}_4$ . Therefore, the instability is present even for neutral scalar fields if their mass violates the two-dimensional BF bound. This instability has found various applications to superconductivity based on the gauge/gravity correspondence.

Concepts from the gauge/gravity duality have been used to model various phase transitions in condensed matter systems, such as superfluids or superconductors [65, 69, 66]. In this area, a bottom-up approach is usually taken, where a manageable gravitational theory is used to gain insight into the behaviour of strongly coupled field theories. A minimal holographic superconductor model is the four-dimensional planar

RNAdS black hole with a minimally coupled charged scalar field, also known as the Abelian-Higgs model. At low temperatures  $T < T_c$ , the charged black hole is unstable to the formation of scalar hair due to the effective mass of the scalar violating the near-horizon BF bound. The hairy phase describes the superconducting phase with order parameter  $\langle \mathcal{O}_\phi \rangle$ , and the normal phase for  $T > T_c$  is the stable RNAdS solution. The AdS/CMT correspondence is a thriving area of research, for which there is plenty of excellent review material available, *e.g.* see [70–73].

# Chapter 2

## Numerical Construction of Stationary Solutions in AdS

### 2.1 The Einstein equation

The theory of general relativity is described by a set of coupled non-linear second order partial differential equations for the metric tensor  $g_{\mu\nu}$ , together with gauge and matter fields, on a  $d$ -dimensional Lorentzian spacetime manifold  $\mathcal{M}$ . In the fully non-linear, strong-field regime, analytic methods for solving the equations are scarce and have considerable limitations, which necessitates the use of numerical techniques to make meaningful progress. In the last couple of decades, the field of numerical relativity has enjoyed a tremendous amount of success. Some of the most notable results include the simulation of gravitational collapse [74] and simulation of black hole binary inspiral (for a review see *e.g.* [75]), which has recently been observed in a breakthrough detection of gravitational waves at LIGO [76, 77].

Notwithstanding the dynamical nature at the heart of general relativity, stationary solutions play a key role in understanding the full breadth of the theory. Finding stationary solutions aids the understanding of the global structure of the phase space, which provides insights into the properties of the stable solutions. In addition, obtaining suitable initial conditions can be a non-trivial problem in itself, once spherical symmetry is broken. Lastly, even if a steady-state can be reached through the dynamical evolution,

it would require considerable resources and would be complicated to implement in practice.

The Einstein equation does not have a definite character due to the underlying diffeomorphism invariance. It was shown in [78] that in the harmonic gauge, in which the coordinates satisfy the wave equation, the Einstein equation is strongly hyperbolic. This implies that the initial value problem is locally well-posed, allowing for dynamical time evolution.

Finding stationary solutions amounts to formulating a well-posed boundary value problem, for which the elliptic description of the equations is preferred. The Einstein equation can be modified to have the elliptic signature via the DeTurck method first introduced by Headrick, Kitchen and Wiseman [79] (for reviews see [80, 27]). This is an elegant and versatile algorithm which can be implemented for a wide class of metrics, and recently has been extensively employed in numerical construction of various asymptotically AdS solutions. Ellipticity was shown for static vacuum metrics in [79], and was generalised to include stationarity with the Lorentzian signature in [81]. In this chapter we will briefly outline the DeTurck method and the numerical techniques that have been used throughout this thesis.

## 2.2 The Einstein-DeTurck equation

### 2.2.1 Ellipticity

Consider the  $d$ -dimensional Einstein equation with a cosmological constant  $\Lambda$ ,

$$R_{\mu\nu} = \frac{2\Lambda}{d-2}g_{\mu\nu}, \quad (2.1)$$

where  $g_{\mu\nu}$  is the metric tensor and  $R_{\mu\nu}$  is the Ricci tensor. The following discussion can be generalised to include matter fields and gauge fields, for instance see [27]. There are  $d(d+1)/2$  equations for the same number of the metric components, owing to the fact that  $R_{\mu\nu}$  and  $g_{\mu\nu}$  are symmetric. The Ricci tensor obeys the contracted Bianchi identity

$$\nabla_{\mu} \left( R^{\mu\nu} - \frac{1}{2} g^{\mu\nu} R \right) = 0, \quad (2.2)$$

where  $\nabla$  is the Levi-Civita connection associated to the metric  $g_{\mu\nu}$ , and  $R$  is the trace of the Ricci tensor. This represents additional  $d$  constraints, *i.e.* there are only  $d(d-1)/2$  independent equations, implying that the Einstein equation is underdetermined. Therefore, we need to place  $d$  conditions on the coordinates to fix the gauge degrees of freedom in order to make the PDE system well posed.

Suppose that  $g_{\mu\nu}$  is a static Lorentzian metric which is analytically continued to the Euclidean signature. Under small metric perturbations  $g_{\mu\nu} \rightarrow g_{\mu\nu} + h_{\mu\nu}$ , the Ricci tensor locally transforms as

$$\delta R_{\mu\nu} = \Delta_L h_{\mu\nu} + \Delta_{(\mu} v_{\nu)}, \quad (2.3)$$

where

$$\Delta_L h_{\mu\nu} = -\frac{1}{2}\nabla^2 h_{\mu\nu} - R_{\mu}{}^{\rho}{}_{\nu}{}^{\sigma} h_{\rho\sigma} + R_{(\mu}{}^{\rho} h_{\nu)\rho}, \quad v_{\mu} = \nabla_{\nu} h^{\nu}{}_{\mu} - \frac{1}{2}\partial_{\mu} h. \quad (2.4)$$

Let us consider the operator  $\Delta_R h_{\mu\nu} = \delta R_{\mu\nu}$ . The principal part of  $\Delta_R$ , determining the character of the partial differential equations, is governed by the second order metric derivatives and reads

$$\mathcal{P}h_{\mu\nu} = \frac{1}{2}g^{\rho\sigma} \left( -\partial_{\rho}\partial_{\sigma}h_{\mu\nu} + 2\partial_{\rho}\partial_{(\mu}h_{\nu)\sigma} - \partial_{\mu}\partial_{\nu}h_{\rho\sigma} \right). \quad (2.5)$$

For the Einstein equation to be elliptic with respect to some background, we wish for any perturbation of the form  $h_{\mu\nu} = H_{\mu\nu}e^{ik_{\sigma}x^{\sigma}}$ , where  $H_{\mu\nu}$  is constant and  $k_{\mu} \in \mathbb{R}_{>0}^d$ , to give  $\mathcal{P}h_{\mu\nu} \neq 0$  for all  $x$  in  $\mathcal{M}$ . Interpreted physically, this requirement can be regarded as forbidding wave-like propagation of short wavelength perturbations.

The perturbation can be decomposed in the form  $h_{\mu\nu} = \tilde{h}_{\mu\nu} + \partial_{(\mu}w_{\nu)}$ , with  $\partial_{\mu}\tilde{h}^{\mu}{}_{\nu} - \frac{1}{2}\partial_{\nu}\tilde{h} = 0$ . Then it follows that  $\mathcal{P}h_{\mu\nu} = \mathcal{P}\tilde{h}_{\mu\nu}$ , which demonstrates that the operator  $\mathcal{P}$  removes infinitesimal diffeomorphisms generated by the vector field  $w^{\mu}$ . The remaining part is manifestly elliptic

$$\mathcal{P}\tilde{h}_{\mu\nu} = -\frac{1}{2}\partial^{\rho}\partial_{\rho}\tilde{h}_{\mu\nu}, \quad (2.6)$$

*i.e.* the pure gauge fluctuations are spoiling the ellipticity. Let us consider the 1-form

$$\xi_{\mu} = g^{\rho\nu} \left( \partial_{\rho}g_{\nu\mu} - \frac{1}{2}\partial_{\mu}g_{\rho\nu} \right), \quad (2.7)$$

which locally varies as  $\delta\xi_\mu = \partial_\mu h^\mu{}_\nu - \frac{1}{2}\partial_\nu h = 0$ . Demanding  $\partial_\mu h^\mu{}_\nu - \frac{1}{2}\partial_\nu h = 0$ , i.e.  $\delta\xi_\mu = 0$ , is equivalent to imposing *the harmonic gauge*. The gauge fixing condition for the chart  $x^\mu$ , when the coordinates are regarded as scalar functions, can be written in a more familiar form as

$$\xi^\mu = g^{\rho\nu}\Gamma_{\rho\nu}^\mu = -\nabla^2 x^\mu = 0. \quad (2.8)$$

The condition  $\xi^\mu = 0$  eliminates the pure gauge degrees of freedom, as it imposes  $d$  constraints on the coordinates. However, the harmonic gauge is local and we would like to obtain a covariant formulation.

Suppose we pick an appropriate reference metric  $\tilde{g}_{\mu\nu}$  on  $\mathcal{M}$  of our choice such that it possesses the same causal structure of our desired solution  $g$ , and covariantly define

$$\xi_\mu = g^{\rho\nu}(\tilde{\nabla}_\rho g_{\nu\mu} - \frac{1}{2}\tilde{\nabla}_\mu g_{\nu\rho}), \quad \xi^\mu = g^{\nu\rho}(\Gamma_{\nu\rho}^\mu - \tilde{\Gamma}_{\nu\rho}^\mu). \quad (2.9)$$

Here  $\tilde{\Gamma}_{\rho\nu}^\mu$  is the associated Levi-Civita connection for  $\tilde{g}_{\mu\nu}$ , and  $\tilde{\nabla}_\mu$  is the covariant derivative with respect to  $\tilde{g}_{\mu\nu}$ .  $\xi^\mu$  is *the DeTurck vector*, and is globally defined through the difference between two connections, which is a tensor.

The gauge fixing condition  $\xi^\mu = 0$ , termed *the generalised harmonic gauge* [79, 80], is a differential equation for the metric. We will be solving the condition simultaneously with the Einstein equation (2.1), by combining the two to form the Einstein-DeTurck equation (also known as Harmonic Einstein equation)

$$R_{\mu\nu}^H = R_{\mu\nu} - \nabla_{(\mu}\xi_{\nu)} = \frac{2\Lambda}{d-2}g_{\mu\nu}, \quad (2.10)$$

where we defined the modified Ricci tensor  $R_{\mu\nu}^H = R_{\mu\nu} - \nabla_{(\mu}\xi_{\nu)}$ . Under local linear metric perturbations the Ricci tensor transforms as

$$\delta R_{\mu\nu}^H = \Delta h_{\mu\nu} = \Delta_L h_{\mu\nu} - \frac{1}{2}\mathcal{L}_\xi h_{\mu\nu} + \nabla_{(\mu}u_{\nu)}, \quad u^\mu = (\Gamma_{\nu\rho}^\mu - \tilde{\Gamma}_{\nu\rho}^\mu)h^{\nu\rho}, \quad (2.11)$$

where  $\mathcal{L}_\xi$  is the Lie derivative with respect to the field  $\xi$ . From here we find that the principal part of the equation is

$$\mathcal{P}h_{\mu\nu} = -\frac{1}{2}g^{\rho\sigma}\partial_\rho\partial_\sigma h_{\mu\nu}. \quad (2.12)$$

The perturbation  $h_{\mu\nu} = H_{\mu\nu}e^{ik_\sigma x^\sigma}$  gives  $\mathcal{P}h_{\mu\nu} = H_{\mu\nu}k^2 \neq 0$  for non-zero  $H_{\mu\nu}$  and  $k_\mu$ . Hence the Einstein-DeTurck equation is strictly elliptic for Euclidean signature, and strongly hyperbolic for Lorentzian signature.

### 2.2.2 Stationarity

For static metrics the Einstein-DeTurck equation is invariant under the analytic time continuation, and hence remains elliptic for Lorentzian metrics. We wish to generalize the ellipticity argument to non-extremal, asymptotically AdS vacuum black holes, for which the Killing vector field  $\partial_t$  is not always globally timelike. In particular, we focus on rotating black holes with an ergoregion, which have a timelike (outside ergoregion) Killing vector  $T$ , the norm of which is vanishing on the horizon or at the ergosurface. For simplicity, we will assume a single Killing horizon.

The metric class ansatz is motivated by the rigidity theorem for stationary black holes, including those in higher dimensions [82, 83], which ensures the axisymmetry once certain conditions are met. Let  $(\mathcal{M}, g)$  be a stationary (analytic) asymptotically AdS (or flat) vacuum black hole spacetime. Suppose that  $T^\mu$  is a stationary killing vector field, which is not necessarily globally timelike. Then for a sufficiently well behaved horizon of such a black hole, there exists a Killing field  $K^\mu$  which is normal to the horizon and commutes with  $T^\mu$ . In addition, there exists a non-empty set of mutually commuting Killing fields  $R^\mu$  commuting with  $T^\mu$ . The fields generate asymptotic spatial rotations with period  $2\pi$ . It follows that  $K^\mu$  is the Killing horizon generator and can be written as a linear combination  $K^\mu = T^\mu + \sum_i \Omega_i R_{(i)}^\mu$ , where  $\Omega_i$  are constant angular velocities at each rotation plane.

The Lorentzian metric ansatz which is adapted to the isometries  $\{T, R_{(i)}\}$ , and is manifestly stationary can be written as

$$ds^2 = G_{AB}(x)(dy^A + C_i^A(x)dx^i)(dy^B + C_j^B(x)dx^j) + h_{ij}(x)dx^i dx^j, \quad (2.13)$$

where  $T = \partial_t$ ,  $R^i = \partial_{y^i}$ , coordinates  $y^A = \{t, y^i\}$  are associated with the rotational<sup>1</sup> (or translational) isometries. The indices  $A, B$  indicate the Killing directions, and  $i, j$  are the indices on  $\mathcal{M}$ , and  $G_{AB}$  is Lorentzian outside the horizon. We note that all

<sup>1</sup>For rotational isometries the corresponding orbit is normalised to have period  $2\pi$ , therefore we identify  $y^i \sim y^i + 2\pi$ .

hitherto known stationary solutions have vanishing  $C_i^A = 0$ , and obey the additional discrete symmetry  $t \rightarrow -t$ ,  $y^i \rightarrow -y^i$ .

The Lorentzian spacetime can be regarded as fibration of the orbits of the mutually commuting set  $\{T^\mu, R_{(i)}^\mu\}$  over a base manifold  $\mathcal{M}$ . We will assume that the orbit space  $(\mathcal{M}, h)$  is a smooth Riemannian manifold, having boundaries at the Killing horizon and axes of the rotational symmetries. This implies that there always exist a combination of  $\{T, R_{(i)}\}$  that is timelike outside the horizon.

Consider the Einstein-DeTurck equation for the metric. We note here that we choose the reference metric  $\tilde{g}$  to share the isometries  $\{T, R_{(i)}\}$  with  $g$ , to make sure that the harmonic operator  $R_{\mu\nu}^H$  has the same symmetries as the original metric. This ensures that our numerical method preserves the class of stationary metrics (2.13). The second order derivative terms are

$$\begin{aligned} R_{AB}^H &= -\frac{1}{2}h^{kl}\partial_k\partial_l G_{AB} + \dots, \\ R_{Ai}^H &= -\frac{1}{2}h^{kl}\partial_k\partial_l(G_{AB}C_i^B) + \dots, \\ R_{ij}^H &= -\frac{1}{2}h^{kl}\partial_k\partial_l(h_{ij} + G_{AB}C_i^A C_j^B) + \dots, \end{aligned} \tag{2.14}$$

and the character is governed by the Riemannian metric  $h_{ij}$ , therefore implying ellipticity.

We also note that the Deturck method has been successfully used to numerically construct certain classes of geometries for which ellipticity has not been shown or does not hold, such as solutions with helical Killing vector fields, for instance, black resonators [52] and geons [84], and flowing geometries, which do not possess a Killing horizon [85, 86].

In order to obtain a well-posed boundary problem, we also need suitable boundary conditions. A physical set of boundary conditions at the conformal boundary of AdS ensures the desired asymptotic behaviour, which determines the properties of the dual CFT. In the Lorentzian signature, the black hole horizon is regarded as a boundary, at which the boundary conditions are prescribed by the requirement of the horizon regularity. The DeTurck method also fixes the surface gravity associated with the horizon generator, which can be useful for the analysis of the canonical ensemble. For the stationary solutions, axes of symmetries of the rotational isometries are also regarded as boundaries, where suitable regularity conditions must be imposed. A more

detailed treatment of the boundary conditions for the metric (2.13) can be found, e.g. in [27].

### 2.2.3 Ricci solitons

Solutions of the Einstein-DeTurck equation that do not solve the Einstein equation, i.e. have  $\xi^\mu \neq 0$ , are called *Ricci solitons*. It has been shown in [80] that they do not exist for static metrics with a number of physically motivated boundary conditions. The argument was extended to stationary spacetimes possessing a  $(t, \phi) \rightarrow -(t, \phi)$  reflection symmetry [87], including metrics which are asymptotically AdS.

Ellipticity guarantees that solutions are locally unique, thus the Ricci solitons can be distinguished from the solutions with  $\xi^\mu = 0$  in almost all moduli space. We can thus monitor the norm of  $\xi^\mu$  to provide a global measure of our numerical integration scheme. Practically we check *a posteriori* that  $\max \xi^\mu \xi_\mu = 0$  is satisfied to required precision, and also demonstrate expected convergence properties in accord with the numerical method used. In particular, this is important once the matter fields are included.

## 2.3 The Newton-Raphson method

We will solve the resulting PDE system using relaxation methods, which iteratively adjust the initial seed vector according to the linearised operator, until a solution to the equations is obtained within desired error tolerance. Suppose we wish to solve a system of  $n$  non-linear second order PDE's

$$F_i[\mathbf{u}] = 0, \quad i = 1, \dots, n. \quad (2.15)$$

Here  $\mathbf{u}$  is a vector of  $n$  unknown functions which appear in a metric ansatz, and depend on some number of coordinates  $\mathbf{x}$ . Taylor expansion about a point  $\mathbf{u}^{(k)}$  to first order is

$$F_i[\mathbf{u}] = F_i[\mathbf{u}^{(k)}] + \frac{\delta F_i}{\delta u_j}[\mathbf{u}^{(k)}] \delta u_j + \mathcal{O}(\delta u^2), \quad (2.16)$$

where  $\delta u_j = u_j - u_j^{(k)}$ , and therefore a better approximation to the true solution is given by

$$\tilde{u}_i = u_i^{(k)} - \left( \frac{\delta F}{\delta u} [\mathbf{u}^{(k)}] \right)^{-1}_{i,j} F_j[\mathbf{u}^{(k)}]. \quad (2.17)$$

This describes the iterative procedure, whereby starting with a suitable seed vector  $\mathbf{u}^{(0)}$  we obtain a successively better approximation to the true solution. We note that this is to be solved subject to appropriate linearised boundary conditions.

One advantage of Newton's method is the rate of convergence, which is typically quadratic in the number of iterations. However, the initial seed has to lie in the basin of attraction, which often requires some luck. The attraction region depends on a number of factors, such as the choice of the reference metric and the position in the parameter space. For the kinds of metrics considered in this thesis, namely hairy black holes and deformed geometries, there fortunately exist parameters continuously connected to a known geometry. In order to ensure that the method converges to a new solution branch, we can impose suitable boundary conditions which enforce desired qualities of the solution. We then are able to explore the moduli space deep into the non-linear regime by varying the governing parameters. However, generally it can be difficult for the method to converge onto a new branch if the background solution is too attractive, or if the boundary conditions are rather particular. In some cases it is possible to find eigenfunctions associated with zero modes, which then can provide a good initial seed.

Another challenge for Newton's method is the turning points in solution space. If there exists a maximum value of a parameter describing a family of solutions which is not due to singular behaviour, a jump between basins of attraction is required in order to obtain the second branch. Sometimes a better parameter can be found instead, which uniquely characterises the family, however, generically it is necessary to perturb the solution in the vicinity of the curving point towards the new region.

## 2.4 Numerical approach

We start our discussion by considering the one-dimensional problem, i.e. a differential equation depending on one coordinate  $x$ , although these methods are straightforward to generalise to both higher dimensions and more unknown functions. The domain is discretised by introducing a number of collocation points at positions  $x_i$ , where the

functions take values  $f_i = f(x_i)$ . The derivatives  $f_i^{(m)} = f'(x_i)$  are approximated as a matrix product  $f_i^{(m)} = D_{ij}^{(m)} f_j$ , where the computation of the matrices  $D_{ij}^{(m)}$  depends on the method of choice.

We will use pseudospectral collocation, which has been successfully implemented in the construction of the stationary AdS solutions, and remains the method of choice for many numerical schemes in numerical relativity. There is a trove of excellent literature on the spectral methods with many pedagogical examples [88–91], and in this section we will provide a broad overview of the topic.

Spectral methods are global numerical methods (as opposed to *e.g.* the finite difference method), where the derivatives are computed by using the interpolation function on all grid points. Any non-periodic equidistant grid is well known to exhibit Runge’s phenomenon, which introduces numerical instabilities. This is a major concern, especially as we are interested in the near-boundary data due to the AdS/CFT correspondence.

A particularly useful grid is given by the Chebyshev-Gauss-Lobatto nodes

$$x_i = \frac{1}{2}(x_0 + x_n) + \frac{1}{2}(x_0 - x_n) \cos \frac{i\pi}{n}, \quad i = 0, 1, \dots, n, \quad (2.18)$$

where  $x \in [x_0, x_n]$ . This can be seen as a stereographic projection of equally spaced points on the upper half circle onto the line interval. This grid is clustered near the edges, and is distributed in a way which minimises Runge’s phenomenon.

The functions are evaluated on the nodes (2.18), and fit by the interpolating polynomial of degree  $n$ , which interpolates over the entire grid. We will use the Lagrange interpolant, which is given by the linear combination

$$p_n(x) = \sum_{i=0}^n q_i \ell_i(x), \quad (2.19)$$

with

$$\ell_i(x) = \prod_{j=0, j \neq i}^n \left( \frac{x - x_j}{x_i - x_j} \right). \quad (2.20)$$

The derivatives at the nodes are then given by

$$p'_n(x_i) = \sum_{j=0}^n q_j \ell'_j(x_i) = (D_n)_{ij} q_j. \quad (2.21)$$

From here we can see that the Chebyshev differentiation operator is  $(D_n)_{ij} = \ell'_j(x_i)$ , which is an  $(n + 1) \times (n + 1)$  matrix.

These methods typically yield dense differentiation matrices. However, the payoff is significant, as for analytic functions the pseudospectral collocation on such a grid provides exponential convergence with increasing grid size. For larger grids, obtaining the final functional Jacobian  $\delta F/\delta u$  matrix in Newton's method (2.17) can be computationally intensive. The numerical cost associated with inverting said linear operator is also considerable. In this thesis we used the *Mathematica* package, and we found that its `LinearSolve` routine was sufficient for our purposes.

Sometimes, at a fixed resolution, Newton's method will converge to spurious solutions. It is important to perform convergence tests, especially in the regions of parameter space where the functions exhibit large gradients. We have tested that all our solutions presented in this thesis display expected convergence properties, by running the tests on a selected representative sample of solutions.

The combination of these methods has been successfully utilised to tackle highly complex systems of differential equations in general relativity (*e.g.* see [27] and references therein). Due to its user-friendly implementation, high numerical accuracy and versatility, it is suitable for a wide range of problems.

# Chapter 3

## Hairy Black Holes in $\text{AdS}_5 \times S^5$

The work presented in this chapter was published as [92], in collaboration with Jorge E. Santos. The numerical results were generated by the author with their own code.

### 3.1 Introduction

In this chapter we focus on  $\mathcal{N} = 4$  SYM with gauge group  $SU(N)$  on the Einstein static universe  $\mathbb{R}_t \times S^3$ . This is the conformal field theory for which the AdS/CFT correspondence was first formulated in [2], and for which our holographic dictionary is best understood [8, 9, 12]. In [2], the strong coupling limit of  $\mathcal{N} = 4$  SYM at large 't Hooft coupling and at infinite gauge group rank  $N$  was conjectured to be IIB supergravity on  $\text{AdS}_5 \times S^5$ . Classical black hole solutions of IIB supergravity with  $\text{AdS}_5 \times S^5$  asymptotics are dual to the states on the CFT at energies of order  $N^2$ , and are important in understanding the thermodynamic saddle points of the CFT.

In order to make this problem numerically tractable, we will consider consistent truncations of the ten-dimensional supergravity theory. Studying the full IIB on  $\text{AdS}_5 \times S^5$  presents a number of challenges, for instance, small Schwarzschild-AdS black holes have been shown to be unstable to a localisation on the  $S^5$  if their radius in AdS units is sufficiently small [34–36, 93]. The bumpy black holes in  $\text{AdS}_5 \times S^5$  that branch from the onset of this instability were only recently constructed in [37].

The five-dimensional gauged  $\mathcal{N} = 8$   $SO(6)$  supergravity arises as a consistent truncation of type IIB SUGRA on  $\text{S}^5$ , where the isometry group of  $\text{S}^5$  corresponds to global R-symmetry of the dual field theory [94–100]. The bosonic sector has 42 scalars, which are organised in  $SO(6)$  irreducible representations with masses  $m_\phi^2 L^2 = -4, -3, 0$ . A further truncation is given by [101], where the 20 scalars are in the multiplet that transforms in the  $\mathbf{20}'$  sector of the  $SO(6)$ . To simplify this even more, we will work in the consistent truncation provided by Bhattacharyya *et al* [62], where the three diagonal  $U(1)$  charges in the maximal  $U^3$  subgroup of  $SO(6)$  are set equal. The consistent truncation retains one non-minimally coupled scalar field charged under a  $U(1)$  gauge field, and when the scalar field vanishes, the action reduces to that of the bosonic action for  $D = 5$  minimal gauged supergravity.

A bottom-up approach was analysed in [61], where the authors considered the massless Abelian Higgs model in  $\text{AdS}_5$ . The small (compared to the radius of  $\text{AdS}$ ), near extremal charged black holes were found to be unstable against forming scalar field condensate, and the endpoint hairy black holes were constructed perturbatively. The instability in this case was driven by the charged superradiance in  $\text{AdS}$ , and it was found to affect the small charged black holes with scalar field charges  $e$  satisfying  $e\mu \geq \Delta_0$ , where the energy of the lowest scalar mode is given by  $\Delta_0 = 4$  for  $m_\phi^2 = 0$  (the radius of curvature of  $\text{AdS}_5$  is set to be  $L = 1$ ). If we work in units where the chemical potential  $\mu$  of a small RNAdS black hole is bounded above by  $\mu \leq 1$ , we find that the marginal scalar field charge for the instability is  $e_c = 4$ .

In [60] these solutions were constructed numerically and the hairy black hole phase diagram was found to depend qualitatively on the massless scalar field charge  $e$ , the magnitude of which influences the two kinds of instabilities. The tachyonic instability was found to set in for lower charges than the superradiance. For charges  $e > e_c$  where the two regimes coexist, the hairy black holes were found at all charges. They reduce to the smooth, ground state soliton branch in the  $T \rightarrow \infty$  limit for  $Q < Q_{\max}(e)$ , and for  $Q > Q_{\max}(e)$  reduce to some extremal, possibly singular, configurations. For  $e > e_c$ , the smooth soliton exists for all charges  $Q$ , while  $e \leq e_c$  solitons approach the ‘‘Chandrasekhar’’ bound in a spiraling fashion<sup>1</sup>, where they become singular. However, they are never limiting solutions for the hairy black holes. At  $e = e_c$ ,  $Q_{\max}(e) = 0$  and

<sup>1</sup>The soliton solution space exhibits interesting structure and there also exist other branches of solutions [63].

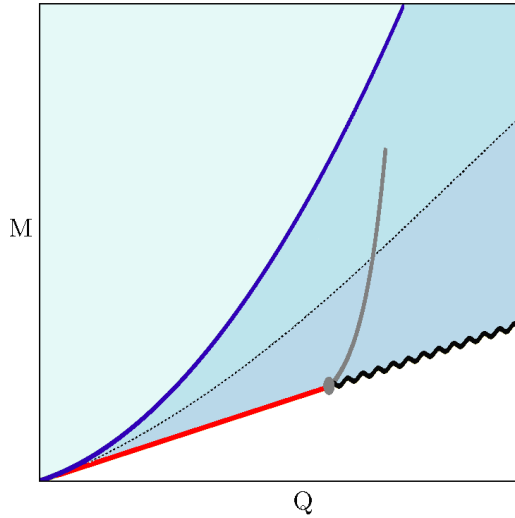


**Fig. 3.1** The proposed microcanonical phase diagram by Bhattacharyya *et al* (taken from [62], not drawn to scale). The lower solid line is the BPS bound on which the supersymmetric soliton resides. The straight red segment represents smooth branch and the wiggly black part represents singular soliton. Hairy black holes were proposed to exist between the curve indicating the onset of the superradiant instability (solid blue) and the BPS bound. The dotted black curve is the extremal RNAdS black holes. The grey solid line shows a possible phase transition between two different types of hairy black holes, with different zero size limits.

the lowest mass limit is the  $T = 0$  extremal limit, which does not coincide with the soliton.

In this chapter we consider the model which was first studied in [62]. As mentioned at the start of the introduction, the five-dimensional model can be embedded in the type IIB string theory. It contains one complex scalar field  $\phi$  with charge  $e = 2$ , charged under a  $U(1)$  gauge field, and has mass saturating the five-dimensional Breitenlohner-Freedman (BF) bound [26],  $m_\phi^2 = -4$ . The bound ensures the perturbative stability of AdS. In the AdS/CFT dictionary the operator which is dual to the complex scalar field has conformal dimension  $m_\phi^2 = \Delta(\Delta - 4) = -4$ , and hence  $\Delta = 2$ . Because  $e = \Delta$  (and  $\mu = 1$ ), this particular truncation is a marginal case for the superradiant instability of the small near extremal charged black holes.

In [62] small hairy black holes were constructed in a matched asymptotic expansion, along with smooth supersymmetric soliton solutions, which lie on the BPS bound  $M = 3|Q|$ . The smooth soliton is continuously connected to the vacuum  $\text{AdS}_5$ , in the sense that in the small charge limit it reduces to the global AdS perturbed by the

ground state excitation of the scalar field. These solitonic solutions were found to be the  $T = 0$  limit of the small hairy black holes. Bhattacharyya *et al.* also constructed the singular solitonic solution using the BPS equations [102–105, 62], which extends to arbitrarily large charges. These two families were found to join at the unique singular soliton  $Q_c$  in a spiralling fashion. We will see later, that these three soliton families play an important role in understanding the hairy black hole solution space.

The authors of [62] also conjectured the hairy black hole behaviour in the nonlinear regime, which is briefly summarised in Fig. 3.1. In this chapter we construct numerical solutions of [62], and unravel the full phase diagram. We find that, as conjectured, the hairy black holes get arbitrarily close to saturating the BPS bound for all charges. However, they do so in an unexpected and intricately elegant manner, so that the smooth soliton is the  $T \rightarrow 0$  hairy black hole limit, while the singular soliton is the  $T \rightarrow \infty$  limit.

This chapter is organised as follows. In section 3.2 we introduce the action and give the equations of motion. We provide numerical details in section 3.4, and review the BPS solitons in 3.3. Section 3.5 presents the phase space for the static hairy black holes, including the planar horizon limit, and analyses the thermodynamics across different ensembles. Section 3.6 compares our numerical results to the perturbative expansion of [62], where we show that our findings are consistent with those of [62] for sufficiently small asymptotic charges. Section 3.7 concludes the paper with discussion, and a prelude to the Chapter 4, which generalises these hairy solutions to include rotation.

## 3.2 Setup

### 3.2.1 The action and equations of motion

The consistent truncation is described by the five-dimensional Einstein-Maxwell AdS gravity coupled to a charged complex scalar field with action given as

$$S = \frac{1}{16\pi G_5} \int d^5x \sqrt{g} \left\{ R[g] + 12 - \frac{3}{4} F_{\mu\nu} F^{\mu\nu} - \frac{3}{8} \left[ (D_\mu \phi)(D^\mu \phi)^\dagger - \frac{\nabla_\mu(\phi\phi^\dagger) \nabla^\mu(\phi\phi^\dagger)}{4(4 + \phi\phi^\dagger)} - 4\phi\phi^\dagger \right] \right\} - \frac{1}{16\pi G_5} \int F \wedge F \wedge A, \quad (3.1)$$

where  $F_{\mu\nu} = 2\partial_{[\mu}A_{\nu]}$ ,  $D_\mu\phi = \nabla_\mu\phi - ieA_\mu\phi$ ,  $e = 2$ , the radius of AdS<sub>5</sub> is set to unity, and  $G_5 = \pi/(2N^2)$  is the five-dimensional Newton's constant. We note that at this stage we have already used AdS/CFT, in the sense that  $G_5$  is given in terms of the rank of the gauge group of  $\mathcal{N} = 4$  SYM. The tachyonic scalar field  $\phi$  has the charge  $e = 2$  and  $m_\phi^2 = -4$ .

The equations of motion derived from (3.1) are

$$G_{\mu\nu} - 6g_{\mu\nu} = \frac{3}{2}T_{\mu\nu}^{\text{em}} + \frac{3}{8}T_{\mu\nu}^{\text{mat}} \quad (3.2a)$$

$$\nabla_\rho F^\rho{}_\mu = \frac{1}{4}\varepsilon_{\mu\lambda\nu\rho\sigma} F^{\lambda\nu} F^{\rho\sigma} - \frac{i}{4} [\phi(D_\mu\phi)^\dagger - \phi^\dagger D_\mu\phi] \quad (3.2b)$$

$$D_\mu D^\mu\phi + \phi \left[ \frac{(\nabla_\mu(\phi\phi^\dagger))(\nabla^\mu(\phi\phi^\dagger))}{4(4 + \phi\phi^\dagger)^2} - \frac{\nabla_\mu\nabla^\mu(\phi\phi^\dagger)}{2(4 + \phi\phi^\dagger)} + 4 \right] = 0, \quad (3.2c)$$

and the energy-momentum tensor is given by

$$T_{\mu\nu}^{\text{em}} = F_\mu{}^\lambda F_{\nu\lambda} - \frac{1}{4}g_{\mu\nu} F^2, \quad (3.3a)$$

$$T_{\mu\nu}^{\text{mat}} = \frac{1}{2} [D_\mu\phi (D_\nu\phi)^\dagger + D_\nu\phi (D_\mu\phi)^\dagger] - \frac{1}{2}g_{\mu\nu} (D_\lambda\phi)(D^\lambda\phi)^\dagger + 2g_{\mu\nu} \phi\phi^\dagger - \frac{1}{4(4 + \phi\phi^\dagger)} \left[ (\nabla_\mu(\phi\phi^\dagger))(\nabla_\nu(\phi\phi^\dagger)) - \frac{1}{2}g_{\mu\nu}(\nabla_\lambda(\phi\phi^\dagger))(\nabla^\lambda(\phi\phi^\dagger)) \right]. \quad (3.3b)$$

We look for static, spherically symmetric and asymptotically global AdS<sub>5</sub> solutions and for now we will not specify our gauge choice<sup>2</sup>:

$$ds^2 = -f(r)dt^2 + g(r)dr^2 + \Sigma(r)^2 d\Omega_3^2, \quad A_\mu dx^\mu = A(r)dt, \quad \phi = \phi^\dagger = \phi(r). \quad (3.4)$$

Since our solutions are only electrically charged, the Chern-Simons term plays no role. The Einstein equation, the Maxwell equation and the scalar equation (3.2c) yield a system of four equations [62]:

$$\begin{aligned} f' - \frac{f}{2\Sigma\Sigma'} \left[ 4g + g\Sigma^2 (8 + \phi^2) - 4\Sigma'^2 + \frac{\Sigma^2\phi'^2}{4 + \phi^2} \right] - \frac{\Sigma}{2\Sigma'} (A^2\phi^2g - A'^2) &= 0, \\ g' + g^2 \left( \frac{4}{\Sigma\Sigma'} + \frac{8\Sigma}{\Sigma'} + \frac{\Sigma\phi^2}{\Sigma'} \right) + g \left( \frac{f'}{f} + \frac{\Sigma A'^2}{f\Sigma'} + \frac{4\Sigma'}{\Sigma} + \frac{2\Sigma''}{\Sigma'} \right) &= 0, \\ A'' + \frac{1}{2} \left( \frac{6\Sigma'}{\Sigma} - \frac{f'}{f} - \frac{g'}{g} \right) A' - g\phi^2 A &= 0, \\ \phi'' + \frac{1}{2} \left( \frac{6\Sigma'}{\Sigma} + \frac{f'}{f} - \frac{g'}{g} \right) \phi' - \frac{\phi}{4 + \phi^2} \phi'^2 + \frac{g}{f} (A^2 + f) (4 + \phi^2) \phi &= 0. \end{aligned} \quad (3.5)$$

The ' denotes the derivative with respect to  $r$ .

At this point we pick a gauge where  $\Sigma(r) = r$ , so that  $r$  measures the radius of the round  $S^3$  in AdS<sub>5</sub>. In this gauge, we require that our solutions are asymptotically AdS<sub>5</sub>, *i.e.* at large  $r$  they must satisfy the following expansion [106–108, 20]

$$\begin{aligned} f(r) &= r^2 + 1 + \mathcal{O}(r^{-2}), \quad g(r) = \frac{1}{1 + r^2} + \mathcal{O}(r^{-6}), \\ A(r) &= \mu + \mathcal{O}(r^{-2}), \quad \phi(r) = \frac{\varepsilon}{r^2} + V \frac{\log r}{r^2} + \mathcal{O}(r^{-4}), \end{aligned} \quad (3.6)$$

where  $\mu$  is the chemical potential and the constants  $V$  and  $\varepsilon$  will shortly be identified. Using the AdS/CFT correspondence [8, 9],  $V$  is regarded as the source for the operator dual to  $\phi$  and  $\varepsilon$  is its expectation value, *i.e.*  $\varepsilon = \langle \mathcal{O}_\phi \rangle$ . This choice implicitly assumes standard quantisation. The operator dual to  $\phi$  has conformal scaling dimension  $\Delta = 2$ . We will be interested in solutions representing states of the conformal field theory that are not sourced, so we will set  $V = 0$ . These normalizable conditions give rise to a four parameter set of asymptotically AdS<sub>5</sub> solutions to (3.5) [62]. Further imposing suitable regularity and normalisability conditions results in two parameter space of solutions

<sup>2</sup>Note that we have fixed the  $U(1)$  gauge freedom by taking  $\phi$  to be real.

which may be taken to be the mass ( $M$ ) and charge ( $Q$ ) of the black hole, with  $\varepsilon$  and  $\mu$  being determined as a function of  $M$  and  $Q$ .

All known solutions are found in the radial gauge where  $\Sigma(r) = r$ . There are a handful of solutions to the equations of motion derived from (3.1) that are known to be analytic, the most general being the Kerr-Reissner-Nordström black hole [109–119].

If we switch off the scalar field we recover the familiar Reissner-Nordström two parameter set of solutions to (3.5)

$$\begin{aligned} f(r) &= \frac{\mu^2 R^4}{r^4} - \frac{(R^2 + \mu^2 + 1)R^2}{r^2} + r^2 + 1, \\ g(r) &= \frac{1}{f(r)}, \quad A(r) = \mu \left(1 - \frac{R^2}{r^2}\right), \quad \phi(r) = 0. \end{aligned} \tag{3.7}$$

We record the thermodynamic formulae for later use (henceforth all the thermodynamic quantities will be scaled by  $N^2$ )

$$\begin{aligned} M &= \frac{3}{4}R^2 (1 + R^2 + \mu^2), & Q &= \frac{1}{2}\mu R^2, & S &= \pi R^3, \\ T &= \frac{1}{2\pi R} (1 + 2R^2 - \mu^2). \end{aligned} \tag{3.8}$$

Note that  $R$  is the outer horizon if the condition  $\mu^2 \leq (1 + 2R^2)$  is satisfied. This inequality is saturated at extremality, where  $T = 0$ . The resulting extremal black hole is regular, and has a degenerate bifurcating Killing horizon.

The frequency of the lowest normal mode of  $\phi$  is  $\Delta = 2$ . In [61] it was shown that small Reissner-Nordström AdS (RNAdS) black holes suffer from superradiant instability whenever  $e\mu > \Delta$ , where  $\mu$  is a chemical potential of the black hole. For RNAdS black holes  $\mu \leq (1 + 2R^2)$ , where  $R$  is the Schwarzschild radius of the black hole<sup>3</sup>, therefore, small black holes satisfy  $\mu \leq 1$  (saturating at extremality). Hence small charged black holes are always stable when  $e < e_c = \Delta$  and in our setup small near extremal black holes lie at the edge of the instability. These small near extremal charged black holes are unstable to the superradiant tachyon condensation and evolve towards a small black hole with the charged scalar hair.

---

<sup>3</sup>Defined so that the entropy for the RNAdS BH is  $S = \pi R^3$ .

### 3.3 The BPS solitons

In this section we briefly outline the numerical study of the spherically symmetric smooth and singular solitons given in [62]. We shall see later that these can be regarded as the BPS limit of the hairy black hole configurations. Soliton solutions are easier to determine, since they are known to be supersymmetric. Instead of solving the equations of motion (3.5) directly one resorts to searching for nontrivial solutions of the Killing spinor equations, which are first order in space. After some nontrivial manipulations, one can cast *any* spherically symmetric supersymmetric solution of the action (3.1) into the following form

$$f(r) = \frac{1 + \rho^2 h^3}{h^2}, \quad g(r) = \frac{4\rho^2 h^2}{(2\rho h + \rho^2 \dot{h})^2 (1 + \rho^2 h^3)}$$

$$A(r) = \frac{1}{h(r)}, \quad \phi(r) = 2 \left[ \left( h + \frac{\rho \dot{h}}{2} \right)^2 - 1 \right]^{1/2} \quad (3.9)$$

where the  $\dot{\phantom{x}}$  denotes the derivative with respect to the variable  $\rho$ , given by  $r^2 = \rho^2 h$ , and  $h$  has to satisfy the following second order differential equation

$$\rho (1 + \rho^2 h^3) \ddot{h} + (3 + 7\rho^2 h^3 + \rho^3 h^2 \dot{h}) \dot{h} - 4\rho (1 - h^2) h^2 = 0. \quad (3.10)$$

This equation has a number of remarkable properties. Perhaps the most striking being that at large  $\rho$  it demands  $h(\rho)|_{\rho \rightarrow \infty} = 1$ . This condition automatically ensures normalisability of the physical fields  $f$ ,  $g$ ,  $A$  and  $\phi$ . At the origin,  $r = 0$  or equivalently  $\rho = 0$ , there are a number of possibilities. Assuming that solutions to (3.10) behave as

$$\lim_{\rho \rightarrow 0} h = \frac{h_\alpha}{\rho^\alpha}, \quad (3.11)$$

gives the following possible exponents  $\alpha = 0, 1, 2/3, 2$ . Solutions with  $\alpha = 0$  are regular, and the remaining are singular. For each of these exponents we can find solitonic solutions, but the dimension of their moduli space strongly depends on  $\alpha$ . For  $\alpha = 0$ , 1 there is a one parameter family of solutions, for  $\alpha = 2/3$  there is a unique solution and for  $\alpha = 2$  the solution spans a two dimensional moduli space. In addition, in [62] it was shown that the smooth soliton solutions with  $\alpha = 0$  exist for small values of the charge  $Q$  and that the singular solitonic solution with  $\alpha = 1$  exists for large values of

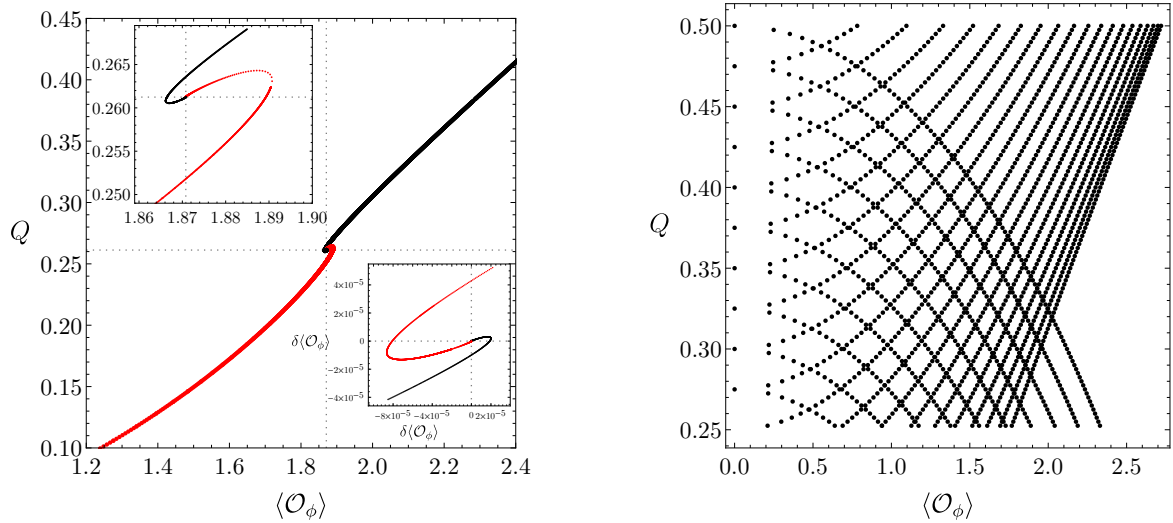


**Fig. 3.2** *Left:* Charge of the solitonic solutions  $Q$  versus the vacuum expectation value of the dual operator  $\langle \mathcal{O}_\phi \rangle$ . The black solid line from above is the singular soliton and the red line from below is the smooth solution. The dotted gridlines show coordinates of the special solution with  $\alpha = 2/3$ . *Right:* The  $\alpha = 2$  soliton solutions. The wedges are for constant  $h_2$  which decreases from 1. These solution curves appear to extend to  $|Q| \rightarrow +\infty$ . We also did not find any limiting value for  $\langle \mathcal{O}_\phi \rangle$ .

$Q$ . The two families merge precisely at a special point which is given by the singular soliton with  $\alpha = 2/3$ .

We reproduce the results of [62]. The line of smooth solitons terminates at the singular solution with the “critical” value  $Q_c \simeq 0.2613$  as the central density  $h_0 \rightarrow \infty$ ; the family of singular solitons with  $\alpha = 1$  branches out of this point at  $h_1 \rightarrow 0$ , extending to higher charges. The critical charge  $Q_c$  can also be obtained by solving for the solution with  $\alpha = 2/3$  and  $h_{2/3} = 1$ , thus confirming the picture of [62]. In addition, Bhattacharyya *et al.* analysed the asymptotic behaviour around the limiting solution analytically and proposed that these two soliton branches exhibit damped (possibly periodic) oscillations around  $Q_c$  in the space parametrized by  $Q$  and  $\langle \mathcal{O}_\phi \rangle$ , resulting in an infinite discrete non-uniqueness of the soliton solutions as  $Q \rightarrow Q_c$  (see Fig. 3.2). Note that there exists a maximum charge  $Q_{max} \simeq 0.2643$  for the  $\alpha = 0$  family and a minimum charge  $Q_{min} \simeq 0.2605$  for the  $\alpha = 1$  singular soliton. The limiting expectation value for the operator dual to the scalar field is  $\langle \mathcal{O}_\phi \rangle >_c \simeq 1.8710$ , and corresponds to the  $\alpha = 2/3$  singular solution.

We also compute the singular  $\alpha = 2$  case which provides a two parameter class of solutions parametrized by  $h_2$  and  $\rho^3 \partial_\rho h \Big|_{\rho \rightarrow \infty}$ <sup>4</sup>. The latter can be regarded as setting the charge  $Q$ , therefore, for any  $h_2$ , solutions exist with any value of the charge. It appears that these solutions are not connected to the other solutions studied in this chapter (see Fig. 3.2).

### 3.4 Numerical construction of hairy black holes

We make a compact coordinate change  $r = \frac{y_+}{\sqrt{1-y^2}}$  so that  $y = 1$  corresponds to  $r = \infty$  and  $y = 0$  to  $r = y_+$ . The first metric *ansatz* that we use is

$$ds_1^2 = \frac{1}{1-y^2} \left[ -y^2 \Delta(y) q_1 dt^2 + \frac{y_+^2 q_2 dy^2}{(1-y^2) \Delta(y)} + y_+^2 q_3 d\Omega_3^2 \right] \quad (3.12)$$

together with

$$A(r) = y^2 q_4(y), \quad \phi(r) = (1-y^2) q_5(y) \\ \text{and} \quad \Delta(y) = 1 + 2y_+^2 - \tilde{\mu}^2 - (1 + y_+^2 - 2\tilde{\mu}^2) y^2 - \tilde{\mu}^2 y^4. \quad (3.13)$$

Our reference metric  $\tilde{g}$  used in the DeTurck method is obtained from (3.12) by setting  $q_1 = q_2 = q_3 = 1$ . This is simply the metric of a RNAdS when  $\tilde{\mu} = \mu$  (3.7). The parameter  $\tilde{\mu}$  is left to be specified freely as it just sets the reference metric and is in general different from the chemical potential of the physical metric.

As we want to explore the solution space we start somewhere on the merger line, *i.e.* on a solution with some parameter coordinates  $(\mu, y_+)$  for which  $\phi$  is arbitrarily small. If we want to probe low temperatures a natural choice is  $\mu = 1$  (as black holes with  $y_+ < 1/2$  are small and have  $\mu \sim 1$ ). The physical chemical potential of the black hole is then given by the gauge field on the boundary,  $\mu = A(r)|_{r \rightarrow \infty} = q_4(1)$  (see the expansion (3.6)).

At the conformal boundary, located at  $y = 1$ , we demand that  $q_1(1) = q_2(1) = q_3(1) = 1$ ,  $q_5(1) = \epsilon$  and a Robin condition  $\left[ y_+^2 q_5' - 2q_4^2 q_5 \right]_{y=1} = 0$  for the gauge field which ensures

---

<sup>4</sup>In this case we use the same numerical method as for the hairy black holes, instead of solving (3.10) directly. We will detail the numerical method shortly.

that Newton's method converges to the hairy solution if we specify nonzero  $\epsilon$ . Note that  $\epsilon$  is related to  $\varepsilon$  via  $\epsilon = y_+^2 \varepsilon$ .

Regularity at the horizon demands  $q_1(0) = q_2(0)$  and pure Neumann for the remaining functions, *i.e.*  $q'_i(0) = 0$ . In many regions of the parameter space,  $\epsilon$  will not uniquely parametrise a solution, however the strength of the scalar field at the horizon,  $q_5(0) \equiv \epsilon_0$ , will. Depending on which region of parameter space we want to probe, we might decide to parametrise our solution with  $\epsilon$  or  $\epsilon_0$ . Thus we are left with two parameters after we fix  $\tilde{\mu}$ , namely  $(y_+, \epsilon)$  or  $(y_+, \epsilon_0)$ .

However, the RNAdS-like *ansatz* (3.12) does not have good convergence properties almost everywhere in moduli space. We found that the following *ansatz* has better convergence properties (at least a few order of magnitudes better!) if we simply set  $\Delta(y) = y_+^2$  in (3.12), yielding:

$$ds_2^2 = \frac{1}{1-y^2} \left[ -y^2 y_+^2 q_1 dt^2 + \frac{q_2 dy^2}{(1-y^2)} + y_+^2 q_3 d\Omega_3^2 \right]. \quad (3.14)$$

The trade off is that now the functions at high central field density  $\epsilon_0$  are more peaked at high temperatures, therefore we use the *ansatz* (3.12) to extend our solution curves in the high  $\epsilon_0$ , high  $T$  regime. The boundary conditions remain the same except for the gauge field, which in the new *ansatz* obeys to the following boundary condition  $\left[ y_+^2 (q_5 + q'_5) + q_5 - 2q_4^2 q_5 \right]_{y=1} = 0$ . This boundary condition can be obtained by solving the Einstein-DeTurck equations near the boundary.

It is not always easy to find a reference metric for the DeTurck method, but here we have the luxury of having two good reference metrics. The results obtained with the two different reference metrics match at least to 0.1% numerical accuracy in all the physical quantities such as energy (for the quantitative comparison of the two *ansatz* see Fig. 3.16).

We present thermodynamic formulae for the line element (3.14) since this was the *ansatz* we used the most. The electric charge is obtained by computing the flux of the electromagnetic field tensor at infinity

$$Q = \frac{1}{4} A'(r)|_{r \rightarrow \infty} = \frac{y_+^2}{4} \left( 2q_4 + \frac{dq_4}{dy} \right) \Big|_{y=1}. \quad (3.15)$$

We compute the Hawking temperature of the black hole by requiring smoothness of the Euclidean spacetime and it is simply given by

$$T = \frac{y_+}{2\pi}. \quad (3.16)$$

The entropy of a BH is proportional to its horizon area and is given by

$$S = \pi y_+^3 q_3(0)^{3/2}. \quad (3.17)$$

To compute the mass of the black hole we use the Ashtekar-Das formalism [120]

$$M = \frac{y_+^2}{8} \left[ 1 + 3y_+^2 + y_+^4 (2 - q_5^2 - q_1'') \right]_{y=1}. \quad (3.18)$$

We further checked that this matched the holographic renormalization technique of [108, 121, 20] up to the energy of the ground state of the global  $\text{AdS}_5$ . Our mass is computed with respect to pure  $\text{AdS}_5$ .

We verified that these quantities obey the first law of black hole thermodynamics  $dM = TdS + 3\mu dQ$  at least to 0.01%.

## 3.5 Static Hairy Black Holes

### 3.5.1 Phase diagram

In this subsection we present a comprehensive picture of the phase diagram of the hairy black holes in the microcanonical ensemble and analyse its rich structure.

The black holes with a non-zero scalar condensate first start to exist where the RNAdS black holes become superradiantly unstable. The RNAdS black holes are uniquely specified by the two parameters  $(R, \mu)$  and given the horizon radius we look for the value of the chemical potential  $\mu$  at which zero-mode of the scalar field first appears. We generate this one parameter family of solutions separately by linearising the scalar equation (3.2c) in the compact variable  $y$  around the RNAdS black hole. Let  $\delta q_5$  be an infinitesimal perturbation of  $q_5$  defined in (3.13). Following [67, 60] we

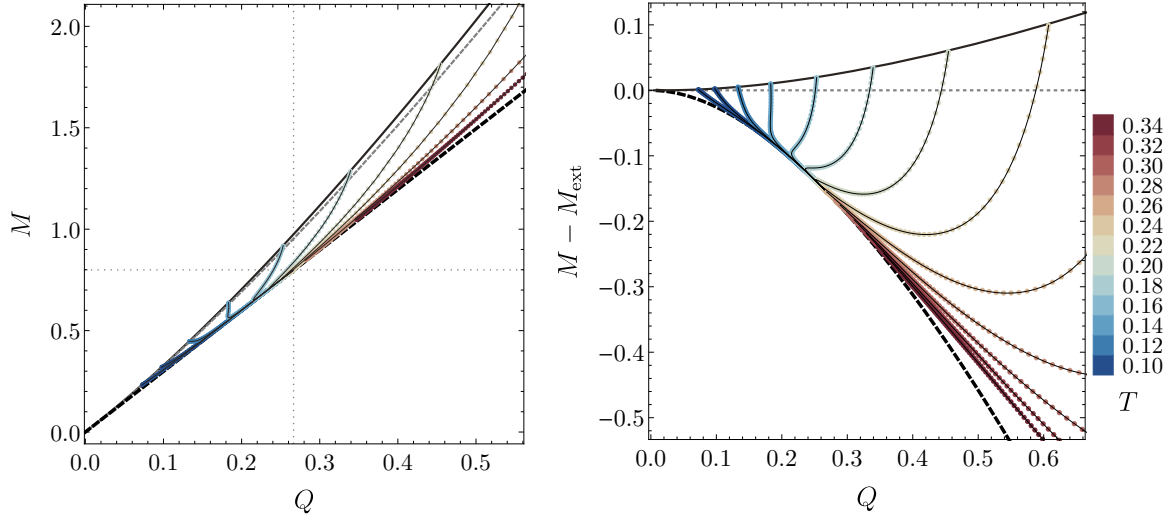


**Fig. 3.3** *Left:* Phase diagram for the hairy black holes. The merger curve (solid black) indicates the onset of the superradiant instability. The line of extremal RNAdS solutions is shown as a dashed gray line. The BPS bound is given by  $M_{\text{BPS}}(Q) = 3Q$  (dashed black). The gray dotted gridlines indicate the position of the special soliton with  $\alpha = 2/3$ .

*Right:* For clarity, we plot the mass difference  $\Delta M = M - M_{\text{ext}}$ , where  $M_{\text{ext}}$  is the mass of an extremal RNAdS black hole with the same charge  $Q$ .

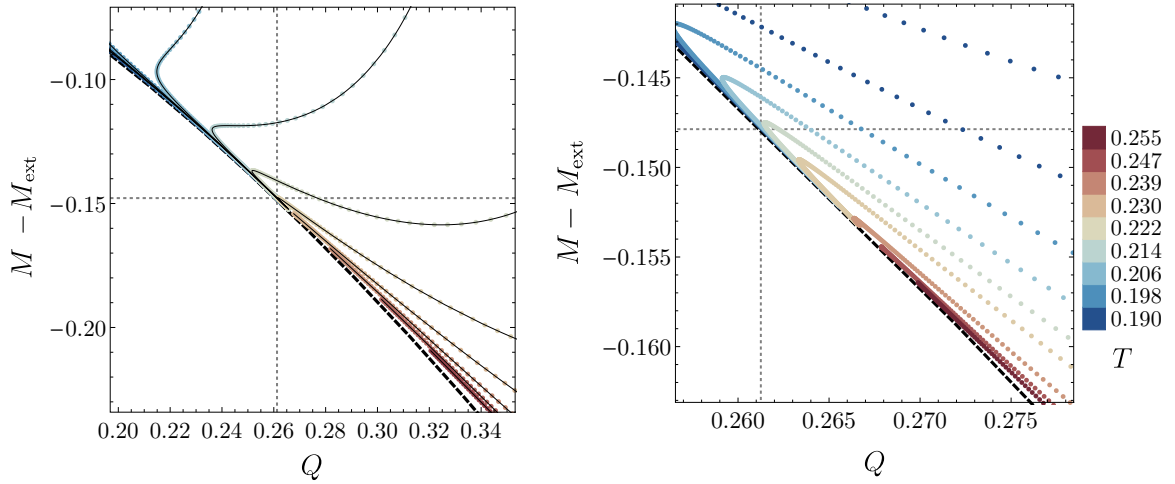


**Fig. 3.4** *Left:* Zooming in around  $Q = Q_c$ , and observing the transition between  $T < T_2$  and  $T > T_2$ . The color legend is the same as in Fig. 3.3.

*Right:* An even closer look for  $Q$  near  $Q_c = 0.261$ . The hairy black hole isotherms terminate at charges above the special singular soliton.

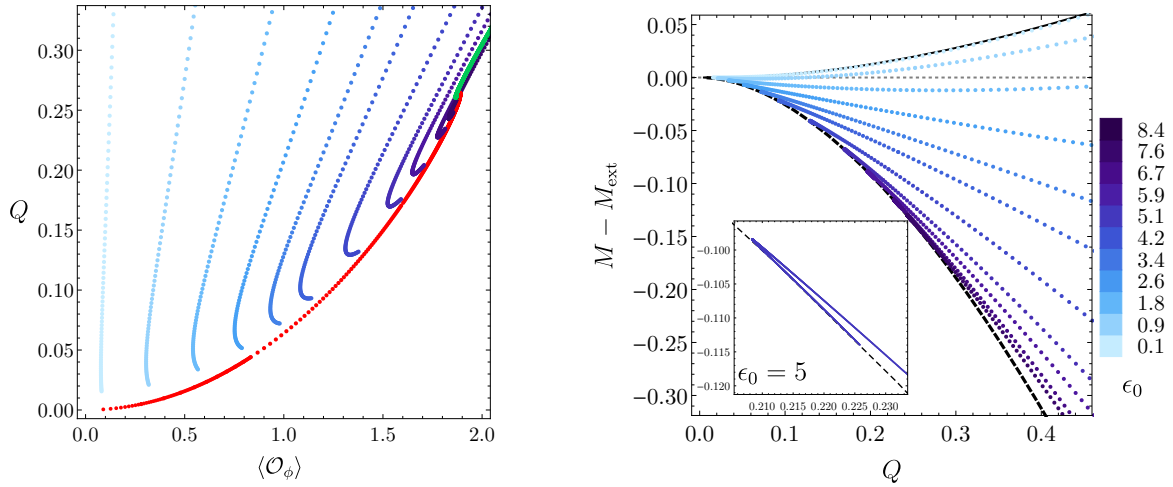


**Fig. 3.5** *Left:* The hairy black hole charge  $Q$  versus  $\langle \mathcal{O}_\phi \rangle$  for constant central scalar field density  $\epsilon_0$  curves. Red line is the smooth soliton and the green line is the singular soliton. *Right:* Mass difference versus charge  $Q$ . The constant parameter  $\epsilon_0$  curves extend down to  $T = 0.055$ . The inset is a zoomed in plot around  $Q = Q_c$  for some value of  $\epsilon_0$ .

numerically solve the resulting generalised eigenvalue problem

$$L(y)\delta q_5(y) = \mu^2 \Lambda(y)\delta q_5(y) \quad (3.19)$$

with boundary conditions  $\delta q_5'(0) = 0$  and  $2\mu^2\delta q_5(1) - R^2\delta q_5'(1) = 0$  which follow from imposing regularity at the horizon and solving (3.2c) near the asymptotic infinity. The  $L(y)$  and  $\Lambda(y)$  are both second order differential operators independent of  $\mu$ . The chemical potential of the corresponding marginally stable RNAdS black hole appears as the generalised eigenvalue. The line of solutions representing the onset of the condensation is also obtained by solving the full non-linear equations of motion (4.4) setting  $q_5(0) = \epsilon_0$  to be small. These two methods to generate the merger line are found to be in very good agreement.

Our numerical results are presented in Fig. 3.3. We find that the hairy black holes exist between the instability curve all the way down to the BPS bound and we verified it for a wide range of charges. Numerically we did not find any upper bound on the charge up to  $Q \sim 100$  and from the structure of the phase diagram it would be natural to infer that the hairy black hole solutions exist between the merger line and the BPS bound for every charge. At the lower bound the hairy black holes join the solitonic

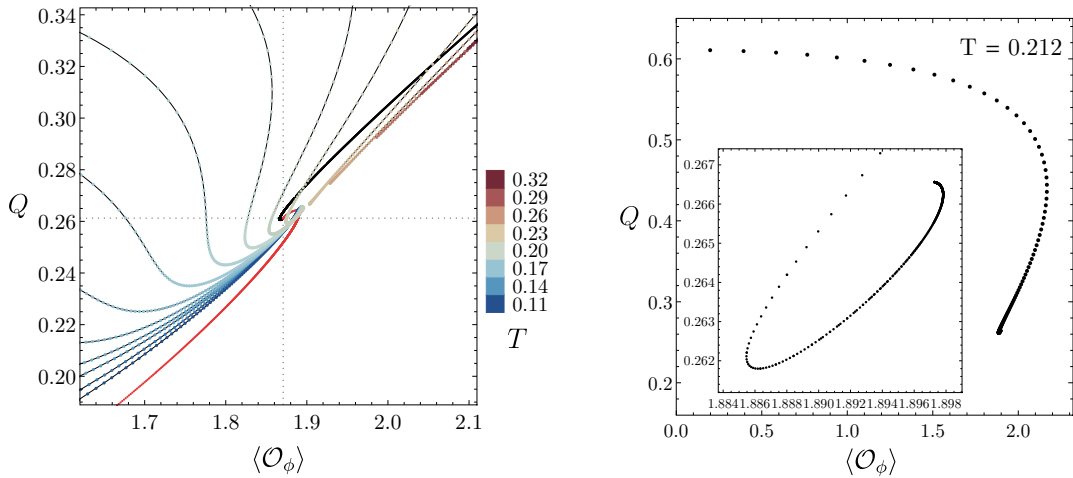


**Fig. 3.6** *Left:* Charge versus the vacuum expectation value of the operator dual to the scalar field for constant temperature hairy black hole solutions. The black and red data points are singular and smooth solitons respectively. Dotted gridlines show the point where these two merge. *Right:* The charge of the hairy solutions as we approach the singular soliton with  $\alpha = 1$ , exhibits damped oscillations. This data was collected with  $n = 1000$  grid points.

solution in the phase diagram, in particular, in the limit  $T \rightarrow 0$ , hairy black holes approach the smooth soliton, just as predicted in [62].

In more detail, in Fig. 3.5 we plot the charge  $Q$  as a function of  $\langle \mathcal{O}_\phi \rangle$  for constant values of  $\epsilon_0$ . In order to parametrise each of these constant  $\epsilon_0$  curves we dial the temperature  $T$ . As we lower the temperature, we see that hairy solutions join smoothly to the smooth soliton curve. Furthermore, the higher value of  $\epsilon_0$  we choose, the closer the hairy solutions get to  $Q = Q_c$ . In particular, as  $\epsilon_0 \rightarrow +\infty$  we see that the hairy black hole solution inherits the spiralling behaviour of the smooth solitonic branch (see right panel of Fig. 3.5 where we can see two arms of the spiral). Note that exactly for  $\epsilon = \langle \mathcal{O}_\phi \rangle = 1.8710$  we expect even the hairy black hole to have infinite non-uniqueness as we approach  $T \rightarrow 0$  from above.

The behaviour of the isothermal curves changes as a function of the temperature. In particular, if we fix a temperature in the interval  $T_1 < T < T_2$  while increasing  $\epsilon_0$ , with  $T_1 = 0.139_{-0.002}^{+0.002}$  and  $T_2 = 0.23_0^{+0.01}$ , we find two solutions for the same value of the charge  $Q$  (corresponding to two different values of  $\epsilon_0$ ). This can be seen for instance on the left panel of Fig. 3.4. We shall shortly see that this feature will give an

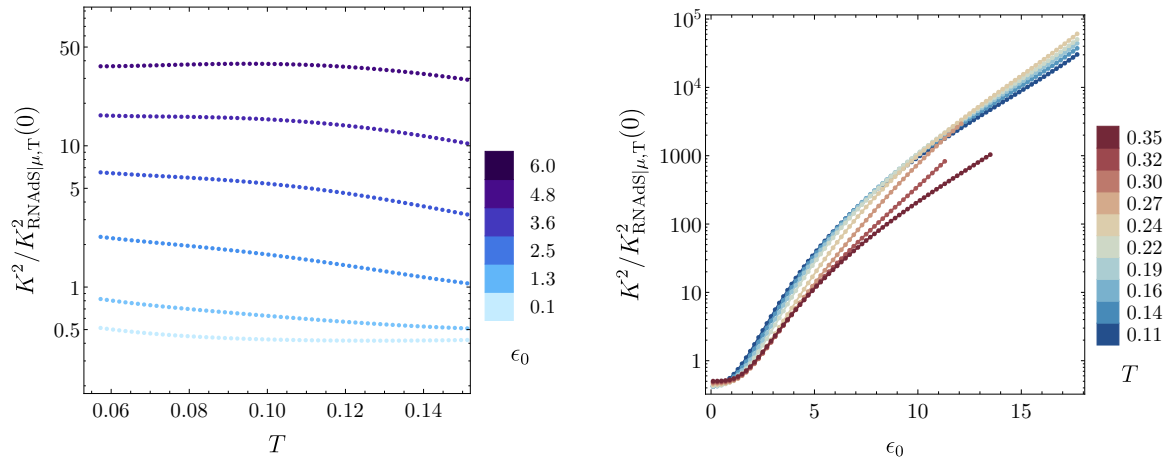


**Fig. 3.7** *Left:* Curvature invariants at the origin for a range of temperatures for constant  $\epsilon_0$ . The Kretschmann scalar remains finite. For lower values of  $\epsilon_0$  it takes longer for the hairy black holes to approach the BPS bound, hence for larger values of the parameter the curves flatten out quicker.

*Right:* Kretschmann invariant  $K^2$  for the range of temperatures scaled by the  $K^2$  of the corresponding RNAdS black hole in the grand-canonical ensemble. As  $\epsilon_0$  increases the invariant increases without a bound.

intricate phase diagram in the canonical ensemble, where the temperature and charge are held fixed.

One can finally ask what is the fate of the isothermal curves as we increase  $\epsilon_0$ . According to what we described above, these cannot be connected to the smooth soliton (except for the special isothermal with  $T = 0$ ). Indeed, we find numerical evidence that they connect to the singular soliton with  $\alpha = 1$ , see for instance the right panel of Fig. 3.4 where we see constant temperature curves joining the BPS bound at  $M_\star = 3Q_\star > Q_c$ , with the limiting  $Q_\star$  increasing further away from  $Q_c$  as we increase the temperature. This behaviour can also be seen on the left panel of Fig. 3.6. Finally, we note that as the hairy black hole isothermals approach the singular soliton, we find evidence for spiralling behaviour, which is depicted on the right panel of Fig. 3.6.

In order to support the claim that  $T \rightarrow 0$  hairy black holes do not tend to some configuration possessing irregular geometry we compute the Kretschmann invariant  $K^2 = R_{abcd}R^{abcd}$  following [60]. Because for RNAdS  $K^2 \sim 1/R^4$  when  $T \rightarrow 0$ , we normalise the  $K^2$  by that of the corresponding RNAdS black hole with the same

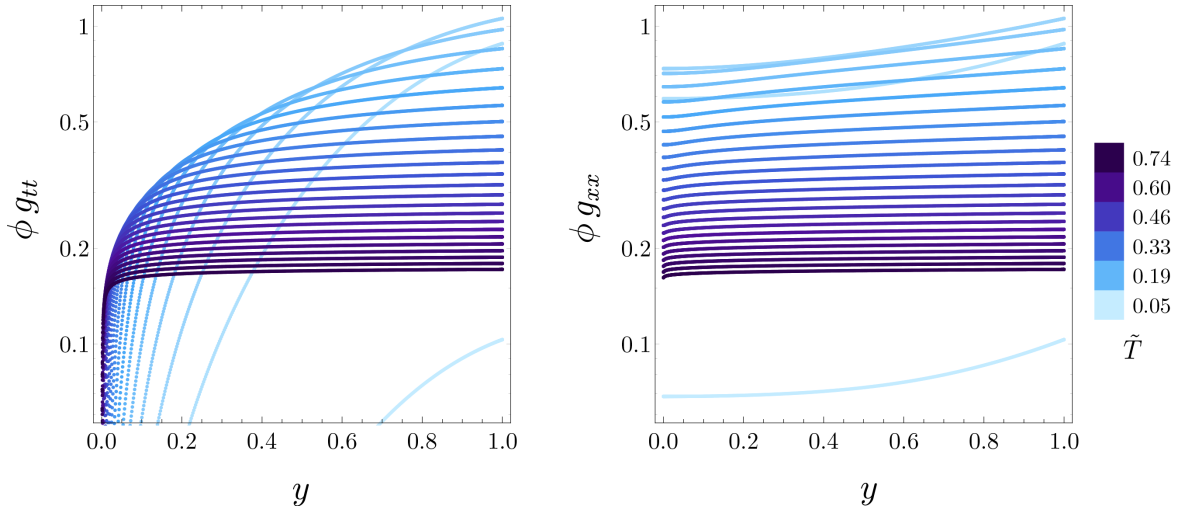


**Fig. 3.8** Gauge invariant quantities  $\phi g_{xx}$  and  $\phi g_{rr}$  for the hairy planar solutions, versus the compact coordinate  $y$ . According to the exact solution, both these curves should approach the same constant value when  $\tilde{T} \rightarrow +\infty$ .

chemical potential and temperature. In Fig. 3.7 (left) we show that the normalised curvature invariant remains bounded as we approach the smooth soliton.

On the other hand, keeping the temperature fixed and increasing  $\epsilon_0$  the normalised Kretschmann invariant appears to blow up (see Fig. 3.7, right) as we approach the BPS bound. For solutions with  $T > T_2$  we found the metric *ansatz* (3.12) to be more numerically stable.

As we increase  $\epsilon_0$ , the hairy black hole isotherms are approaching the BPS bound, as the chemical potential  $\mu \rightarrow 1$  and the entropy  $S \rightarrow 0$ . This together with the fact that the Kretschmann invariant blows up as  $\epsilon_0 \rightarrow +\infty$ , even when normalized by the Reissner-Nortström solution, suggests that the isothermals will merge with the  $\alpha = 1$  soliton, for any value of  $T$ .

### 3.5.2 The planar limit

In this subsection we consider the planar horizon limit of our global AdS<sub>5</sub> solutions. The resulting black brane solutions were first studied in great detail in [122]. Our numerical approach is similar to the one we used for the spherical black holes, so here we just quote the final results. In the large charge limit the singular soliton branch admits an exact analytical solution from which the planar limit solution can be

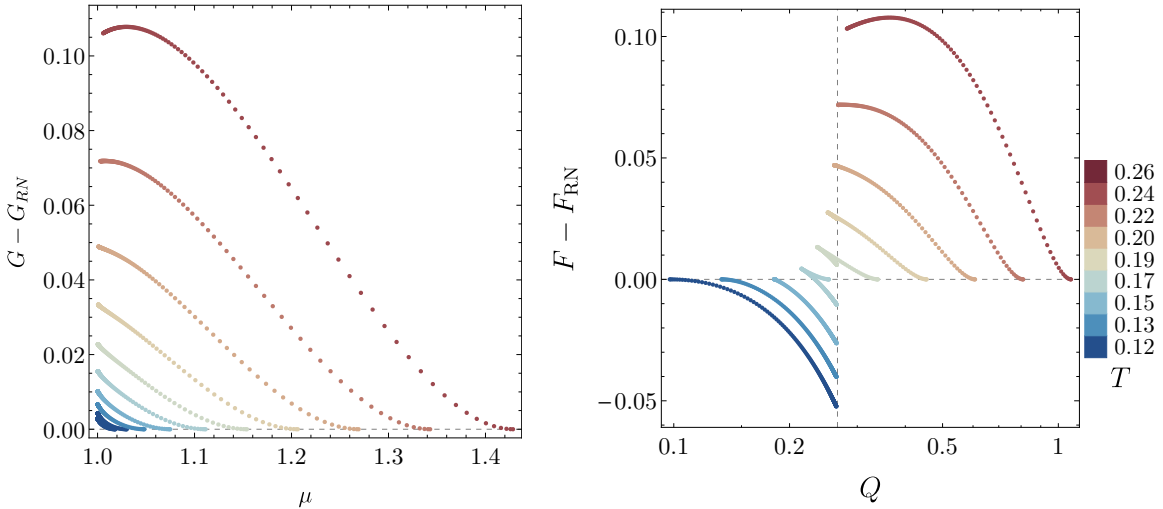


**Fig. 3.9** *Left:* The difference between the Gibbs free energies of hairy and RNAdS solutions with the same chemical potential and temperature. *Right:* Difference of the Helmholtz free energies of the Reissner-Nortström and the hairy solution with the same temperature and charge.

recovered [62]

$$ds^2 = -r^2 dt^2 + \frac{r^2 dr^2}{b^2 + r^4} + r^2 dx^2, \quad \phi(r) = \frac{2b}{r^2}, \quad A(r) = 0. \quad (3.20)$$

Note that the choice of the constant  $b$  amounts to a coordinate transformation, therefore, this is a single asymptotically Poincarè patch solution. The planar solution exhibits explicit scaling invariance, since the field theory is suppose to live on Minkowski spacetime. Thus, in order to have a well defined planar limit, we always look at conformal invariant ratios, which should have a smooth limit as the black holes become infinitely large. For instance, to measure temperature we introduce  $\tilde{T} \equiv \sqrt{\varepsilon_0} T$ . The planar hairy solutions are thus a one parameter family of solutions, with the singular soliton solution (3.20) being a point. We choose to parametrise the hairy branes by  $\tilde{T}$ .

We have constructed planar hairy black holes, *i.e.* hairy black branes, and checked that our spherical hairy black holes do approach the hairy branes in the limit  $S \rightarrow +\infty$ , *i.e.* hairy black holes become infinitely large. Furthermore, the singular soliton solution (3.20) is the zero  $M/T^4$  and  $Q/T^3$  limit of the hairy black branes, which is reached as we take  $\tilde{T}$  to be large (Fig. 3.13). In order to test this, we have plotted the following gauge invariant quantities  $g_{tt}\phi$  and  $g_{xx}\phi$  and checked that they approach the same value at large  $\tilde{T}$ , see Fig. 3.8. This is what is predicted by the exact soliton solution (3.20).

### 3.5.3 Thermodynamics

#### 3.5.3.1 Grand-canonical ensemble

In this section we analyse phase diagrams arising in different thermodynamic ensembles. In the grand-canonical ensemble the system is in equilibrium with a thermodynamic reservoir with a temperature  $T$  and chemical potential  $\mu$ , but is allowed to exchange energy and electric charge. The preferred phase of such a system minimises the Gibbs free energy  $G = M - TS - 3\mu Q$ . The results are presented in the left panel of Fig. 3.9 as a difference between hairy black holes and RNAdS potentials (absolute quantities for a few regions in moduli space are shown Fig. 3.11). We find that in the grand-canonical ensemble RNAdS black holes have lower Gibbs free energy than the hairy black holes with the same chemical potential  $\mu$  and temperature  $T$ . Note that our hairy solutions all have  $G < 0$ , so  $G > G_{RN}$  and that the RNAdS black holes and the hairy black holes phases are identical at the merger points. For RNAdS,  $G = \frac{1}{4}R^2(1 - R^2 - \mu^2)$  and as shown in the Fig. 3.11) the Gibbs free energy for the hairy black holes is always negative and approaching zero as we increase  $\epsilon_0$ . Note that it would only be exactly zero if  $\mu$  could reach 1, but that can only happen at infinite  $\epsilon_0$ . Finally, so far we have only considered the transition between the hairy black holes and RNAdS black holes. However, we note that the RNAdS black holes can themselves become subdominant with respect to AdS [123]. As all our energies are measured with respect to pure AdS, so that the energy of AdS simply corresponds to  $M = 0$  and therefore zero thermodynamic potentials, black holes with negative free energy are thermally favoured over pure AdS. The small RNAdS branch has  $\mu \leq 1$  and thus these black holes never compete with the hairy solutions.

We have also studied local thermodynamic stability of the hairy black holes in the grand-canonical ensemble. We find that the specific heat at constant chemical potential is always positive, but the isothermal capacitance, defined as:

$$C_T = \left( \frac{\partial Q}{\partial \mu} \right)_T,$$

exhibits an interesting behaviour. For  $T > T_2$  it is always positive and for  $T < T_1$  we find  $C_T < 0$ . In the interval  $T_1 < T < T_2$ , each isothermal has two solutions at fixed electric charge. The most energetic of these solutions has  $C_T > 0$ , whereas the least energetic has  $C_T < 0$ .

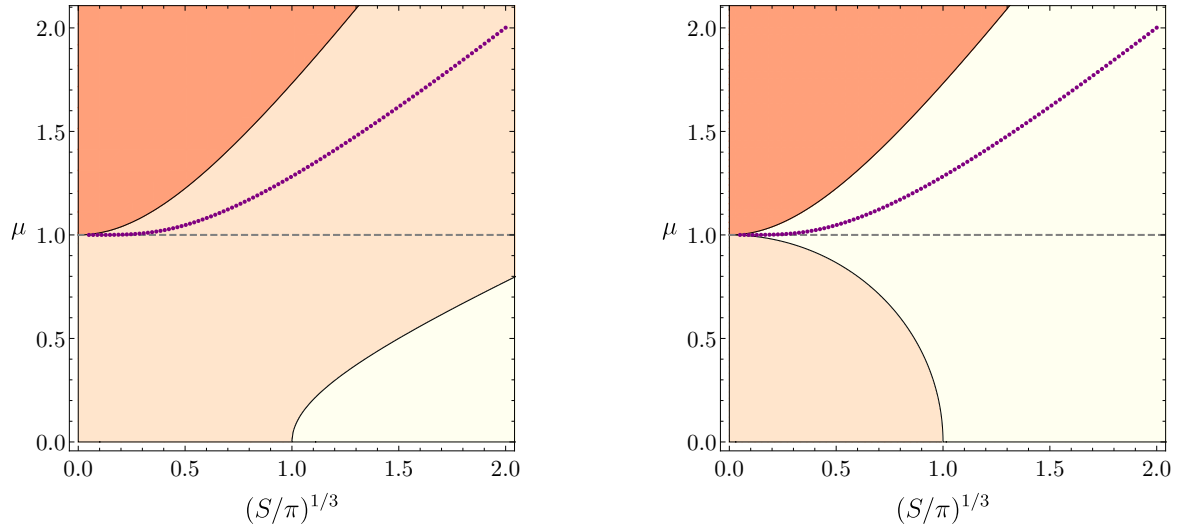


**Fig. 3.10** *Left:* Canonical ensemble: RNAdS black holes exist below the extremality curve (the curve separating orange (top left) and light-orange (middle) regions) and the hairy black holes exist above the merger curve (purple data points) and for  $\mu > 1$ . RNAdS dominate over pure AdS only in the yellow region (bottom right). The hairy black holes have a higher free energy than thermal AdS and thus are not the preferred phase in the ensemble. *Right:* Grand-canonical ensemble: when both solutions coexist (again above the merger curve), the hairy black holes have a higher free energy than the corresponding RNAdS with the same  $\mu$  and  $T$ . The yellow region (middle) shows the parameter space in which the RNAdS dominates over thermal AdS. The orange region (top left) is the extremal RNAdS and light-orange region (bottom left) is the sector in which pure AdS is preferred over the RNAdS black holes.

### 3.5.3.2 Canonical ensemble

In the canonical ensemble we restrict exchanges with the reservoir such that  $\delta Q = 0$ , but  $\delta M \neq 0$ , while keeping the temperature constant. The dominant phase minimises the Helmholtz free energy  $F = M - TS$ . The results are presented in the right panel of Fig. 3.9. We see an interesting interplay between the RNAdS and the hairy solutions which shows a phase transition in the constant temperature family of hairy solutions, occurring at  $T_1$  and ending at  $T_2$ . The higher  $\epsilon_0$  branch has lower  $F$  than the corresponding RNAdS black hole, see Fig. 3.11. For  $T > T_2$  RNAdS has lower free energy than the hairy black hole. Note however that in the region where the hairy solutions dominate over the RNAdS black hole,  $F$  is positive indicating that thermal AdS is the dominant phase in this region of moduli space. We have also studied the local thermodynamic stability of the hairy solutions in the region where they dominate over the corresponding RNAdS black holes. Local thermodynamic stability in the

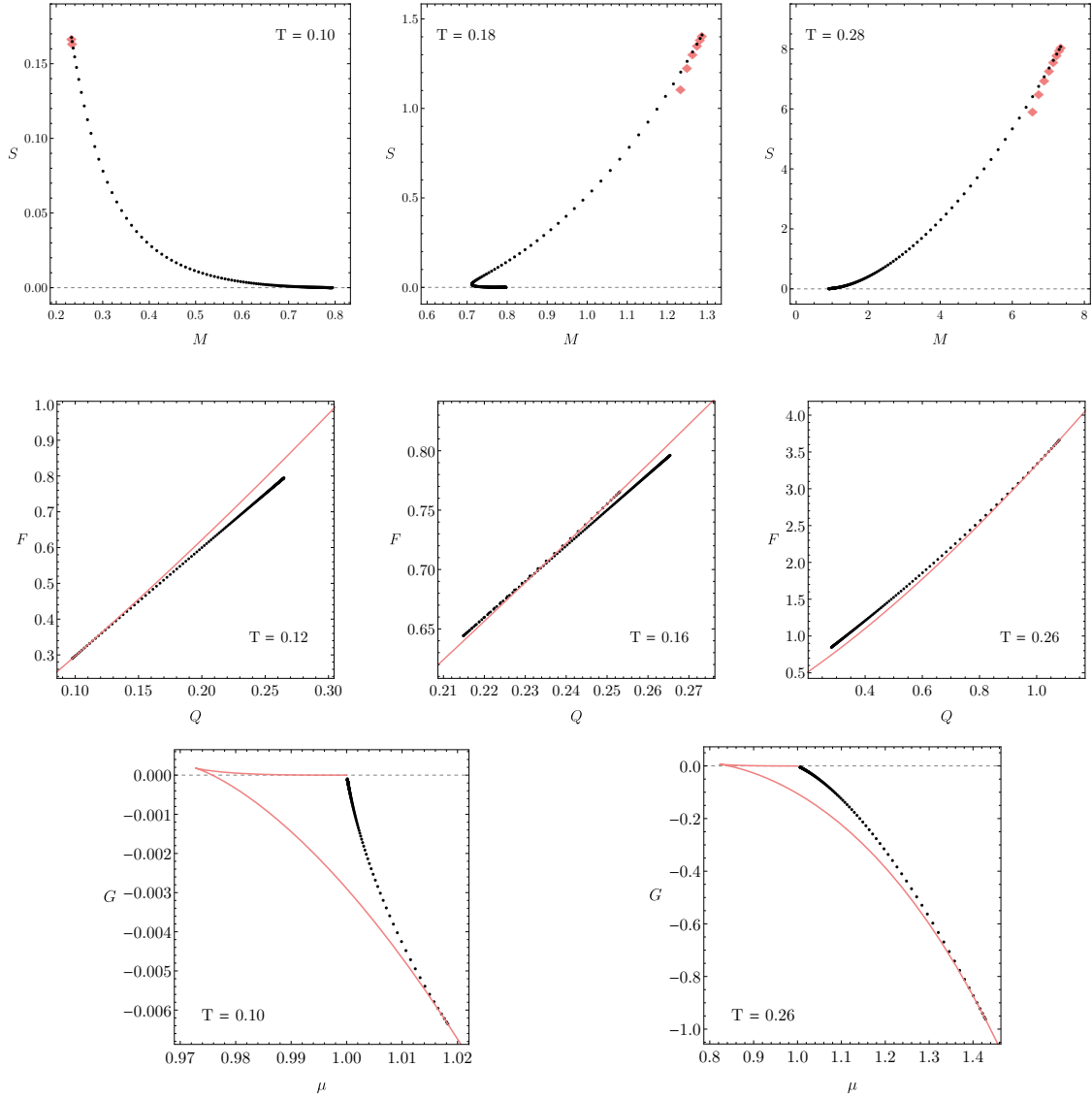


**Fig. 3.11** *Top row:* Entropy versus mass for the hairy solutions for three different temperatures. Red diamonds correspond to the RNAdS black hole with the same charge.

*Middle row:* Canonical free energy versus charge for the hairy solutions for three different temperatures. Red solid line is the corresponding RNAdS solution. For  $T < T_1$ , (left panel) the hairy solutions dominate over the RNAdS black hole. For  $T_1 < T < T_2$ , the three solutions coexist: two hairy black holes and RNAdS. One of the hairy solutions dominates over the RNAdS, while the other is subdominant (middle panel). For  $T > T_2$ , the RNAdS black hole is always dominant in the canonical ensemble.

*Bottom row:* Gibbs free energy versus chemical potential for the hairy global black holes. Red solid line is the corresponding RNAdS solution.

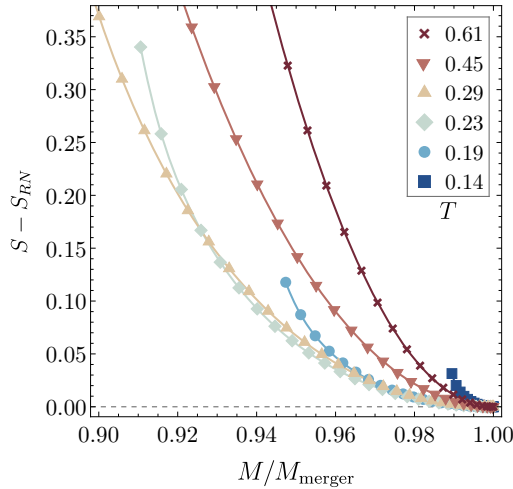


**Fig. 3.12** The entropy difference  $S - S_{RN}$  of the hairy black holes and the corresponding RNAdS with the same values of  $Q$  and  $M$ , as a function of the scaled mass  $M/M_{\text{merger}}$  plotted for a range of temperatures. Here  $M_{\text{merger}}$  is the mass at the onset of the superradiant instability, where by definition  $S - S_{RN} = 0$ .

canonical ensemble is controlled by the sign of the specific heat at constant charge, which turns out to be positive for this range of  $T$  and  $Q$ . We summarise our results for these two ensembles in Fig. 3.10.

### 3.5.3.3 Microcanonical ensemble

Finally the system in which  $\delta Q = 0$  and  $\delta M = 0$  is described by the microcanonical ensemble. The preferred phase in this case maximises the entropy. We find that hairy black holes are *only* dominant in this ensemble, see Fig. 3.12 (and Fig. 3.11). Also in this ensemble  $T_2$  plays an important role. In Fig. 3.12 we plot  $S - S_{RN}$  as a function of  $M/M_{\text{merger}}$ . Here,  $S_{RN}$  corresponds to the entropy of a RNAdS black hole with the same values of  $Q$  and  $M$  as the hairy solution we are considering, and  $M_{\text{merger}}$  to the mass of the RNAdS solution at the onset of the superradiant instability with the same  $T$ . We see that  $S - S_{RN}$  has maximum slope at  $M/M_{\text{merger}} = 1$ , becoming the smallest at  $T = T_2$ , and increasing again for  $T > T_2$ . This is a simple consequence of the first law of thermodynamics.

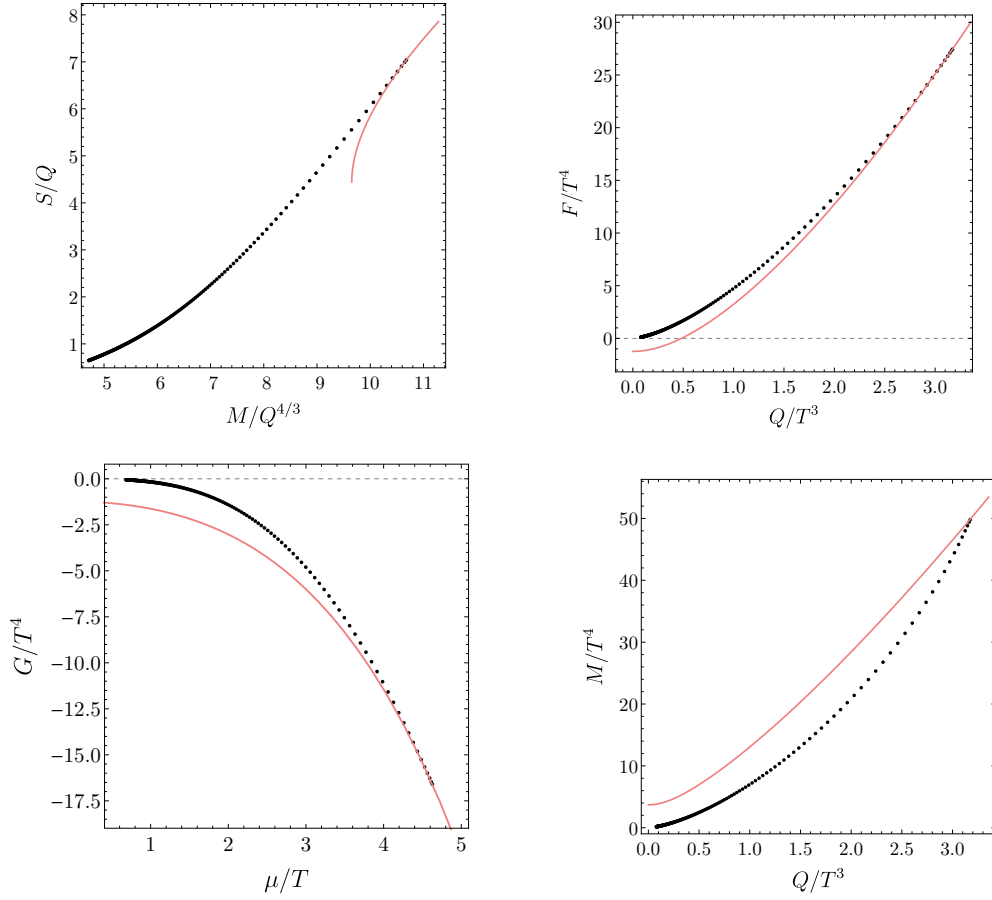


**Fig. 3.13** Scaled thermodynamic potentials for the planar hairy black holes. The red line in each figure is the RNAdS solution in the corresponding ensemble (microcanonical in *top left*, canonical in *top right*, grand-canonical in *bottom left*). The hairy black branes are only dominant in the microcanonical ensemble.

*Bottom right:* Planar hairy black hole masses against charge, in terms of the scale invariant quantities. Red line shows the RNAdS black holes, and black data points are the hairy counterparts.

### 3.5.3.4 Planar limit

The planar limit of our results match the results of [122], which we reproduced using our own code. For completeness in Fig. 3.13 we present a complete analysis of the several ensembles in the planar limit. In particular, we find that the hairy black branes are only dominant in the microcanonical ensemble, but never in the canonical or grand-canonical ensembles.

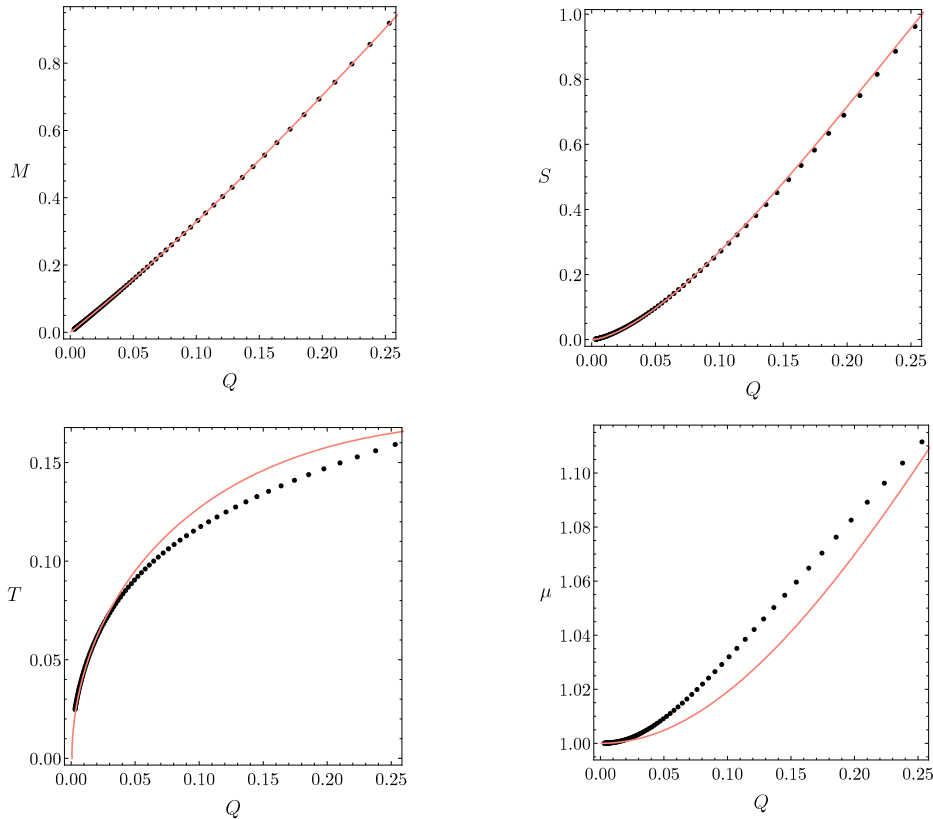


**Fig. 3.14** Comparison of the data to the small charge perturbative expansion for the four main thermodynamic quantities. The black disks are the numerical data for the hairy black holes (with  $\varepsilon = 0.1$ ) and the red solid line shows the prediction of [62]. As expected, we observe larger deviations in the temperature and chemical potential.

### 3.6 Comparison with perturbative results

In this section we compare our numerical results with the perturbative expansion of the hairy black hole solutions of [62], which are only valid at small asymptotic charges. In [62] the mass and charge are given to sixth order in  $\mathcal{O}(\varepsilon^6, R^6, \varepsilon^2 R^4, \varepsilon^4 R^2)$ , however, the chemical potential is only given to  $\mathcal{O}(R^4, \varepsilon^2 R^2, \varepsilon^4)$  and the temperature to  $\mathcal{O}(R^3, \varepsilon^2 R^3, \varepsilon^4 R)$ . In Fig. (3.14) we present a detailed comparison between our numerical solutions, represented by the black disks, and the expansion of [62] represented by the red solid line. Since the chemical potential and temperature are only determined up to a lower order than the energy, we expect a worse agreement with the numerical data. This is indeed what we observe in Fig. (3.14). Nevertheless, the observed agreement between the numerical data and the analytic expansion of [62] is reassuring.

## 3.7 Summary and discussion

In this chapter we have analysed hairy black hole solutions in global  $\text{AdS}_5$  spacetime using numerical methods. The action that yields these new black hole solutions arises from a consistent truncation of IIB string theory on  $\text{AdS}_5 \times S^5$ . We provided strong numerical evidence that the black hole solutions with the scalar condensate exist between the onset of the superradiant instability and the BPS limit for all values of the hairy black hole charge.

We obtain the smooth horizonless soliton with  $\alpha = 0$  in the limit  $T \rightarrow 0$ , while the singular soliton with  $\alpha = 1$  is reached for any isothermal with  $T \neq 0$  in the limit where  $\epsilon_0$  (scalar field evaluated at the horizon) becomes infinitely large. The fact that these new solutions extend all the way to the BPS limit makes them interesting from the field theory perspective. In fact, from the field theory it is natural that solutions with mass and charge arbitrarily close to the BPS bound should exist, and yet the RNAdS black hole does not saturate such a bound. It is thus reassuring that we did find solutions that saturate the BPS bound; that they turn out to be hairy solutions could have not been anticipated.

We identify the temperature range  $T_1 < T < T_2$  for which  $(\partial M/\partial Q)|_T$  diverges and is marked by complex thermodynamic properties. Globally, we find that the hairy solutions, when they exist, are the preferred phase in the microcanonical ensemble, however, they are subdominant in the canonical and grand-canonical ensembles. In the canonical ensemble, the hairy black holes dominate over RNAdS black holes at low temperatures and become subdominant at high temperatures, however, the hairy solutions are never preferred over pure AdS. Finally, in the grand-canonical ensemble, the RNAdS black holes always dominate over the hairy solutions. These results are recovered in the planar limit.

This setup can also be used to analyse other consistent truncations, for instance, consistent truncations of the holographic dual on  $\text{AdS}_4 \times S^7$ . In this case the existence of hairy supersymmetric solutions is known (e.g. [124]) and it would be interesting to explore how non extremal configurations approach these supersymmetric hairy solutions.

A natural extension of this work is the inclusion of rotation in our setup. For this system it is known that there exist a one parameter family of supersymmetric

asymptotically  $\text{AdS}_5$  black holes [117] with zero scalar field. In the following chapter we will explore the hairy, rotating and charged black hole solution space in great detail, and construct the three-dimensional phase diagram numerically.

### 3.A Numerical validity

We check *a posteriori* that the solutions presented in this chapter satisfy  $\xi^\mu = 0$  at least to  $\mathcal{O}(10^{-10})$  precision, *i.e.* that our Einstein-DeTurck solutions are also Einstein (see Fig. 3.15). We find that low temperature hairy black holes have the highest  $\xi$  norm. The pseudospectral methods guarantee exponential convergence with an increasing grid size and we check that all our physical quantities and the norm of the DeTurck vector have this property (Fig. 3.17, 3.18).

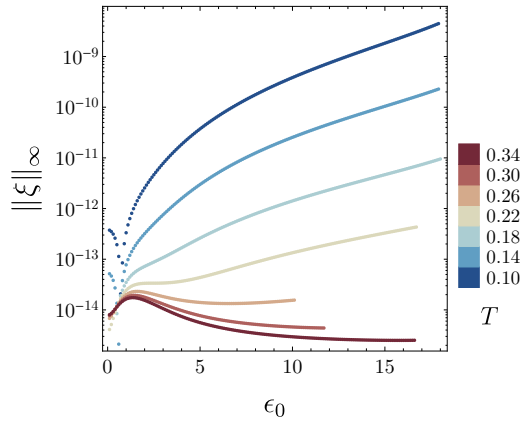


**Fig. 3.15** The infinity norm of the DeTurck vector across a range temperatures with the number of gridpoints  $n = 600$ . Lower temperature hairy global solutions have the highest norm.

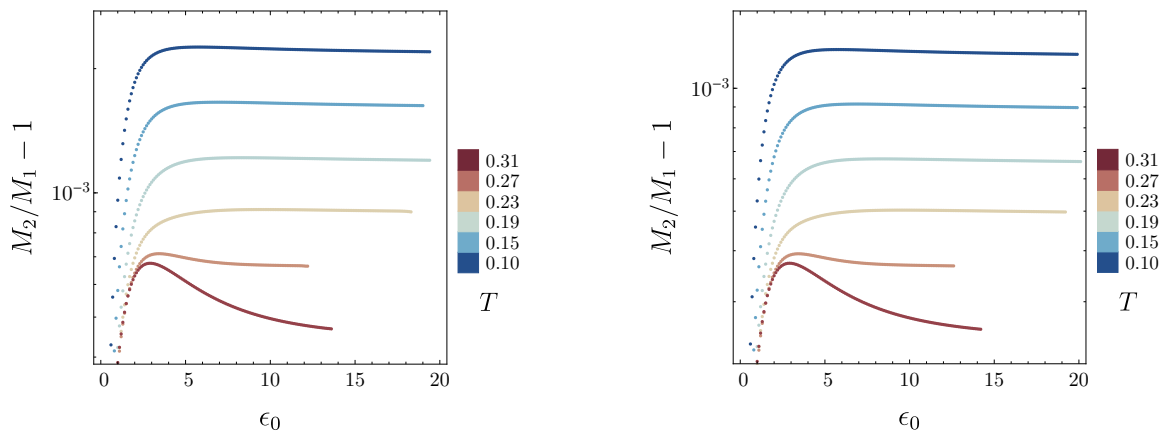


**Fig. 3.16** Comparison of the two *ansatz*.  $M_1$  is the (3.12) *ansatz*,  $M_2$  is the (3.14) *ansatz*. *Left*:  $n = 400$  data. *Right*:  $n = 600$  data. The highest temperature solutions agree the best and the agreement gets worse as we lower the temperature.

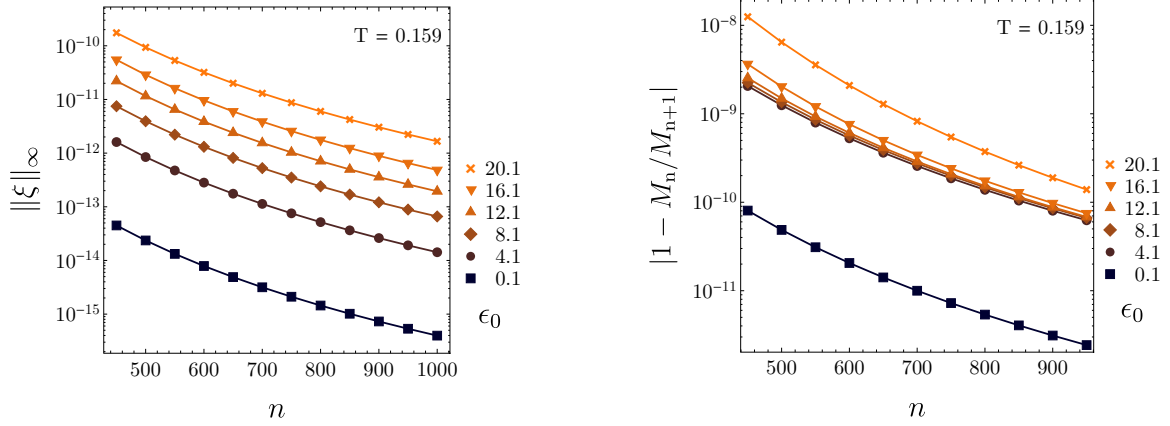


**Fig. 3.17** Convergence for the hairy global solutions for different values of the central scalar field density  $\epsilon_0$  for one particular temperature. Convergence for the first *ansatz* is at least few orders of magnitude worse. *Left*: The norm of the DeTurck vector versus the grid size. *Right*: Hairy black hole mass error versus the grid size. As the mass involves second derivatives other thermodynamical quantities have at least two order of magnitude better convergence. For  $\epsilon_0 > 20$  convergence falls rapidly.

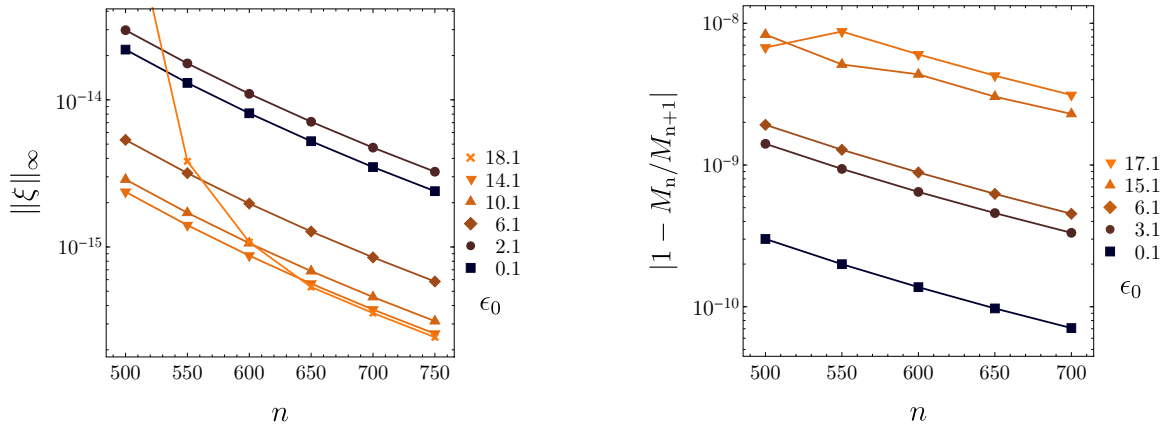


**Fig. 3.18** Convergence for the hairy planar solutions for different values of the central scalar field density  $\epsilon_0$ . As expected it is much better than for the hairy solutions.

# Chapter 4

## Rotating Hairy Black Holes in $\text{AdS}_5 \times \text{S}^5$

The majority of the work presented in this chapter was published as [125] by the author alone. A part of the results was published as [126] in collaboration with Jorge E. Santos, and the near BPS analysis should be regarded as a collaborative effort. The numerical results were generated by the author alone with their own code. Some of the results of [126] were also obtained by Jorge E. Santos with their own code for verification.

### 4.1 Introduction

Perhaps one of the main achievements of string theory is understanding the Bekenstein-Hawking entropy of supersymmetric black holes in terms of microstate counting, both in flat and asymptotically AdS spaces [14–17]. However, this has not yet been accomplished in Maldacena’s original correspondence, even though much has been understood about the dual CFT. An immediate obstacle for the stringy microstate counting is the discrepancy between the number of parameters on each side of the duality [127, 128]. One possible resolution to this inconsistency is that a more general family of supersymmetric black holes might exist [129]. Supersymmetric solutions in this theory necessarily rotate, thus prompting the interest in rotating hairy black holes.

In this chapter we will study the stationary solutions of the action considered in the chapter 3. When the scalar field vanishes, the action reduces to that of the bosonic action for  $D = 5$  minimal gauged supergravity, for which rotating, charged black hole solutions are known in analytic form [130, 111, 115, 113, 112, 114, 119]. They admit a regular supersymmetric black hole limit, the Gutowski and Reall black hole [117, 116, 118], which can be uplifted to type IIB string theory on  $\text{AdS}_5 \times \text{S}^5$  [131, 132].

From the ten-dimensional perspective, the supersymmetric black holes with three R-charges and independent angular momenta preserve two supercharges, i.e. are dual to 1/16 BPS states. We will consider the truncation in which these black holes have self dual spin and three equal magnitude charges, and thus are described by one free parameter [117]; the BPS relation is given by  $M = J_1 + J_2 + \sum_i Q_i = 2J + 3Q$ . However, the general 1/16 BPS state in the dual field theory within our symmetry class depends on two fugacities.

In this work we present a limit in which hairy rotating black holes with finite entropy  $S > 0$  exist arbitrarily close to the BPS bound, and have arbitrarily low temperatures. These solutions have no divergence in the scalar field, as well as possess finite curvature invariants, even in the near extremal regime. The near extremal hairy black holes display parallelly propagated tidal force singularities. It is worth emphasising that all the hairy black holes, including the ones just above the BPS bound are smooth solutions, and the tidal forces diverge only at extremality. Such singularities can be regarded “good” in the sense of [133, 134]. In addition, we further argue that the divergences exhibited in the extremal limit of these solutions can be consistently studied within the supergravity approximation as the Jacobi fields remain bounded. Such solutions are termed Tipler-weak, and admit a consistent propagation of infalling classical objects.

We argue that the limiting  $T = 0$  solutions constitute a one parameter generalization of the supersymmetric Gutowski-Reall black hole, and therefore play an important role in resolving the long-standing problem of black hole microstate counting in type IIB supergravity. In particular, we propose that the missing parameter is the horizon scalar hair. We focus on exploring the moduli space near the BPS bound, and provide numerical evidence supporting the existence of a novel class of hairy rotating black holes which are supersymmetric. We construct the phase diagram for the rotating hairy black holes, which is governed by three parameters  $\{Q, M, J\}$ .

Primarily we are interested in solutions with global AdS<sub>5</sub> asymptotics, *i.e.* the black hole solutions that are dual to the states of the CFT residing on  $\mathbb{R}_t \times S^3$ . However, we will also study the large horizon radius limit, in which the black holes are (locally) described by solutions with planar horizon topology. Here we find that our ansatz allows for a spontaneously generated current in the dual field theory.

We summarize the phase diagram of chapter 3 in section 4.2. The authors of [62] have proposed a number of intriguing possibilities for the hairy rotating black hole solution space in this truncation, and theorized the existence of regular hairy supersymmetric black holes based on a non-interacting thermodynamic model. We find numerical evidence supporting this idea and conjecture a two parameter family of supersymmetric hairy rotating black holes, characterised by the angular momentum  $J$  and the horizon scalar field  $\varepsilon_H$ . We suggest that these solutions continuously connect to the smooth solitons, and a small amount of angular momentum supports a small spinning black hole immersed in a sea of static scalar field.

This chapter is organised as follows. In section 4.2 we briefly recall the results of chapter 3, and present the phase diagram for the rotating, charged hairy black holes. We comment on the possible behaviour of the solutions in the regimes which were inaccessible to our numerical scheme. In section 4.3 we detail the setup and ansatz for the solutions, and give the equations of motion explicitly. Next, in section 4.4, we describe the numerical approach and the construction of the solutions, followed by the numerical results in section 4.5. We obtain the onset of the superradiance via linear analysis, and we show that it agrees with the full non-linear results. We discuss the parameter space and provide different ways of tracing out the phase diagram, and we thoroughly study the near extremal behaviour of the hairy solutions. In section 4.7 we analyse the thermodynamics, and section 4.8 is devoted to the planar limit of our solutions. We obtain a two parameter family of “rotating” hairy branes which are not Lorentz boosted, and analyse their properties. We close with discussion and prospects for future work in section 4.10.

## 4.2 Summary of the phase diagram

We briefly summarize the results of the static case presented the previous chapter in Fig. 4.1 (*left*). The Reisner–Nordström black holes (RNAdS) are bounded below by

the  $T = 0$  extremality curve (dashed black), and the hairy black holes exist between the merger line which indicates the appearance of a marginal mode (solid orange) and the BPS bound given by  $M = 3Q$  (dashed red). There are three families of solitonic solutions which are relevant to the hairy black hole phase diagram<sup>1</sup>. The smooth solitons, shown by the purple wavy line, are perturbatively connected to the pure AdS, and as we increase the central scalar field density to infinity this branch terminates at the unique singular solution with  $Q_c \simeq 0.2613$ . We will see that this solution is quite special even in the  $J > 0$  phase space. Here, the smooth and the singular soliton branches merge; the singular soliton family has no upper bound on the charge and admits a scaling limit. The smooth BPS solitons can be regarded as the zero temperature limit of the hairy black hole families with a constant horizon scalar  $\varepsilon_H$  [62, 92], and the singular solitons represent the  $\varepsilon_H \rightarrow \infty$ ,  $T \rightarrow \infty$  limit of the hairy black holes. In the planar limit, we have a one parameter class of hairy black branes that connect to the large charge limit of the singular soliton branch as  $\varepsilon_H \rightarrow \infty$ .

In this chapter we are extending the results of 3, by considering rotating solutions, which include a one parameter family of supersymmetric Gutowski-Reall black holes. Charged, rotating solutions in this theory have analytic expressions, and were first presented by Cvetič, Lü and Pope (CLP) [130]. The hairy black holes extend the non-rotating solution space up to the BPS bound, and on the BPS bound smoothly connect to the soliton solutions. Once rotation is included, the picture is surprisingly similar, and the hairy black holes interpolate the solution space between the extremal plane and the BPS bound for all charges<sup>2</sup>. We find rotating hairy black holes arbitrarily close to the supersymmetric limit, and, for charges sufficiently close to the Gutowski-Reall black hole, the hairy solutions maintain finite entropy and are free from scalar curvature singularities.

The results of this chapter are summarised in Fig. 4.1 (*right*), where we present the microcanonical phase diagram of the hairy solutions at a fixed angular momentum  $J$ . The hairy black holes exist between the solid orange line which marks the onset of the superradiant instability, and the red dashed curve showing the BPS bound, which is given by  $M = 3Q + 2J$ . The extremality for the charged rotating black holes is given by the dashed black curve. The solid grey line shows the charged rotating black

<sup>1</sup>There is at least one more known family of solitons which does not connect to black hole solutions.

<sup>2</sup>We find that only black holes with horizon angular velocity  $\Omega_H < 1$  are unstable to forming scalar hair, and all hairy black holes in this truncation have  $\Omega_H \leq 1$ .

holes with  $\Omega_H = 1$ , and the black holes below this line have  $\Omega_H > 1$ <sup>3</sup>. The black disk shows the supersymmetric Gutowski-Reall black hole, and the purple wavy line shows the conjectured supersymmetric rotating hairy black holes, which exist up to some maximal charge  $Q_{\max}(J)$ , where the entropy  $S \rightarrow 0$ . At that point a special solution might exist at which all isotherms intersect. For larger charges the BPS solutions are singular, and can be regarded as a  $T \rightarrow \infty$  ( $\varepsilon_H \rightarrow \infty$ ) limit of the regular hairy black hole solutions. As we are constrained by the scope of our numerical methods, we can only conjecture the possible limiting behaviour of these solutions. In the following chapters, we will aim to give a convincing numerical evidence which supports this picture. For a further discussion on the extent of the evidence we refer the reader to the concluding section 4.10.

Finally, the large charge rotating hairy solutions admit a scaling limit. While the planar CLP black holes can be obtained from the RNAdS holes via a simple boost, we argue that the hairy rotating branes cannot be boosts of the non-rotating counterparts due to a non-vanishing magnetic field on the horizon. The two parameter family of solutions has interesting properties, and displays a phase transition in the canonical ensemble. Such black holes exhibit retrograde condensation, as found in the non-rotating case, and in the large temperature limit they approach the singular soliton of [62].

## 4.3 Setup

### 4.3.1 The field equations for the stationary ansatz

We are interested in stationary, asymptotically anti-de Sitter black holes, with spherical horizon topology. The most general such solution can have two independent angular momenta, but we will consider a doubly spinning solution for which the magnitude of angular momenta along the two rotation directions is the same. Keeping the gauge arbitrary, we can write down the following general cohomogeneity-one ansatz [47],

$$ds^2 = -f(r) dt^2 + g(r) dr^2 + \Sigma(r)^2 \left[ h(r) \left( d\psi + \frac{1}{2} \cos \theta d\phi - \Omega(r) dt \right)^2 + \frac{1}{4} d\Omega_2^2 \right]. \quad (4.1)$$

---

<sup>3</sup>All CLP black holes above this line have  $\Omega_H < 1$ .

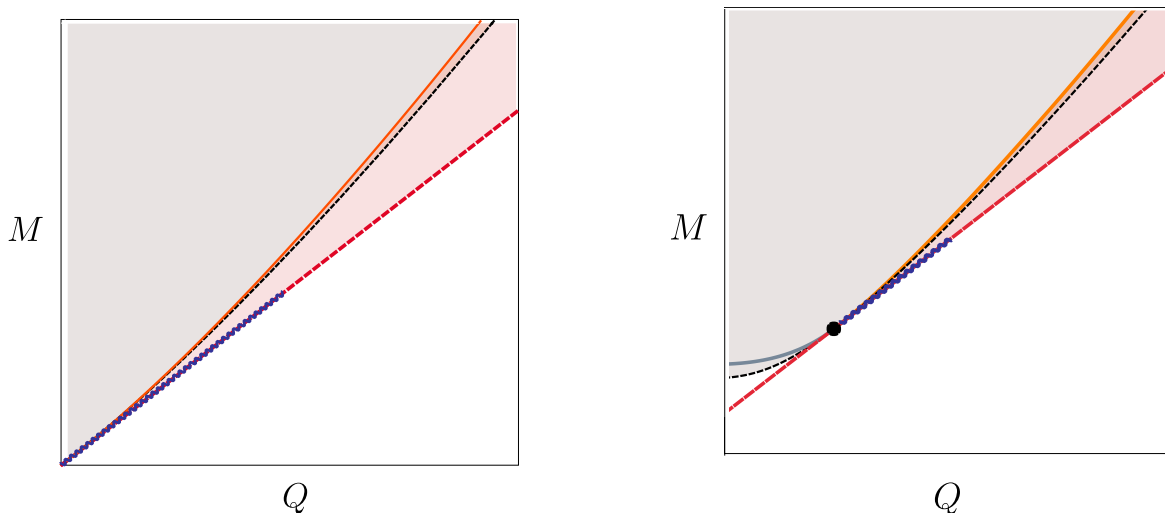


**Fig. 4.1** *Left:* Microcanonical phase diagram of charged, non-rotating hairy black holes [62, 92]. The Reissner-Nordström black holes exist above their extremal limit (black dashed line), and the hairy black holes exist below the bold orange line, which shows the onset of the superradiant instability. These solutions extend down to the BPS bound, where they reduce to the smooth soliton (the purple wavy line) in the limit  $T \rightarrow 0$ , while keeping the value of the scalar field at the horizon  $\varepsilon_H$  fixed. *Right:* Microcanonical phase diagram of charged, rotating hairy black holes at a constant angular momentum  $J$ . The hairy black holes exist between the merger line (orange) and the BPS bound (dashed red), in the region shaded in light red. The black disk is the supersymmetric Gutowski-Reall black hole [117], which lies at the intersection of the extremal and the BPS planes. The purple wavy line shows a line of the conjectured supersymmetric hairy black holes, which terminates at a finite charge  $Q_{\max}(J)$ , where the black holes become singular.

When considering the AdS limit of the ansatz, we can see that the metric on the round three sphere is written as a Hopf fibration over the unit  $\mathbb{CP}^1$  space, with the corresponding Kähler potential<sup>4</sup>  $\mathcal{A} = \mathcal{A}_a dx^a = \frac{1}{2} \cos \theta d\phi$ . It is given by  $d\Omega_3^2 = (d\psi + \mathcal{A})^2 + d\tilde{\Omega}_2^2$ , with the standard Fubini-Study metric  $d\tilde{\Omega}_2^2 = \frac{1}{4} (d\theta^2 + \sin^2 \theta d\phi^2)$ . The fiber is parametrised by the coordinate  $\psi$  with a period  $2\pi$ <sup>5</sup>, where  $\theta, \phi$  are the standard polar coordinates on  $S^2$ . The level surfaces of the ansatz are given by homogeneously squashed 3-spheres.

<sup>4</sup>In the sense that the Kähler form for  $\mathbb{CP}^1$  is given by  $J = \frac{1}{2} d\mathcal{A}$ .

<sup>5</sup>The Hopf fibration requires that the coordinate parametrising the  $S^1$  fiber has  $\psi \rightarrow \psi + \pi$  when  $\phi \rightarrow \phi + 2\pi$ . The two orthogonal planes of rotation are at  $\theta = 0$  and  $\theta = \pi$ .

The gauge field ansatz which respects the symmetries of (4.1) is given by

$$A = A_t(r)dt + A_\psi(r)(d\psi + \mathcal{A}), \quad (4.2)$$

and we also take  $\phi = \phi^\dagger = \phi(r)$ , as the phase of the scalar field is removed by a  $U(1)$  gauge transformation. The ansatz (4.1) has a residual gauge freedom

$$\psi \rightarrow \psi + \alpha t, \quad \Omega \rightarrow \Omega + \alpha, \quad (4.3)$$

where  $\alpha$  is a constant. The gauge in which the frame is static at asymptotic infinity simplifies the thermodynamic analysis [135, 136, 110], thus we will make use of (4.3) to set the angular velocity  $\Omega(r) \rightarrow 0$  as  $r \rightarrow \infty$ .

The Einstein, Maxwell and scalar equations comprise a system of seven non-linear differential equations, two of first order and five of second order. Using the ansatz (4.1) the equations can be compactly written as

$$\begin{aligned} f'' + f' \left( \Xi - \frac{h'}{h} - \frac{f'}{f} - \frac{5\Sigma'}{\Sigma} \right) - f \left( \Pi - \frac{3\phi'^2}{\phi^2 + 4} \right) - 5 \left( A' + \Omega A'_\psi \right)^2 - 2h\Sigma^2\Omega'^2 &= 0, \\ g' + 2g \left( \Xi - \frac{f'}{2f} - \frac{h'}{2h} - \frac{2\Sigma'}{\Sigma} \right) &= 0, \\ h'' + h' \left( \Xi + \frac{\Sigma'}{\Sigma} - \frac{h'}{h} \right) + h^2 \left( \frac{\Sigma^2\Omega'^2}{f} - \frac{8g}{\Sigma^2} \right) + \frac{4gh}{\Sigma^4} (2\Sigma^2 - 3A_\psi^2) + \frac{3}{\Sigma^2} (A_\psi^2 g \phi^2 + A_\psi'^2) &= 0, \\ \Omega'' + \Omega' \left( \Xi - \frac{f'}{f} + \frac{h'}{h} + \frac{3\Sigma'}{\Sigma} \right) - \frac{3\Omega}{h\Sigma^2} (A_\psi^2 g \phi^2 + A_\psi'^2) - \frac{3}{h\Sigma^2} (A' A'_\psi + A A_\psi g \phi^2) &= 0, \\ A'' - \frac{1}{2} A' \left( \frac{g'}{g} - \frac{h'}{h} + \frac{f'}{f} - \frac{6\Sigma'}{\Sigma} - X \right) - A g \phi^2 \\ &+ A'_\psi \left[ \frac{4A_\psi \sqrt{fgh}}{h\Sigma^3} - \Omega \left( \frac{f'}{f} - \frac{h'}{h} - \frac{2\Sigma'}{\Sigma} - \frac{1}{2} X \right) + \Omega' \right] + \frac{4A_\psi g h \Omega}{\Sigma^2} = 0, \\ A_\psi'' - \frac{1}{2} A'_\psi \left( -\frac{f'}{f} + \frac{g'}{g} + \frac{h'}{h} - \frac{2\Sigma'}{\Sigma} + X \right) - A_\psi g \left( \frac{4h}{\Sigma^2} + \phi^2 \right) - \frac{1}{2\Omega} A' X &= 0, \\ \phi'' + \frac{1}{2} \phi' \left( \frac{f'}{f} - \frac{g'}{g} + \frac{h'}{h} + \frac{6\Sigma'}{\Sigma} \right) + g \phi (\phi^2 + 4) \left[ \frac{(A + A_\psi \Omega)^2}{f} - \frac{A_\psi^2}{h\Sigma^2} + 1 \right] - \frac{\phi \phi'^2}{\phi^2 + 4} &= 0, \end{aligned} \quad (4.4)$$

with an additional constraint equation. Here

$$\begin{aligned}\Xi &= \frac{A_\psi'^2}{2h\Sigma\Sigma'} - \frac{\Sigma}{2f\Sigma'} (A' + \Omega A_\psi')^2 - \frac{\Sigma''}{\Sigma'} + \frac{g}{2\Sigma^3\Sigma'} \left[ \Sigma^2 (-4h + \Sigma^2 (\phi^2 + 8) + 8) - 8A_\psi'^2 \right], \\ \Pi &= \frac{1}{h\Sigma^2} \left[ 3A_\psi'^2 g \phi^2 - 2A_\psi'^2 + 4\Sigma' (\Sigma h' + 3h\Sigma') \right] - \frac{2g}{\Sigma^4} \left[ \Sigma^2 (-2h + \Sigma^2 (\phi^2 + 8) + 8) - 8A_\psi'^2 \right], \\ X &= \frac{2\Omega}{\Sigma f} \left[ h\Sigma^3 \Omega' - 4A_\psi \sqrt{fgh} \right],\end{aligned}\tag{4.5}$$

and the  $'$  denotes the differentiation with respect to the coordinate  $r$ . It is possible to obtain a first order differential equation for  $f(r)$  and subsequently eliminate it altogether, but the equations get increasingly complicated.

Known solutions to (4.4) have been obtained in the gauge where  $\Sigma(r) = r$ , and we will use this radial gauge throughout unless otherwise stated. In the radial gauge we are looking for solutions asymptoting to  $\text{AdS}_5$  [106–108, 20], *i.e.* obeying

$$\begin{aligned}f(r) &= r^2 + 1 + \frac{C_f}{r^2} + \mathcal{O}(r^{-4}), & g(r) &= \frac{1}{r^2} - \frac{1}{r^4} + \mathcal{O}(r^{-6}), & h(r) &= 1 + \frac{C_h}{r^4} + \mathcal{O}(r^{-6}), \\ \Omega(r) &= \frac{2J}{r^4} + \mathcal{O}(r^{-5}), & A_t(r) &= \mu_\infty + \frac{2Q}{r^2} + \mathcal{O}(r^{-6}), & A_\psi(r) &= \mathcal{O}(r^{-2}), \\ \phi(r) &= \frac{C_\phi}{r^2} + \mathcal{O}(r^{-4}).\end{aligned}\tag{4.6}$$

Here  $\mu_\infty$  is the electrostatic potential at the boundary,  $Q$  is the black hole charge,  $J$  is the black hole angular momentum, and the black hole mass is given by  $M = \frac{1}{4}(C_h - 3C_f)$ , where the constants  $C_h$  and  $C_f$  are to be extracted from the large  $r$  behaviour of the functions. We note that here, and throughout the chapter, the conserved charges of the system are rescaled by  $N^2$ . Further discussion on the thermodynamics will be given in subsection 4.4.2. The constant  $C_\phi$  is the expectation value of the operator dual to the scalar field,  $C_\phi = \langle \mathcal{O}_\phi \rangle$ ; here we assume the standard quantisation and the operator is not sourced.

The black hole horizon  $r_+$  is defined as the largest root where  $f(r_+) = 0$ , and all other functions are regular. We also identify  $\Omega_H = \Omega(r_+)$  as the horizon angular velocity.

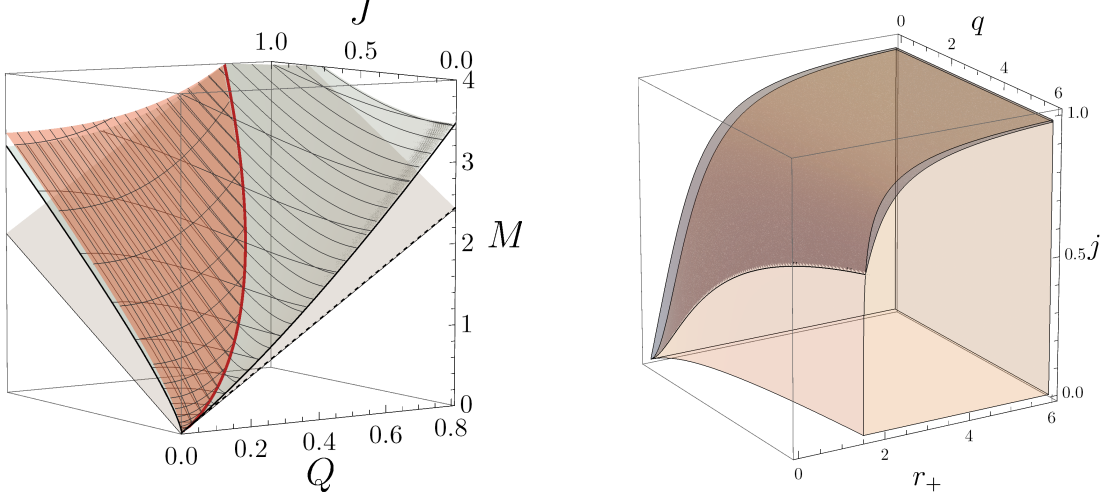


**Fig. 4.2** *Left:* Phase diagram for the regular CLP black hole solutions, showing possible  $Q$ ,  $M$  and  $J$  values. The grey plane shows the BPS limit  $M = 2J + 3Q$ , the blue plane is the extremal limit with  $T = 0$ . The red line shows Real-Gutowski holes, which are extremal BPS solutions, and lie on the intersection of the extremal and BPS planes. The orange plane shows the  $\Omega_H = 1$  limit for regular black holes with  $T > 0$ . Such black holes exist above the extremal plane, and regular solutions with  $\Omega_H > 1$  exist only between the orange and blue planes. For  $J = 0$ , we recover RNAdS solutions, and for  $Q = 0$  we recover MPAdS holes. *Right:* Allowed parameter space for regular CLP black holes. It is bounded by the extremal surface, which also guarantees a non-negative entropy. The grey region on top shows the moduli space with  $\Omega_H \geq 1$ . The Gutowski-Reall black holes are the curve on the front left face, where the grey region meets the orange region.

### 4.3.2 Charged, equally-rotating black holes

General five-dimensional, charged and equally rotating black hole solutions with a cosmological constant were first presented by Cvetič, Lü and Pope (CLP) [130], in the bosonic sector of minimal gauged supergravity, which is the  $\phi = 0$  limit of our action. The black holes are governed by three parameters  $\{q, j, m\}$ , which are related to the conserved charges  $\{Q, J, M\}$  [137]. In terms of our ansatz (4.1), the solutions in a static frame at infinity are given as

$$\begin{aligned}
 f(r) &= F(r)/h(r), & g(r) &= 1/F(r), & h(r) &= j^2 \left( \frac{m}{r^4} - \frac{q^2}{r^6} \right) + 1, & \Sigma(r) &= r, \\
 \Omega(r) &= \frac{j}{h(r)} \left( \frac{m - q}{r^4} - \frac{q^2}{r^6} \right), & A(r) &= q/r^2, & A_\psi(r) &= -jq/r^2,
 \end{aligned}
 \tag{4.7}$$

where

$$F(r) = \frac{1}{r^4} \left[ q^2 \left( 1 - \frac{j^2}{L^2} \right) + j^2 m \right] - \frac{1}{r^2} \left[ m \left( 1 - \frac{j^2}{L^2} \right) - 2q \right] + \frac{r^2}{L^2} + 1, \quad (4.8)$$

and we keep the AdS radius  $L$  for clarity, in this subsection only. The thermodynamic quantities temperature  $T$ , entropy  $S$ , chemical potential  $\mu$ , electric charge  $Q$ , horizon angular velocity  $\Omega_H$ , angular momentum  $J$  and mass  $M$  are given by

$$\begin{aligned} T &= \frac{F'(r_+)}{4\pi\sqrt{h(r_+)}} = \frac{r_+^6 - j^2(2L^2m + mr_+^2 - 2q^2) + L^2(r_+^2(m - 2q) - 2q^2)}{2\pi L^2 r_+^2 \sqrt{j^2(mr_+^2 - q^2) + r_+^6}}, \\ S &= \pi \sqrt{j^2(mr_+^2 - q^2) + r_+^6}, \quad \mu = q \frac{r_+^2 - j^2(1 + r_+^2/L^2)}{j^2q + r_+^4}, \\ Q &= \frac{1}{2}q, \quad \Omega_H = j \frac{q + r_+^2(1 + r_+^2/L^2)}{j^2q + r_+^4}, \end{aligned}$$

$$J = \frac{1}{2}j(m - q), \quad M = \frac{1}{4} \left[ m \left( 3 + \frac{j^2}{L^2} \right) - 6q \right], \quad (4.9)$$

where the parameter  $m$  can be written as

$$m = \frac{(q + r_+^2)^2 - j^2q^2/l^2 + r_+^6/L^2}{r_+^2 - j^2(1 + r_+^2/L^2)}, \quad (4.10)$$

and parameter  $r_+$  is determined by requiring that  $F(r_+) = 0$ . The supersymmetric limit is given by [138]

$$M = 2J + 3Q. \quad (4.11)$$

All extremal CLP's have  $\Omega_H \leq 1$  (and  $\mu \geq 1$ ), where it is equal to one only on the supersymmetric bound.

The solution space of the regular CLP black holes with thermodynamics described by (4.9) is shown in Fig. 4.2 (left), together with the allowed parameter range in Fig. 4.2 (right). We note that the presence of the Chern-Simons term breaks charge reversal

invariance  $Q \rightarrow -Q$ , and in this chapter we will only consider  $Q > 0$ , and hence  $\mu > 0$  solutions.

The non-rotating solutions are the Reissner-Nordström black holes (RNAdS) and can be recovered by taking  $j = 0$ ,  $m = R^2 (R^2 + (\mu + 1)^2)$  and  $q = \mu R^2$ . For completeness we note down the solution in terms of (4.1)

$$\begin{aligned} f(r) &= 1 + \frac{r^2}{L^2} - \frac{(R^2/L^2 + \mu^2 + 1)R^2}{r^2} + \frac{\mu^2 R^4}{r^4}, & \Sigma(r) &= r, \\ g(r) &= \frac{1}{f(r)}, & A(r) &= \mu \left(1 - \frac{R^2}{r^2}\right), & A_\psi(r) &= 0, & \Omega(r) &= 0, & \phi(r) &= 0. \end{aligned} \quad (4.12)$$

The thermodynamic quantities are given as

$$\begin{aligned} M &= \frac{3}{4}R^2 (1 + R^2/L^2 + \mu^2), & Q &= \frac{1}{2}\mu R^2, & S &= \pi R^3, \\ T &= \frac{1}{2\pi R} (1 + 2R^2/L^2 - \mu^2), \end{aligned} \quad (4.13)$$

and the black holes are extremal if  $\mu = \sqrt{1 + 2R^2/L^2}$ . Another well known solution is the zero charge limit of (4.7), the five-dimensional equally-rotating Myers-Perry-AdS (MPAdS) black hole [139, 135].

The supersymmetric limit [116] is a one parameter family, and can be obtained by setting

$$q = \left(1 + \frac{r_+^2}{2L^2}\right) r_+^2, \quad j = \left(1 + \frac{r_+^2}{2L^2}\right)^{-1} \frac{r_+^2}{2}, \quad m = 4 \left(1 + \frac{r_+^2}{2L^2}\right)^2 r_+^2. \quad (4.14)$$

These solutions are both extremal and supersymmetric; they have  $\mu = 1$  and  $\Omega_H = 1$ .

## 4.4 Hairy Black holes

### 4.4.1 Numerical setup

In this subsection we will briefly outline the numerical ansatz we used to construct the rotating hairy black hole solutions. We will work in both the radial and the DeTurck gauges, the former offers better convergence, and the latter allows us to fix the black hole temperature  $T$ . The solution space is governed by three parameters: the charge  $Q$ ,

the mass  $M$  and the dual angular momentum  $J$ . In practice we vary some combination of free parameters which are related to the black hole horizon, scalar field and rotation.

First we compactify the radial coordinate  $r = \frac{y_+}{\sqrt{1-y^2}}$ , so that  $y = 1$  coincides with  $r = \infty$ , and  $y = 0$  with  $r = r_+ = y_+$ . The metric *ansatz* (4.1) is

$$\begin{aligned} ds^2 = \frac{1}{1-y^2} & \left[ -(y_+y)^2 q_1(y) dt^2 + \frac{q_2(y) dy^2}{1-y^2} \right. \\ & \left. + y_+^2 \left\{ q_3(y) \left[ d\psi + \frac{1}{2} x d\phi - \Omega(y) dt \right]^2 + \frac{1}{4} q_4(y) \left[ (1-x^2) d\phi^2 + \frac{dx^2}{1-x^2} \right] \right\} \right], \end{aligned} \quad (4.15)$$

where  $x = \cos \theta$  and  $\phi$  are the usual polar angles on the  $S^2$ .

The gauge fields (4.2) and the scalar field take the form

$$A_t(r) = y^2 q_6(y) - q_5(y) q_7(y), \quad A_\psi(r) = q_7(y), \quad \phi(r) = (1-y^2) q_8(y). \quad (4.16)$$

To change into the frame which is non-rotating at the boundary  $y = 1$ , we factorize  $\Omega(y) = (1-y^2)^2 q_5(y)$ , and at  $y = 0$  we identify  $q_5(0) = \Omega_H$ , where  $\Omega_H$  is the angular velocity at the black hole horizon. We can choose to impose the boundary condition on  $q_5(y)$  either at the horizon or at the conformal boundary, and both of these choices will give a complementary view of the solution space.

A good reference metric  $\tilde{g}$  for the DeTurck method can be obtained from (4.15) if we set  $\tilde{q}_1 = \tilde{q}_2 = \tilde{q}_3 = \tilde{q}_4 = 1$ , and  $\tilde{q}_5 = q_5$ . Overall this ansatz is incredibly simple, and is allowed by the fact that the hairy black holes can reach arbitrarily low temperatures.

Requiring the correct asymptotics (4.6), in the radial gauge, we find that at the boundary  $y = 1$  we should specify

$$q_1 = q_2 = q_3 = q_4 = 1, \quad (4.17)$$

$$2y_+^2 q_5' - q_5 q_7'^2 + 4q_5 (y_+^2 + 1) + (q_6' + 2q_6) q_7' = 0, \quad (4.18)$$

$$y_+^2 q_8' - 2q_6^2 q_8 = 0, \quad (4.19)$$

$$q_7 = 0. \quad (4.20)$$

In the DeTurck gauge replace (4.18) by  $2y_+^2 q'_5 + 2q_6 q'_7 + q'_6 q'_7 - q_5 q_7'^2 = 0$ , and (4.19) by  $y_+^2 q'_8 + q_8 (y_+^2 + 1 - 2q_6^2) = 0$ . There is some freedom in specifying these conditions, depending on which variables we want to keep fixed as we explore the parameter space. For instance, we can impose the fall-off of the scalar field, however, this condition may not guarantee the unique parametrization of solutions [92]. We will find that it is convenient to fix the angular momentum, which is equivalent to setting the  $\Omega(y)$  fall-off at infinity, replacing the condition (4.18) with  $q_5 = \Omega_{\text{inf}}$ .

At the horizon  $y = 0$ , regularity imposes

$$q'_1 = 0, \quad (4.21)$$

$$q'_2 = q'_3 = q'_4 = q'_6 = q'_7 = q'_8 = 0, \quad (4.22)$$

$$q_5 = \Omega_H, \quad (4.23)$$

$$q_8 = \varepsilon_H. \quad (4.24)$$

Here we choose to specify the scalar field value at the horizon and label it  $\varepsilon_H$ , and angular velocity at the horizon  $\Omega_H$ . If instead we specify the angular momentum, we would change (4.23) to the Neumann condition  $q'_5 = 0$ . For the DeTurck gauge, replace (4.21) by  $q_1 - q_2(1 - q_5^2) = 0$ . We can also specify the expectation value of the dual operator, by fixing  $q_8 = \langle \mathcal{O}_\phi \rangle / y_+^2$  at infinity.

We did not find any rotating smooth soliton solutions<sup>6</sup>. For completeness, we give the numerical ansatz for the smooth non-rotating soliton, as these solutions play an important role in the phase space of hairy rotating black holes. With the compactified radial coordinate  $r = \frac{y}{\sqrt{1-y^2}}$  it can be written as

$$\begin{aligned} ds^2 &= \frac{1}{1-y^2} \left[ -q_1(y) dt^2 + \frac{q_2(y) dy^2}{1-y^2} + q_3(y) y^2 \left\{ \frac{dx^2}{1-x^2} + (1-x^2) d\theta^2 + x^2 d\psi^2 \right\} \right], \\ A(y) &= q_4(y), \\ \phi(y) &= (1-y^2) q_5(y). \end{aligned} \quad (4.25)$$

<sup>6</sup>One can globally rotate the solution (4.25) using the gauge freedom (4.3). However, such solutions don't seem to play any important role in the phase space.

The boundary conditions at  $y = 1$  are given by  $q_1 = 1, q_2 = 1, q_3 = 1, (q_4^2 - 1)q_5 - q_5' = 0$  and at  $y = 0$   $q_1' = 0, q_2 = q_3, q_3 = 1, q_4' = 0, q_5' = 0, q_5 = \varepsilon_H$ .

#### 4.4.2 Thermodynamic quantities

The global charges of the system,  $M, J, Q$  and the chemical potential  $\mu_\infty$  can be found from the fall-off of the metric (4.6). The asymptotic Killing vectors  $\partial_t$  and  $\partial_\psi$  will have associated conserved quantities, which in AdS spacetimes can be computed using the Ashtekar-Das method [120]. The mass and the angular momentum in the radial gauge are given by

$$M = \frac{1}{32} y_+^2 \left[ 18 + y_+^2 (18 - 3q_1'' + q_3'') \right]_{y=1}, \quad (4.26)$$

$$J = \frac{1}{2} y_+^4 q_5|_{y=1}, \quad (4.27)$$

where all functions are evaluated at the  $y = 1$  boundary, and the background  $\text{AdS}_5$  has zero mass. The electric  $U(1)$  charge is given by the electromagnetic flux integral at infinity

$$Q = \frac{1}{16\pi G_5} \int_{\text{S}^3_\infty} (\star F - F \wedge A) = \frac{1}{4} y_+^2 (-q_6' - 2q_6 + q_5 q_7')|_{y=1}, \quad (4.28)$$

where we note that the Chern-Simons term vanishes due to no magnetic field at the boundary. The chemical potential, which is a thermodynamic conjugate quantity to the electric charge, is given by

$$\mu = \xi^\nu A_\nu|_H - \xi^\nu A_\nu|_\infty = -q_6|_{y=1}, \quad (4.29)$$

where  $\xi^\nu \partial_\nu = \partial_t + \Omega_H \partial_\psi$  is the null generator of the horizon. The conjugate potential to the angular momentum is given by

$$\Omega = \Omega_H - \Omega_\infty = q_5|_{y=0}, \quad (4.30)$$

as we work in the frame which is non-rotating at infinity with  $\Omega_\infty = 0$ . The Hawking temperature is found in the usual way by requiring the periodicity of the Euclidean time

$$T = \frac{y_+}{2\pi} \sqrt{\frac{q_1}{q_2}} \Big|_{y=0}, \quad (4.31)$$

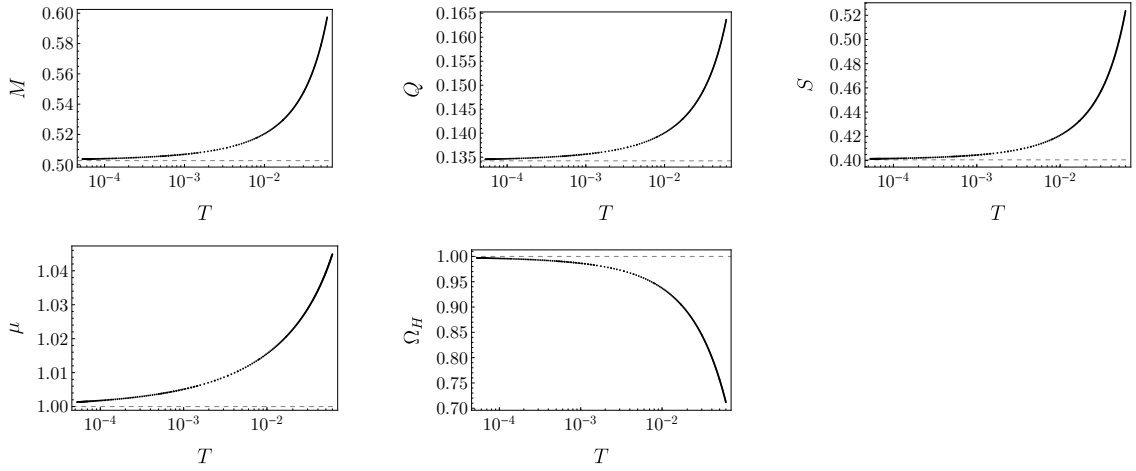


**Fig. 4.3** Thermodynamic quantities against the temperature  $T$ , for black holes with fixed angular momentum  $J = 0.05$  and horizon scalar field  $\varepsilon_H = 10^{-4}$  (black data points). The dashed gridlines show the values for the supersymmetric black hole with the same  $J$ .

and the Bekenstein-Hawking entropy of the black hole is given by

$$S = \pi y_+^3 \sqrt{q_3} q_4 |_{y=0}, \quad (4.32)$$

which is proportional to the area of its event horizon.

The thermodynamic quantities satisfy the first law

$$dM = TdS + 3\mu dQ + 2\Omega dJ, \quad (4.33)$$

and we verified that numerical rotating hairy solutions obey the first law to at least 0.1% accuracy in the DeTurck gauge, and to better than 0.001% in the radial gauge.

## 4.5 Phase diagram of hairy black holes

### 4.5.1 Linear instability and the onset plane

In order to directly compute the onset plane of the superradiant instability<sup>7</sup>, we linearise the scalar equation about the CLP black hole background (4.7). We obtain a second order equation for the infinitesimal perturbation  $\delta q_8$  of  $q_8$  defined in (4.16), which has three parameters  $y_+, j, q$ . The lowest order parameter is  $q$ , and the linearized equation can be solved as an 8th order eigenvalue equation in  $q$ . Alternatively, we can fix two parameters and regard the third parameter as an extra variable in the Newton's method. We follow this approach, the details of which can be found in [67, 60, 140, 141], and numerically solve the resulting equation

$$L(y; y_+) \delta q_8(y) = 0, \quad (4.34)$$

where  $L(y; y_+)$  is a second order differential operator, which is a non-linear function of  $y_+$  once we fix  $j$  and  $q$ . This way we can choose  $y_+$  to be a parameter which is determined once we fix the overall charge of the black hole  $Q$ , and approach the  $T \rightarrow 0$  limit when  $j$  is increased from zero. The boundary conditions can be found by demanding regularity at the horizon and expanding the scalar field equation off the asymptotic infinity. The boundary conditions are

$$\delta q_8'(0) = 0, \quad -2(y_+^2 - j^2(1 + y_+^2))^2 q^2 \delta q_8(1) + y_+(y_+^4 + j^2 q) \delta q_8'(1) = 0. \quad (4.35)$$

The linear results at constant charge  $Q = 0.1315$  are presented in Fig. (4.4). We find that for all charges that are feasible to track numerically, the family of black holes at the onset of the instability approaches the supersymmetric black hole, and exists just above the extremality plane of the CLP solutions.

The plane representing the onset of the scalar field instability can also be generated by solving the non-linear equations (4.4) by fixing the horizon scalar  $q_8(0) = \varepsilon_H$  to be very small, and both methods were found to be in a very good agreement where the

---

<sup>7</sup>At large charges the tachyonic instability is the dominant one, however, in this section we are mostly focusing on relatively small black holes.

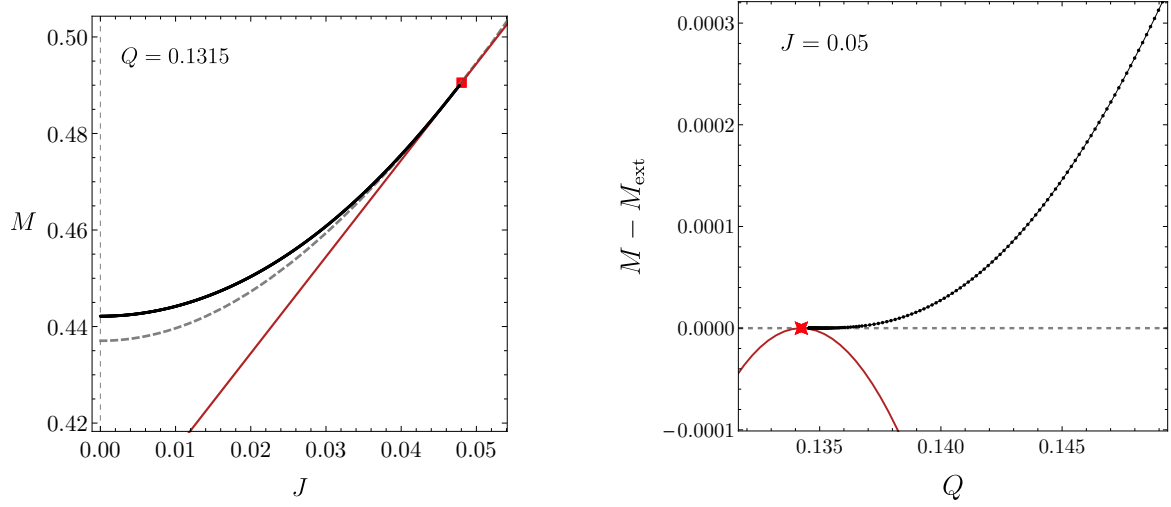


**Fig. 4.4** *Left*: The line of solutions showing the onset of the superradiance for the CLP black holes at constant charge  $Q = 0.1315$  (black points). These solutions extend arbitrarily close to the supersymmetric black holes (red square), with the temperature asymptotically approaching  $T = 0$ . The grey dashed line shows the extremality, and the red bold line shows the BPS bound  $M = 3Q + 2J$ . *Right*: The difference  $M - M_{\text{ext}}$  against the charge  $Q$ , for black holes with fixed  $J = 0.05$  and  $\varepsilon_H = 10^{-4}$  (black data points), where  $M_{\text{ext}}$  is mass of the extremal CLP black hole with the same  $Q$ . Red solid line is the BPS bound, and the red star shows the Gutowski-Reall solution.

comparison is possible<sup>8</sup>. In the radial gauge, we were able to achieve temperatures lower than  $T \simeq 10^{-4}$ . The results are presented in Fig. 4.4 (*right*), where we plot the mass difference  $M - M_{\text{ext}}$  for fixed  $J = 0.05$ , where  $M_{\text{ext}}$  is the mass of the corresponding extremal black hole in the microcanonical ensemble. As in the linear case, we find hairy black holes arbitrarily close to the Gutowski-Reall black hole. The non-linear equations are much harder to solve near the extremality than the linearised equation. In Fig. 4.3, we also show various thermodynamic quantities along the family of a constant  $J$  and  $\varepsilon_H$ , as  $T \rightarrow 0$ . As expected, the quantities approach those of the corresponding supersymmetric black hole with the fixed  $J$ , in particular  $\Omega_H \rightarrow 1$  and  $\mu \rightarrow 1$ .

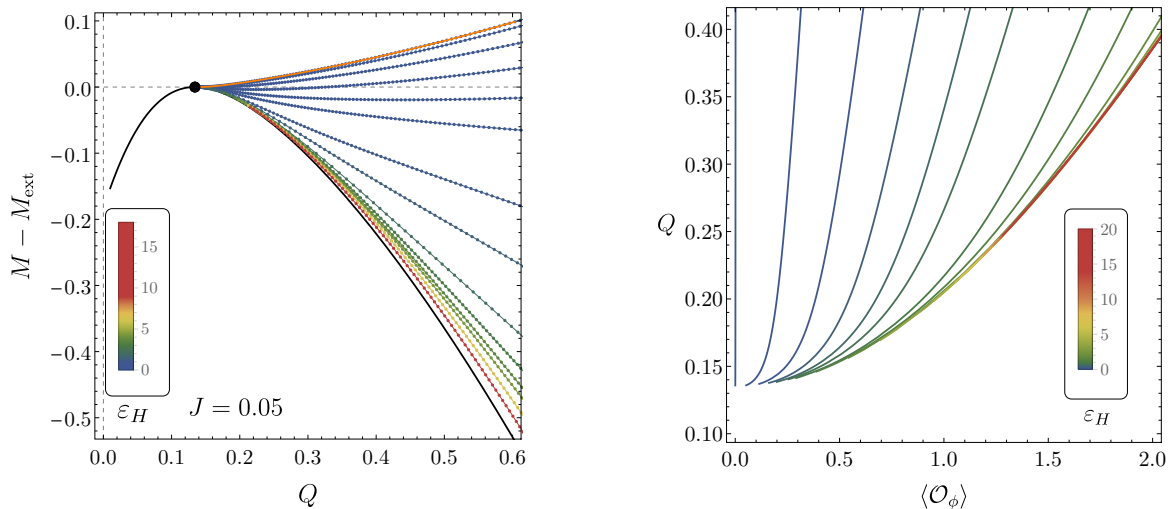


**Fig. 4.5** *Left*: The mass difference  $M - M_{\text{ext}}$  against the charge  $Q$  for fixed angular momentum  $J = 0.05$  and different values of the horizon scalar  $\epsilon_H$  (coloured disks; the lower curves have higher  $\epsilon_H$ ), where  $M_{\text{ext}}$  is the mass of the corresponding extremal CLP black hole with the same  $J$  and  $Q$ . The black disk shows the supersymmetric black hole, the black solid line shows the BPS bound (the lowest curve), the orange solid line (the top curve) shows the onset of the instability. *Right*: The charge  $Q$  against the expectation value of the operator dual to the scalar field, for families of hairy black holes with constant  $J = 0.05$  and various values of the horizon scalar  $\epsilon_H$ .

## 4.5.2 Constant $J$ planes

In order to explore the hairy solution space, we need to decide how to fix the free constants at the boundaries. To ensure that our solutions are rotating, we can fix the value of  $q_5(y)$  at the horizon, or at infinity, and both of these choices will give us a different way of understanding the hairy solution space. The latter is equivalent to setting the total angular momentum  $J$  (4.27). We found in the previous subsection that the hairy black holes at a constant  $J$  slice with very small horizon hair  $\epsilon_H$  (just on the merger line), approach the supersymmetric black hole on the BPS bound as we lower  $y_+$ , and hence the temperature  $T$ . In such limit  $T \rightarrow 0$ , and numerically we can achieve temperatures as low as  $10^{-4}$  (Fig. 4.3).

As we increase  $\epsilon_H$  and decrease  $y_+$ , the constant  $J$  and  $\epsilon_H$  hairy black hole families approach the BPS bound and  $T \rightarrow 0$ , for all  $\epsilon_H$ , with larger horizon scalar curves

<sup>8</sup>A direct comparison is somewhat difficult, as we are fixing different conserved charges in each case. In the full non-linear setup it is possible to fix the overall charge  $Q$ , but this requires the other two free parameters to be  $y_+$  and  $\epsilon_H$ , which causes  $J$  to vary slightly.

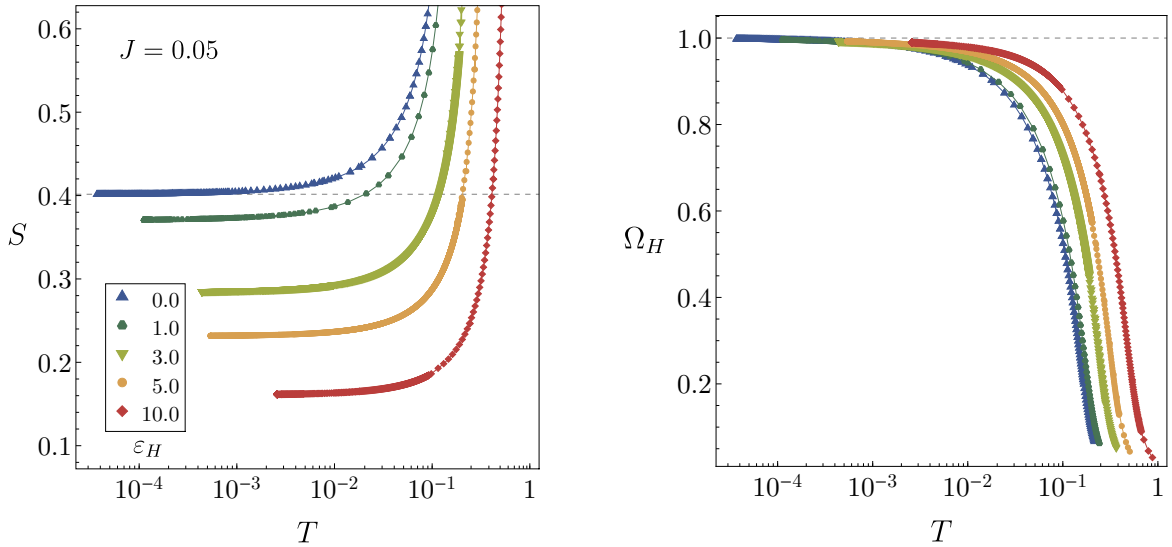


**Fig. 4.6** Log-linear plot of the entropy (*left*) and the horizon angular velocity (*right*, the legend is the same as for  $S$ ) of the hairy solutions with fixed angular momentum  $J = 0.05$  against the temperature, for several values of the horizon scalar  $\varepsilon_H$ . The horizontal dashed gridline shows the values for the supersymmetric black hole with the same  $J$ .

advancing towards the BPS bound at larger charges (Fig. 4.5). We were able to reach extremely low temperatures, and the coldest hairy black hole solutions satisfy the supersymmetric bound  $M = 3Q + 2J$  to better than  $\mathcal{O}(10^{-6})$  accuracy. In this near-extremal regime the functions acquire large gradients and our numerical method yields slow convergence. We will discuss the approach to the BPS bound in more detail in the next subsection.

As we increase  $\varepsilon_H$ , the numerics becomes increasingly difficult, and for larger horizon scalar fields we do not yet see the mass and the charge settle (Fig. 4.7). Finally, varying  $J$  gives a very similar picture. As expected, the larger values of  $J$  increase the numerical error.

#### 4.5.2.1 The extremal limit and the entropy

In this subsection we are considering black hole families with fixed angular momentum  $J$  and horizon scalar  $\varepsilon_H$ , and varying the parameter  $y_+$ . Perhaps the most intriguing property of the  $T \rightarrow 0$  limit is the fact that these hairy black holes retain finite entropy (Fig. 4.6, *left*) while approaching arbitrarily close the the BPS bound, *i.e.*

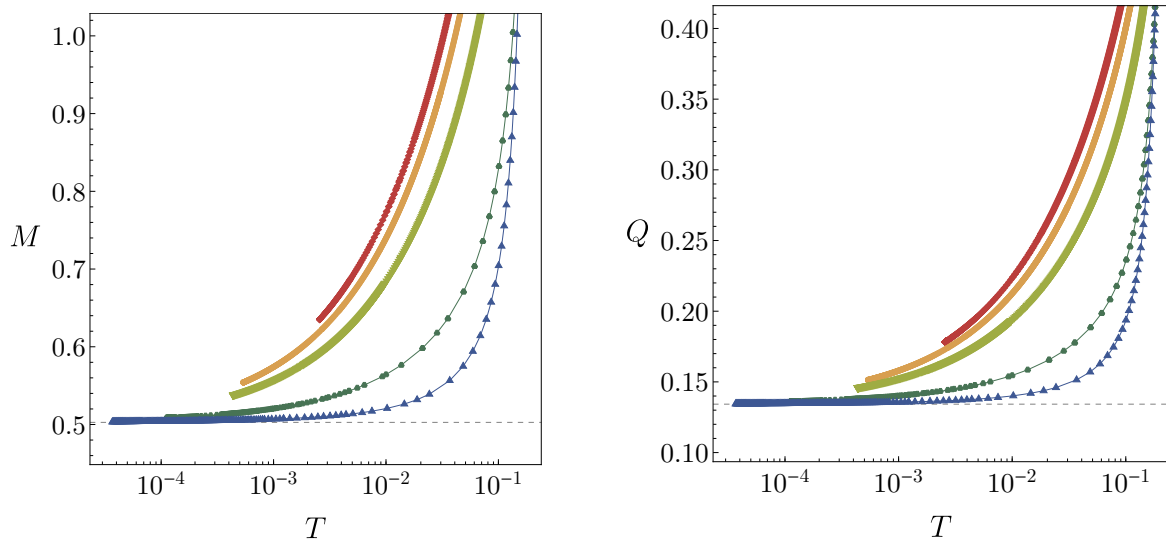


**Fig. 4.7** Log-linear plot of the mass (*left*) and the charge (*right*) of the hairy solutions with angular momentum  $J = 0.05$  versus  $T$ , for several values of  $\varepsilon_H$ . The horizontal dashed gridline shows the values for the supersymmetric black hole with the same  $J$ . The legend is the same as in Fig. 4.6.

$\Omega_H \rightarrow 1$  (Fig. 4.6, *right*),  $\mu \rightarrow 1$ ,  $T \rightarrow 0$  and  $|M - (3Q + 2J)| \rightarrow 0$ . We generated several solutions at fixed  $J$ , and monitored the black hole entropy for fixed  $\varepsilon_H$  as the temperature decreased down to  $T = 5 \times 10^{-3}$ . We could have decreased  $T$  further (at the expense of using a denser numerical grid), but we see no reason to do so, since the entropy has only changed at the 0.1% level when changing the temperature from  $10^{-2}$  to  $10^{-3}$ . The results of our numerical experiment can be found in Fig. 4.8, where we plot the extrapolated zero temperature entropy at several fixed values of  $J$ , as a function of  $\varepsilon_H$ . We find that the entropy behaves like a power law  $S \propto (\varepsilon_H)^\alpha$  at large  $\varepsilon_H$  with an exponent  $1/2 < \alpha < 1$ . The limiting solution has  $\Omega \rightarrow 1$  and  $\mu \rightarrow 1$  as well as satisfying  $M = 2J + 3Q$  to better than 0.2% accuracy. We conjecture that all finite  $\varepsilon_H$ ,  $\Omega_H = 1$ ,  $J \neq 0$  hairy black holes have non-zero entropy.

Let us investigate the extremal limit further. The temperature for these solutions is given by  $T = \frac{y_+}{2\pi} \sqrt{\frac{q_1(0)}{q_2(0)}}$ , where the functions  $q_1, q_2$  appear in the ansatz (4.15). As we lower the parameter  $y_+$ , which tends to some non-zero value, the function  $q_2$  tends to a constant at the horizon  $y = 0$ , and  $q_1(0) \rightarrow 0$  (Fig. 4.9, (*left*)), and thus  $T \rightarrow 0$ . This seems to be true for all fixed  $\varepsilon_H$  and  $J$ .

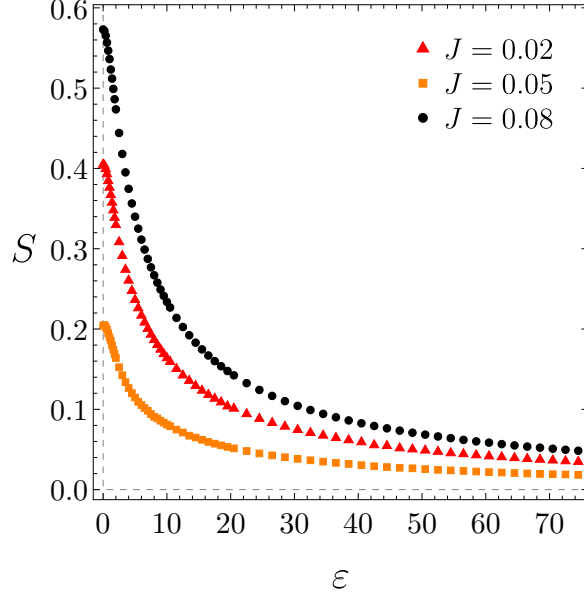


**Fig. 4.8** Extrapolated zero temperature entropy of the hairy black holes with constant  $J = 0.02$  (orange disks),  $J = 0.05$  (red squares) and  $J = 0.08$  (black diamonds) against the central scalar field  $\varepsilon_H$ . The variation in the entropy as we lower the temperature further gives error less than 0.1%.

From the field equations we find the second derivative to be

$$q_1''(0) = \frac{q_3(0)}{y_+^2 q_7(0)^2} (q_2(0)q_3(0) - 4y_+^2) (2q_5(0)q_7(0) - q_6(0))^2 + \mathcal{O}(T^{1/2}), \quad (4.36)$$

which will vanish provided that the condition  $2q_5(0)q_7(0) - q_6(0) = 0$  is satisfied (Fig. 4.9, (*middle*)), which does not appear to be the case for small  $\varepsilon_H$  (Fig. 4.9, (*right*)). However, when plotting this relation for a range of  $\varepsilon_H$ , a pattern emerges which suggests that this relation could hold for all  $\varepsilon_H$ . In fact for  $\varepsilon_H = 1$ , already  $q_1''(0) \simeq 0.0025$  at  $T = 1.2 \times 10^{-4}$ . If the condition is satisfied, then from the field equations it is straightforward to check that  $q_1$  derivatives at least up to fifth derivative scale at least as  $\mathcal{O}(T)$ , regardless of the fixed constants. As  $\varepsilon_H$  is increasing, the scaling for  $q_1(0)$  tends to  $T^2$ . If the condition (4.36) holds, then as  $q_5(0) \rightarrow 1$  we would also have  $q_5''(0) = 4$ .

We also cannot eliminate the case that relation (4.36) doesn't hold, in which case  $q_1(y) \sim y^2$ ; for instance, the Gutowski-Reall black hole has  $q_1 \simeq y^2$ , but also  $q_2 \simeq y^2$ . We were unable to find a horizon expansion for the extremal hairy solutions with a finite horizon scalar field, and it seems that in order to satisfy the equations of motion

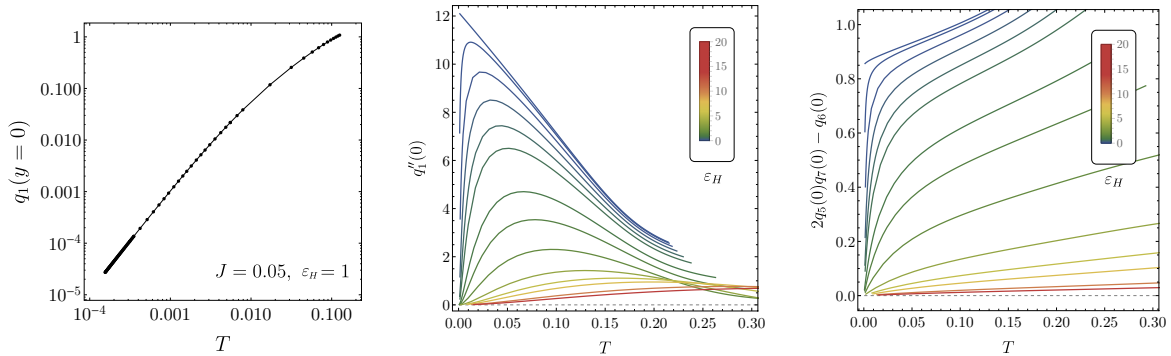


**Fig. 4.9** The value of  $q_1$  at the horizon  $y = 0$  against the temperature, for a black hole family with  $J = 0.05$  and  $\varepsilon_H = 1$ . *Middle:* The value of  $q_1''$  against  $T$ , for several values of  $\varepsilon_H$ . *Right:* the value of  $2q_5q_7 - q_6$  at the horizon against the temperature, for several values of the horizon scalar field.

some non-analytic piece must be included. In addition, the near-horizon geometry of the extremal limit of our hairy solutions does not appear to be of  $\text{AdS}_2 \times \mathbb{R}^2$ , but could be of Lifshitz [142], or hyperscaling violating type [143]. For instance, global hyperscaling violating black holes were recently constructed in the Einstein-Maxwell-Dilaton theory [144], which retain finite entropy in the extremal limit and have exotic horizon topology.

The attractor mechanism in ungauged supergravity [145–151] states that the scalar fields at the extremal horizon are usually fixed by the black hole charges, and the Bekenstein-Hawking entropy can be expressed in terms of those charges only. However, the attractor mechanism for BPS rotating black holes in five-dimensional gauged supergravity has not been completely understood, although recently some interesting progress has been made [152, 153]. The entropy of the one parameter Gutowski-Reall black hole in terms of its charges can be written as [154]

$$S^2 = 12\pi^2 Q(J)^2 - 4\pi^2 J. \quad (4.37)$$

We find that this relation is not satisfied by the hairy black hole solutions away from the Gutowski-Reall solution. There may be another relation for the extremal hairy black hole entropy in terms of its charges, however, since the extremal horizon does not appear to be smooth, we do not expect the attractor mechanism to apply.

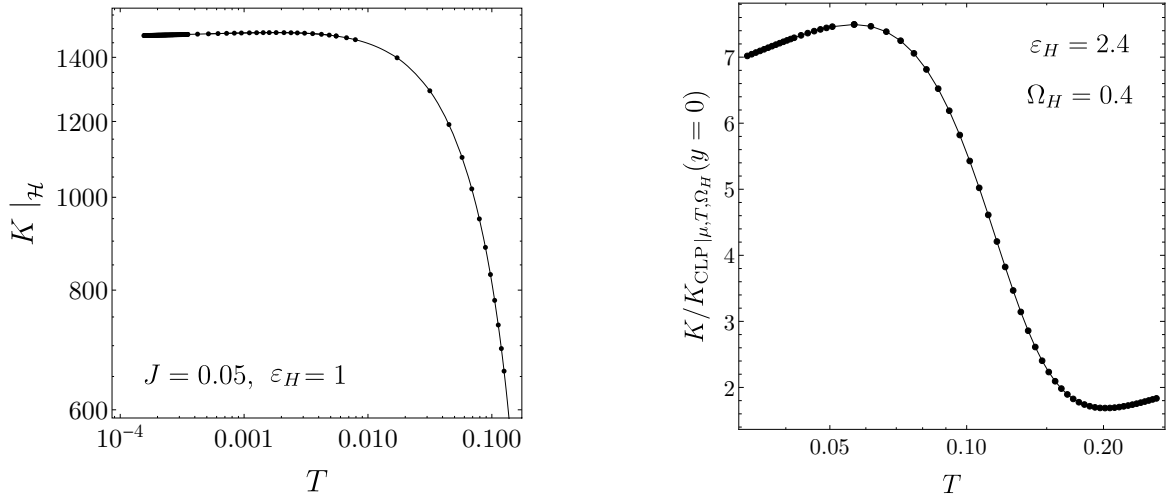


**Fig. 4.10** *Left*: The log-log plot of the Kretschmann curvature scalar  $K = R_{abcd}R^{abcd}$  against the temperature, for fixed angular momentum  $J = 0.05$  and horizon scalar field  $\varepsilon_H = 1$ . *Right*: Kretschmann curvature invariant at the horizon  $y = 0$  for the hairy black hole with constant horizon values  $\varepsilon_H$  and  $\Omega_H$ , scaled by the  $K$  value of a corresponding CLP black hole in the grand-canonical ensemble, *i.e.* with the same  $\mu$ ,  $T$  and  $\Omega_H$ . The ratio remains finite as we approach the BPS bound, and the black hole family shrinks to a smooth solitonic solution.

#### 4.5.2.2 Isotherms

For  $J = 0$ , zero temperature limit corresponds to the line of the smooth solitons, which terminates at the special soliton  $Q_c \simeq 0.2613$  in a spiraling fashion. This is where the  $T = 0$  and  $T = \infty$  limits of the hairy black holes intersect, and all other isotherms are drawn to the vicinity of  $Q_c$  (Fig. 4.11). Therefore if such a point exists for  $J > 0$ , which we will label  $Q_{\max}(J)$ , it should be indicated by the behaviour of the isotherms. We conjecture that such a point is the  $\varepsilon_H \rightarrow \infty$  and  $S \rightarrow 0$  limit of the extremal rotating hairy solutions, and the  $T \rightarrow \infty$  limit corresponding to some singular configurations would branch off the special  $Q_{\max}(J)$  solution for large charges. This conjecture is supported by the observed continuity from the  $J = 0$  case.

In Fig. 4.11 we present hairy black hole isotherms for a variety of angular momenta<sup>9</sup>. The system at fixed small angular momentum  $J = 0.001$  is a small deformation of the non-rotating case. The large  $\varepsilon_H$  isotherms extend past the  $Q_c$  and curiously exhibit a “swallowtail” phase transitions in the canonical ensemble (to be discussed in Section 4.7).

<sup>9</sup>These results were obtained in the DeTurck gauge, therefore we could only access a limited range of temperature and horizon scalar field values. In these figures,  $\varepsilon_H \simeq 40$ .

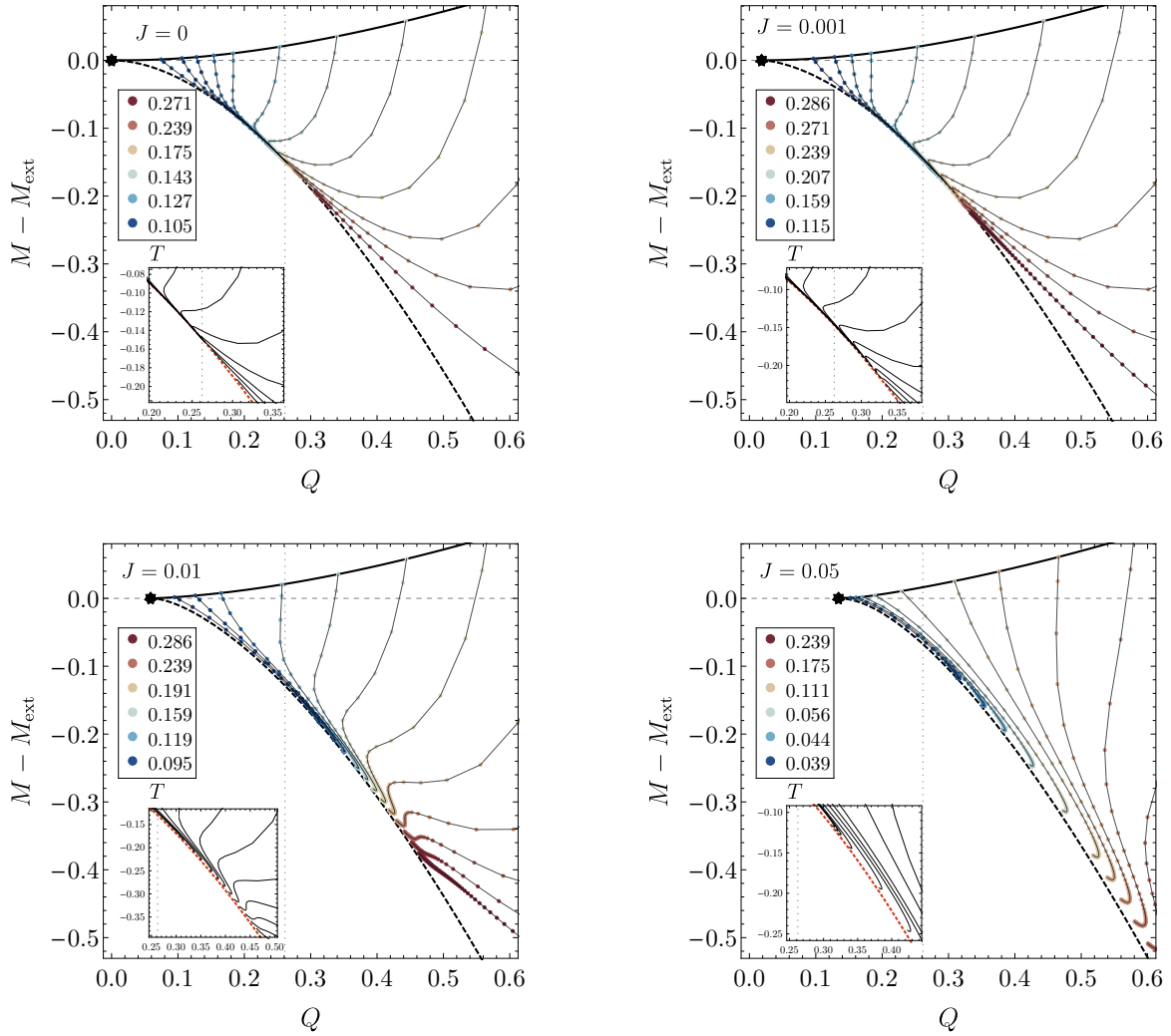


**Fig. 4.11** Rotating hairy black holes at fixed temperature, for different fixed angular momenta  $J = 0, 0.001, 0.01, 0.05$ , while varying the horizon scalar field  $\varepsilon_H$ . We plot the mass difference  $M - M_{\text{ext}}$  against the charge  $Q$ , where  $M_{\text{ext}}$  is the mass of the corresponding extremal CLP black hole. The solid black line is the scalar instability curve, dashed black line (or red line in the insets) is the BPS bound, black star is the Gutowski-Reall black hole. The vertical dotted line shows the special soliton  $Q_{\text{max}}(J = 0) = Q_c$ . Insets zoom around interesting isotherm behaviour.

Just near the BPS bound the isotherms turn towards the  $Q_c = Q_{\text{max}}(0)$  solution, and advance up along the BPS bound as  $\varepsilon_H \rightarrow \infty$ . This gives us an upper bound on  $Q_{\text{max}}(J)$ , which for small  $J$  is close to the  $Q_c$ . Unfortunately, the most interesting isotherms have very low temperatures, which we cannot access with the DeTurck method.

Such behaviour is even more apparent for larger values of  $J$ . For angular momentum  $J = 0.05$ , the isotherm turning point is further from the BPS bound, and the isotherm shape is becoming more pronounced. The canonical phase transition is occurring at larger charges and temperatures, and over a broader range. It could also be the case that, if  $J$  is large enough that the charge of the corresponding Gutowski-Reall black hole  $Q_{\text{GR}}(J)$  is larger than  $Q_c$ ,  $Q_{\text{max}}(J)$  would coincide with  $Q_{\text{GR}}(J)$ .

We would also like to entertain the idea that  $Q_{\text{max}}(J) = Q_{\text{GR}}(J)$  for all  $J$ . This would require the isotherms to have a rather dramatic behaviour near the BPS bound, especially for low angular momenta where we see continuity from the non-rotating case. The isotherms would “loop” the supersymmetric black hole, and the  $T = 0$  limit does not exist, or in fact consists of a single point with  $\varepsilon_H = 0$ . The whole of the BPS plane would be populated by the  $T = \infty$  singular solutions, which could in principle be identified by solving the BPS equations directly. We stress, however, that this would only be possible if some large extra scale is involved due to the extremal horizon, and this scenario would be out of reach for our numerical scheme.

### 4.5.3 Constant $Q$ planes

We cannot rule out the possibility that the constant horizon scalar charge limit is not the most suitable choice to reveal the correct approach to the BPS bound. In the non-rotating case we found that this limit worked incredibly well, and at  $T = 0$  provided a mechanism to pack an infinite amount of these hairy black hole families onto a small strip of the microcanonical phase space [92]. We can impose (4.28) as a boundary condition, yielding a system of three free parameters  $\{y_+, Q, q_5(1)\}$ , i.e. effectively at the same time we can control  $\{T, Q, J\}$ . Starting with a hairy seed, we can fix the total angular momentum  $J$  and charge  $Q$ , and lower the parameter  $y_+$ . If the charge is sufficiently low, the temperature is monotonic in  $y_+$  (Fig. 4.11), however, for larger charge a more complicated picture emerges. At fixed  $J$ , there is a charge range at which there are at least three hairy black holes with the same temperature<sup>10</sup> (Fig. 4.11, Fig. 4.18).

We present constant  $J = 0.01$  results in Fig. 4.12, for three different charges  $Q$ . The supersymmetric black hole has  $Q_{\text{GR}} = 0.0588$ . The large charge ( $Q = 0.659$ ) behaviour is similar to the large charge behaviour of the non-rotating case. As we lower  $y_+$ , we

<sup>10</sup>At least for relatively small values of  $J$ .

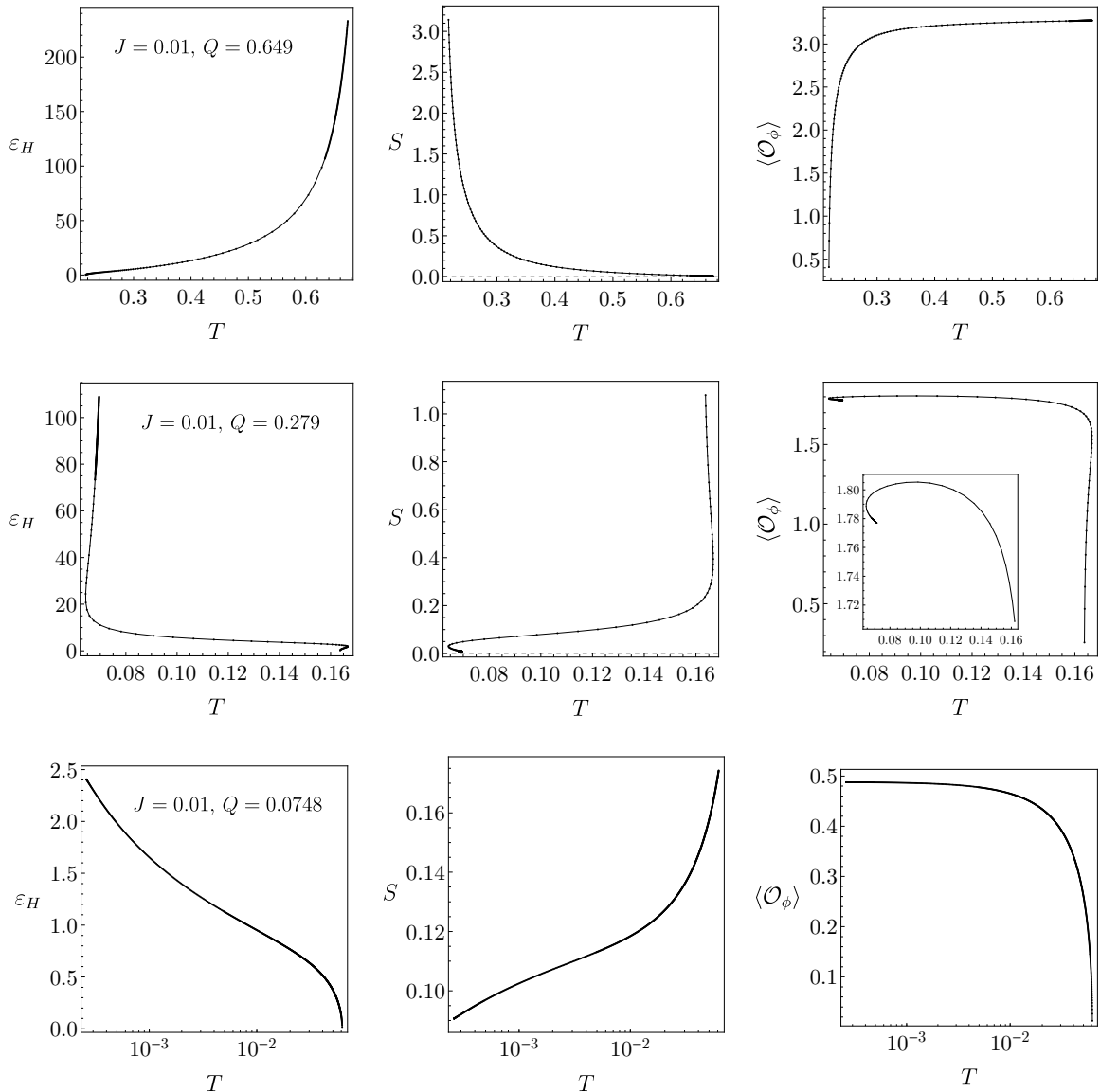


**Fig. 4.12** Constant angular momentum  $J$  and charge  $Q$  solutions, with the parameter  $y_+$  being varied. We present the horizon scalar field  $\varepsilon_H$  (*left*), the entropy (*middle*), and the expectation value of the dual operator  $\langle \mathcal{O}_\phi \rangle$  (*right*), for three different charges  $Q = 0.0748$  (*bottom row*),  $Q = 0.279$  (*middle row*),  $Q = 0.649$  (*top row*).

find that the temperature increases, and the hairy black holes approach the BPS bound. The entropy tends to zero, horizon scalar field diverges and the  $\langle \mathcal{O}_\phi \rangle$  is tending to some constant value. We also managed to reach as close as  $M - M_{\text{BPS}} < 0.001$  to the BPS bound, with  $\mu$  and  $\Omega_H$  tending to one. This suggests that we are approaching the supersymmetric bound, where there is a singular solution, which can be interpreted as

the  $T = \infty$  limit of the hairy black holes. We also observe retrograde condensation, that is the hairy black hole exists for  $T > T_c$ , which carries over to the planar limit (see section 4.8).

Of course we are most interested in lower charges. For intermediate charges  $Q \sim Q_c \simeq 0.26$  we know that there exist at least three black holes with the same temperature. Indeed this is what we find for  $J = 0.01$ ,  $Q = 0.279$ . When we decrease  $y_+$ , the temperature increases initially, then decreases, and finally starts to increase again, sending  $\varepsilon_H \rightarrow \infty$  and  $S \rightarrow 0$ . We also see interesting trend in  $\langle \mathcal{O}_\phi \rangle$ , perhaps suggesting a loop, as we expect that either  $T \rightarrow \infty$ , or  $T \rightarrow 0$ . For these black holes, the closest approach is  $M - M_{\text{BPS}} < 0.0006$ .

Finally, at low charges, if our conjectures hold, we expect to see  $\varepsilon_H$  increasing and tending to a constant value, and  $S$  decreasing to a constant non-zero value, while  $\langle \mathcal{O}_\phi \rangle$  settles to a non-zero constant. Indeed this is what we observe in Fig. 4.12 (*bottom row*). As the low temperature isotherms are very dense near the BPS bound, we do expect to see a sharp growth in  $\varepsilon_H$ . While we do not observe the values blowing up, we were able to fit both divergent and convergent logarithmic functions to the low temperature data, of the form  $a + bT^\alpha \log T$ . Numerical convergence at low temperatures gets increasingly worse (see Fig. 4.24), and it is difficult to extract good quality data for the temperature range where the change in  $\langle \mathcal{O}_\phi \rangle$  is very small ( $T < 10^{-3}$ ). This is where we would expect the hairy solutions to enter the scaling regime. In addition, at small charges we do not see any sign of  $T$  increasing with the parameter  $y_+$ .

#### 4.5.4 Constant $\Omega_H$ planes

In Subsection 4.5.2 we fix the value of  $q_5(y)$  at infinity,  $y = 1$ . Alternatively, we can fix the value at the horizon  $q_5(0) = \Omega_H$ , where we will find that  $0 \leq \Omega_H < 1$ . We again track fixed horizon scalar  $\varepsilon_H$  curves, and lower the temperature. For the non-rotating solutions we found that plotting the black hole charge  $Q$  against the vev of the boundary operator dual to the scalar field  $\langle \mathcal{O}_\phi \rangle = y_+^2 q_8(1)$  allowed us to better understand the approach of the hairy solutions to the BPS bound (Fig. 4.14 black curves) [92]. They curve towards the smooth soliton curve (in grey), where in the  $T \rightarrow 0$  limit they smoothly reduce to the regular soliton solution. The soliton solution has a maximum charge, however there is a regular limiting solution for every such black hole family, allowed by the spiraling behaviour of the smooth soliton branch.

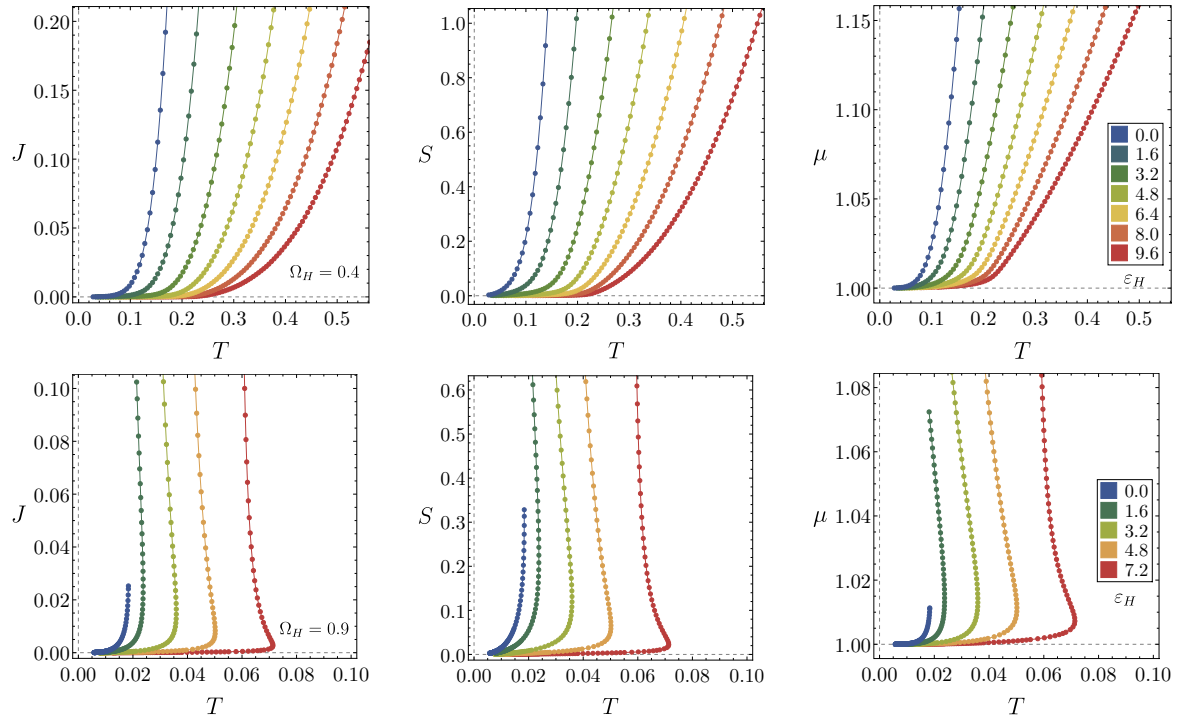


**Fig. 4.13** Thermodynamic quantities for the hairy black hole families with fixed horizon velocity  $\Omega_H = 0.4$  (*top row*) and  $\Omega_H = 0.9$  (*bottom row*), and a constant horizon scalar  $\varepsilon_H$ . As the temperature  $T \rightarrow 0$ , angular momentum  $J \rightarrow 0$  (*left*), entropy  $S \rightarrow 0$  (*middle*), and chemical potential  $\mu \rightarrow 1$  (*right*). For large horizon velocity, there exists a maximum temperature for the hairy black holes.

If we turn on the horizon angular velocity (in the non-rotating frame at the infinity), we find a surprisingly similar picture. In Fig. 4.14 we present numerical results for  $\Omega_H = 0.4$  and  $\Omega_H = 0.9$ , and also plot  $\Omega_H = 0$  for reference. We find that the constant horizon angular velocity and horizon scalar field hairy black hole families in the zero temperature limit approach the same smooth soliton, *i.e.*  $\mu \rightarrow 1$ ,  $S \rightarrow 0$  and  $J \rightarrow 0$ , and close to it, appear to have analogous spiral-like behaviour. As  $S \rightarrow 0$ , the curvature becomes very large, and we see the Kretschmann invariant  $K = R_{\mu\nu\rho\sigma}R^{\mu\nu\rho\sigma}$  blowing up as  $T \rightarrow 0$ . However, if we compare it with the corresponding CLP black hole in the grand-canonical ensemble, we obtain a finite limit (see Fig. 4.10, *right*). This seems to hold for any  $\varepsilon_H$  and  $\Omega_H$ , and again is similar to the non-rotating case [92]. In fact, by considering gauge invariant quantities, we find that the limiting solutions are the same non-rotating  $J = 0$  smooth solitons. These solution curves are shown in the microcanonical diagram in Fig 4.15.

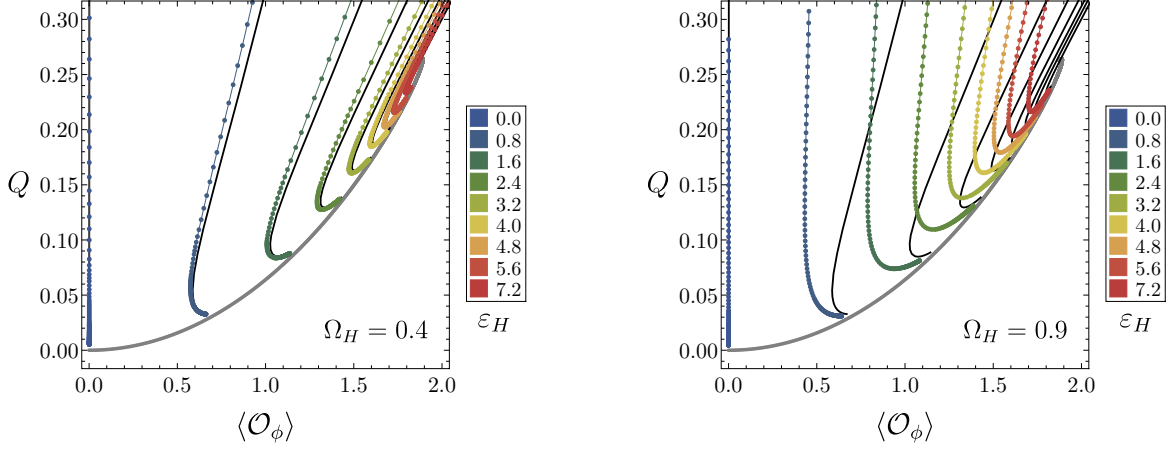


**Fig. 4.14** Black hole charge  $Q$  against the vacuum expectation value  $\langle \mathcal{O}_\phi \rangle$  of the operator dual to the scalar field  $\phi$ , at fixed horizon scalar charge  $\varepsilon_H$ , and fixed horizon angular velocity  $\Omega_H = 0.4$  (left), and  $\Omega_H = 0.9$  (right), in the non-rotating frame at infinity. In black are the corresponding values for the non-rotating solutions  $\Omega_H = 0$ ,  $J = 0$ . The smooth BPS soliton family is shown in gray.

In Fig. 4.13 we present some of the thermodynamic quantities (angular momentum  $J$ , entropy  $S$  and chemical potential  $\mu$ ) for such hairy black hole curves. As we increase  $\Omega_H$ , the hairy black holes exist only up to some maximum temperature  $T_{\max}(\varepsilon_H, \Omega_H)$ . This reflects the fact that the limit  $\Omega_H \rightarrow 1$  is the extremal limit for hairy black holes. It would be very interesting to know this structure changes as  $\Omega_H \rightarrow 1$ , however it is difficult to resolve large  $\Omega_H$ , low  $T$  solutions.

## 4.6 Tidal forces

The ultra-cold hairy black hole solutions are free of curvature singularities, and in the coordinate frame (4.15) the components of the Riemann tensor  $R_{abcd}$  and its derivatives are finite everywhere, in particular at the horizon, which results in the curvature invariants derived from the Riemann tensor being finite as well. We have explicitly checked that curvature invariants  $R_{ab}R^{ab}$ ,  $R_{abcd}R^{abcd}$  (presented in Fig. 4.10 (left)),  $C_{abcd}C^{abcd}$  where  $C_{abcd}$  is the Weyl tensor,  $T_{ab}T^{ab}$ ,  $F_{ab}F^{ab}$  and  $|\Phi|^2$  are everywhere finite as  $T \rightarrow 0$ .

Static, charged, near extremal black holes can exhibit diverging tidal forces as measured by a freely infalling observer, while having all curvature scalars finite at the

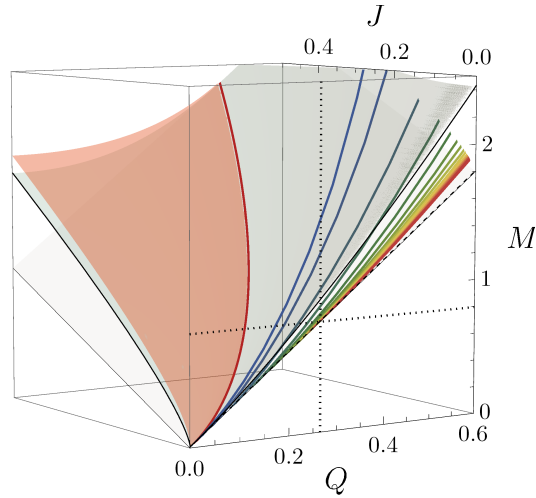


**Fig. 4.15** A 3D solution space of the hairy black holes. The CLP black holes exist above the dark gray plane, and intersect the BPS limit  $M = 3Q + 2J$  (the white plane below) at the Gutowski-Reall family (red bold line). The orange plane is the CLP solutions with  $\Omega_H = 1$ , below which the solutions have  $\Omega_H > 1$ . The solid bold lines in rainbow are the hairy solutions with fixed horizon velocity  $\Omega_H = 0.4$ , and fixed horizon scalar value  $\varepsilon_H$ . The first line in blue is the merger line for the constant  $\Omega_H = 0.4$ , and exists just above the extremal plane. The dotted black gridlines on the front right face show the special soliton with  $Q_c \simeq 0.26$ .

horizon [155]. In order to test whether the near extremal hairy solutions possess the tidal force singularity, we need to analyse the geodesic motion in these backgrounds. We start by considering the metric *ansatz*, and look for radial, timelike ingoing geodesics parametrised by the proper time  $\tau$  and with the tangent vector  $\dot{X}^a = dX^a/d\lambda$ . The Killing vector fields  $\partial_t$ ,  $\partial_\psi$  and  $\partial_\phi$  give us three conserved quantities

$$E = -g_{ta}\dot{X}^a, \quad L_\psi = g_{\psi a}\dot{X}^a, \quad L_\phi = g_{\phi a}\dot{X}^a, \quad (4.38)$$

and we consider radial static geodesics on the  $S^2$  with  $\dot{\theta} = 0$  and  $\dot{\phi} = 0$ , and zero angular momentum in the  $\psi$  direction. Using the normalization condition  $\dot{X}^a \dot{X}_a = -1$  we obtain

$$\dot{X}^a = \left\{ \frac{E}{f(r)}, -\frac{\sqrt{E^2 - f(r)}}{\sqrt{f(r)g(r)}}, E \frac{\Omega(r)}{f(r)}, 0, 0 \right\}, \quad (4.39)$$

where the coordinates are ordered as  $\{t, r, \psi, x, \phi\}$ . Here we use the angular coordinate  $x = \cos \theta$  for numerical convenience.

In order to compute the curvature measured by a freely falling observer along the radial timelike ingoing geodesic, we change into a parallelly propagated orthonormal frame (PPON). In the PPON, we require  $(\tilde{e}_0)_a = \dot{X}_a$ . We choose

$$\begin{aligned}
(\tilde{e}_0)_a &= -E \partial_a t - \sqrt{E^2 \frac{g(r)}{f(r)} - g(r)} \partial_a r, \\
(\tilde{e}_1)_a &= \sqrt{E^2 - f(r)} \partial_a t - E \sqrt{\frac{g(r)}{f(r)}} \partial_a r, \\
(\tilde{e}_2)_a &= \frac{1}{2} \sqrt{1 - x^2} r \partial_a \phi, \\
(\tilde{e}_3)_a &= \frac{1}{2} \sqrt{\frac{1}{1 - x^2}} r \partial_a x, \\
(\tilde{e}_4)_a &= -\sqrt{h(r)} r \Omega(r) \partial_a t + \sqrt{h(r)} r \partial_a \psi + \frac{1}{2} x \sqrt{h(r)} r \partial_a \phi,
\end{aligned} \tag{4.40}$$

which satisfies the orthonormality condition

$$g^{ab}(\tilde{e}_\alpha)_a(\tilde{e}_\beta)_b = \eta_{\alpha\beta}. \tag{4.41}$$

The components of the Riemann tensor in the PPON frame are related to the components in the coordinate frame by

$$R_{\alpha\beta\gamma\delta} = R_{abcd}(\tilde{e}_\alpha)^a(\tilde{e}_\beta)^b(\tilde{e}_\gamma)^c(\tilde{e}_\delta)^d. \tag{4.42}$$

As we lower the temperature, these components, for instance  $R^t_{\psi t \psi}$ , are rapidly increasing at the horizon, while the horizon radius remains non-zero. This suggests that in the extremal limit there is a parallelly propagated curvature singularity.

We have also studied the tidal forces as felt by an observer infalling into the black hole. We compute the measure  $T_{ab}\dot{X}^a\dot{X}^b$ , where  $\dot{X}^a$  is the tangent vector of a timelike ingoing geodesic parametrised by the proper time  $\tau$ , and  $T_{ab}$  is the stress energy tensor associated with our action. We find that the tidal forces diverge when we approach  $T = 0$ , as it can be observed in Fig. 4.16 (*left*). Furthermore, the Riemann tensor components measured in a freely falling frame diverge as we approach the extremality, confirming that there is a parallelly propagated (pp) curvature singularity. We will, however, argue that such divergence can be consistently studied within the supergravity approximation.

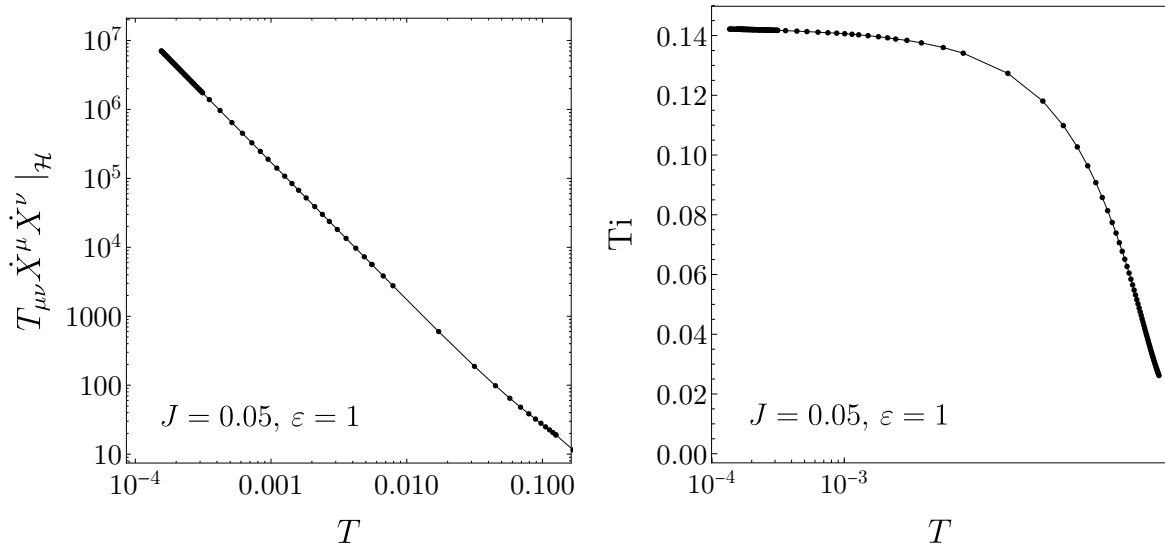


**Fig. 4.16** *Left:* The measure of tidal forces, as felt by a unit energy particle infalling along a radial geodesic,  $T_{ab} \dot{X}^a \dot{X}^b$  at the hairy black hole horizon against the temperature. The quantity shown is for a black hole family with fixed  $j = 0.05$  and  $\varepsilon_H = 1$ , and the plot is in a log-log scale. *Right:* The log-log plot of the Tipler integral, for hairy black hole family with constant angular momentum  $j = 0.05$  and horizon scalar  $\varepsilon_H = 1$ . The integral was computed using the  $R^t_{\psi t \psi}$  component found in a PPON frame. Different components have similar qualitative behaviour.

Such singularities in supergravity theories are not rare, and there have been many examples where the extremal solutions exhibit pp singularities [156–159, 155, 160–165]. The hairy black holes constructed in this paper are smooth and non-extremal, and the tidal forces diverge only in the  $T = 0$  limit, thus the limiting solutions can be regarded as physical [133, 134].

We will further investigate these singularities by considering propagation of infalling objects. The notion of strong curvature singularities was first introduced by [166], which were defined by the ability to crush any objects passing through the singularity to zero volume. This idea was made more precise by [167, 168], where the weak curvature singularities were defined such that an extended object falling into the singularity retains a non-zero volume. The physical dimension of the object is defined by linearly independent spacelike (vorticity-free) Jacobi fields along the timelike geodesic which extends to the singularity. The weak curvature singularity is defined in a similar way. In such singularities, even though the tidal forces diverge, it is still possible to have the overall effect on the volume deformation to be bounded.

The necessary and sufficient conditions for the singularity to be weak were given by Clarke and Krolak [168], and Tipler [167]. If the singularity resides at an affine parameter  $\tau_*$  and the particle is at rest at  $\tau = 0$ , then for a timelike geodesic meeting the singularity at  $\tau_*$ , the integral of the components of the Riemann tensor in a parallelly propagated orthonormal frame

$$\text{Ti} = \int_{\tau_0}^{\tau_*} \int_{\tau_0}^{\tau'} |R^i{}_{0j0}(\tau'')| d\tau'' d\tau' \quad (4.43)$$

will not diverge, for any  $\tau_0 \in [0, \tau_*)$ . The finiteness of Ti guarantees that the volume defined by the Jacobi fields remains non-zero when crossing the singularity, and thus the curvature singularity is weak.

In addition to the volume being non-zero as the object crosses the singularity, one might require the norm of the Jacobi fields themselves to remain finite [169–171], so that there is no divergent distortion in any of the directions. The convergence of (4.43) implies that the Jacobi fields themselves are bounded [170]. We find that the Tipler integral (4.43) remains finite, as can be seen in Fig. 4.16 (*right*). For different values of  $J$  and  $\varepsilon_H$  the curves quantitatively change, but otherwise behave in the same qualitative manner. We anticipate that finiteness of the Jacobi fields should be sufficient to control the classical and quantum propagation of strings, however, this remains to be explored in more detail.

There are situations where Ti diverge and yet, stringy perturbation theory seems to be under good control [172]. It is also worth mentioning that our limiting solutions have bounded  $L^2$  curvature norm, and thus can be continued as solutions of the Einstein equation past the black hole horizon [173]<sup>11</sup>. We believe that the limiting solutions found here behave very much like the extremal black holes of [48].

## 4.7 Thermodynamics

In this section we analyse the rich and complicated thermodynamic behaviour of the rotating hairy black hole solutions in the microcanonical, canonical and grand-canonical ensembles [175, 176, 115, 177, 178]. We find that the thermodynamics is very similar to the non-rotating case [92]. Curiously, in all three ensembles studied,

<sup>11</sup>Consequently, they are also weak solutions in the sense of Christodoulou [174].

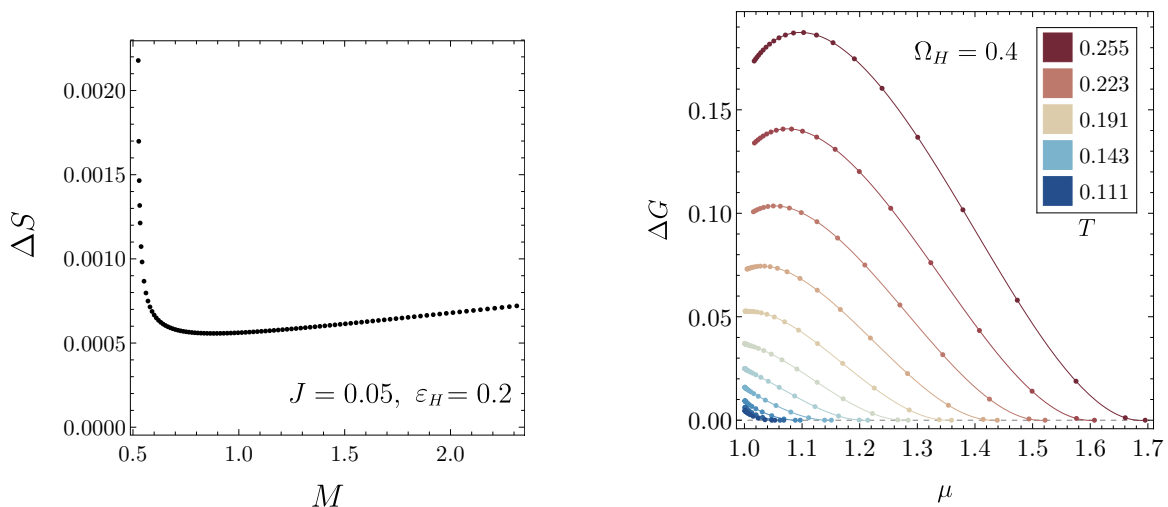


**Fig. 4.17** *Left:* The entropy difference  $\Delta S = S - S_{\text{CLP}}$  against the mass  $M$ , for black holes with fixed  $J = 0.05$  and  $\varepsilon_H = 0.2$  (black data points), where  $S_{\text{CLP}}$  is the entropy of the CLP black hole with the same charge  $Q$  and angular momentum  $J$ . *Right:* The difference in Gibbs free energy  $\Delta G = G - G_{\text{CLP}}$ , where  $G_{\text{CLP}}$  is the free energy for the corresponding CLP solution with the same temperature  $T$ , and thermodynamic angular velocity  $\Omega_H$ . We find that for all hairy solutions have  $G < 0$ , hence at fixed chemical potential  $\mu$ ,  $\Delta G > 0$  indicates that the phase without hair dominates the ensemble.

a different phase is the dominant one. In this section we assume that the thermodynamics is dominated by one of the three classes of solutions considered in this chapter.

*Microcanonical ensemble:* We find that for all horizon scalar values  $\varepsilon_H$  and all  $J$  the entropy difference between the hairy black hole and the CLP counterpart at fixed charge, mass and angular momentum  $\{Q, M, J\}$ , is positive (see Fig. 4.17, left), *i.e.*  $\Delta S = S - S_{\text{CLP}} > 0$ . Hence, the hairy black holes dominate the microcanonical ensemble.

*Canonical ensemble:* In the canonical ensemble the associated thermodynamic potential is the Helmholtz free energy  $F = M - TS$ , and we fix the temperature, charge and angular momentum  $\{T, Q, J\}$ . In the non-rotating case [92] we observed complicated phase transitions between the hairy and non-hairy phases in the canonical ensemble, where for large temperatures the hairy black holes have larger free energy compared to the RNAdS black hole, *i.e.*  $F > F_{\text{RN}}$ . The opposite behaviour is seen for low  $T$ , where  $F < F_{\text{RN}}$ . However, as  $F > 0$  for all the black hole solutions, we expect

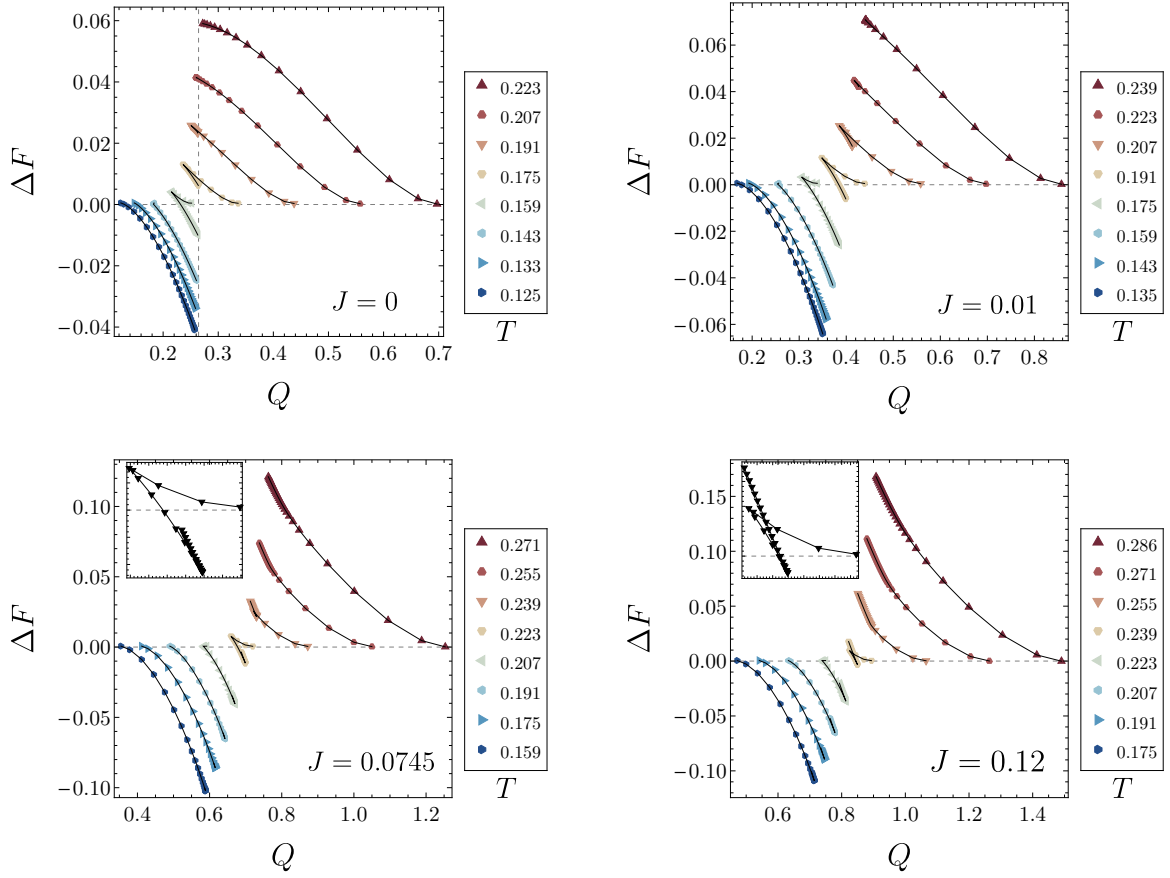


**Fig. 4.18** Difference in the Helmholtz free energy  $\Delta F = F - F_{\text{CLP}}$ , where  $F_{\text{CLP}}$  is the free energy for the corresponding CLP black hole with the same angular momentum  $J$ , temperature  $T$  and charge  $Q$ . Here  $\varepsilon_H \leq 15$ , and the dashed vertical gridline for  $J = 0$  correspond to the critical charge  $Q_c \simeq 0.26$ . In general the isotherms demonstrate a complicated behaviour, exhibiting cusp and swallowtail type phase transitions. For all hairy black holes  $F > 0$  with respect to the thermal AdS.

this ensemble to display the Hawking-Page [30] transition to some AdS geometry with the same total charge.

For  $J > 0$  we observe a similar picture. The results for several values of  $J$  are presented in Fig. 4.18. For  $J = 0$  the isotherms, when the horizon scalar  $\varepsilon_H \rightarrow \infty$ , cluster around the special soliton  $Q_c \simeq 0.26$ , and we observe a complicated relation to the corresponding RNAdS black hole phases. When  $J > 0$ , the approach to the extremal limit at fixed  $Q$  is non-monotonic in  $T$  for a broader range of charges and the isotherms display a new feature near the BPS bound, namely the “swallowtail” type phase transition [131]. The analysis of  $\Delta F = F - F_{\text{CLP}}$  where  $F_{\text{CLP}}$  is the free energy

of the corresponding CLP black holes reveals a complicated picture. For any  $J > 0$  there is a temperature range where at fixed  $Q$  and  $J$  there are at least three hairy black holes with the same temperature (*e.g.*  $J = 0.0745$ ,  $T = 0.239$  (Fig. 4.18, *bottom left* orange triangles),  $J = 0.12$ ,  $T = 0.239$  (Fig. 4.18, *bottom right* yellow hexagons)). The transition temperature increases with the angular momentum  $J$ .

Ultimately all the black hole solutions have  $F > 0$  with respect to the background geometry, thus we expect that these black holes might not be the dominant phase in the ensemble. This analysis also gives us some insight into the complicated behaviour of the isotherms at fixed  $J > 0$ . The phase transition could suggest the location of the maximal charge  $Q_{\text{max}}(J)$ , where in analogy with the  $J = 0$  case we expect all isotherms to spiral around some special solution separating the  $T = 0$  and  $T = \infty$  limits.

Local thermodynamic stability is ensured by the entropy  $S(M, Q, J)$  being concave as a function of the extensive variables  $X_i$ , *i.e.* the Hessian matrix  $\left[\partial^2 S / \partial X_i \partial X_j\right]_{ij}$  being negative definite [179]. In the canonical ensemble the charge and the angular momenta do not vary, thus the sufficient condition for the stability is that the heat capacity  $C_{J,Q} = T(\partial S / \partial T)_{J,Q}$  is positive. This is what we find for hairy black holes with sufficiently low charges (Fig. 4.12), however, for general  $Q$  the behaviour of  $C_{J,Q}$  is complicated. When the charge is sufficiently large, we find  $C_{J,Q} < 0$ , implying that the large  $Q$  hairy black holes are locally thermodynamically unstable.

*Grand-canonical ensemble:* The preferred phase in this ensemble minimises the Gibbs potential given by  $G = E - TS - 3\mu Q - 2\Omega_H J$ , where we keep the intensive variables  $\{T, \Omega_H, \mu\}$  fixed. We find that for the hairy black holes  $G < 0$ , and the preferred phase is always the non-hairy black hole. The hairy phase always has  $\mu > 1$ , and the CLP black holes have two branches exhibiting the Hawking-Page transition to the pure AdS [30, 176].

## 4.8 Rotating black branes

### 4.8.1 Ansatz

Even though the focus of this chapter is the global solutions, it is also interesting to look at the planar horizon limit due to applications of various hairy black branes to the

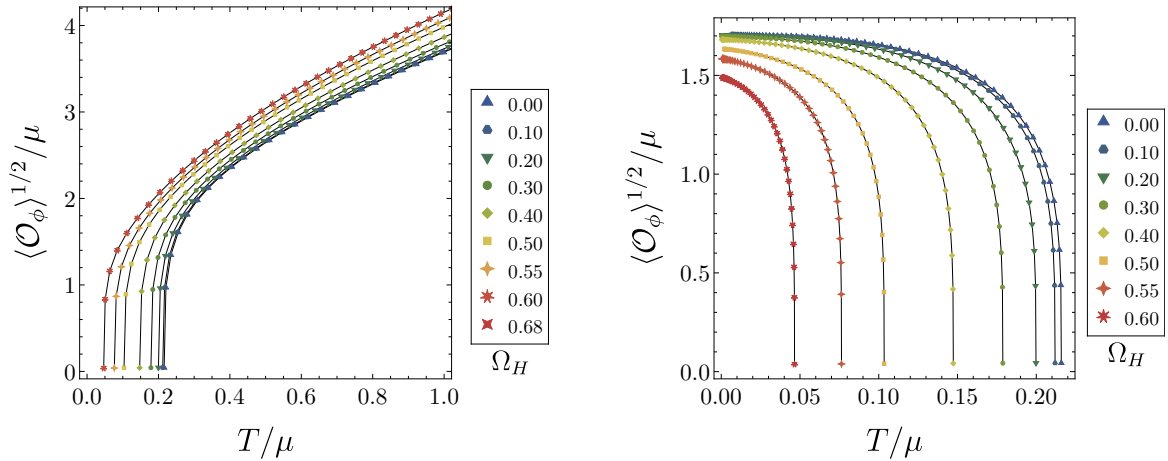


**Fig. 4.19** *Left:* Condensate against the temperature, for families of rotating hairy black branes with different values of  $\Omega_H$ . The critical temperature  $T_c$ , at which the hairy solutions first appear, decreases with  $\Omega_H$ . *Right:* Expectation value of the dual operator as a function of temperature for a phenomenological Abelian-Higgs model, as a scale invariant quantity, for various values of the horizon velocity  $\Omega_H$ .

study of holographic superconductors (*e.g.* [69, 66, 180, 73], and references therein). *A priori*, one could suspect that our “rotating” branes are boosted solutions of the static counterparts which were analysed in [122, 92]. However, we will find that rotating hairy branes obtained as the scaling limit of (4.1) cannot be boosts of the non-rotating hairy branes. In the gauge where  $A_t = 0$  on the horizon, a Lorentz boost will keep both  $A_t = 0$  and  $A_\psi = 0$  on the horizon. However, we find that  $A_\psi$  does not vanish on the horizon, regardless of the residual transformations (4.52), and that the current in the dual description is non-zero. Similar solutions with a non-trivial source were studied in [181] and in a consistent type IIB truncation [182].

The planar limit of the ansatz (4.16) with a flat  $\mathbb{R}^3$  horizon can be obtained via the following scaling

$$t \rightarrow \alpha t, \quad y_+ \rightarrow \frac{y_+}{\alpha}, \quad \psi \rightarrow \alpha x_1, \quad \phi \rightarrow \alpha x_2, \quad x \rightarrow \alpha x_3 \quad (4.44)$$

and taking the limit  $\alpha \rightarrow 0$ . We can set  $y_+ = 1$ , leaving us a two-parameter family of branes. This limit can also be obtained by boosting, for instance, a planar Schwarzschild-AdS<sub>5</sub> along the  $x_1$  direction, and promoting angular velocity to be a function of the radial coordinate. This analysis gives us the following ansatz for the hairy rotating

black branes with a planar horizon

$$ds^2 = \frac{1}{1-y^2} \left[ -y^2 q_1(y) dt^2 + \frac{q_2(y) dy^2}{1-y^2} + \left\{ q_3(y) [dx_1 - \tilde{\Omega}(y) dt]^2 + \frac{1}{4} q_4(y) [dx_2^2 + dx_3^2] \right\} \right], \quad (4.45)$$

where  $\tilde{\Omega}(y) = (1-y^2)^2 q_5(y)$ , and the gauge and scalar fields are given by

$$\tilde{A}_t(y) = y^2 q_6(y) - q_5(y) q_7(y), \quad \tilde{A}_{x_1}(y) = q_7(y), \quad \tilde{\phi}(y) = (1-y^2) q_8(y). \quad (4.46)$$

The boundary conditions at the horizon  $y = 0$  are given by  $q'_i = 0$  for all  $i \neq 5$ , and  $q_5 = \Omega_H$ . At infinity we have  $q_i = 1$  for  $i = 1, 2, 3, 4$  and

$$-q'_5 - \frac{1}{2} q'_7 (-q_5 q'_7 + q'_6 + 2q_6) = 0, \quad q'_8 - 2q_6^2 q_8 = 0, \quad q_7 = 0. \quad (4.47)$$

We will work in the radial gauge where  $q_4 = 1$ , and will find that  $q_3 > 1$ , therefore breaking the isotropy of the homogeneous brane. The rotational symmetry in  $x_2 - x_3$  plane is preserved, and there is also a translational invariance along the direction in which the momentum is carried. The expectation value of the current in the dual field theory is proportional to  $\tilde{A}_{x_1}(1)$ , which is non-vanishing, and is not sourced.

The CLP solution (4.7) admits the scaling limit

$$t \rightarrow \alpha t, \quad r \rightarrow \frac{r}{\alpha}, \quad \psi \rightarrow \alpha x_1, \quad \phi \rightarrow \alpha x_2, \quad x \rightarrow \alpha x_3, \quad q \rightarrow \frac{q}{\alpha^3}, \quad r_+ \rightarrow \frac{r_+}{\alpha}, \quad j \rightarrow j, \quad (4.48)$$

which yields a two-parameter family of planar black holes describing the normal phase. They are related to the planar RNAdS holes by the boost

$$\begin{aligned} t &= \frac{1}{\sqrt{1-j^2}} \tilde{t} + \frac{j}{\sqrt{1-j^2}} \tilde{x}_1, \\ x_1 &= \frac{j}{\sqrt{1-j^2}} \tilde{t} + \frac{1}{\sqrt{1-j^2}} \tilde{x}_1. \end{aligned} \quad (4.49)$$

Their thermodynamic quantities are given as

$$\hat{M} = \frac{(3+j^2)((1-j^2)q^2 + r_+^6)}{4r_+^2(1-j^2)}, \quad T = \frac{\sqrt{1-j^2}(2r_+^6 - (1-j^2)q^2)}{2\pi r_+^5}, \quad \Omega_H = j, \quad (4.50)$$

$$\hat{J} = j \frac{(1-j^2)q^2 + r_+^6}{2r_+^2(1-j^2)}, \quad \mu = q \frac{1-j^2}{r_+^2}, \quad \hat{Q} = \frac{q}{2}, \quad (4.51)$$

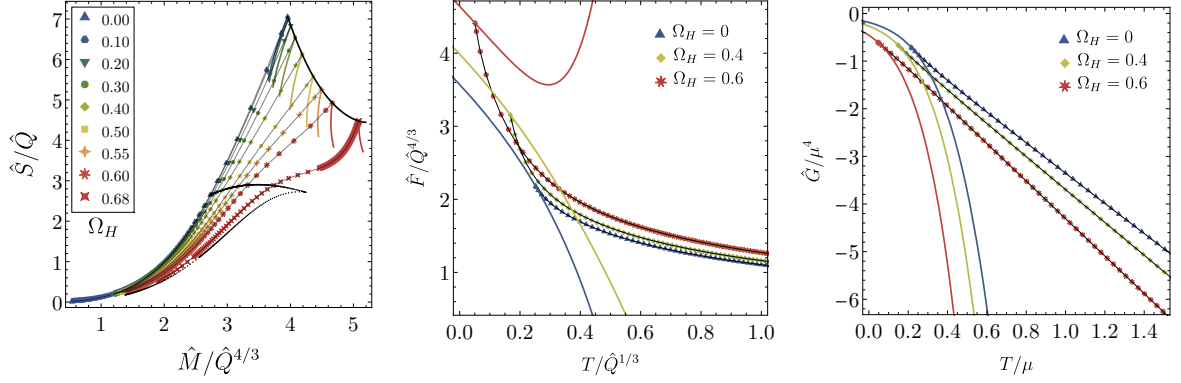


**Fig. 4.20** *Left*: Rotating hairy brane entropy density as a function of the mass density in the microcanonical ensemble, for different values of  $\Omega_H$  (data points in rainbow). Solid black line shows the onset of the instability, and solid rainbow lines are the corresponding solutions without hair. The black data points show two hairy black hole families, one of constant  $\varepsilon_H = 3.5$ , and one of constant  $\Omega_H = 0.72$ . *Middle*: Hairy black brane free energy density as a function of temperature in canonical ensemble, for different values of  $\Omega_H$  (see the inset legend). The solid lines show the corresponding solutions without hair. *Right*: The free energy density in the grand-canonical ensemble, against the temperature.

which satisfy the first law (4.33).

## 4.8.2 Solution space and thermodynamics

To generate the two parameter family of hairy branes, we will vary the black hole horizon velocity  $\Omega_H = q_5(0)$ , and the horizon scalar field  $\varepsilon_H$ . The non-rotating solutions exhibit the retrograde condensation, i.e. exist for  $T > T_c$ , which remains unchanged if we turn on the linear momentum (Fig. 4.19, *left*). Such phenomena is commonly observed in branes with supergravity potentials, and is usually associated with a subdominant phase [183, 122, 184–187].

In [92] it was shown that in the large temperature<sup>12</sup> limit the hairy branes connect to the singular soliton branch through the planar limit of the singular, large charge soliton solution

$$ds^2 = -r^2 dt^2 + \frac{r^2 dr^2}{1+r^4} + r^2 d\mathbf{x}^2, \quad \phi(r) = \frac{2}{r^2}, \quad A(r) = 0. \quad (4.52)$$

<sup>12</sup>Equivalently, the large horizon scalar field limit.

We find that the rotating solutions in the large temperature limit also approach the same solution<sup>13</sup>. Another interesting feature of the solution space is that the maximal value of  $\Omega_H$  depends on the scalar field  $\varepsilon_H$ ; the merger curve extends to  $\Omega_H \simeq 0.699$ , while for instance hairy branes with fixed  $\varepsilon_H = 3.5$  can reach up to  $\omega_H \simeq 0.720$ . These results are illustrated in Fig. 4.20 (*left*).

Rotating hairy branes are the large charge limit of the global hairy black holes, which dominate only the microcanonical ensemble. In the moduli space where the CLP and hairy branes coexist, the hairy solutions have the higher entropy density at the fixed charge density  $\hat{Q}$  and therefore dominate the microcanonical ensemble (Fig. 4.20, *left*).

The canonical ensemble exhibits first order phase transition between the hairy and non-hairy phases, when we vary  $\Omega_H$  (Fig 4.20, *middle*). For any  $\Omega_H > 0$ , there exists a temperature range for which the hairy phase is dominant for some  $T_c(\Omega_H) \leq T \leq T_{\text{max}}(\Omega_H)$ . For sufficiently large  $\Omega_H$ , the hairy phase is always dominant (Fig. 4.20, *middle*). These results are somewhat surprising, as the large charge  $Q$  and fixed  $J$  black holes in global AdS have larger free energy  $F$  than the hairy solutions. However, we observe that with the increasing  $J$  the transition temperature increases (Fig. 4.18), therefore it is plausible that such a phase transition is also seen in the planar limit. However, these branches have negative specific heat and are locally thermodynamically unstable.

Finally, the hairy branes never dominate the grand-canonical ensemble (Fig. 4.20, *right*) just as in the global case.

### 4.8.3 The Abelian-Higgs model

The retrograde condensation typically indicates that a condensed phase has larger free energy and therefore represents an unstable branch. The thermodynamic behaviour is largely governed by the truncation. The scalar potentials from supergravity truncations are complicated and can induce rich dynamics. In this subsection we contrast our supergravity model to the minimally coupled charged scalar field (also see [122]); in what follows, the Chern-Simons term will not be important.

<sup>13</sup>This can be confirmed, for instance, by computing the scalars  $g_{tt}$ ,  $g_{\psi\psi}$  in the DeTurck gauge, which fixes the conformal class.

A holographic dual to the  $d = 5$  planar Abelian-Higgs model with minimally coupled charged scalar field  $V(|\phi|) = m_\phi^2 \phi \phi^\dagger$  was studied by [188, 189]. As before, we take the mass saturating the five-dimensional BF bound  $m_\phi^2 = -4$  with  $e = 2$ , and consider the stationary ansatz (4.45). We find that the condensate  $\langle \mathcal{O}_\phi \rangle$  exists for  $T < T_c$  (Fig. 4.19, right), and saturates at low  $T$ . Furthermore, the hairy branes dominate over the normal phase in all three thermodynamic ensembles. Once we turn on the “rotation”, the superconducting behaviour is preserved and the transition temperature  $T_c$  decreases with increasing  $\Omega_H$ , which was also observed in holographic rotating superfluids [190] and holographic superfluids with supercurrents [181]. We also find a critical value of  $\Omega_H$  above which there are no hairy solutions, *i.e.* there exists a critical magnetic field which destroys the superconductivity.

The ansatz (4.45) provides a simple way to realise a spontaneously generated current in the holographic dual description, and merits further investigation. While we do not find the stable condensed phase in this particular truncation, such phases have been found in different consistent truncations of the five-dimensional  $\mathcal{N} = 8$  gauged supergravity (*e.g.* [122, 185]). It would be interesting to study the spontaneous currents in these models.

## 4.9 The non-interacting thermodynamic model

One might wonder whether we can access the near extremal regime of the small rotating hairy black holes perturbatively. The small hairy non-rotating black holes were studied in [62], where a matched asymptotic expansion was carried out<sup>14</sup>. The hairy solutions were also modeled as a non interacting mix of the small RNAdS black hole and the supersymmetric ( $\mu = 1$ ,  $M = 3Q$ ) soliton, and the leading order thermodynamics of the matched expansion were reproduced. Such approach has also been successfully employed in a similar context by [61, 60, 64, 191, 192].

The authors of [62] also modeled small hairy rotating black holes as a non interacting mix of the CLP black hole with  $\mu = 1$  (but not necessarily  $\Omega_H = 1$ , which is only equal at the supersymmetry) and the supersymmetric soliton, *i.e.* the system is in thermodynamic equilibrium. In  $J = 0$  plane, hairy black holes with fixed horizon

<sup>14</sup>In [92] we found a good agreement with fully non-linear numerical results, for small asymptotic charges.

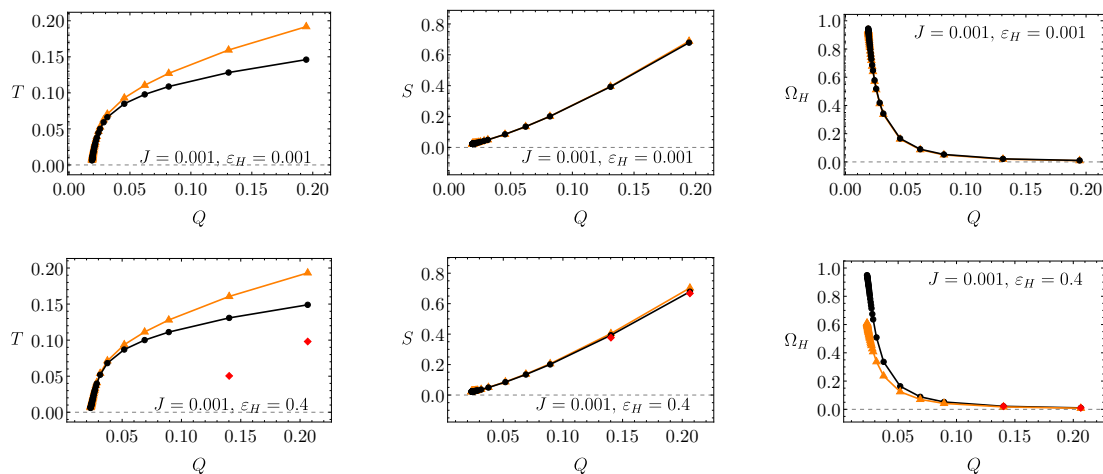


**Fig. 4.21** *First line:* The comparison with the approximation of [62] for the same charge, mass, and angular momentum  $J = 0.001$ . Black disks are numerical results, and orange triangles are the predicted curves. We expect the model to be valid for small  $Q$ , small  $J$ , and near extremality. For small horizon scalar  $\varepsilon_H$ , the hairy black holes are just above the extremality and coexist with CLP solutions. As  $T \rightarrow 0$ , they approach the Gutowski-Reall solution. For small charge the participating soliton contributes  $Q_s/Q \simeq 0.5\%$  of the total charge. Here the lowest  $T = 0.00633$ , and  $S = 0.0228$ . The error of the approximation to  $S$  close to the BPS bound is less than 1%.

*Second line:* The constant  $\varepsilon_H = 0.4$  curve crosses the extremality line. The red rhombi are the corresponding CLPs where they coexist in micro-canonical ensemble. For small charge,  $Q_s/Q \simeq 20\%$ . Here lowest  $T = 0.00597$ , and  $S = 0.0224$ . The error of the approximation to  $S$  close to the BPS bound is 2 – 4%.

scalar charge reduce to the smooth soliton as  $T \rightarrow 0$ . We find that the hairy rotating black holes exist arbitrarily close to the BPS bound, therefore it would be reasonable to expect that for small  $J$  some mix of the soliton and the CLP black hole could approximate the hairy solutions, if we are sufficiently close to the Gutowski-Reall solution, *i.e.* both to the extremal, and BPS limits.

We briefly describe the results of [62]. We assume that<sup>15</sup>

$$Q = Q_b + Q_s, \quad jQ^2 = j_b Q_b^2, \quad M = M_b + M_s, \quad (4.53)$$

where angular momentum is given by  $J = jQ^2$ , charge  $Q$  is small, and parameter  $j$  is arbitrary. For CLP black holes  $j_b \leq 3$ , saturating at extremality. Requiring  $Q_s > 0$  implies  $j_b > j$ , so  $j < 3$ . Leading order entropy, temperature and rotational charge are

<sup>15</sup>Here  $b$  is the black hole index, and  $s$  is the soliton index.

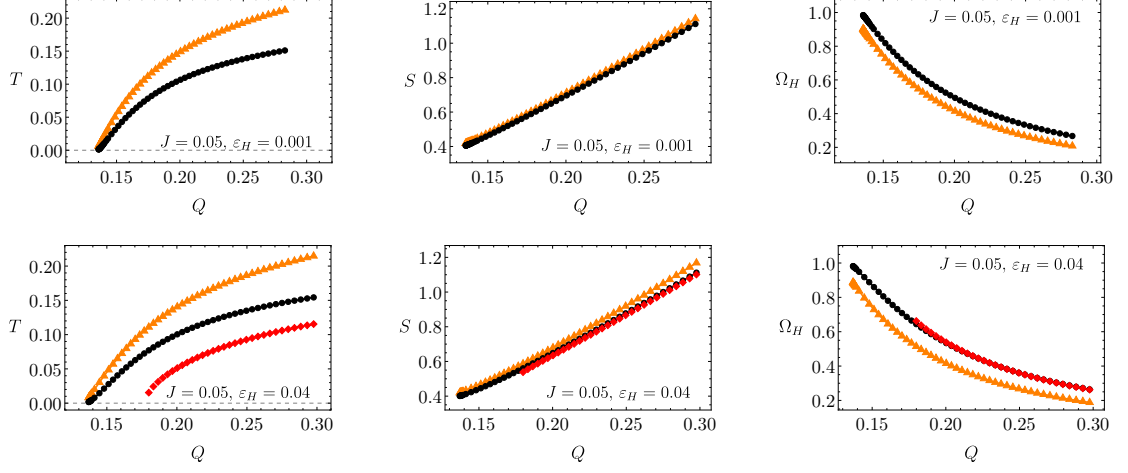


**Fig. 4.22** *First line:* The comparison with the approximation of [62] for the same charge, mass, and angular momentum  $J = 0.05$ . Black disks are numerical results, and orange triangles are the predicted curves. For small charge,  $Q_s/Q \simeq 0.5\%$ . Here the lowest  $T = 0.00127$ , and  $S = 0.405$ . The error in  $S$  close to the BPS bound is 2 – 4%. Note that in particular as  $T \rightarrow 0$ ,  $\Omega_H \rightarrow 1$ .

*Second line:* Red rhombi show the coexisting CLP black holes. For small charge,  $Q_s/Q \simeq 0.6\%$ . Here lowest  $T = 0.00164$ , and  $S = 0.401$ . The error in  $S$  close to the BPS bound is 5%.

given by

$$\begin{aligned}
 S &= 2\sqrt{2}\pi \left( \frac{1}{6}\Delta + \frac{1}{6}\sqrt{\Delta^2 - 4J^2} \right)^{3/4}, \\
 T &= \frac{\sqrt{2}}{\pi} \left( \frac{1}{6}\Delta + \frac{1}{6}\sqrt{\Delta^2 - 4J^2} \right)^{1/4} \left( 1 - 4J^2 \left( \Delta + \sqrt{\Delta^2 - 4J^2} \right)^{-2} \right), \\
 \Omega_H &= \frac{1}{3}j, \\
 \Delta &= M - 3Q.
 \end{aligned} \tag{4.54}$$

We present a comparison with the numerical results in Fig. 4.21 and Fig. 4.22. For small  $J$ ,  $Q$  and the horizon scalar field  $\varepsilon_H$  we find a good agreement, as the hairy black holes approach the supersymmetric black hole along the merger line (Fig. 4.21, *first line*). If we increase the  $\varepsilon_H$ , constant  $\varepsilon_H$  curves will cross the extremality plane for the CLP black holes (Fig. 4.21, *second line*), and no longer coexist with the non-hairy solutions. We still find a relatively good agreement in  $T$  and  $S$ , however there is a clear difference in the behaviour of  $\Omega_H$ . As we have seen in [92], intensive thermodynamic variables typically require higher order terms.

The hairy solutions exist for

$$3Q + 2J \leq M \leq 3Q + \frac{1}{3}(j^2 + 9)Q^2 - \frac{2}{81}j^2(j^2 + 9)Q^3 + \mathcal{O}(Q^4), \quad (4.55)$$

where at the upper range there is no contribution from the soliton, and the CLP black hole is recovered. Note, that in this regime the merger and extremality lines are very close to each other. In the limit  $j \rightarrow 3$ , the upper and lower limits coincide, and we obtain the Gutowski-Reall solution at the intersection of the extremal and BPS planes.

At the lower range the hairy black holes approach the BPS bound where  $T = 0$ . We also have that  $j_b = 3$  [62], and the black hole is supersymmetric; the mix on the BPS can be seen as a weakly interacting black hole and a scalar cloud configuration, both of which are itself supersymmetric. We assume that  $j < 3$ , and thus  $\Omega_H < 1$ . Numerical results indicate that  $\Omega_H \rightarrow 1$ , which might be a non-linear effect. In [62] it was conjectured that these hairy black holes comprise a two parameter family of supersymmetric hairy black holes. On the BPS bound, the prediction for the entropy only matches when we are close to the Gutowski-Reall solution, and for a fixed  $J$  is given by  $S = 2\sqrt{2}\pi J^{3/4}/3^{3/4}$ . We find that for a fixed  $J$ , away from Gutowski-Reall black hole, the entropy is always decreasing.

## 4.10 Discussion and future directions

In this chapter we have analysed rotating, charged, hairy black holes in five-dimensional AdS, in both global and planar spacetimes. These black holes can be embedded in the  $\mathcal{N} = 8$   $SO(6)$  gauged supergravity model with the three diagonal  $U(1)$  charges set equal. We have analysed the three dimensional solution space by considering various limits, and we have shown that these black holes extend the CLP solutions to the BPS bound for all charges. These new hairy states above the supersymmetry contribute to the state space of  $\mathcal{N} = 4$  SYM at energies  $\mathcal{O}(N^2)$  at large  $N$ , and demonstrate the existence of new phases at all charges. We have also examined the non-trivial approach to the BPS bound in detail. Facilitated by the radial gauge we were able to reach extremely low temperatures, however, we were not able to fully unravel the nature of the extremal hairy solutions.

We conjectured the existence of a one parameter extension of the supersymmetric Gutowski-Reall black hole. The constant horizon scalar  $\varepsilon_H$  hairy black hole families retain a finite entropy in the zero temperature limit, as well as possess regular curvature scalars. We also provide further evidence to support this conjecture, namely the indication of the zero temperature limit by the isotherms, and regularity of the fixed low charge limit.

It is important to note, however, that the extremal limit is challenging to resolve numerically, and the slow, possibly logarithmic, approach renders some of our results inconclusive. It is not clear to what extent the rotating hairy black holes continuously connect to the  $J = 0$  case. It would be very interesting if a small amount of rotation allows a nucleation of a small rotating black hole at the centre of the scalar field cloud. Numerical results support the idea of some continuity, albeit that we cannot rule out a completely different mechanism governing the near BPS regime. Numerically we found it difficult to locate the maximal charge for the  $T = 0$  family  $Q_{\max}(J)$ , and we do not know if it is connected to  $Q_c = Q_{\max}(0)$ . We also cannot eliminate the possibility of the extremal hairy solutions all having  $S = 0$  and  $\varepsilon_H = \infty$ . However, this would require dramatic near extremal behaviour, and such a picture is hard to reconcile with our numerical results. Lastly, we have not analysed large  $J$  hairy black holes in detail as these solutions also have large charge, and it is conceivable that some such solutions could become singular.

Numerics at low temperatures become increasingly challenging, and we can only infer the expected qualities of the limiting solution. It would be preferable to study the extremal limit analytically, by directly using the supersymmetry. However, our numerical results indicate non-analytic behaviour which would complicate the near horizon expansion of the BPS solutions, and the near horizon geometry does not appear to be of the usual  $\text{AdS}_2 \times \text{S}^2$  type. This could explain how the no-hair theorem of [193] is evaded for such extremal hairy black holes. We can also look for singular (large charge) BPS solutions with  $J > 0$  directly, and find the lowest allowed charge. Work in these directions is in progress.

Perhaps it is possible to choose a better ansatz and to simplify the equations enough that some analytic treatment is possible. We found that the Abelian-Higgs scalar potential  $V(\phi) = -4\phi\phi^\dagger$  displays some similarities, and in particular a similar zero temperature, finite entropy limit appears to exist. Varying the Chern-Simons coupling

slightly, or setting it to zero also appears to maintain the aforementioned limit<sup>16</sup>. The phase space is reminiscent of the  $e = e_c$  case in [60]. Evidence of five-dimensional finite entropy rotating, hairy extremal black holes has been also seen in rotating black holes with a complex doublet scalar field [48], and black holes in Einstein-Maxwell-Scalar theory [194]. It might be worthwhile to study the limiting solutions in these models further. Finally, we have not analysed  $Q < 0$  solutions in detail, however they exhibit distinctly different behaviour. The fixed  $\varepsilon_H, J$  solutions when lowering the temperature tend to some singular  $S = 0$  configurations and have  $\Omega_H < 1$ , and furthermore due to the highly singular behaviour it is not clear if  $T = 0$  limit exists.

An immediate way to extend this work is to consider non-equally rotating black holes, as the general supersymmetric black hole has two angular momenta [116, 113]. It would be intriguing if the onset of the superradiance still coincides with the BPS bound. A more complicated task is to analyse black holes with independent diagonal  $SO(6)$  charges, including when some of the charges vanish. This would necessarily involve consistent truncations with more scalar fields, such as in [122].

The scalar field  $\phi$  considered in this chapter is dual to the lightest chiral SYM operator with dimension  $\Delta = 2 = e$ , and the small black holes lie at the edge of the superradiant instability. We expect these hairy phases to be thermodynamically relevant at small charges. It is not known whether the hairy black holes found in this chapter are indeed the thermodynamically dominant saddle points above the supersymmetry from the full ten-dimensional point of view. It is very difficult to tackle this problem in full generality, especially in the non-linear, near-BPS regime. On the other hand, the hairy black holes constructed in this chapter can be oxidized to ten dimensions, which could reveal further insights into the approach to the BPS bound. For instance, singular solutions from the five-dimensional perspective can have regular higher dimensional embedding.

We expect that different scalars are relevant across the moduli space (*e.g.* see [195, 122], and references therein), depending on which instability dominates. We find that large charge hairy black holes have negative specific heat and are locally thermodynamically unstable. The large charge hairy SUSY black holes are singular, and it would be intriguing if there exist scalars which produce finite entropy hairy rotating BPS black holes for  $Q > Q_{\max}(J)$ .

---

<sup>16</sup>Only for the supergravity coupling the marginal mode extends to the BPS bound, and the lowest mass rotating hairy black holes never saturate it.

The planar limit solutions display retrograde condensation, *i.e.* exist for  $T > T_c$ . In [122] it was found that in the ensemble with three equal charges a scalar with a larger mass and larger charge condenses for  $T < T_c$ , and has lower free energy. It would be very interesting to construct large charge global hairy holes in this truncation, which was first studied by [196]. The scalar has  $\Delta = 3 = e$ , therefore we also expect rich phase diagram at lower charges. Within the  $\mathcal{N} = 8$  supergravity truncation we anticipate the operators with low dimensions and higher charge to condense first<sup>17</sup> (*e.g.* see [196]), and thus we consider operators dual to light modes of the  $\mathcal{N} = 8$  supergravity; however, there is clearly some competition between different influencing factors.

Finally, it would be instructive to construct rotating, charged, hairy global black hole phase space in consistent truncations of  $\text{AdS}_4 \times \text{S}^7$  and  $\text{AdS}_7 \times \text{S}^4$ . In particular, equally rotating black holes in odd dimensions preserve cohomogeneity-one, thus the problem is readily tractable. It would be fascinating if in these theories new families of hairy supersymmetric black holes exist, which account for missing BPS states in the stringy entropy calculations.

---

<sup>17</sup>This might not be generic for non-minimally coupled scalars.

### 4.A.1 Numerical convergence

Most of our numerical calculations were performed in the radial gauge, which is allowed by the fact that our problem is reduced to be of co-homogeneity one. The solutions in this gauge exhibit exponential convergence (Fig. 4.23, *right*), and it is well suited to study low temperature regime of the hairy solutions. In order to obtain constant temperature solutions in various thermodynamic ensembles we will also use the DeTurck method. The gauge condition  $\xi^\mu = 0$  is tracked numerically, and solutions presented in this chapter obey  $\max \xi_\mu \xi^\mu = 0$  at least to  $\mathcal{O}(10^{-10})$  precision.

We find that the radial gauge provides exponential convergence with increasing grid size  $n$ , but in the DeTurck gauge the convergence worsens to a power law (Fig. 4.23). Nonetheless, the DeTurck gauge allows us to set the black hole temperature  $T$ , and we will utilise this to study the canonical ensemble in sections 4.5.2.2 and 4.7. In Fig. 4.24, we present convergence test for the black hole energy, plotting the fractional error

$$\Delta m_n = |1 - m_{n+1}/m_n| \tag{4.56}$$

against the grid size  $n$ . The convergence worsens significantly at very low temperatures (Fig. 4.24 *left*), large horizon scalar fields  $\varepsilon_H$  (Fig. 4.24 *right*) and large angular momenta, due to steep gradients in the functions.

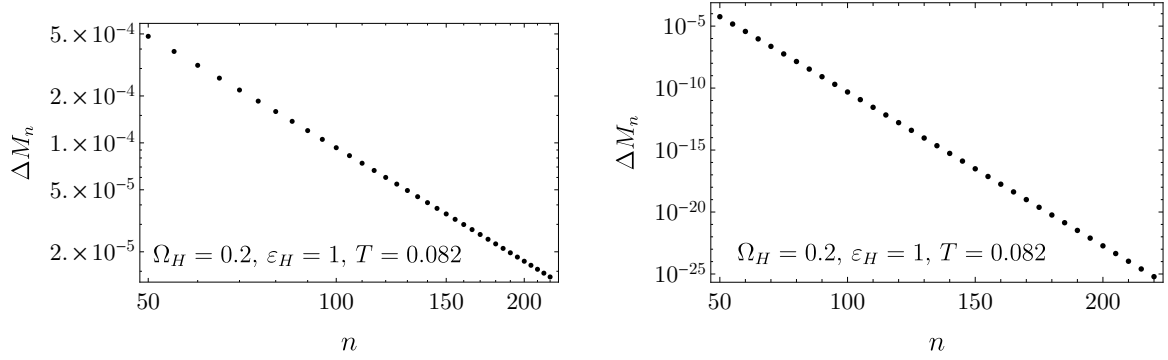


**Fig. 4.23** Convergence of fractional error in black hole energy  $\Delta M_n = |1 - M_{n+1}/M_n|$  against the grid size  $n$ . *Left:* Hairy black hole solution in DeTurck gauge. The scale is log-log, and the convergence is a power law. *Right:* Convergence in radial gauge, for the same hairy black hole. The scale now is log-linear, exhibiting an exponential decay.

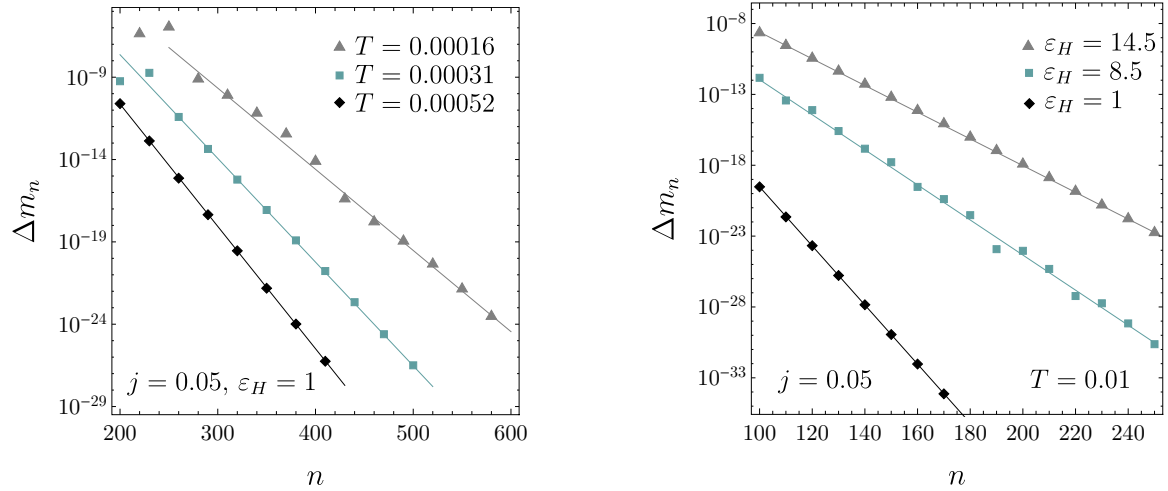


**Fig. 4.24** *Left:* Convergence of the energy for a few coldest  $J = 0.05$ ,  $\varepsilon_H = 1$  hairy black holes considered in the paper, with  $T = 0.00052$  (black rhombi),  $T = 0.00031$  (blue squares) and  $T = 0.00016$  (gray triangles). Here we plot the fractional error  $\Delta$  against the grid size  $n$ . *Right:* Low temperature ( $T = 10^{-2} \pm 10^{-3}$ ) hairy black hole energy convergence for a few different horizon scalar values  $\varepsilon_H$ . Black rhombi are for  $\varepsilon_H = 1$ , blue squares for  $\varepsilon_H = 8.5$ , and gray triangles for  $\varepsilon_H = 14.5$ . Here we show the fractional error against the grid size in a log scale.



# Chapter 5

## Stirring a Black Hole

The work presented in this chapter was published as [141] in collaboration with Jorge E. Santos. The numerical results were generated by the author alone with their own code, except for the contents of section 5.6. The latter was performed by Jorge E. Santos, along with the construction of hairy solutions which is not presented here. Some of the results were verified by Jorge E. Santos with their own code.

### 5.1 Introduction

The theory of quantum field theory (QFT) in fixed curved spacetimes is notoriously difficult to study, due to both conceptual and technical limitations. One of the most notable quantum phenomena in this context is that of particle creation from the vacuum, which allows black holes to emit Hawking radiation [197, 198, 13, 199]. A full theoretical understanding of the phenomenon together with the associated black hole information paradox remains an open question. In addition, the understanding of QFTs in curved classical gravity backgrounds can provide us with valuable insights into the full theory of quantum gravity.

A standard numerical approach to study nonperturbative aspects of QFTs is lattice simulations, whereby a continuous spacetime is approximated by a discrete lattice of points. However, a successfully implemented lattice formulation for a QFT on a generic curved spacetime is currently not known. This is particularly relevant in the strong coupling region, where many perturbative techniques are not feasible. Through

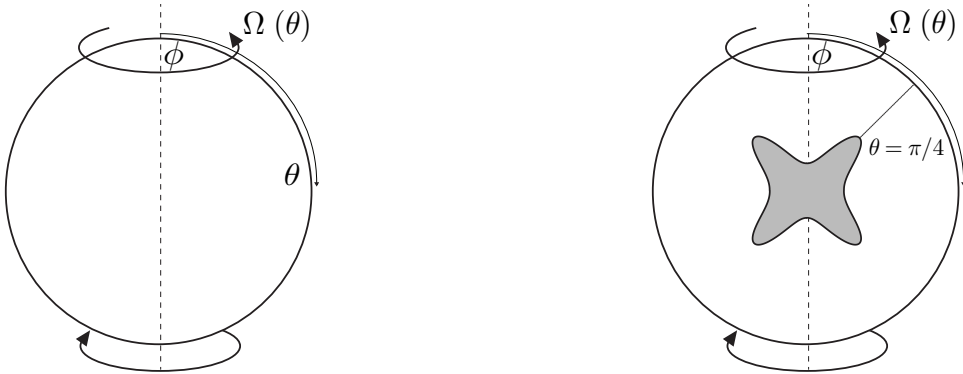


**Fig. 5.1** Illustration of the novel  $\text{AdS}_4$  geometries. *Left*: Solitonic solutions with a differentially rotating boundary. *Right*: Black hole solutions. The rotational pull force is maximal at  $\theta = \pi/4$ , deforming the black hole horizon into an hourglass shape.

the gauge/gravity duality we are able to probe the physics of the strongly coupled theories, and in contemporary physics it remains a valuable tool to study the underlying thermodynamics in this otherwise inaccessible regime. Many condensed matter systems are strongly coupled, for which we expect interesting new phenomena to emerge.

The gauge/gravity duality maps a class of gravitational theories with AdS boundary conditions to certain conformal quantum field theories in fewer dimensions. On the gravity side, the superradiant instability is expected to influence the phase diagram for CFTs in compact spacetimes. While this is certainly true in the context of the microcanonical ensemble, in the grand-canonical ensemble the region of moduli space unstable to superradiance is cloaked by a first order Hawking-Page phase transition [123]. This implies that, for a fixed temperature and angular velocity at which the Kerr-AdS black hole exhibits the instability, the preferred phase is simply thermal AdS.

In this chapter we consider conformal field theories on nontrivial metrics that are equipped with a dipolar differential rotation. By employing the gauge/gravity duality, we study asymptotically AdS spacetimes for which the boundary takes the following form

$$ds_{\partial}^2 = -dt^2 + d\theta^2 + \sin^2 \theta (d\phi + \varepsilon \cos \theta dt)^2,$$

where the parameter  $\varepsilon$  controls the rotation. For each boundary profile metric, we find two classes of solutions: a solitonic horizonless spacetime and a deformed black hole, which are schematically pictured in Fig. 5.1. The solitonic solutions have no horizon, and correspond to deformations of global  $\text{AdS}_4$ , while black hole solutions

can be seen as continuous deformations of Schwarzschild-AdS<sub>4</sub> black holes. We will find that both phases develop hair due to superradiance if the boundary rotation is sufficiently large. In addition, we shall see that the phase diagram of solutions is rather intricate, including certain regions of moduli space with up to six-fold degeneracy.

Aided by the simplicity of our gravitational setup we were able to reconstruct the critical value of the amplitude for which the system develops hair from pure CFT data. This will allow us to identify which CFT observables might be sensitive to this phenomenon and to the hypothetical violation of weak cosmic censorship in the bulk.

This paper is organised as follows. Section 5.3 details the construction of soliton and black hole solutions. In section 5.4 we present results, and carry out thermodynamical analysis. Section 5.5 presents stability analysis in which we consider a massless scalar field. Section 5.6 discusses the CFT interpretation of our results and attempts to identify the field theory variables that best describe it. In section 5.7, we study possible multi horizon equilibrium configurations for spinning test particles. Section 5.8 briefly analyses the holographic dual of theories living on a fixed rotating background geometry containing no ergoregions. We conclude in section 5.9 with discussion.

## 5.2 Setup

We start with the four-dimensional Einstein-Hilbert action supplemented by the Gibbons-Hawking-York boundary term [200, 201]:

$$S = \frac{1}{16\pi G_N} \int_{\mathcal{M}} d^4x \sqrt{-g} \left( R[g] + \frac{6}{L^2} \right) + \frac{1}{8\pi G_N} \int_{\partial\mathcal{M}} d^3x \sqrt{-\gamma} K, \quad (5.1)$$

where  $\partial\mathcal{M}$  is the boundary of AdS<sub>4</sub>,  $\gamma_{\mu\nu}$  is the induced metric on the boundary,  $K$  is the trace of the extrinsic curvature of the boundary,  $L$  is the length scale of AdS<sub>4</sub> and  $R[g]$  the Ricci scalar. The equations of motion derived from (5.1) read

$$R_{\mu\nu} + \frac{3}{L^2} g_{\mu\nu} = 0,$$

and we are looking for asymptotically AdS<sub>4</sub> solutions, with a rotating conformal boundary given by

$$ds_{\theta}^2 = -dt^2 + d\theta^2 + \sin^2 \theta [d\phi + \Omega(\theta)dt]^2, \quad (5.2)$$

with a dipolar differential rotation profile  $\Omega(\theta) = \varepsilon \cos \theta$ . We will be interested in finding solutions where  $\partial_t$  and  $\partial_{\phi}$  extend as Killing fields into the bulk. Close to the poles and on the equator,  $\partial_t$  is always timelike for any value of  $\varepsilon$ . However, its norm

$$\|\partial_t\|^2 = -1 + \frac{\varepsilon^2}{4} \sin^2 2\theta \quad (5.3)$$

is maximal at  $\theta = \pi/4$ , and  $\partial_t$  becomes spacelike for certain regions of  $\theta$  if  $\varepsilon > 2$ . We shall see that both black holes and solitons develop hair due to superradiance if  $\varepsilon > 2$ . One might wonder whether this could have been anticipated using the results of Green, Hollands, Ishibashi and Wald [53]. However, the theorems presented in [53] were deduced under the assumption that the boundary metric was metrically that of the Einstein static universe, which is not the case in our setup. Our results suggest that a generalisation of the results in [53] should exist even for nontrivial boundary metrics such as ours.

## 5.3 Numerical Construction

### 5.3.1 Soliton

In order to find solitonic solutions we consider the following numerical ansatz

$$ds^2 = \frac{L^2}{(1-y^2)^2} \left\{ -Q_1 dt^2 + \frac{4Q_2 dy^2}{2-y^2} + y^2(2-y^2) \left[ \frac{4Q_3}{2-x^2} \left( dx + \frac{x}{y} \sqrt{2-x^2} Q_4 dy \right)^2 + (1-x^2)^2 Q_5 \left( d\phi + yx \sqrt{2-x^2} Q_6 dt \right)^2 \right] \right\}, \quad (5.4)$$

with  $Q_i$ ,  $i \in \{1, \dots, 6\}$ , being functions of  $(x, y)$ . If  $Q_1 = Q_2 = Q_3 = Q_5 = 1$  and  $Q_4 = Q_6 = 0$ , the line element (5.4) reduces to that of pure AdS<sub>4</sub> in global coordinates, with  $y$  being related to the usual radial coordinate in AdS<sub>4</sub> via  $r = L y \sqrt{2-y^2}/(1-y^2)$ , and  $x$  parametrising the standard polar angle on  $S^2$  with the identification  $\sin \theta = 1-x^2$ .

The powers of  $y$  and  $1 - x^2$  appearing in the ansatz ensure that the metric is regular at the origin  $y = 0$  and axis of rotation  $x = \pm 1$  for smooth functions  $Q_i$ .

The reference metric  $\tilde{g}$  used in the DeTurck method is chosen by setting  $Q_6 = \varepsilon$ , and  $Q_1 = Q_2 = Q_3 = Q_5 = Q_4 + 1 = 1$ , everywhere in the bulk. The parameter  $\varepsilon$  controls the rotation on the boundary and in turn the stirring of the bulk.

As we are considering a dipolar problem we have reflection symmetry  $x \rightarrow -x$  and thus both coordinates take values in the square domain  $[0, 1] \times [0, 1]$ . Because the functions  $Q_i$  are constructed to be even around  $x = 0$  (the equator) and  $y = 0$  (the origin), we can use a square half-half Chebyshev grid clustering around the  $x = 1$  and  $y = 1$  boundaries and thus effectively interpolate the functions with half the number of points. This is especially advantageous as spectral convergence is exponential with grid size. In addition, it fixes smoothness of the geometry at the reflection boundary.

This leaves us with two boundaries, one at the conformal boundary located at  $y = 1$ , and one at  $x = 1$ . The latter is a physical boundary, whereas the former is a fictitious boundary where regularity must be imposed. Expanding the equations of motion near  $x = 1$  as a power series in  $(1 - x)$  gives  $Q_3(1, y) = Q_5(1, y)$  and  $Q_4(1, y) = 0$ , as well as  $\partial_x Q_1 = \partial_x Q_2 = \partial_x Q_3 = \partial_x Q_4 = \partial_x Q_5 = 0$ .

At the conformal boundary, we demand the metric (5.4) approaches global  $\text{AdS}_4$  with a rotating conformal boundary metric, that is to say, we require

$$Q_1(x, 1) = Q_2(x, 1) = Q_3(x, 1) = Q_5(x, 1) = Q_4(x, 1) + 1 = 1, \quad \text{and} \quad Q_6(x, 1) = \varepsilon. \quad (5.5)$$

Comparing the conformal boundary metric obtained from our boundary conditions (5.5) and (5.2), gives  $\Omega(\theta) = \varepsilon \cos \theta$ , in standard polar coordinates on  $S^2$ .

### 5.3.2 Black Holes

For the black hole solutions we use the ansatz

$$ds^2 = \frac{L^2}{(1 - y^2)^2} \left\{ -y^2 \tilde{\Delta}(y) Q_1 dt^2 + \frac{4 y_+^2 Q_2 dy^2}{\tilde{\Delta}(y)} + y_+^2 \left[ \frac{4 Q_3}{2 - x^2} (dx + x \sqrt{2 - x^2} y Q_4 dy)^2 \right. \right. \\ \left. \left. + (1 - x^2)^2 Q_5 (d\phi + y^2 x \sqrt{2 - x^2} Q_6 dt)^2 \right] \right\}, \quad (5.6a)$$

where

$$\Delta(y) = (1 - y^2)^2 + y_+^2(3 - 3y^2 + y^4), \quad \text{and} \quad \tilde{\Delta}(y) = \Delta(y)\delta + y_+^2(1 - \delta), \quad (5.6b)$$

with  $Q_i$ ,  $i \in \{1, \dots, 6\}$ , being functions of  $(x, y)$ . If  $Q_1 = Q_2 = Q_3 = Q_5 = \delta = 1$  and  $Q_4 = Q_6 = 0$ , the line element (5.4) reduces to that of Schwarzschild-AdS<sub>4</sub> black hole in global coordinates, with  $y$  being related to the usual radial coordinate via  $r = L y_+ / (1 - y^2)$ , and  $x$  parametrising the standard polar angle on  $S^2$  with the identification  $\sin \theta = 1 - x^2$ .

The reference metric is chosen to have  $Q_6 = \varepsilon$  and, similarly to the soliton case, we work on a unit square grid. Regularity at  $x = 1$  demands  $\partial_x Q_i(x, y) = 0$  ( $i \neq 4$ ),  $Q_4(x, y) = 0$ , and  $Q_3(x, y) = Q_5(x, y)$ . At the conformal boundary, we set  $Q_i(x, 1) = 1$  for  $i = 1, 2, 3, 5$ ,  $Q_4(x, 1) = 0$  and  $Q_6(x, 1) = \varepsilon$ .

In the ansatz (5.6a) we have three parameters:  $\varepsilon$ , which sets the amplitude of the boundary rotation, and  $(y_+, \delta)$ , which set the black hole temperature. The Hawking temperature is computed in the usual way by requiring smoothness of the Euclidean spacetime and is given by

$$T = \frac{(1 - \delta)y_+^2 + \delta(3y_+^2 + 1)}{4\pi y_+}. \quad (5.7)$$

For  $\delta = 1$ , the temperature has a minimum at  $y_+ = 1/\sqrt{3}$ , coinciding with the minimal temperature of a Schwarzschild-AdS<sub>4</sub>, occurring at  $T_{\min}^{\text{Schw}} \equiv \sqrt{3}/(2\pi)$ . In general we will have two branches of solutions with the same temperature which we will refer to as *large* and *small* black holes. However, when  $\varepsilon \neq 0$ , our new deformed black holes can have a minimum temperature below that of the Schwarzschild-AdS<sub>4</sub> black hole. In order to bypass this, we introduced a parameter  $\delta$  which allows us to get arbitrarily close to zero temperature<sup>1</sup>. Computations with  $T > T_{\min}^{\text{Schw}}$  were performed using the ansatz where  $\delta = 1$ , and the results with  $\delta \neq 1$  enjoy similarly sufficient convergence properties as those with  $\delta = 1$  (see Appendix 5.A).

<sup>1</sup>This ansatz allows us to reach zero temperature, for instance, see [92], where it was used to construct hairy AdS<sub>5</sub> black holes, which in the  $T \rightarrow 0$  limit approach a smooth BPS soliton.

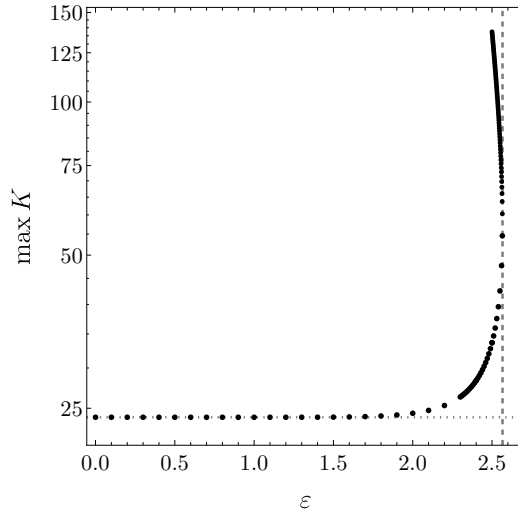


**Fig. 5.2** The log-linear plot of the maximum of the Kretschmann scalar across the whole spacetime against the rotation parameter for the soliton solutions. The dashed gridline marks  $\varepsilon_c$ , and the dotted line shows the  $\max K = 24/L^4$  for pure  $\text{AdS}_4$ .

## 5.4 Numerical Results

For simplicity of presentation, in all of our plots we will set  $L = 1$ .

### 5.4.1 Soliton

One of the most interesting results of our manuscript is that we find no soliton solutions for  $\varepsilon > \varepsilon_c \simeq 2.565$ . In fact, we find no stationary axisymmetric solutions for  $\varepsilon > \varepsilon_c$ . Furthermore, there is a range  $\varepsilon \in (2, \varepsilon_c)$  in which two solitons<sup>2</sup> exist for each value of  $\varepsilon$ , demonstrating non-uniqueness within the soliton family.

We have monitored the behaviour of the maximum of the Kretschmann scalar as a function of  $\varepsilon$ . Since we have no matter fields, besides a negative cosmological constant, the Kretschmann curvature invariant  $K = R_{abcd}R^{abcd}$  is related to the norm of the Weyl tensor in a simple manner

$$L^4 W_{abcd}W^{abcd} = L^4 K - 24,$$

that is to say, the local tidal forces scale like  $K^{1/2}$ .

<sup>2</sup>We cannot exclude the possibility that more than two solutions might exist at some values of  $\varepsilon$  as we approach  $\varepsilon = 2$ .

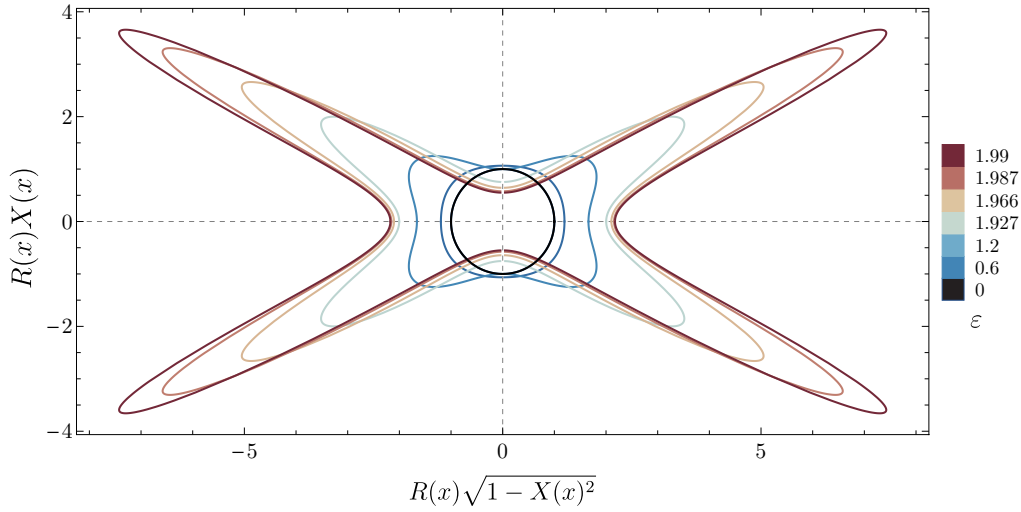


**Fig. 5.3** Hyperbolic embedding of the cross section of the black hole horizons, for several values of the parameter  $\varepsilon$  and a fixed temperature  $T = 1/\pi$ . As we increase  $\varepsilon$ , the arms of the horizon cross section get stretched further apart. This picture is qualitatively the same for  $T \geq 1/\pi$ .

The Kretschmann scalar  $K$  is maximal in the equatorial plane  $x = 0$  (see Fig. 22), and slowly deforms from the pure AdS<sub>4</sub> value of  $24/L^4$  as we increase  $\varepsilon \rightarrow \varepsilon_c$ , forming two large extrema. The minima grows only slightly slower than the maxima, and the latter is plotted against  $\varepsilon$  in Fig 5.2. For  $\varepsilon > 2$ , we can see that two soliton solutions exist for a fixed value of  $\varepsilon$ . We call the upper branch the large branch, and the lower branch the small branch. The large branch of solitons smoothly extends the growth of  $K$ , which increases without bound, indicating formation of a curvature singularity. For more discussion on the Kretschmann scalar see Appendix 5.B.

## 5.4.2 Black Holes

### 5.4.2.1 The horizon geometry

In order to obtain a better understanding of how the black hole horizon behaves under the increase of the boundary rotation amplitude we analyze horizon embedding diagrams. As with Schwarzschild-AdS<sub>4</sub> black holes, for a given temperature (5.7) there exist two solutions which we will call *small* and *large* black holes. In the case of the small black hole branch, we could successfully embed horizons into Euclidean space  $\mathbb{E}^3$  for all  $\varepsilon$  - they are small and round spheres, slightly squashed through the

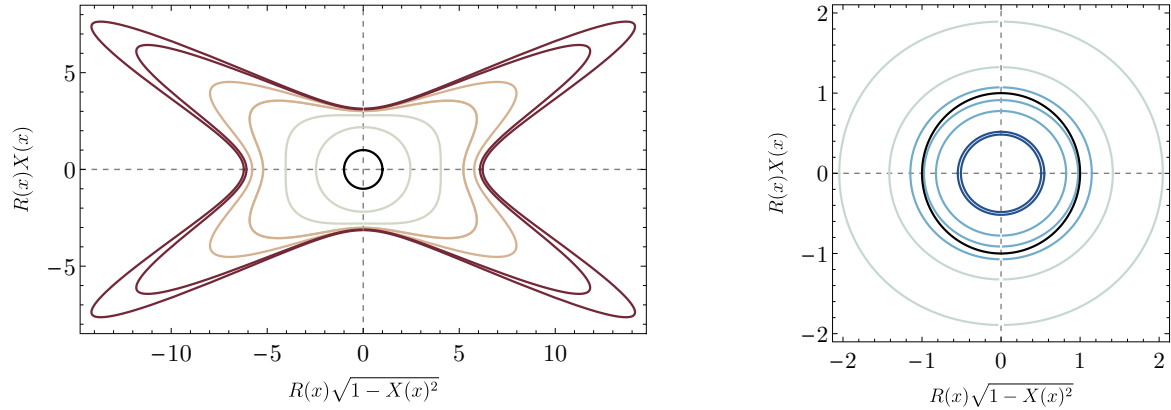


**Fig. 5.4** Hyperbolic embedding of the cross section of the black hole solution horizons, for several values of the parameter  $\varepsilon$  and a fixed low temperature  $T = 0.2506$ . In this regime, there is a four-fold black hole non-uniqueness. *Left*: Embeddings for the upper, thermodynamically dominant branch of solutions with  $\varepsilon \in (1.520, 2.059)$ , and the largest entropy branch (two outer curves in red,  $\varepsilon = 2.055, 2.05$ ). The black circle is the  $T = 1/\pi$ ,  $\varepsilon = 0$  black hole. *Right*: Embeddings for the two small black hole branches. The higher entropy branch has  $\varepsilon \in (1.520, 2.557)$ , and the two inner circles in dark blue represent the lowest branch ( $\varepsilon = 2.55, 2.53$ ). The embeddings are qualitatively similar for the low  $T$  regime.

poles. However, for the large branch, the scalar Gaussian curvature of the horizon spatial sections becomes too negative and the procedure is only successful for very small  $\varepsilon$ . Instead, we embed spatial cross sections of the horizon into hyperbolic  $\mathbb{H}^3$  space [202] in global coordinates

$$ds_{\mathbb{H}^3}^2 = \frac{dR^2}{1 + R^2/\tilde{\ell}^2} + R^2 \left[ \frac{dX^2}{1 - X^2} + (1 - X^2) d\phi^2 \right], \quad (5.8)$$

where  $\tilde{\ell}$  is the radius of the hyperbolic space. For sufficiently small values of  $\tilde{\ell}$  the embedding always exists. The induced metric on the intersection of the horizon with a partial Cauchy surface of constant  $t$  of the black hole line element (5.6a) is given by

$$ds_H^2 = L^2 \left[ \frac{4y_+^2 Q_3(x, 0)}{2 - x^2} dx^2 + y_+^2 (1 - x^2)^2 Q_5(x, 0) d\phi^2 \right]. \quad (5.9)$$

The embedding is given by a parametric curve  $\{R(x), X(x)\}$ . The pull back of (5.8) to this curve induces a two-dimensional line element with the following form

$$ds_{\text{pb}}^2 = \left[ \frac{R'(x)^2}{1 + \frac{R(x)^2}{\tilde{\ell}^2}} + \frac{R(x)^2 X'(x)^2}{1 - X(x)^2} \right] dx^2 + R(x)^2 (1 - X(x)^2) d\phi^2. \quad (5.10)$$

Equating this line element with (5.9) gives the following first order differential equation for the polar coordinate

$$0 = 4H(x)P(x)(X(x)^2 - 1)^2 \left[ P(x) - \tilde{\ell}^2 (X(x)^2 - 1) \right] + 4\tilde{\ell}^2 P(x)X(x)(X(x)^2 - 1)P'(x)X'(x) - (X(x)^2 - 1)^2 \tilde{\ell}^2 P'(x)^2 - 4P(x)^2 (\tilde{\ell}^2 + P(x))X'(x)^2 \quad (5.11)$$

with  $H(x) = (2 - x^2)^{-1}(4y_+^2 Q_3(x, 0))$  and  $P(x) = y_+^2 (1 - x^2)^2 Q_5(x, 0)$ . The numerical results for several values of  $\varepsilon$  are presented in Fig. 5.3 where we set  $\tilde{\ell} = 0.73$ . Here we are fixing the black hole temperature to be  $T = 1/\pi$ , and the results for other temperatures are qualitatively similar (Fig. 5.4).

For  $\varepsilon < 1$ , the large black holes are round and the deformation is small. As we approach  $\varepsilon \rightarrow 2^-$ , the black hole horizon gets significantly distorted and develops remarkable extended features. These cross-section ‘‘spikes’’ peak at  $x = \sqrt{1 - \sqrt{2}/2}$ , *i.e.*  $\theta = \pi/4$ , where the gravitational pull is the strongest<sup>3</sup>. The horizons are squashed through the poles, and extended sideways, with the circumference slowly increasing. The black hole diameter through the poles tends to some non-zero value<sup>4</sup>, and for very large rotation parameter the thickness of the cross section arms is surprisingly uniform throughout its length, and as a function of  $\varepsilon$ . As we increase the temperature, the horizon deforms faster. We conjecture that for sufficiently high temperatures, these static, axially symmetric solutions exist for any  $\varepsilon < 2$ , endlessly stretching the black hole horizon towards the  $\text{AdS}_4$  boundary. This is difficult to check numerically, but our results indicate that there is no upper bound to how extended these black holes can become as we approach  $\varepsilon \rightarrow 2^-$ .

Colder black holes turn out to be less elastic, and more extended through the equator. In Fig. 5.4 we plot embeddings for a low temperature  $T = 0.2506$ , where for a

<sup>3</sup>As measured by the conformal boundary metric.

<sup>4</sup>This feature is not very apparent in the embedding diagrams.

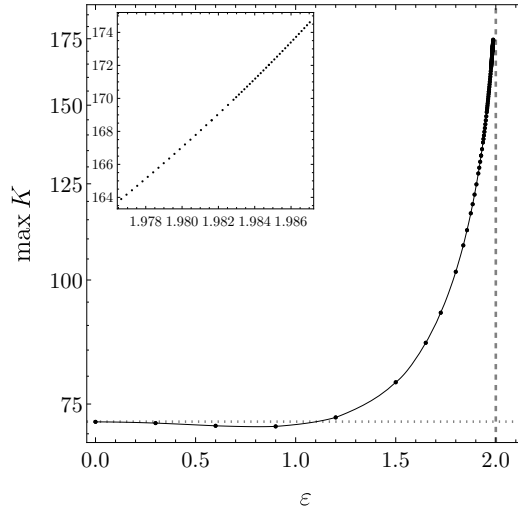


**Fig. 5.5** Log-linear plot of the curvature scalar maximum against  $\varepsilon$ , for a large black hole with  $T = 1/\pi$ . The dashed gridline marks the critical value of  $\varepsilon$ , and the dotted gridline shows  $K_{\max} = 72$  for a Schwarzschild-AdS<sub>4</sub> black hole. The inset is a log-log plot for high values of the rotation amplitude.

fixed  $\varepsilon$  we find two or four black holes. Even though this phase is inelastic, as  $\varepsilon \rightarrow 2^+$ , we expect the stretched solutions to enter a scaling regime as with the hot solutions.

#### 5.4.2.2 Curvature invariants

As we tune the boundary rotation parameter, thus “stirring” the bulk, the black hole becomes ever more stretched and we expect the curvature on the horizon to increase correspondingly.

In Fig. 5.5, we show the maximum of the Kretschmann scalar as a function of  $\varepsilon$  for large black holes. For the black holes, the Kretschmann scalar is maximal on the horizon, located at  $y = 0$ , and as  $\varepsilon \rightarrow 2^-$ , it peaks closer to  $\theta = \pi/4$ . For Schwarzschild-AdS<sub>4</sub>,  $L^4 K|_{\mathcal{H}} = 12/y_+^4 + 24/y_+^2 + 36$ , and thus for  $T = 1/\pi$  the maximal value is  $72/L^4$ . As the boundary amplitude approaches  $\varepsilon = 2^-$ , the Kretschmann scalar grows without bound (see Fig. 5.5) and we expect the maximum of the Kretschmann scalar to enter a scaling regime. This quantity is difficult to extract accurately, however we find some numerical evidence that it behaves as a power law as  $\varepsilon \rightarrow 2^-$ .

For completeness, we present plots of the Kretschmann scalar of the thermodynamically dominant solutions in Appendix 5.B, Fig. 22.

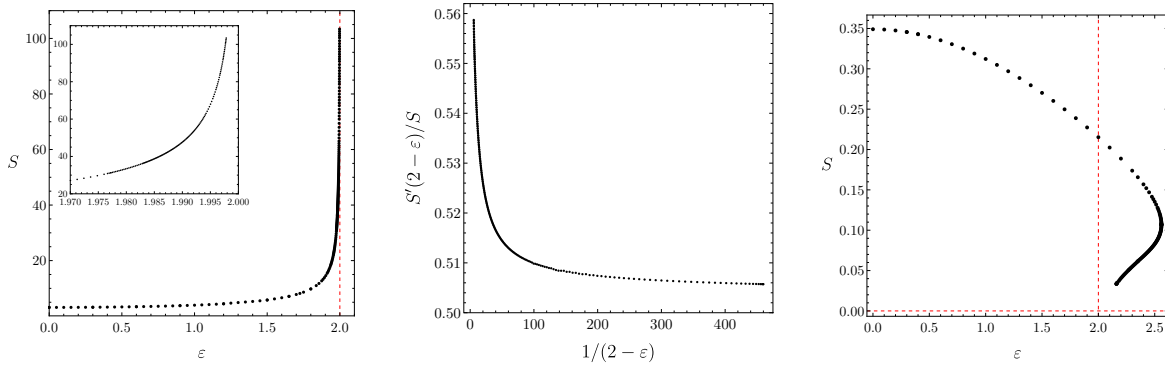


**Fig. 5.6** *Left*: Entropy against the rotation parameter  $\varepsilon$  for the large branch of black holes with  $T = 1/\pi$ . The inset zooms around the limit, demonstrating the asymptotic behavior. Red dashed gridlines mark the  $\varepsilon = 2$  limit. *Middle*: Logarithmic derivative of  $S$  for the large black hole with  $T = 1/\pi$ . As  $\varepsilon \rightarrow 2$ , the entropy of the large black hole blows up as an inverse power law. *Right*: Entropy of the small branch of black holes with the same temperature. Red dashed gridlines show where  $\varepsilon = 2$  and  $S = 0$ .

### 5.4.2.3 Entropy

The entropy associated with the black hole horizon is given by

$$S = \frac{A}{4G_N} = \frac{2\pi y_+^2 L^2}{G_N} \int_0^1 dx \frac{1-x^2}{\sqrt{2-x^2}} \sqrt{Q_3(x, 0)Q_5(x, 0)}. \quad (5.12)$$

In Fig. 5.6, we present our results for the small and large branches of black hole solutions with a temperature  $T = 1/\pi$ . For the large black holes, we find that the entropy is always an increasing function of  $\varepsilon$ , and as  $\varepsilon \rightarrow 2^-$ , it grows without bound. When  $\varepsilon$  is sufficiently close to 2, the entropy enters a scaling regime as we saw with the Kretschmann scalar, and  $S \propto (2-\varepsilon)^{-\alpha}$  (see the middle panel of Fig. 5.6). Numerically<sup>5</sup> we find that  $\alpha$  is consistent with being  $1/2$  within a 1% error.

For the small branch (see right panel of Fig. 5.6), and fixed temperature, the entropy is a decreasing function of  $\varepsilon$ . In this case we can reach values  $\varepsilon > 2$ , although we still find a maximum value of  $\varepsilon$  beyond which we cannot find axially symmetric black hole solutions. We call this maximum value  $\varepsilon_{\max}(T)$ . As the temperature decreases,  $\varepsilon_{\max}(T)$  approaches  $\varepsilon_c$  from below, which is a turning point for the small branch of solutions, below which we obtain a second set of unstable solutions with lower entropy. In this

<sup>5</sup>Numerically, this is difficult to explore for temperatures much larger, and smaller than  $T = 1/\pi$ . The hot, large black holes reach the limit  $\varepsilon = 2$  slowly, and the cold black holes are more difficult to resolve. However, we would expect that near the critical boundary value parameter  $\varepsilon = 2$ , the scalar invariants, such as entropy and curvature blow up according to some scaling laws.

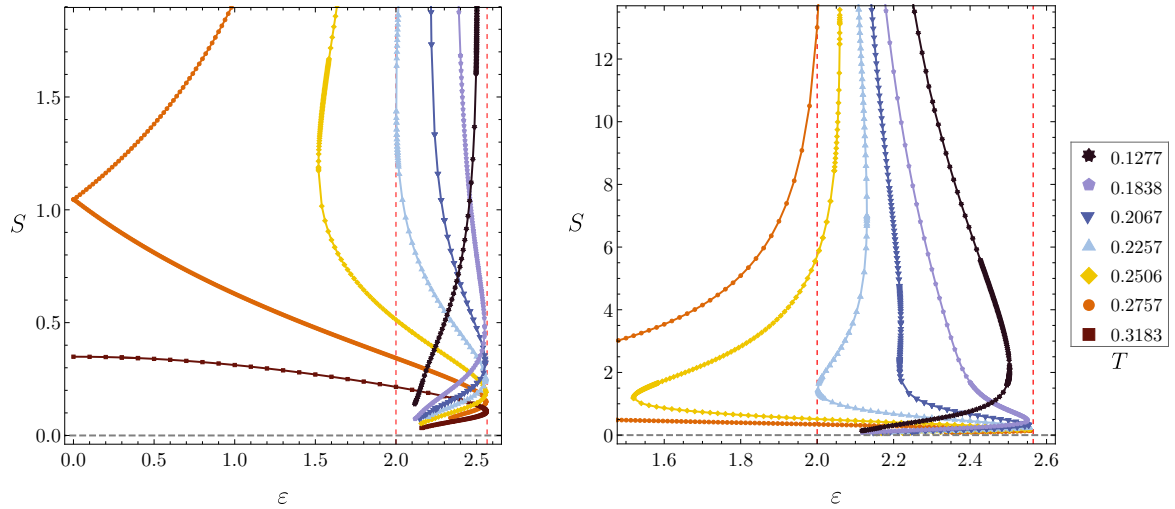


**Fig. 5.7** *Left*: Entropy against the boundary parameter for low temperature black holes with  $T < T_{\min}^{\text{Schw}} \simeq 0.2757$ . The orange disks show black holes with  $T \simeq T_{\min}^{\text{Schw}}$ . The brown squares show the (hot) small black holes with  $T = 1/\pi$  for reference. As we lower the temperature, the large black holes begin to exist for  $\varepsilon > 2$ . *Right*: The asymptotic behavior of isothermal entropy curves. Both solution branches approach  $\varepsilon = 2$ , with the large branch having a steeply increasing  $S$ , and the small branch having  $S \rightarrow 0$ . The red gridlines show  $\varepsilon = 2$  and  $\varepsilon = \varepsilon_c$ .

region of the solution space numerical errors are increasingly large, and we were unable to extend the solutions by further decreasing  $\varepsilon$ . We conjecture that  $S \rightarrow 0$  in the limit  $\varepsilon \rightarrow 2^+$ , and the singularity might be approached in a non-trivial way<sup>6</sup>.

This picture looks qualitatively the same for black holes with  $T > T_{\min}^{\text{Schw}}$  (recall that  $T_{\min}^{\text{Schw}} \simeq 0.2757$ ), with large solutions expanding and small solutions shrinking down when we increase  $T$ . However, we can find black hole solutions with a minimal temperature  $T_{\min}(\varepsilon) < T_{\min}^{\text{Schw}}$ . This implies that for fixed  $T < T_{\min}^{\text{Schw}}$ , there are no black hole solutions for  $\varepsilon < \varepsilon_{\min}$ . As we cross the  $T_{\min}^{\text{Schw}}$ , the two black hole branches at fixed temperature join up (see orange disks in Fig. 5.7), and as we lower the temperature further, the “left” turning point occurs for higher values of  $\varepsilon$ . The subsequent evolution of the phase space is somewhat intricate. It turns out, that for all fixed  $T < T_{\min}^{\text{Schw}}$ , there exist large black holes with  $\varepsilon > 2$ . There, we find yet another turning point, which bends back towards  $\varepsilon = 2$ . For temperatures  $T \lesssim 0.2257$ , the “left” turning point crosses  $\varepsilon = 2$ , and black holes exist only for  $\varepsilon > 2$ . Soon after, once we reach

<sup>6</sup>In the literature, there have been examples where black hole solutions approaching a singular point in a phase space exhibit a non-trivial non-uniqueness, for instance in a spiralling manner (see *e.g.* [48, 92]).

$T \simeq 0.207$ , the two upper turning points converge and disappear, leaving only the lower turning point, which appears to exist for all finite temperatures.

This analysis reveals interesting non-uniqueness of the black hole solutions. For temperatures  $T > T_{\min}^{\text{Schw}}$ , we have two black hole solutions: for  $\varepsilon < 2$ , there is a large and a small black hole, and for  $\varepsilon > 2$  there are two small black holes, if we assume that we are approaching  $\varepsilon \rightarrow 2^+$  as  $S \rightarrow 0$ . For  $T < T_{\min}^{\text{Schw}}$ , we have two solutions for  $\varepsilon_{\min}(T) < \varepsilon < 2$ , four solutions for  $\varepsilon > 2$  until  $T \simeq 0.2067$ , when these extra phases merge, and then we again have two branches. All these solutions exist up to some value of  $\varepsilon_{\max}(T) < \varepsilon_c$ .

The low temperature regime is hard to access numerically, so we can only conjecture the very low temperature behaviour. The only remaining turning point is decreasing slowly with the temperature, separating the two branches of solutions the lower of which has vanishing horizon area as  $\varepsilon \rightarrow 2^+$ . These solutions look qualitatively very similar to the soliton solutions, and could be thought of as a small black hole placed in a soliton background. The upper branch has increasing entropy, which blows up as  $\varepsilon \rightarrow 2^+$ .

In the following subsections we present physical quantities and carry out an extensive thermodynamic analysis of both black holes and horizonless AdS<sub>4</sub> solutions, further supporting our conjectures.

### 5.4.3 Stress-Energy tensor

The bare on-shell gravity action in AdS<sub>4</sub> is divergent and in order to obtain the boundary stress tensor we need to regularise the action using holographic renormalization techniques [203, 108, 121]. The counterterms that we must add to the bulk action (5.1) are

$$S_{ct} = -\frac{1}{4\pi G_N L} \int_{\partial\mathcal{M}} d^3x \sqrt{-\gamma} \left( 1 - \frac{L^2}{4} R[\gamma] \right), \quad (5.13)$$

and the expectation value of the stress-energy tensor of the dual field theory can be found to be

$$\langle \tilde{T} \rangle_{\mu\nu} = \frac{1}{8\pi G} \left( \Theta_{\mu\nu} - \Theta \gamma_{\mu\nu} + L G_{\mu\nu}[\gamma] - \frac{2}{L} \gamma_{\mu\nu} \right), \quad (5.14)$$

from the on-shell action.

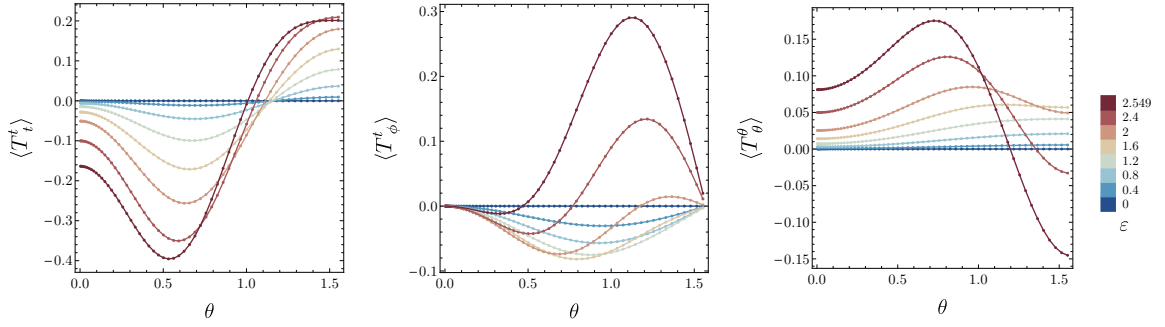


**Fig. 5.8** The stress-energy tensor component  $\langle T_t^t \rangle$  (*left*), component  $\langle T_\phi^t \rangle$  (*middle*), and component  $\langle T_\theta^\theta \rangle$  (*right*) for solitonic solutions as a function of  $\theta$ , the angle on the  $S^2$ . Colours represent different values of the parameter  $\varepsilon$ , with larger values corresponding to larger amplitudes.

As an exercise, following [20], we also compute the holographic stress tensor by recasting the metric (5.6a) into Fefferman-Graham coordinates. Firstly, we solve the equations of motion about the conformal boundary  $y = 1$ , order by order, by expanding the metric functions as shown below

$$Q_i(x, y) = \sum_{n=0}^3 (1-y)^n q_{i,n}(x) + \log(1-y)(1-y)^4 \tau_{i,4}(x) + \mathcal{O}((1-y^2)^3). \quad (5.15)$$

Next we perform an asymptotic coordinate change near the  $\text{AdS}_4$  boundary to the Fefferman-Graham form<sup>7</sup>

$$ds^2 = \frac{1}{z^2} \left[ dz^2 + ds_\partial^2 + z^2 ds_1^2 + z^3 ds_2^2 + \mathcal{O}(z^4) \right]. \quad (5.16)$$

To achieve this, we take

$$\begin{aligned} y &= 1 + \sum_{n=1}^4 z^n Y_n(\theta) + \mathcal{O}(z^4), \\ x &= \sqrt{1 - \sin \theta} + \sum_{n=1}^4 z^n X_n(\theta) + \mathcal{O}(z^4), \end{aligned} \quad (5.17)$$

<sup>7</sup>Here and further in this subsection we set  $G_N L^2 = 1$ .

and determine  $\{Y_n(\theta), X_n(\theta)\}$  order by order in  $z$  so that our line elements can be cast in the form (5.18) with conformal boundary metric

$$ds_\partial^2 = -dt^2 + d\theta^2 + \sin^2 \theta [d\phi + dt \cos \theta \varepsilon]^2. \quad (5.18)$$

The holographic stress-energy tensor is then given by

$$\langle T_{ij} \rangle = \frac{3}{16\pi} g_{(2)ij}, \quad (5.19)$$

where  $g_{(2)ij}$  is the metric associated with  $ds_\partial^2$ . As expected, this stress-energy tensor is traceless and transverse with respect to (5.18). The energy density is simply given by  $\rho(\theta) = -\langle T_t^t \rangle$ , whilst the angular momentum density is simply  $j(\theta) = \langle T_\phi^t \rangle$ .

#### 5.4.3.1 Soliton

The independent boundary stress-energy tensor components for the soliton solution are given by

$$\langle T_t^t \rangle = \frac{1}{768\pi} \left[ 18q_1(\theta) + \varepsilon \sin^2 \theta \left\{ -65\varepsilon + \sin^2 \theta \left( 3\varepsilon^3 \sin^2 2\theta + 46\varepsilon + 18q_6(\theta) \right) - 18q_6(\theta) \right\} \right], \quad (5.20)$$

$$\langle T_\phi^t \rangle = \frac{1}{128\pi} \sin^2 \theta \cos \theta \left[ 2\varepsilon^3 \sin^4 \theta + 3\varepsilon - 3q_6(\theta) \right], \quad (5.21)$$

$$\langle T_\theta^\theta \rangle = \frac{1}{768\pi} \left[ \varepsilon^2 \sin^2 \theta (16 \cos 2\theta - 27) + 18q_3(\theta) \right]. \quad (5.22)$$

Numerical results are presented in Fig. 5.8 where we plot these components against  $\theta$  for several values of the boundary rotation amplitude  $\varepsilon$ . The stress-energy tensor component  $\langle T_t^t \rangle$  is positive at the equator where it is also maximal; it becomes negative at a value which depends on  $\varepsilon$ , and is negative at the poles. As the rotation amplitude increases towards  $\varepsilon_c$ ,  $\langle T_t^t \rangle$  develops a large negative minima in the upper quarter of the sphere.  $\langle T_\phi^t \rangle$ , on the other hand, is negative for small values of  $\varepsilon$ , and is vanishing on both the poles and the equator. As  $\varepsilon \rightarrow \varepsilon_c$ ,  $\langle T_\phi^t \rangle$  develops a broad, large maxima close to the equator, and for the second soliton branch, it becomes entirely positive. The component  $\langle T_\theta^\theta \rangle$ , measuring the pressure along  $\theta$ , is positive and peaked at the equator for small values of  $\varepsilon$ . As the amplitude is increased, the pressure becomes very

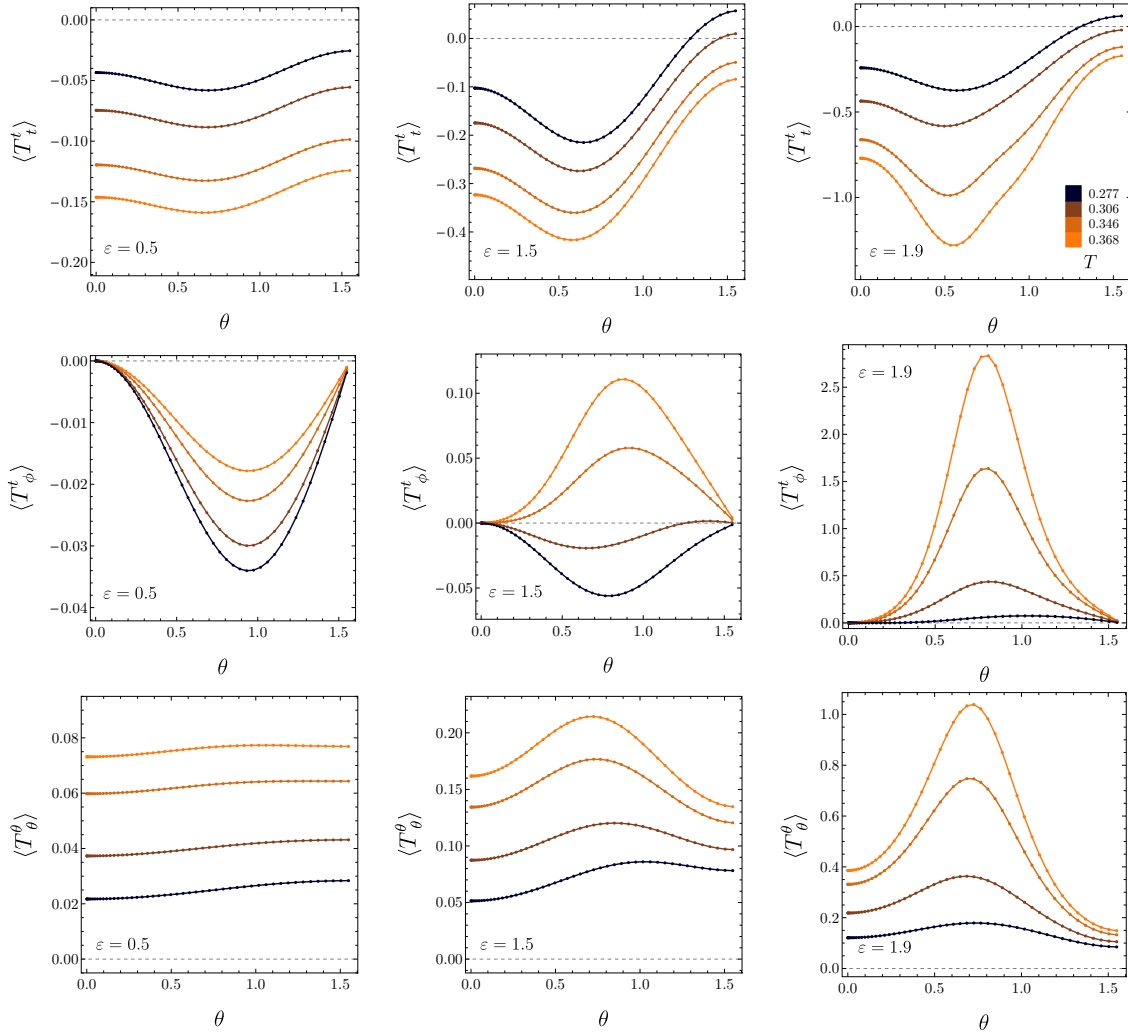


**Fig. 5.9** Independent stress-energy tensor components of the dual to the large black holes against  $\theta$ , for several values of the parameter  $\varepsilon$ . Colouring codes black hole temperature with darker colours representing temperatures closer to  $T_{\min}(\varepsilon)$ .

negative at the equator, increases towards the poles and develops a maxima close to  $\theta = \pi/4$ .

### 5.4.3.2 Black Holes

The independent holographic stress-energy tensor components for the black hole metric (5.6a) are given by

$$\begin{aligned} \langle T_t^t \rangle = & \frac{y_+}{49152\pi} \left[ 3y_+^2 \left( 635\delta^3 - 1533\delta^2 - 887\delta + 384q_1(\theta) - 263 \right) - 192 \left( 29\delta^2 - 14\delta + 17 \right) \right. \\ & + 16\varepsilon \sin^2 \theta \left\{ \sin^2 \theta \left( -12\varepsilon^3 \cos 4\theta + 72q_6(\theta)y_+^2 + \varepsilon \left( -1113\delta + 12\varepsilon^2 - 288y_+^2 + 2285 \right) \right) \right. \\ & \left. \left. - 72q_6(\theta)y_+^2 + 32\varepsilon \left( 27\delta + 9y_+^2 - 65 \right) \right\} \right], \end{aligned} \quad (5.23)$$

$$\langle T_\phi^t \rangle = \frac{y_+}{128\pi} \sin^2 \theta \cos \theta \left[ 4\varepsilon^3 \sin^4 \theta - 3q_6(\theta)y_+^2 + 12\varepsilon \left( 3\delta + y_+^2 - 5 \right) \right], \quad (5.24)$$

$$\begin{aligned} \langle T_\theta^\theta \rangle = & \frac{y_+}{49152\pi} \left[ 192 \left( 7\delta^2 + 26\delta - 17 \right) + 3y_+^2 \left( -109\delta^3 + 315\delta^2 + 721\delta + 384q_3(\theta) + 97 \right) - \right. \\ & \left. 16(33\delta + 139)\varepsilon^2 \sin^4 \theta - 1024\varepsilon^2 \sin^2 \theta \right]. \end{aligned} \quad (5.25)$$

Numerical results for several values of the black hole temperature and boundary rotation amplitude are presented in Fig. 5.9 (and for low temperatures see Appendix 5.B, Fig. 24). For small  $\varepsilon$  and large  $T$ ,  $\langle T_t^t \rangle$  is entirely negative. It is maximal at the equator and minimal at a value which depends on both  $\varepsilon$  and  $T$ , where it also attains its largest absolute value. If we fix  $T$  and increase  $\varepsilon$ , the energy density at the equator decreases, and becomes slightly negative. As expected, for a fixed boundary amplitude, the energy density is an increasing function of temperature.

The component  $\langle T_\phi^t \rangle$  is negative for small  $\varepsilon$  and temperatures close to  $T_{\min}(\varepsilon)$ , and vanishes at the poles and at the equator, similarly to the soliton case. Generally,  $\langle T_\phi^t \rangle$  is a complicated function of  $T$  and  $\varepsilon$ . For a fixed value of  $\varepsilon$ , it is an increasing function of temperature, and for large enough temperatures it becomes large and entirely positive. In particular, when  $\varepsilon \rightarrow 2$ , the density develops a large positive maxima peaked at  $\theta = \pi/4$ .

The anisotropic pressures capture some qualitative behaviour of the system. The normal stress component along  $\theta$  is positive for all  $\varepsilon$  and  $T$ , and for a fixed rotation amplitude is an increasing function of temperature. Furthermore, for a fixed tempera-

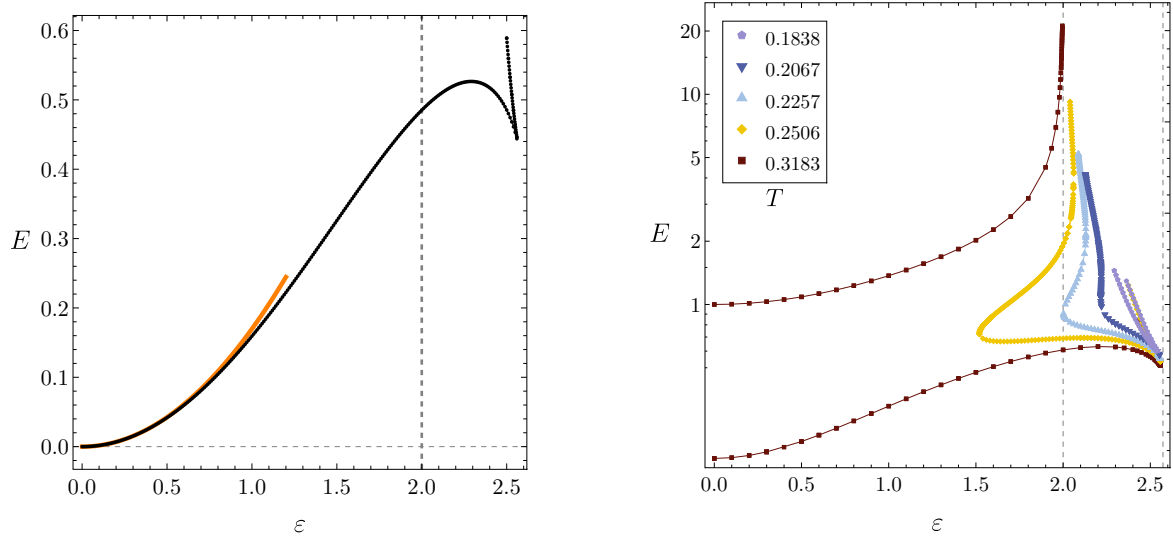


**Fig. 5.10** *Left:* Soliton solution boundary energy against rotation parameter. The dashed vertical gridline marks the critical amplitude  $\varepsilon = 2$ , and the bold orange line is the perturbative result. *Right:* Log-linear plot of the energy for the black hole solutions against  $\varepsilon$ , for several values of  $T$ .

ture, it is an increasing function of  $\varepsilon$ . In the large temperature, large  $\varepsilon$  regime,  $\langle T_\theta^\theta \rangle$  develops a broad positive maxima, peaked in the vicinity of  $\theta = \pi/4$ . The normal stress component in the direction of  $\phi$  (not pictured) can be negative around the equator, and in the large  $\varepsilon$ ,  $T$  regime, it is positive with a sharp dip to negative values at  $\theta = \pi/4$ .

## 5.4.4 Thermodynamics

### 5.4.4.1 Energy

We obtain conserved charges in the usual way by integrating the angular momentum and energy densities [203]. We note that by construction,  $\varepsilon = 0$  solutions take the Schwarzschild-AdS<sub>4</sub> values,  $T = (1 + 3y_+^2)/(4\pi y_+)$ ,  $S = \pi y_+^2$ ,  $M = y_+(1 + y_+^2)/2$  and  $G = y_+(1 - y_+^2)/4$ , discussed below.

The total angular momentum is identically zero, because the upper spacetime hemisphere is rotating in the opposite direction to the lower hemisphere. We present

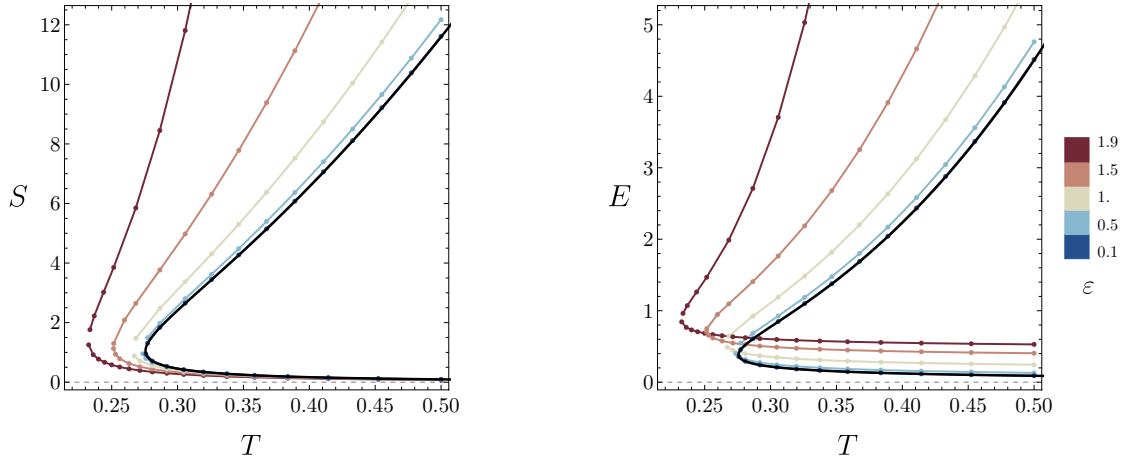


**Fig. 5.11** *Left:* Black hole entropy against temperature for several values of the boundary rotation parameter  $\varepsilon$ , for  $\varepsilon < 2$ . The upper branches correspond to the large solutions and the lower branches to the small solutions. *Right:* Black hole energy as a function of temperature. Colouring codes the value of the boundary amplitude. The bold black curve is the Schwarzschild-AdS<sub>4</sub> solution with  $\varepsilon = 0$ .

the energy<sup>8</sup> for black holes as a function of  $\varepsilon$  and  $T$  on the right panels of Fig. 5.10 and Fig. 5.11, respectively. For a fixed  $\varepsilon$  and varying  $T$ , the large black holes increase their energy, and the small black holes decrease it, asymptotically approaching  $E \rightarrow 0$ . Further, for a fixed  $T$  and increasing  $\varepsilon$ , the large black hole energy increases monotonically, as does the small black hole energy for  $\varepsilon < 2$ , which is the opposite behaviour to that of the entropy (see left panel of Fig. 5.11).

For values  $2 < \varepsilon < \varepsilon_{\max}(T)$ , where  $\max(T)$  was identified in the discussion of Fig. 5.6 and Fig. 5.7, the solution space has extra phases associated with cold temperatures. As we lower the temperature, the black hole energy approaches  $\varepsilon = 2$  from above, but unlike entropy, it appears to blow up for both small and large solution branches. As we lower  $T$  further, black holes eventually exist only for  $\varepsilon > 2$ , and the two branches appear to have similar values of energy.

The holographic energy for the soliton is presented on the left panel of Fig. 5.10. With increasing boundary parameter  $\varepsilon$ , the energy is increasing until it peaks at  $\varepsilon \simeq 2.29$  with maximum energy  $E_{\max} \simeq 0.527$  for the small branch. The large branch has larger energy, which increases steeply when  $\varepsilon \rightarrow 2^+$ . We constructed these solutions

<sup>8</sup>We note that strictly speaking the quantity that we are computing is not an energy, since  $\partial_t$  is changing as we change  $\varepsilon$ . A better defined quantity would be  $\Delta E \equiv E_{\text{black hole}} - E_{\text{soliton}}$ , which could have been regarded as the energy above the vacuum for each value of  $\varepsilon$ .

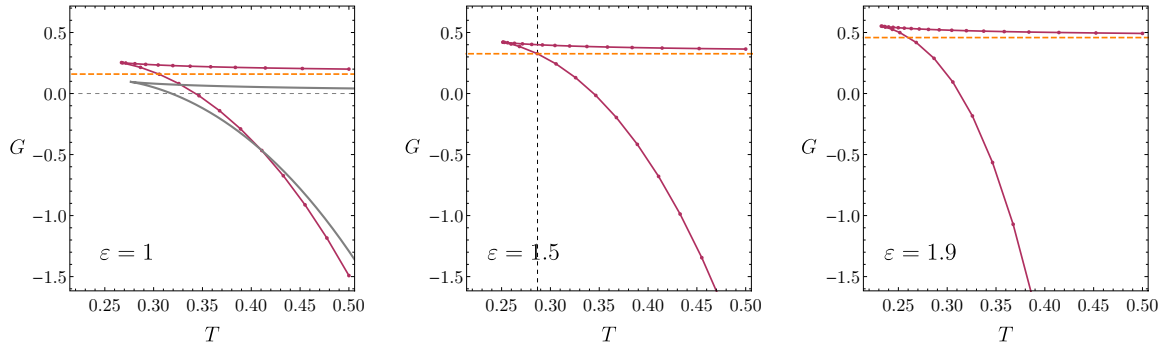


**Fig. 5.12** *Left*: Gibbs free energy for the black holes against temperature for a fixed boundary rotation parameter  $\varepsilon = 1$  (red data points). The orange gridline shows the value for the corresponding AdS<sub>4</sub> soliton with the same  $\varepsilon$ . The grey solid curve traces the values of Schwarzschild-AdS<sub>4</sub>, and the grey-dashed gridline shows  $G_{\text{AdS}} = 0$ . *Middle*: Similar plot for  $\varepsilon = 1.5$ , with the horizontal gridline marking the intersection temperature  $T_{\text{HP}}(\varepsilon)$ . To the right of this line the large black holes will be the dominant solutions, whilst solitons dominate to the left. *Right*: As we approach the critical value of  $\varepsilon$ , the phase transition temperature decreases.

numerically up to  $\varepsilon = 2.3$ , however numerical errors in this region of the parameter space become increasingly large.

#### 5.4.4.2 Grand-canonical ensemble

Because we can fix the boundary chemical potential and temperature  $T$ , the appropriate thermodynamic ensemble for analysing our solutions is the grand-canonical ensemble. In this ensemble the preferred phase minimises the Gibbs free energy

$$G = E - TS. \quad (5.26)$$

Note that in this system the energy,  $E$ , absorbs the chemical potential term, and in particular for solitons we have  $G = E$ . This is further supported by the first law of thermodynamics for these solutions, derived following [204–206], and given by

$$dE = T dS + 4\pi \int_0^{\pi/2} d\Omega(\theta) j(\theta) \sin \theta d\theta, \quad (5.27)$$

where  $\Omega(\theta) = \varepsilon \cos \theta$  is the boundary angular velocity density, and  $j(\theta)$  is the angular momentum density. In order to check the first law we constructed soliton solutions

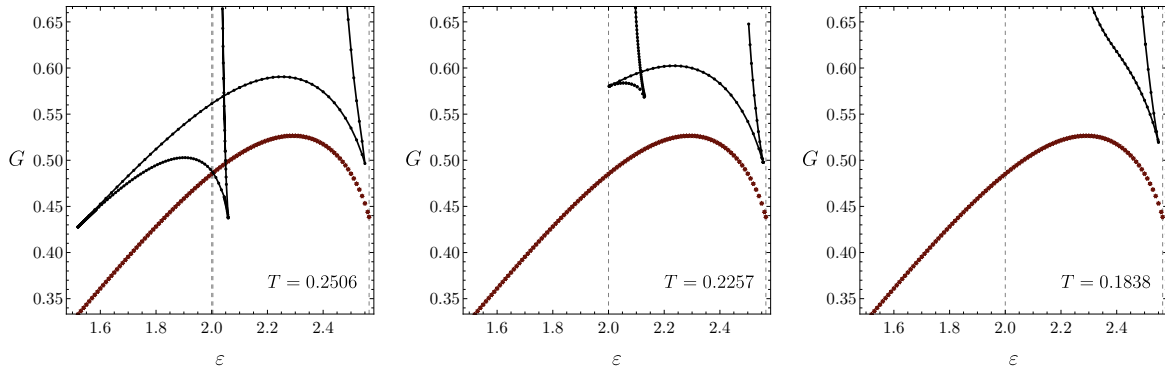


**Fig. 5.13** Gibbs free energy against the boundary parameter for low temperature black holes. It exhibits a swallowtail phase transition between the inelastic black hole phase and the soliton (brown stars).

perturbatively to second order, the procedure for which is detailed in Appendix 5.C. We use the second order expansion to calculate the boundary free energy to be  $E = 8\varepsilon^2/(15\pi)$ , which matches our numerical solutions to small  $\varepsilon$  amplitude (see left panel of Fig. 5.10) and satisfies the first law (5.27) to first order in  $\varepsilon$ . Numerically, the first law is satisfied to at least to 0.1% for the small soliton branch, to 2% for the large branch, and to 0.1% for the black holes (with 2% for the second set of the small black holes), while varying  $\varepsilon$ . For black holes<sup>9</sup> it is also satisfied to 0.1%, while varying temperature and keeping the boundary profile fixed.

We next discuss our results in terms of free energy. In Fig. 5.12, we present  $G$  for the black hole solutions as a function of the temperature for some values of the rotation amplitude. For a fixed  $\varepsilon$ , the corresponding soliton energy (see Fig. 5.10) is constant, which is pictured as a line. The intersection of the two marks the generalised Hawking-Page transition [123]<sup>10</sup>, and the transition temperature  $T_{\text{HP}}(\varepsilon)$  is a decreasing function of  $\varepsilon$ . For temperatures higher than the transition value, the large black hole phase is the dominant one, whilst for  $T < T_{\text{HP}}(\varepsilon)$  the soliton is the preferred phase.

For  $T < T_{\text{HP}}^{\text{Schw}} = 1/\pi$ , we observe curious phase transitions in  $G$ , characterised by a “swallowtail” behaviour in the Gibbs free energy [131, 207] (Fig. 5.13). This occurs because large black holes start to exist past  $\varepsilon = 2$ , where there is a turning point in the parameter space resulting in a four-fold non-uniqueness, and thus there exists a moduli space for which we have four possible black hole phases (and two soliton

<sup>9</sup>Large black holes, and small black holes up to the turning point in the parameter space.

<sup>10</sup>The Hawking-Page transition occurs for  $\varepsilon = 0$  and  $T = 1/\pi$  (see the left panel of Fig. 5.12).

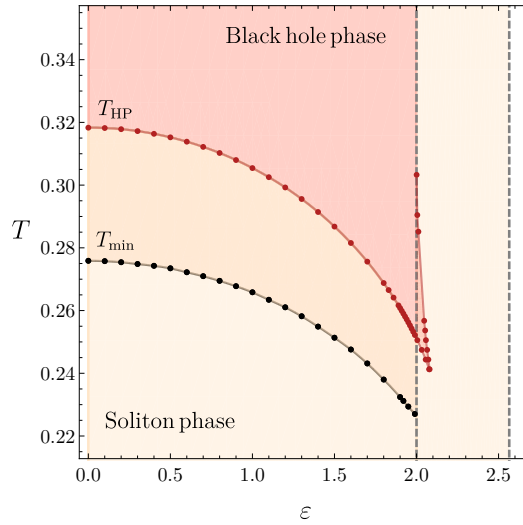


**Fig. 5.14** Phase diagram for the rotationally polarised solutions. For  $\varepsilon < 2$ , black holes exist above  $T_{\text{min}}(\varepsilon)$  (black data points) and are the dominant phase above the  $T_{\text{HP}}(\varepsilon)$  curve (red area) which marks the corresponding Hawking-Page transition. Below the transition line (red data points), the dominant phase is the soliton. For  $\varepsilon > 2$ , there is a cold inelastic black hole phase (red wedge). The elsewhere subdominant black holes exist up to some maximum  $\varepsilon_{\text{max}}(T)$ , but are hidden by the soliton phase.

phases). We find that for  $0.24 < T < 1/\pi$ , there is a temperature dependent interval  $\varepsilon_{\text{HP}}(T) < \varepsilon < \varepsilon_*(T)$  with  $\varepsilon_*(T) > 2$ , where the cold, inelastic black holes dominate the ensemble. Finally, we note that the small black hole branch is never favoured thermodynamically, as it always has higher free energy than both the large black hole and the soliton. The corresponding phase diagram is illustrated in Fig. 5.14. We also present  $G$  as a function of  $\varepsilon$  for a fixed temperature in Appendix 5.B (see the left panel of Fig. 23).

## 5.5 Stability

### 5.5.1 Quasinormal modes

To investigate the stability, we consider a wave equation for a neutral, minimally coupled scalar field

$$\square\Phi = 0. \quad (5.28)$$

Since both solitons and black holes have two commuting Killing fields,  $\partial_t$  and  $\partial_\phi$ , we can decompose the perturbations as follows

$$\Phi = \widehat{\Phi}_{\omega,m}(x,y)e^{-i\omega t + im\phi}.$$

The resulting equation for  $\widehat{\Phi}_{\omega,m}$  is linear and can be regarded as a Sturm-Liouville problem for the eigenpair  $\{\widehat{\Phi}_{\omega,m}, \omega\}$ , once suitable boundary conditions are imposed. The set of all  $\omega$  are called the quasinormal mode (QNM) frequencies. For each value of  $m$ , there is an infinite number of QNM frequencies labelled by two integers. These are in one to one correspondence with the number of nodes along the  $x$  and  $y$  directions. If  $\varepsilon = 0$ , we can use the background spherical symmetry to decompose the angular part in terms of spherical harmonics. These are labeled by  $\ell$  and  $m$ , with  $\ell - |m|$  counting the number of nodes along the polar angular direction. We will be interested in following the modes with  $\ell = |m|$  as a function of  $\varepsilon$ , that is to say, modes with no nodes along the polar direction. Furthermore, we will also be focusing on the modes which have no nodes along the radial direction, *i.e.* with zero overtone. We focus on these modes since they have the largest  $|\text{Im}(\omega)|$  for fixed  $m$ .

We follow the method of [50, 49, 27] and solve the resulting eigenvalue equation system using a Newton-Raphson method, on a fixed numerical solution background with a corresponding numerical grid.

The QNM spectrum with  $\varepsilon = 0$  is well-known: the Schwarzschild  $\text{AdS}_4$  black hole QNM frequencies are given in [208], and the scalar normal mode frequencies of  $\text{AdS}_4$  are given by integers  $L\omega = 3 + \ell$ . As we vary the boundary rotation parameter, the imaginary part of the black hole frequency  $\omega$  becomes positive, indicating the presence of an instability.

The boundary conditions imposed at  $y = 0$  will depend strongly on the background solution we wish to perturb.

### 5.5.1.1 Soliton

We first investigate scalar perturbations (5.28) on soliton backgrounds, and consider the following decomposition

$$\Phi(t, x, y, \phi) = e^{-i\omega t} e^{im\phi} y^{|m|} (1 - y^2)^3 (1 - x^2)^{|m|} \psi(x, y), \quad (5.29)$$

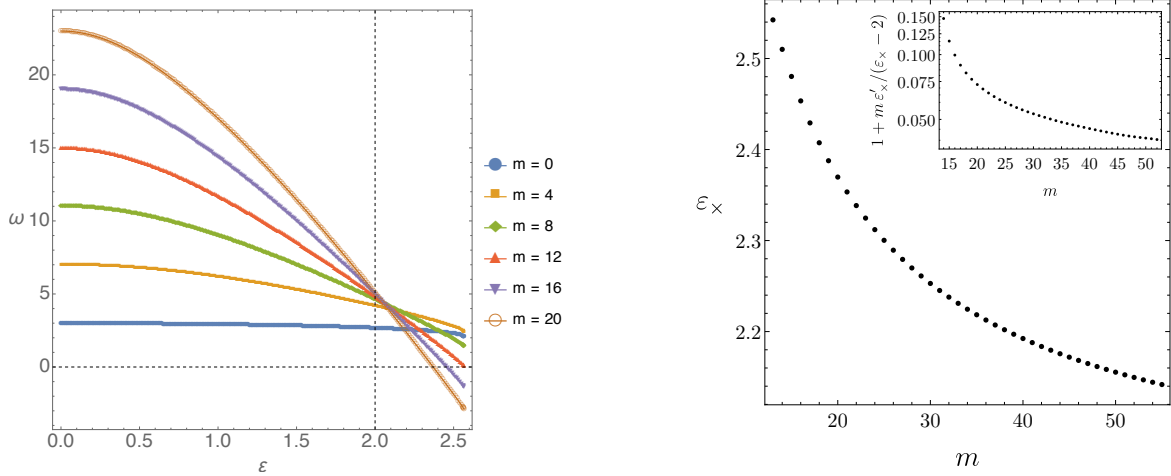


**Fig. 5.15** *Left:* Normal mode frequencies  $\omega$  with  $\ell = m$  vs the boundary rotation parameter  $\varepsilon$  for the soliton metric. At  $\varepsilon = 0$  these reduce to the usual AdS<sub>4</sub> frequencies  $L\omega = 3 + \ell$ . Dashed gridlines show where  $\varepsilon = 2$  (vertical) and  $\text{Re}\omega = 0$  (horizontal). *Right:* Rotation amplitude  $\varepsilon_x$ , where  $\omega$  becomes negative, against  $m$ . The inset shows the logarithmic derivative of  $\varepsilon_x$ . We expect that in the limit  $m \rightarrow \infty$ ,  $\varepsilon_x \rightarrow 2$ .

where the factorisation ensures regularity at the origin for a smooth function  $\psi(x, y)$ . The boundary conditions at  $y = 1$  and  $x = 1$  are obtained by solving the equation (5.28) at the corresponding boundaries and are given by

$$|m| \psi(x, y) + \partial_y \psi(x, y) = 0 \quad \text{at} \quad y = 1, \quad (5.30a)$$

and

$$\partial_x \psi(x, y) = 0 \quad \text{at} \quad x = 1. \quad (5.30b)$$

We also require  $\partial_x \psi(x, y) = 0$  at  $x = -1$  and  $\partial_y \psi(x, y) = 0$  at  $y = 0$ .

On the left panel of Fig. 5.15, we plot the normal mode frequencies  $\omega$  with  $\ell = m$ , against  $\varepsilon$ . The  $\omega$  first becomes negative when  $m = 13$ , and with each subsequent mode,  $\omega$  becomes negative at a lower value of  $\varepsilon$ . We denote the value at which  $\omega$  changes sign by  $\varepsilon_x$ , and we find that  $\varepsilon_x - 2 \sim 1/m$  at large  $m$ <sup>11</sup> (see right panel of Fig. 5.15).

In order to better resolve where  $\omega$  becomes negative for a given  $m$ , we can also set  $\omega = 0$  and look for zero-modes directly, and the results for this approach are presented in Fig. 5.15, right. We find that this method gives us the same values of  $\varepsilon_x$  as the ones

<sup>11</sup>Higher modes are more difficult to obtain numerically, and thus are less reliable, however, we find that the scalar eigenfunctions for these solutions have good convergence properties. For instance, we observe the variation with the grid size in a mode with  $m = 40$ ,  $\varepsilon = 2.5$  to be less than  $10^{-7}$ .

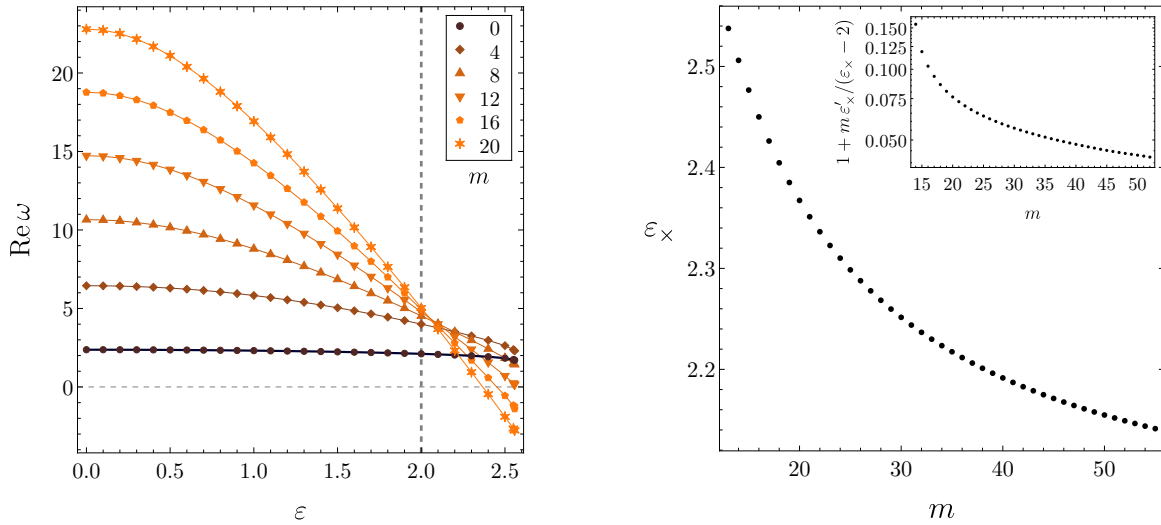


**Fig. 5.16** *Left:* Real part of quasinormal mode frequency with  $\ell = m$  against the boundary rotation parameter  $\varepsilon$ , for small black holes with  $T = 1/\pi$ . At  $\varepsilon = 0$ , these reduce to the Schwarzschild-AdS<sub>4</sub> values. The bold dashed gridline shows the critical  $\varepsilon = 2$  value. *Right:* Rotation amplitude where the zero-mode is for a given  $m$ , against  $m$ . The inset shows the logarithmic derivative of  $\varepsilon_x$ . We expect that in the limit  $m \rightarrow \infty$ ,  $\varepsilon_x \rightarrow 2$ .

inferred from computing  $\omega$  directly. For each pair of values of  $\{m, \varepsilon_x\}$ , we expect a given hairy family with nontrivial  $\Phi$  to condensate. Whether this new family of hairy solutions will extend to large or small values of  $\varepsilon$ , is likely to depend on the model. We have constructed soliton solutions with complex scalar hair within cohomogeneity two, and will present these solutions elsewhere. These were built by minimally coupling a massless complex scalar field to gravity, and are similar in spirit to the black holes with a single Killing field of [48] and to the holographic Q-lattices of [209].

### 5.5.1.2 Black hole

Next, we consider the black hole solutions. A Frobenius analysis at the integration boundaries motivates the following separation ansatz

$$\Phi(t, x, y, \phi) = e^{-i\omega t} e^{im\phi} y^{-i \frac{2\omega y_+}{1+3y_+^2}} (1-y^2)^3 (1-x^2)^{|m|} \psi(x, y), \quad (5.31)$$

where we have implicitly imposed regularity in ingoing Eddington-Finkelstein coordinates [208].

The boundary conditions for  $\psi(x, y)$  at  $y = 1$  and  $x = 1$  are then found by solving (5.28) and demanding that  $\psi(x, y)$  has a regular Taylor expansion at  $y = 1$  and  $x = 1$ . This in turn gives:

$$-2i y_+ \omega \psi(x, y) + (1 + 3y_+^2) \partial_y \psi(x, y) = 0 \quad \text{at } y = 1, \quad (5.32a)$$

and

$$\partial_x \psi(x, y) = 0 \quad \text{at } x = 1. \quad (5.32b)$$

As with the soliton, we require  $\partial_x \psi(x, y) = 0$  at  $x = -1$  and  $\partial_y \psi(x, y) = 0$  at  $y = 0$ .

Numerical results are presented in Fig. 5.16. On the left panel, we plot the real part of the QNM frequencies with  $\ell = m$  against  $\varepsilon$ , for a fixed  $T = 1/\pi$  small black hole branch. We find that the behaviour of  $\text{Re} \omega$  is very similar to that of the soliton, and the first unstable mode appears at  $m = 13$ . The imaginary part,  $\text{Im} \omega$ , becomes positive exactly where  $\text{Re} \omega$  crosses the zero axis, indicating a zero-mode. If we set  $\omega = 0$  and look for these directly, we again find a  $1/m$  fall-off (see right panel of Fig. 5.16) at large  $m$ . The growth rate of the instability is less than  $\Gamma \sim 10^{-20}$ , so it sets in incredibly slowly<sup>12</sup>. We expect that these solutions will become unstable in modes with high  $m$  as we increase the boundary rotation past  $\varepsilon = 2$  and, if we assume the  $1/m$  decay, the instability should manifest itself slowly with increasing  $\varepsilon$ . Finally, for hot, large black holes we do not see any sign of instability, as these solutions never cross  $\varepsilon = 2$ .

The ergoregion induces hairy solutions in both phases, and this opens up new possibilities for the phase diagram, some of which we will discuss in the following sections. This section was devoted entirely to the stability analysis of scalar perturbations, and the issue of the stability of our backgrounds with respect to gravitational perturbations is an open problem. However, if we assume that the physics involved in this instability is any similar to the usual superradiance instability, we expect the gravitational perturbations to be unstable and to have larger instability growth rates.

---

<sup>12</sup>We believe that the rate will increase for low temperatures, but these backgrounds require very high resolutions.

## 5.6 Field Theory

We can obtain insight to the dual field theory by considering a conformally coupled scalar field satisfying the Klein-Gordon equation on  $\mathbb{R}_t \times S^2$ . The idea is to determine the eigenfunctions on this background, and use those to determine the spectrum of a conformally coupled scalar on the rotating background (5.2). This calculation closely follows the one presented in [210] for the free charged scalar field on the two-sphere with the dipolar potential.

If  $\varepsilon = 0$ , the Klein-Gordon equation for a conformally coupled scalar in 1 + 2 reads (where we set the radius of the  $S^2$  to unity):

$$-\frac{\partial^2}{\partial t^2}\varphi + \nabla_{S^2}^2\varphi = \frac{1}{4}\varphi. \quad (5.33)$$

The Hamiltonian eigenstates are given by spherical harmonics  $|\ell, m\rangle$ , with wavefunctions<sup>13</sup>

$$\langle\theta, \phi|\ell, m\rangle = Y_{\ell m}(\theta, \phi). \quad (5.34)$$

In this basis, the Hamiltonian  $\hat{H} = i\partial/\partial t$  has the following spectrum

$$\hat{H}|\ell, m\rangle = \left(\ell + \frac{1}{2}\right)|\ell, m\rangle. \quad (5.35)$$

After turning on the rotation, the Hamiltonian is deformed into

$$H = \sqrt{\frac{1}{4} - \nabla_{S^2}^2 + \frac{\varepsilon^2}{16}\sin^4\theta} + i\varepsilon\cos\theta\frac{\partial}{\partial\phi}. \quad (5.36)$$

Since  $H$  commutes with  $\partial/\partial\phi$ , it will remain diagonal in the azimuthal quantum number  $m$ . However, it is no longer diagonal in  $\ell$ , and its elements have to be

---

<sup>13</sup>Note that Spherical harmonics are normalised such that  $\int_0^{2\pi} d\phi \int_0^\pi d\theta \sin\theta |Y_{\ell m}(\theta, \phi)|^2 = 1$ , for all  $\ell$  and  $|m| \leq \ell$ .

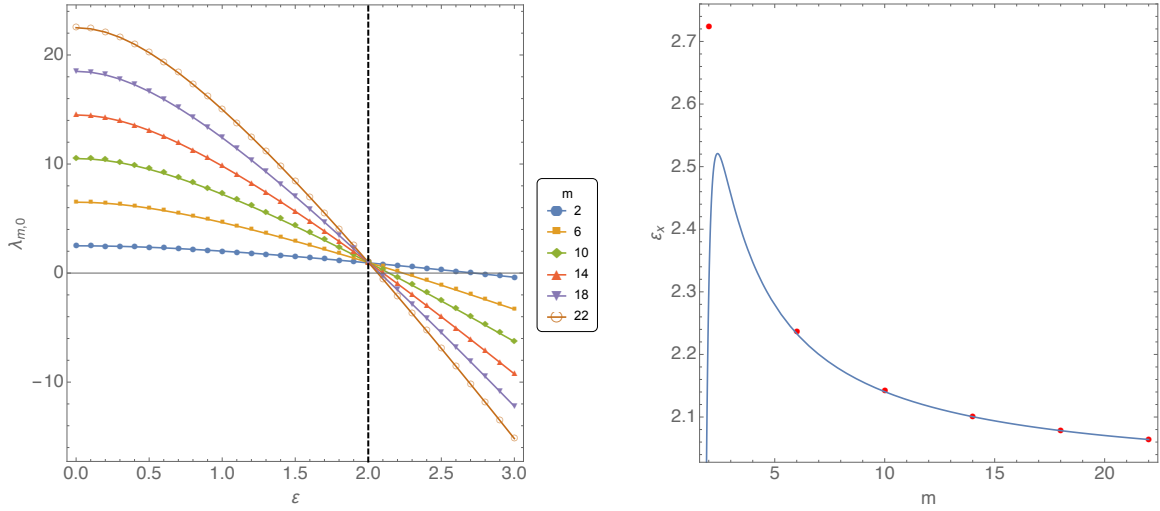


**Fig. 5.17** *Left:* Lowest lying mode eigenvalue of the boundary hamiltonian as a function of the boundary rotation parameter  $\epsilon$ . At  $\epsilon = 0$  these reduce to  $\ell + 1/2$ . *Right:*  $\epsilon$  above which  $\lambda_{m,0}$  becomes negative, plotted as a function of  $m$ . The solid line represents our analytic approximation (5.38) valid at large  $m$ .

computed numerically:

$$\langle \ell' m' | H | \ell m \rangle = \delta_{m,m'} \left\{ \int_0^{2\pi} d\varphi \int_0^\pi d\theta \sin\theta \bar{Y}_{\ell' m} \sqrt{\ell \left( \ell + \frac{1}{2} \right) + \frac{\epsilon^2}{16} \sin^4 \theta} Y_{\ell m} - m \epsilon \left[ \delta_{\ell, \ell'-1} \sqrt{\frac{(\ell+1+m)(\ell+1-m)}{(2\ell+1)(2\ell+3)}} + (\ell \leftrightarrow \ell') \right] \right\}. \quad (5.37)$$

For each value of  $m$ , we can truncate the values of  $\ell$  and  $\ell'$  up to some maximum value  $\ell_{\max}$  and determine the eigenvalues numerically. One can show that if we are only interested in a few low lying modes, the convergence is exponential in  $\ell_{\max}$ . The results are illustrated in Fig. 5.17 where we plot the lowest lying eigenvalue of  $\langle \ell' m | H | \ell m \rangle$ , which we denote by  $\lambda_{m,0}$ , for several values of  $m = 2, 6, 10, 14$ . The similarity between the left panel of Fig. 5.15 and the left panel of Fig. 5.17 is striking.

One can go further and compute the critical value of  $\epsilon$  above which  $\lambda_{m,0}$  becomes negative, and compare it with the right panel of Fig. 5.15. We call this special value  $\epsilon$   $\epsilon_x$ , in accordance to section 5.5. In the large  $m$  limit, the Hamiltonian can be diagonalised using a WKB approximation, and can be used to determine  $\epsilon_x$ . We have

performed this calculation to order  $m^{-12}$ , and it turns out that

$$\begin{aligned} \varepsilon_{\times} = & 2 + \frac{\sqrt{2}}{m} - \frac{3}{32m^2} + \frac{1}{32\sqrt{2}m^3} - \frac{85}{2048m^4} - \frac{5427}{32768\sqrt{2}m^5} - \frac{132879}{524288m^6} - \frac{8720967}{8388608\sqrt{2}m^7} \\ & - \frac{322048277}{134217728m^8} - \frac{109314890677}{8589934592\sqrt{2}m^9} - \frac{5202962510427}{137438953472m^{10}} - \frac{550282627773161}{2199023255552\sqrt{2}m^{11}} \\ & - \frac{32005862571264331}{35184372088832m^{12}} + \mathcal{O}(m^{-13}). \end{aligned} \quad (5.38)$$

The validity of this approximation is tested on the right panel of Fig. 5.17, where we can see that for  $m \geq 10$ , the error is below 0.1% and for  $m \geq 22$  it is below 0.02%.

## 5.7 Equilibrium of spinning test particles

The spacetimes we consider are stationary, however, the black hole solution has zero angular velocity on the horizon, and vanishing total angular momentum. If we place a small Kerr hole on the axis of symmetry, there will be a general relativistic “spin–spin” force acting on the spinning black hole, which for stationary fields can be thought of as analogous to the electromagnetic “dipole–dipole” force with opposite sign [211–213]. In this section, we will investigate whether it is possible to have a spinning test particle hovering above the central black hole, balanced by the pull towards the black hole and the “spin–spin” interaction with the boundary.

Equilibria of spinning test particles can be studied using the Mathisson-Papapetrou (MP) equations [214–220] (for a review see [221]), which are derived by taking a multipole expansion about a suitably defined reference worldline. Truncated at dipole order, they are given by

$$\begin{aligned} \frac{Dp^\mu}{Ds} &= -\frac{1}{2}R^\mu{}_{\nu\rho\sigma}v^\nu S^{\rho\sigma}, \\ \frac{DS^{\mu\nu}}{Ds} &= p^\mu v^\nu - p^\nu v^\mu, \end{aligned} \quad (5.39)$$

where  $p^\mu$  is the four-momentum of the particle, which in general is not co-linear with the kinematic four-velocity  $v^\mu$ . They are related by  $p^\mu = mu^\mu - u_\nu \dot{S}^{\mu\nu}$ , where  $S^{\mu\nu}$  is the anti-symmetric spin matrix and  $m$  is a mass parameter<sup>14</sup>. We also require a supplementary spin condition to fix the center of mass, which we choose to be the

<sup>14</sup>Here the dot is differentiation with respect to the proper time.

Tulczyjew-Dixon condition<sup>15</sup>  $p_\nu S^{\mu\nu} = 0$ . On the rotation axis, it is equivalent to the Mathisson-Pirani condition.

We will be concerned with the static case, thus setting  $\dot{S}^{\mu\nu} = 0$  and  $\dot{p}^\mu = 0$ . This implies  $m = M$  and  $p^\mu = Mu^\mu$ , where  $M$  is the rest mass of the particle  $-M^2 = p_\mu p^\mu$ . Together with the spin magnitude, defined as  $S^2 = S_{\mu\nu} S^{\mu\nu}/2$ , these are constant throughout the motion. These conditions, in conjunction with the MP equations (5.39), are sufficient to determine the static ratio  $S/M$  as a function of the radial coordinate. Equivalently, we can instead consider a conserved quantity which includes the spin potential energy

$$E = -p^\rho \xi_\rho + \frac{1}{2} \xi_{\rho;\sigma} S^{\rho\sigma}, \quad (5.40)$$

where  $\xi = \partial_t$  is the time Killing vector field, and  $E > 0$  is the energy at infinity of a spinning particle. The first term is conserved for a non-spinning particle, and is positive when the Killing vector is future directed and timelike. Using the normalization  $-M^2 = p_\mu p^\mu$ , we can find an effective potential for radial on-axis motion of a spinning particle. In order to find equilibrium points, we look for local minima of the potential  $\dot{r}^2 + V(r) = 0$ , which constrains both the energy  $E$ , and the ratio  $S/M$ .

We calculate these quantities for the black hole metric (5.6a) and the soliton metric (5.4). Because our coordinates are not well-defined on the symmetry axis  $\theta = 0$ , we first perform a local coordinate change

$$1 - x^2 = x_1^2 + x_2^2, \quad \tan \phi = x_2/x_1, \quad (5.41)$$

and the symmetry axis is now given by  $x_1 = 0$  and  $x_2 = 0$ . The supplementary condition implies that the only non-vanishing component of the spin matrix is  $S^{x_1 x_2}$ , making the on-axis calculation considerably easier. The effective potential is then found to be

$$V(r) = (g_{rr} g_{tt})^{-1} \left[ g_{tt} + \left( \frac{E}{M} + \frac{S}{M} y^\alpha Q_6(1, y) \right)^2 \right], \quad (5.42)$$

where  $\alpha = 1$  for the soliton, and  $\alpha = 2$  for the black hole. The spin potential energy term depends on the metric ansatz, and in the expression (5.42) it is evaluated explicitly.

<sup>15</sup>This condition states that momentum is perpendicular to the covariant four-spin vector  $s = \star(S \wedge p)$ .

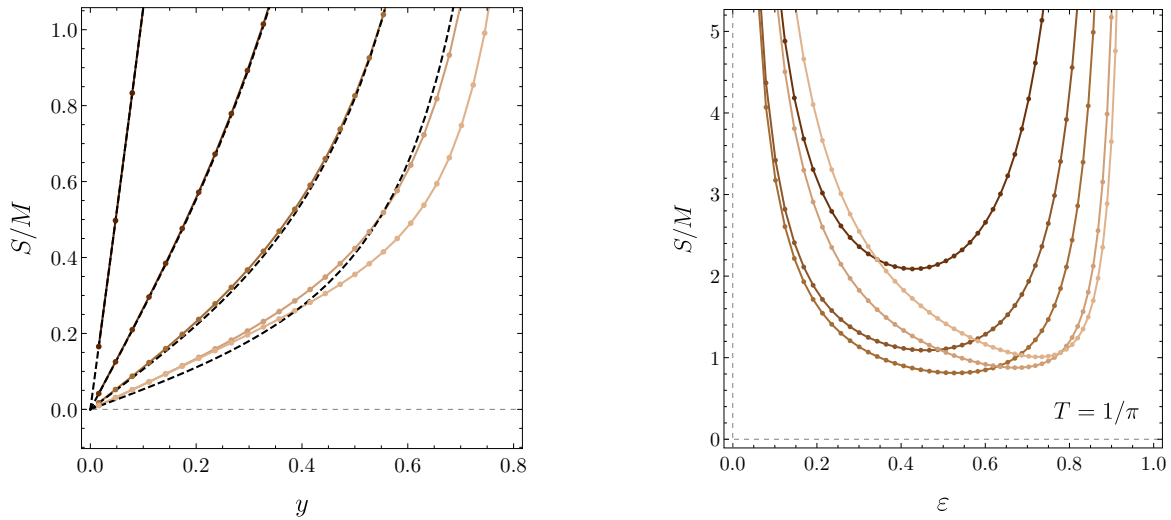


**Fig. 5.18** *Left*: Spin to mass ratio for a spinning test particle in the soliton background with boundary parameter  $\varepsilon = 0.1, 0.4, 1, 2, 2.5$  (corresponding colours vary from dark to light). Dashed black lines show analytic perturbative approximations (53) (pictured for  $\varepsilon \leq 2$ ) which, for small  $\varepsilon$ , are in a very good agreement with numerical solutions. *Right*: Spin to mass ratio for large black holes with  $T = 1/\pi$ , for  $\varepsilon = 0.1, 0.5, 1, 1.5, 1.93, 1.99$  (corresponding colours vary from dark to light).

The total energy of a spinning particle is

$$\frac{E}{M} = \sqrt{-g_{tt}} - \frac{S}{M} y^\alpha Q_6(1, y), \quad (5.43)$$

and the spin to mass ratio of a static spinning test particle on the symmetry axis is

$$\frac{S}{M} = \frac{-\partial_y g_{tt}(1, y)}{2y^{\alpha-1} \sqrt{-g_{tt}(1, y)} (2^{\alpha-1} Q_6(1, y) + y \partial_y Q_6(1, y))}. \quad (5.44)$$

Numerical results for both solutions are presented in Fig. 5.18. For the test body approximation, the Møller radius describing the minimum size of a rotating body is  $R \geq S/M$  [222], and it should be possible to make it arbitrarily small [211]. For the black holes, we do not find such a limiting process. For the soliton, this quantity vanishes as  $y \rightarrow 0$ , thus it is possible to place a spinning particle at this point, whose backreaction would lead to the formation of a small Kerr-AdS<sub>4</sub> black hole.

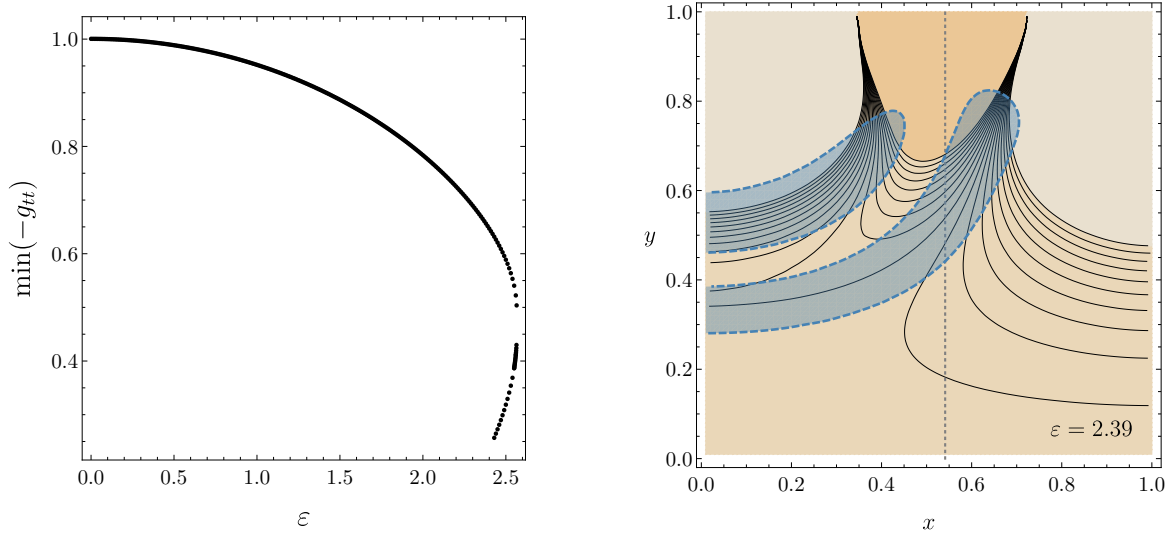


**Fig. 5.19** *Left*: Minima of static potential,  $-g_{tt}$ , for the soliton against the boundary parameter. For  $\varepsilon < 2$ , there is a global minima at  $y = 0$ . For  $\varepsilon > 2$ , the minima is only local, owing to the fact that there is an ergoregion attached to the boundary. For the second branch, the local minima is on the  $x = 0$  axis, and for  $\varepsilon \gtrsim 2.43$ , the minima is no longer local. *Right*: Contour plot for  $-g_{tt}$  for the second branch soliton, at  $\varepsilon = 2.39$ . Black lines mark the contours, with the orange area around  $\theta = \pi/4$  (black dashed gridline) showing the ergoregion, and the fainter orange being the positive areas, where the function increases rapidly. Overplotted in blue are the zero contours of the Kretschmann scalar,  $K$ , whilst the shaded areas are the two minima with a steep maxima between them.

### 5.7.1 Equilibrium of non-spinning test particles

For static spacetimes the equilibrium positions are independent of spin, and can be achieved by balancing electromagnetic and gravitational forces, or coincide with the static radius due to a repulsive cosmological constant  $\Lambda > 0$ . For Kerr black holes [223], it is well known that no equilibrium positions exist [211]. Generally, conditions for equilibrium on the rotation axis are independent of the spin of the test particle. From (5.44), we can see that the requirement  $S/M \rightarrow 0$  implies that the equilibrium conditions coincide with the minima of the static potential  $-g_{tt}$ .

The evolution of  $-g_{tt}$  with the boundary parameter is non-trivial, and is related to the changes in the Kretschmann scalar  $K$ . For the soliton with  $\varepsilon < 2$ , there is a global minima at  $y = 0$  (see the left panel of Fig. 5.19, and *c.f.* [224], Fig. 6). When  $\varepsilon \geq 2$ ,  $-g_{tt}$  becomes very negative near the boundary due to the ergoregion, and the central minima is then local. For the second branch, the minima moves up the equator towards

the boundary, and as  $\varepsilon \rightarrow 2$ , the minima is found closer to where  $K$  has the largest gradient. The ergosurface becomes visibly deformed towards the  $x = 0$  boundary, and the local minima eventually connects to the ergoregion at  $\varepsilon \gtrsim 2.43$  (see the right panel of Fig. 5.19).

For the large hot black hole solutions, the minima of  $-g_{tt}$  is on the horizon, tending to  $\theta = \pi/4$  as  $\varepsilon \rightarrow 2$ . The corresponding small branch has a turning point at  $\varepsilon > 2$ , where the entropy  $S \rightarrow 0$  (see the right panel of Fig. 5.6). The small black holes, for all temperatures, are similar to soliton solutions. When the black hole entropy is small,  $-g_{tt}$  looks very similar to the soliton (see the right panel of Fig. 5.19), but with the local minimum along the horizon.

Finally, we comment on the stability of the test particles. For the stable soliton branch ( $\varepsilon > 2$ ), the (spinning) particles can be put at the global minimum of the static potential, however, such solutions are not thermodynamically favoured. Let us place a small (rotating) black hole at the origin, approximated by a small Kerr black hole. If we parametrise the thermodynamic quantities by the outer horizon radius  $r_+$ , and temperature  $T$ , the entropy is given by

$$S = \frac{2\pi r_+^2}{4\pi r_+ T + 1}. \quad (5.45)$$

In the grand-canonical ensemble, at finite temperature  $T$  and fixed chemical potential  $\mu$ , we find that the change in the free energy is  $\delta G = ME + \mathcal{O}(r_+^2)$ , and thus adding (spinning) particles is not advantageous<sup>16</sup>. In order to achieve a preferred phase, we would like to have  $V_{\min} < 0$ , however, we find that the energy  $E/M$  is positive<sup>17</sup>. This is in agreement with the fact that the small black hole phase is always hidden by the soliton phase.

Once we cross  $\varepsilon = 2$ , any particle will eventually fall into the ergoregion near the boundary. Similarly, this should happen for the small black holes which exist past the critical value  $\varepsilon = 2$ .

It is interesting to contrast these results with a polarised black hole in global AdS<sub>4</sub> [210, 225]. In these papers, solutions with a dipolar chemical potential on the boundary are considered. For the black holes, they find static charged particle orbits, which

<sup>16</sup>In the probe limit  $r_+ \rightarrow 0$ .

<sup>17</sup>The ratio is also independent of the spin sign, which agrees with the sign of  $S$ .

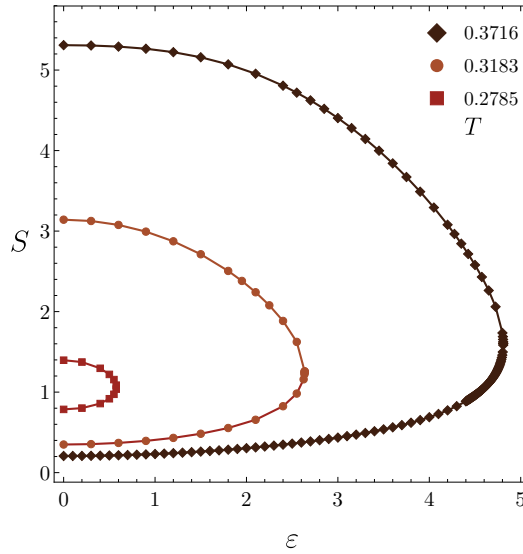


**Fig. 5.20** Entropy vs the boundary rotation parameter, when the metric is adjusted so that there is no ergoregion on the boundary. We observe two branches of black hole solutions which join up at some maximum value of  $\varepsilon$ .

could allow for multi-black hole solutions. In our scenario, we find that the purely gravitational on-axis “spin-spin” interaction is not sufficient to support stationary solutions with more than one black hole.

## 5.8 No Ergoregions

The instabilities that we observe in the rotationally polarised AdS<sub>4</sub> system are primarily due to the induced ergoregion. It is interesting to ask, whether we still see instabilities if we isolate the boundary interaction term in the metric, in such a way that it does not cause the ergoregion to form. We consider the adjustment to the line elements (5.4) and (5.6a), such that  $g_{tt}$  is always negative near the boundary, by choosing the reference metric in the DeTurck method to have  $Q_1(x, y) = 1 + \varepsilon^2 x^2 (1 - x^2)^2 (2 - x^2) y^2$ . In this case, at any given fixed temperature  $T > T_{\min}^{\text{Schw}} = \sqrt{3}/(2\pi)$ , we also find a maximum rotation amplitude past which we do not find stationary black hole solutions (see right panel of Fig. 5.20). As the system heats up, this value of  $\varepsilon$  appears to increase without a bound. We also find a soliton solution, which appears to exist for any value of the

rotation amplitude<sup>18</sup>. We have been able to reach  $\varepsilon = 32$ , and believe that the solution exists for any value of  $\varepsilon$ .

## 5.9 Conclusions

We have applied the gauge/gravity duality to investigate the behaviour of a strongly coupled field theory on a fixed rotating spacetime. Since our bulk field theory depends only on the metric, it lies in the universal sector of the AdS/CFT correspondence, and therefore we can expect our results to be relevant for a much wider class of theories which have a supergravity bulk dual description. In this chapter we focused on spacetimes for which the boundary is of the following form

$$ds_{\partial}^2 = -dt^2 + d\theta^2 + \sin^2\theta(d\phi + \varepsilon \cos\theta dt)^2,$$

and studied the behaviour of several one point functions, such as the expectation value of the stress energy tensor, for several values of  $\varepsilon$ . We have considered both the vacuum state and the thermal state for each value of  $\varepsilon$ . The holographic dual of the latter contains a black hole solution in the interior of the bulk spacetime, setting the temperature of the field theory [9].

We have seen that both the thermal and the vacuum states are non-unique; for a fixed angular boundary profile and fixed energy, more than one solution exists in the bulk. For boundary profiles containing ergoregions, we have observed a rather interesting behaviour. Specifically, singular black hole solutions exist, extending from the bulk all the way to the boundary, whenever the boundary profile has an evanescent ergosurface, *i.e.* when  $\partial/\partial t$  becomes null along the equator at the boundary, but is everywhere else timelike. Furthermore, we have given ample numerical evidence that above the particular value of  $\varepsilon = \varepsilon_c \simeq 2.565$ , no axially symmetric stationary bulk solution exists. This value is always larger than the critical value needed to generate hair. Finally, we provided a first principle derivation of the superradiant bound, *i.e.* we determined the minimum value of  $\varepsilon$  that causes our system to develop hair, purely from CFT data.

---

<sup>18</sup>The Kretschmann scalar exhibits a complicated structure, and for large  $\varepsilon$  has a slowly increasing central maximum, and two opposite sign extrema on the  $x = 0$ , approaching the boundary.

The most interesting question raised by our work remains to be explored. The system constructed in this chapter can be dynamically evolved in time, starting in the vacuum of the theory, *i.e.* pure global AdS<sub>4</sub>, and promoting  $\varepsilon$  to be a function of time. We provided numerical evidence that there are no axially symmetric and stationary solutions above the critical value  $\varepsilon_c$ , and thus the fate of the bulk solutions for values  $\varepsilon > \varepsilon_c$  is unclear. We also found that both the solitonic and the black hole phases can develop hair for  $\varepsilon > 2$ .

We conjecture possible behaviour of the nonlinear evolution of our system, which can be divided into two cases, depending on whether a bulk horizon forms. In the case with no horizon, the superradiant instability controls the dynamics, and the subsequent evolution proceeds as described in [48, 52, 54]. If the superradiance does not manifest quickly, we might observe the curvature growth in the bulk, *e.g.* as a power law in time, until the superradiant instability sets in and controls the dynamics. This scenario is very similar to the one presented in [226, 227]. If a bulk horizon forms, one scenario is that it becomes hot and expands all the way to the boundary, reaching the boundary in a finite amount of time. We anticipate that for this possibility, our class of boundary metrics does not admit a conventional formulation of positivity of energy. The endpoint of rotational superradiance is currently not known, however, there is a considerable amount of evidence that it leads to some form of violation of weak cosmic censorship.

There are several possible extensions of our work. We can study similar setups in supergravity truncations, which can be embedded into a full top-down model of AdS/CFT, such as ABJM [228]. Further, while some of what we describe might follow through to the higher-dimensional case, there are some important differences. For instance, for  $d > 4$ , the Gregory-Laflamme instability might also play a role, and manifest itself before the solutions become superradiantly unstable. However, such an instability is also likely to lead to a violation of the weak cosmic censorship conjecture [33, 229, 230]. In this sense, we expect the relevant physics to be easier to dissect in  $d = 4$ . It would be interesting to understand whether the behaviour we observe depends on the choice of the boundary rotation profile  $\Omega(\theta)$ . Certainly the shape of the bulk black hole would be different, however we anticipate that the once  $\partial_t$  becomes spacelike, there exists a critical amount of rotation past which no stationary solutions exist due to the ever present ergoregion.

Finally, soon after the work presented in this chapter was published, a similar setup was presented in [231]. In this paper the authors considered the Poincaré patch of  $\text{AdS}_4$  with a planar version of our boundary, and performed dynamical time evolution. They saw a scenario in which unbounded curvature growth is visible to an observer at infinity, and suggested that this case leads to a violation of the weak cosmic censorship conjecture. We look forward to further developments in this direction.

## 5.A Numerical validity

We chose our ansätze in such a way that all unknown functions are even about two of the grid edges, therefore, we can halve the Chebyshev grid while effectively interpolating over the full grid. This in turn allows us to use a smaller grid size to achieve a desired numerical accuracy.

Our spacetimes possess a  $(t, \phi) \rightarrow -(t, \phi)$  reflection symmetry, for which the Ricci solitons with  $\xi \neq 0$  have been ruled out [87]. We can thus monitor the norm of  $\xi$  to provide a global measure of our numerical integration scheme (see Appendix 5.A). We verified that our solutions satisfy  $\xi^\mu = 0$  to sufficient precision. In order to compute the stress energy tensor, adequate precision is required as we need to obtain third derivatives about the conformal boundary. We found that double precision was adequate thus significantly speeding up our computation. Nevertheless, we checked that the results converge as expected when the precision is increased.

We monitor convergence of our numerical method by computing the infinity norm of the DeTurck vector  $\|\xi\|_\infty$ , as well as relative errors of physical quantities of interest defined by  $\Delta_N G = |1 - G_{N+1}/G_N|$ , where  $G_N$  denotes the quantity computed with  $N$  grid points on each integration domain. This provides a good check of the numerics, as well as a measure of the error. We present convergence results for free energy in Fig. 21 which, in this work, is the physical quantity which exhibits the largest error. As  $\varepsilon$  increases, the grid size has to be increased accordingly to maintain satisfactory error and typically a  $60 \times 60$  to  $100 \times 100$  grid was used. For the *dominant* soliton branch,  $\|\xi\|_\infty^2$  is never above  $10^{-10}$  and errors in quantities never above 0.01%. For the *large* branch,  $\|\xi\|_\infty^2 < 10^{-7}$ , and the errors are below 1%. For the *large* black holes, we keep  $\|\xi\|_\infty^2 < 10^{-9}$  and  $\Delta_N G < 0.01\%$ , and for the *small* branch,  $10^{-7}$  and

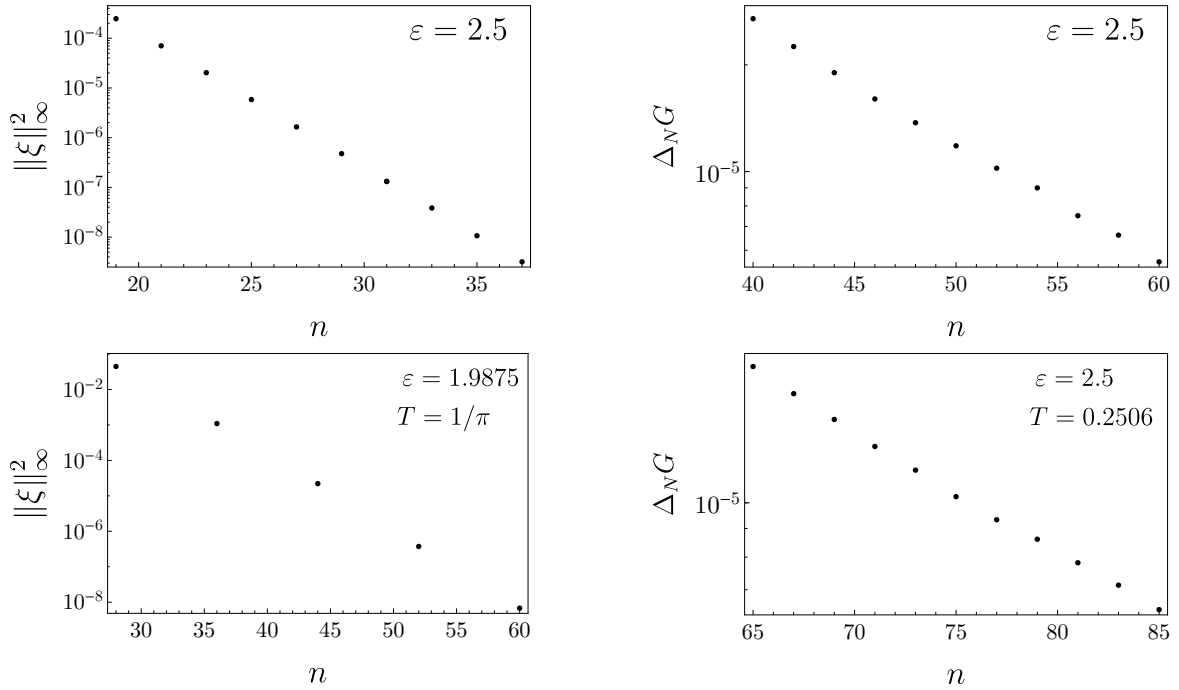


**Fig. 21** *Top left:* Log-linear plot of the DeTurck norm squared for the dominating soliton branch, at  $\varepsilon = 2.5$ . Straight line indicates exponential convergence. *Top right:* Log-linear plot of the relative error in the free energy  $G$  vs the grid size  $n$ , for the same data set as top left. *Bottom left:* Log-linear plot of the DeTurck norm squared vs grid size for a large black hole with  $T = 1/\pi$  and  $\varepsilon = 1.9875$ . *Bottom right:* Log-linear plot of  $\Delta_N G$  against  $n$ , for a cold ( $T = 0.2506$ ), small black hole, upper small branch ( $\varepsilon = 2.5$ ).

1% respectively. Generally, we found that errors increase with both increasing and decreasing the temperature.

For analytic functions, we expect the pseudospectral methods to offer exponential convergence with an increasing grid size. However, we cannot attain these rates of convergence if the error drops below the machine precision. The error settles to an exponential decay until it starts to pivot around the machine error, and this interval is shown in Fig. 21. In order to improve convergence it is then necessary to increase numerical precision.

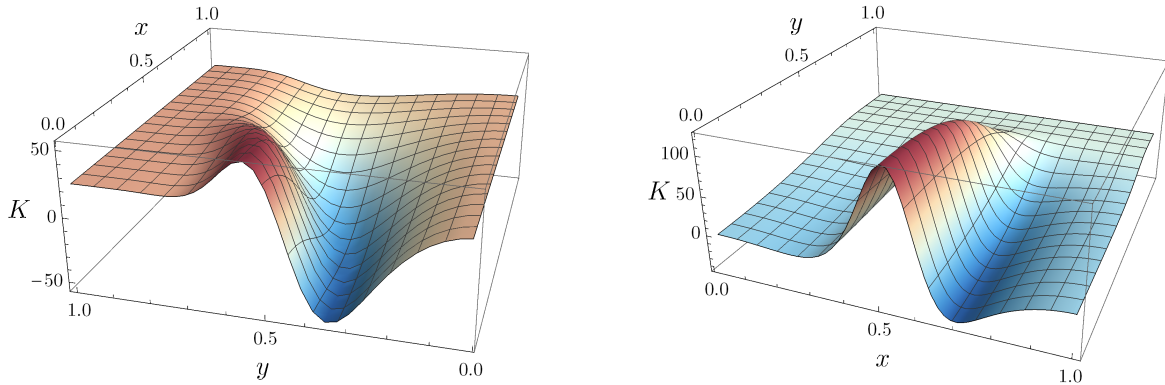


**Fig. 22** *Left:* Kretschmann scalar  $K$  for the dominant soliton branch,  $\varepsilon = 2.564$ . *Right:*  $K$  for a large black hole with  $\varepsilon = 1.9$ .

## 5.B Additional figures

In Fig. 22, we present the Kretschmann scalar  $K$  for a fixed value of the boundary parameter  $\varepsilon \simeq \varepsilon_c$ , where  $\varepsilon_c$  is the maximal value up to which stationary solutions exist. The evolution of  $K$  with the boundary deformation is non-trivial. In the left panel, we plot  $K$  for the small soliton branch. For  $\varepsilon < 1.9$ , the scalar has a positive minima at  $y = 0$ , and for  $\varepsilon > 1.9$ , it starts to display interesting features: the scalar is maximal at the equator  $x = 0$ , displaying two large extrema close to each other, the magnitude of which are growing rapidly with the increase of the boundary rotation amplitude. At the boundary  $y = 1$ , it reduces to the value of  $K_{AdS} = 24$ , as expected for the asymptotically  $AdS_4$  spacetimes. We also observe a local slowly increasing maxima at  $y = 0$ , when  $\varepsilon$  is large. The large, unstable, soliton branch shows a similar behavior, with magnitudes of the both extrema growing further and the distance between them decreasing, and the extrema are slowly moving towards the origin, as  $\varepsilon \rightarrow 2$ . There are also now two minima on each side of the maximum.

In the right panel we present the curvature scalar for the large black hole with  $\varepsilon = 1.9$  and  $T = 1/\pi$ . It is maximal on the black hole horizon  $y = 1$ , and is peaking at  $\theta \rightarrow \pi/4$  as  $\varepsilon \rightarrow 2$ . On either side of the maximum there are two minima one of which is global. As we approach the critical amplitude, the peak, and the minima, become narrower. For  $\varepsilon$  sufficiently large, the  $K$  is small and positive on the poles and the equator.

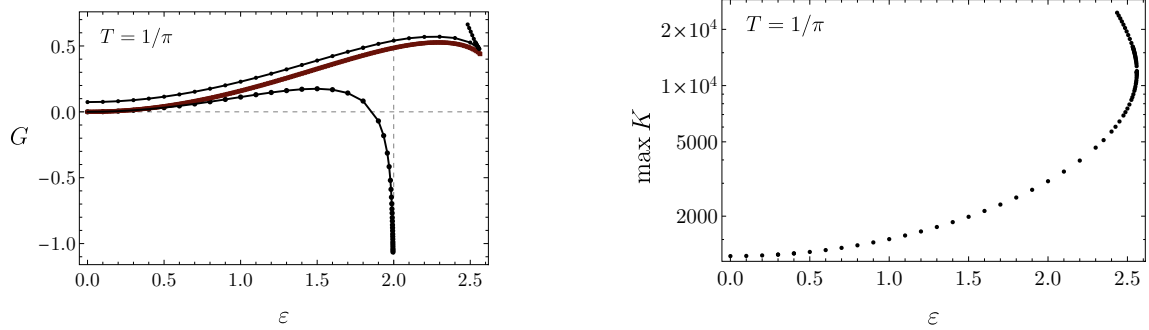


**Fig. 23** *Left:* Gibbs free energy against the boundary profile for black holes with a fixed temperature  $T = 1/\pi$  (black disks), and soliton (brown squares). The dashed gridline marks the  $\varepsilon \rightarrow 2$  limit. *Right:* Maximum of the Kretschmann invariant against  $\varepsilon$  for the small black hole with a fixed temperature. As  $\max K$  increases, the  $K$  looks very similar to that of the soliton.

## 5.C Perturbative expansion

In this section we present the perturbative expansion of the solitonic solution to order  $\varepsilon^2$ , where  $\varepsilon$  is the boundary rotation parameter defined in section 5.2. The following procedure can be easily generalized to yield higher orders of the expansion, however the solutions become increasingly complicated. We will work in null quasi-spherical gauge [232] in which the solution reads

$$ds^2 = - \left(1 + \frac{r^2}{L^2}\right) Q_1(r, \theta) dt^2 + \left(1 + \frac{r^2}{L^2}\right)^{-1} Q_2(r, \theta) dr^2 + r^2 Q_3(r, \theta) [d\theta^2 + \sin^2 \theta (d\phi + \Omega(r, \theta) dt)^2] \quad (46)$$

where  $\{\theta, \phi\}$  are the standard polar coordinates of unit two-sphere, and  $L$  is the  $\text{AdS}_4$  length. The gauge requires that the functions  $Q_i$  ( $i = 1, 2, 3$ ) and  $\Omega$  depend only on  $r$  and  $\theta$ , and we will also use the fact that if  $Q_i = Q_i(r)$  (and  $\Omega = 0$ ), we can additionally fix  $Q_3 = 1$ . As the induced stress-energy tensor is of order  $\varepsilon^2$  in the angular velocity, consider an expansion in  $\varepsilon$  given by

$$Q_i(r, \theta) = \sum_{i=0}^{+\infty} \varepsilon^{2i} q_i^{(2i)}(r, \theta), \quad \Omega(r, \theta) = \sum_{i=0}^{+\infty} \varepsilon^{2i+1} \Omega^{(2i+1)}(r, \theta) \quad (47)$$

where we are expanding around a pure  $\text{AdS}_4$  background given by  $q_i^{(0)} = 1$ . At linear order we obtain a second order partial differential equation for  $\Omega^{(1)}$  which can be solved

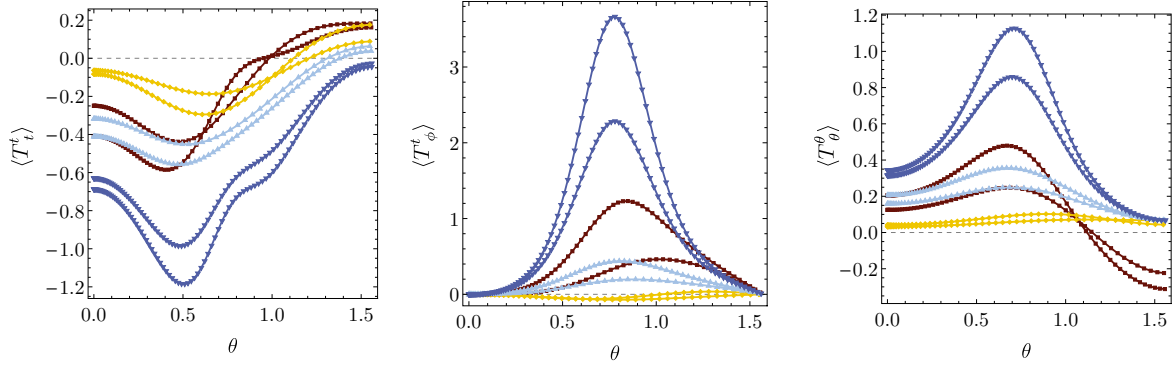


**Fig. 24** Boundary energy-stress tensor components for a fixed low temperature ( $T = 0.2506$ ), where there are four possible black hole phases: lowest entropy black hole branch (brown squares), small black hole branch (yellow diamonds), thermodynamically dominant middle branch (faint blue triangles) and largest entropy large black holes (blue upside-down triangles).

using separation of variables subject to regularity at the origin. The solution is given by

$$\Omega^{(1)}(r, \theta) = \frac{2}{3\sqrt{\pi}} \sum_{l=0}^{+\infty} c_l^{(1)} \frac{\Gamma\left(\frac{l+3}{2}\right) \Gamma\left(\frac{l+5}{2}\right)}{\Gamma\left(l + \frac{5}{2}\right)} P'_{l+1}(\cos \theta) \left(\frac{r}{L}\right)^l {}_2F_1\left(\frac{l}{2}, \frac{l+3}{2}; l + \frac{5}{2}; -\frac{r^2}{L^2}\right), \quad (48)$$

where  $l$  is the harmonic number,  $c_l^{(1)}$  are real numbers depending on the boundary profile,  $P_l$  is Legendre polynomial of degree  $l$  and  ${}_2F_1$  is ordinary hypergeometric function. At the boundary the perturbation reduces to

$$\lim_{r \rightarrow +\infty} \Omega^{(1)}(r, \theta) = \sum_{l=0}^{+\infty} c_l^{(1)} P'_{l+1}(\cos \theta), \quad (49)$$

and at first order the first harmonic  $l = 1$  gives us the dipolar boundary rotation profile  $\Omega(r, \theta) = \varepsilon \cos \theta$ . The final expression is

$$\Omega^{(1)}(r, \theta) = \frac{2L^4}{\pi r^4} \cos \theta \left[ \frac{r}{L} \left( \frac{r^2}{L^2} + 3 \right) + \left( \frac{r^2}{L^2} - 3 \right) \left( \frac{r^2}{L^2} + 1 \right) \arctan \left( \frac{r}{L} \right) \right]. \quad (50)$$

The first order angular velocity perturbation effectively sources the stress energy tensor at  $\varepsilon^2$ . We decompose the second order perturbations as [233]

$$q_i^{(2)}(r, \theta) = \gamma_i(r) + \alpha_i(r)P_2(\cos \theta) + \beta_i(r)P_4(\cos \theta), \quad (51)$$

where the remaining gauge freedom is used to set  $\gamma_3(r) = 0$ . We solve the equations requiring that the functions are regular at the origin  $r = 0$  and, that up to a diffeomorphism, they asymptotically satisfy AdS<sub>4</sub> boundary conditions. Below we provide the full perturbative functions:

$$\begin{aligned} \gamma_1(r) &= \frac{2L^2}{15\pi^2 r^6 (L^2 + r^2)} \left( 24L^6 r^2 + 20L^4 r^4 - 9(\pi^2 - 4)L^2 r^6 - 8 \left( 6L^7 r + 7L^5 r^3 - 6L^3 r^5 \right. \right. \\ &\quad \left. \left. - 9Lr^7 \right) \arctan\left(\frac{r}{L}\right) + 4 \left( 6L^8 + 9L^6 r^2 + L^4 r^4 + 7L^2 r^6 + 9r^8 \right) \arctan\left(\frac{r}{L}\right)^2 - 9\pi^2 r^8 \right), \\ \gamma_2(r) &= -\frac{8L^4}{15\pi^2 r^6 (L^2 + r^2)} \left( (3L^2 - r^2)(L^2 + r^2) \arctan\left(\frac{r}{L}\right) - Lr(3L^2 + r^2) \right) \end{aligned}$$

$$\begin{aligned}
& \times \left( (3L^2 + r^2) \arctan\left(\frac{r}{L}\right) - 3Lr \right), \\
\alpha_1(r) = & \frac{L^2}{84\pi^2 r^6 (L^2 + r^2)} \left( 96L^6 r^2 + L^4(-752 + 63\pi^2)r^4 + 7L^2(-16 + 15\pi^2)r^6 \right. \\
& + \arctan\left(\frac{r}{L}\right) \left( -192L^7 r + 7L^5(176 - 9\pi^2)r^3 + 2L^3(368 - 63\pi^2)r^5 + L(80 - 63\pi^2)r^7 \right. \\
& \left. \left. + 32(L^2 + r^2) \left( 3L^6 - 18L^4 r^2 + L^2 r^4 + 6r^6 \right) \arctan\left(\frac{r}{L}\right) \right) \right), \\
\alpha_2(r) = & \frac{L^3}{84\pi^2 r^6 (L^2 + r^2)} \left( 3936L^5 r^2 + (4208 - 63\pi^2)L^3 r^4 + \arctan\left(\frac{r}{L}\right) \left( -7872L^6 r + \right. \right. \\
& (63\pi^2 - 10832)L^4 r^3 + 2(63\pi^2 - 944)L^2 r^5 + 32L(L^2 + r^2) \left( 123L^4 + 84L^2 r^2 - 23r^4 \right) \\
& \left. \left. \times \arctan\left(\frac{r}{L}\right) + (304 + 63\pi^2)r^7 \right) + (304 - 105\pi^2)Lr^6 \right), \\
\alpha_3(r) = & \frac{L^2}{84\pi^2 r^6} \left( -384L^4 r^2 - 7(64 + 9\pi^2)L^2 r^4 + \arctan\left(\frac{r}{L}\right) \left( 768L^5 r + (1360 + 63\pi^2) \right. \right. \\
& \left. \left. \times L^3 r^3 - 48 \left( 8L^6 + 19L^4 r^2 - 10L^2 r^4 + 3r^6 \right) \arctan\left(\frac{r}{L}\right) - (592 + 63\pi^2)Lr^5 \right) + 84\pi^2 r^6 \right), \\
\beta_1(r) = & \frac{L^2}{1680\pi^2 r^6 (L^2 + r^2)} \left( 3(5408 + 735\pi^2)L^6 r^2 + 38(608 + 105\pi^2)L^4 r^4 \right. \\
& + 21(224 + 81\pi^2)L^2 r^6 + \arctan\left(\frac{r}{L}\right) \left( 3(1504 - 735\pi^2)L^7 r + 63(352 - 75\pi^2)L^5 r^3 \right. \\
& + 3(7712 - 945\pi^2)L^3 r^5 - 256(L^2 + r^2) \left( 81L^6 + 144L^4 r^2 + 48L^2 r^4 + r^6 \right) \arctan\left(\frac{r}{L}\right) \\
& \left. \left. + (4448 - 315\pi^2)Lr^7 \right) \right), \\
\beta_2(r) = & \frac{L^3}{1680\pi^2 r^6 (L^2 + r^2)} \left( -3(32 + 735\pi^2)L^5 r^2 - 2(3104 + 1995\pi^2)L^3 r^4 \right. \\
& + \arctan\left(\frac{r}{L}\right) \left( 3(735\pi^2 - 12256)L^6 r + 15(315\pi^2 - 4448)L^4 r^3 \right. \\
& + (2835\pi^2 - 35936)L^2 r^5 + 256L(L^2 + r^2) \left( 144L^4 + 189L^2 r^2 + 61r^4 \right) \\
& \left. \left. \times \arctan\left(\frac{r}{L}\right) + 5(63\pi^2 - 992)r^7 \right) - (4960 + 1701\pi^2)Lr^6 \right), \\
\beta_3(r) = & \frac{L^2}{1680\pi^2 r^6} \left( -3L^4(7072 + 735\pi^2)r^2 + 7L^2(544 - 45\pi^2)r^4 + 224\pi^2 r^6 \right. \\
& + \arctan\left(\frac{r}{L}\right) \left( 9L^5(608 + 245\pi^2)r + 2L^3(-5536 + 525\pi^2)r^3 + L(2656 - 315\pi^2)r^5 \right. \\
& \left. \left. + 128 \left( 123L^6 + 153L^4 r^2 - 19L^2 r^4 - 9r^6 \right) \arctan\left(\frac{r}{L}\right) \right) \right).
\end{aligned} \tag{52}$$

Using this second order expansion we compute thermodynamic quantities, and test the first law (see subsec. 5.4.4). We also find equilibrium conditions for spinning test particles on the rotation axis  $\theta = 0$ . For the metric (46), the spin to mass ratio (see sec. 5.7) is given by

$$\frac{S}{M} = \frac{\pi r^6}{16\varepsilon L^2 \sqrt{r^2 + 1} \left[ (3L^2 + r^2) \tan^{-1}(r/L) - 3Lr \right]} + \mathcal{O}(\varepsilon), \quad (53)$$

and vanishes when  $r \rightarrow 0$ . The comparison with the full non-linear numerical results are presented in Fig. 5.18.



# Chapter 6

## Summary and Future Outlook

In this dissertation, we applied current numerical techniques to construct novel geometries in asymptotically anti-de Sitter spacetimes, motivated by the gauge/gravity duality. In chapter 1 we reviewed main concepts of the duality, and introduced the underlying dictionary which relates gravitational solutions of the Einstein equation to the conformal field theories. We also discussed aspects of black hole instabilities in AdS. Chapter 2 was devoted to the numerical approach used throughout our work, which considers the elliptic Einstein-DeTurck equations. This technique enforces the generalized harmonic gauge, and the equations are solved with the aid of the spectral collocation methods on a Chebyshev grid.

In chapters 3 and 4 we presented a numerical study of five-dimensional stationary hairy black holes which can be embedded in type IIB string theory, and are dual to thermal states of strongly coupled  $\mathcal{N} = 4$  Yang Mills theory living on the Einstein static universe. We found that the hairy black holes populate the solution space between the extremal and the supersymmetric bounds, demonstrating that the field theory has  $\mathcal{O}(N^2)$  entropy above supersymmetry. We provided evidence for the existence of a new class of supersymmetric black holes with finite horizon scalar hair. These solutions are free from curvature singularities, and, remarkably, retain non-zero entropy. We propose that the missing parameter in the string theory black hole microstate counting is the horizon scalar hair. Our work opens new possibilities for resolving this long-standing entropy puzzle, and unlocks a number of avenues for further research on hairy solutions in supergravity. We have not managed to construct the limiting hairy supersymmetric solutions, and instead we approach these solutions from finite temperature. It would

be very interesting to find a numerical or analytical procedure that would be able to capture these elusive solutions directly, for instance by solving the corresponding BPS equation. It might prove challenging, as we find some evidence of non-analytic behaviour at extremality, which would complicate the near horizon expansion. In the non-perturbative regime, we expect different scalars to be dominant across the moduli space, and it would be intriguing to perform a systematic survey of phase diagrams in different truncations. Finally, a similar analysis can be performed in consistent truncations of 11-dimensional supergravity.

In chapter 5 we studied spatially deformed geometries in four-dimensional global AdS with a dipolar differentially rotating boundary. Through the AdS/CFT correspondence these solutions allow us to investigate thermodynamics of the dual strongly coupled field theory on the rotating background. In this chapter we relied on a bottom-up approach, and it would be interesting to further consider our model from the top-down point of view in order to study ABJM field theory at strong coupling. We found black hole and soliton solutions which exist up to some maximum values of the rotation parameter, and constructed the resulting phase diagram. Once a certain value of the parameter is exceeded, both phases develop an ergoregion attached to the boundary, and are superradiantly unstable. This should be contrasted with the Kerr-AdS black hole, for which, in the grand-canonical ensemble, the unstable phase is subdominant to pure AdS. Our solutions provide a distinctive arena in which to study the phenomenon of superradiance. In particular, it would be very interesting to perform time evolution of this system in the parameter region where no axisymmetric solutions were found.

Recent advances in numerical relativity have opened new possibilities, allowing us to probe old, and capture new, unanticipated physical phenomena, previously inaccessible to analytical methods. Computing full black hole phase diagrams can be a very informative, albeit a challenging task: in order to scan the full parameter space, we had to generate hundreds of thousands of solutions. However, often the most mysterious regions of the parameter space are the most difficult to reach numerically, and yet, these regimes are highly non-linear and thus largely analytically intractable. We anticipate that numerical methods in general relativity will remain an exciting and active area of research, which promise many exciting discoveries in years to come.

# References

- [1] R. P. Kerr, *Gravitational field of a spinning mass as an example of algebraically special metrics*, *Phys. Rev. Lett.* **11** (Sep, 1963) 237–238.
- [2] J. M. Maldacena, *The Large  $N$  limit of superconformal field theories and supergravity*, *Int.J.Theor.Phys.* **38** (1999) 1113–1133, [[hep-th/9711200](#)].
- [3] R. Emparan and H. S. Reall, *A Rotating black ring solution in five-dimensions*, *Phys. Rev. Lett.* **88** (2002) 101101, [[hep-th/0110260](#)].
- [4] H. Elvang and P. Figueras, *Black Saturn*, *JHEP* **05** (2007) 050, [[hep-th/0701035](#)].
- [5] H. Elvang, R. Emparan, and P. Figueras, *Phases of five-dimensional black holes*, *JHEP* **05** (2007) 056, [[hep-th/0702111](#)].
- [6] T. Kaluza, *Zum Unitatsproblem der Physik*, *Sitzungsber. Preuss. Akad. Wiss. Berlin (Math. Phys.)* **1921** (1921) 966–972, [[arXiv:1803.08616](#)].
- [7] O. Klein, *Quantum Theory and Five-Dimensional Theory of Relativity*. (In German and English), *Z. Phys.* **37** (1926) 895–906. [,76(1926)].
- [8] S. S. Gubser, I. R. Klebanov, and A. M. Polyakov, *Gauge theory correlators from noncritical string theory*, *Phys. Lett.* **B428** (1998) 105–114, [[hep-th/9802109](#)].
- [9] E. Witten, *Anti-de Sitter space and holography*, *Adv. Theor. Math. Phys.* **2** (1998) 253–291, [[hep-th/9802150](#)].
- [10] V. E. Hubeny, *The AdS/CFT Correspondence*, *Class. Quant. Grav.* **32** (2015), no. 12 124010, [[arXiv:1501.00007](#)].

- [11] G. 't Hooft, *A Planar Diagram Theory for Strong Interactions*, *Nucl. Phys.* **B72** (1974) 461. [[337\(1973\)](#)].
- [12] O. Aharony, S. S. Gubser, J. M. Maldacena, H. Ooguri, and Y. Oz, *Large N field theories, string theory and gravity*, *Phys. Rept.* **323** (2000) 183–386, [[hep-th/9905111](#)].
- [13] S. W. Hawking, *Particle creation by black holes*, *Communications in Mathematical Physics* **43** (Aug, 1975) 199–220.
- [14] A. Strominger and C. Vafa, *Microscopic origin of the Bekenstein-Hawking entropy*, *Phys. Lett.* **B379** (1996) 99–104, [[hep-th/9601029](#)].
- [15] A. Strominger, *Black hole entropy from near horizon microstates*, *JHEP* **02** (1998) 009, [[hep-th/9712251](#)].
- [16] F. Benini, K. Hristov, and A. Zaffaroni, *Black hole microstates in  $AdS_4$  from supersymmetric localization*, *JHEP* **05** (2016) 054, [[arXiv:1511.04085](#)].
- [17] F. Benini, K. Hristov, and A. Zaffaroni, *Exact microstate counting for dyonic black holes in  $AdS_4$* , *Phys. Lett.* **B771** (2017) 462–466, [[arXiv:1608.07294](#)].
- [18] A. Zaffaroni, *Lectures on AdS Black Holes, Holography and Localization*, 2019. [arXiv:1902.07176](#).
- [19] L. Susskind and E. Witten, *The Holographic bound in anti-de Sitter space*, [hep-th/9805114](#).
- [20] S. de Haro, S. N. Solodukhin, and K. Skenderis, *Holographic reconstruction of space-time and renormalization in the AdS / CFT correspondence*, *Commun. Math. Phys.* **217** (2001) 595–622, [[hep-th/0002230](#)].
- [21] M. Bianchi, D. Z. Freedman, and K. Skenderis, *How to go with an RG flow*, *JHEP* **08** (2001) 041, [[hep-th/0105276](#)].
- [22] M. Bianchi, D. Z. Freedman, and K. Skenderis, *Holographic renormalization*, *Nucl. Phys.* **B631** (2002) 159–194, [[hep-th/0112119](#)].
- [23] K. Skenderis, *Lecture notes on holographic renormalization*, *Class. Quant. Grav.* **19** (2002) 5849–5876, [[hep-th/0209067](#)].

- [24] C. Fefferman and C. R. Graham, *Conformal invariants*, *Astérisque* (1985), no. Numéro Hors Série 95–116. The mathematical heritage of Élie Cartan (Lyon, 1984).
- [25] C. R. Graham and J. M. Lee, *Einstein metrics with prescribed conformal infinity on the ball*, *Adv. Math.* **87** (1991), no. 2 186–225.
- [26] P. Breitenlohner and D. Z. Freedman, *Stability in Gauged Extended Supergravity*, *Annals Phys.* **144** (1982) 249.
- [27] Ó. J. C. Dias, J. E. Santos, and B. Way, *Numerical methods for finding stationary gravitational solutions*, *Classical and Quantum Gravity* **33** (July, 2016) 133001, [[arXiv:1510.02804](#)].
- [28] V. E. Hubeny, X. Liu, M. Rangamani, and S. Shenker, *Comments on cosmic censorship in AdS / CFT*, *JHEP* **12** (2004) 067, [[hep-th/0403198](#)].
- [29] G. T. Horowitz and J. Polchinski, *A Correspondence principle for black holes and strings*, *Phys. Rev.* **D55** (1997) 6189–6197, [[hep-th/9612146](#)].
- [30] S. W. Hawking and D. N. Page, *Thermodynamics of black holes in anti-de sitter space*, *Communications in Mathematical Physics* **87** (Dec, 1983) 577–588.
- [31] E. Witten, *Anti-de Sitter space, thermal phase transition, and confinement in gauge theories*, *Adv. Theor. Math. Phys.* **2** (1998) 505–532, [[hep-th/9803131](#)].
- [32] R. Gregory and R. Laflamme, *Black strings and p-branes are unstable*, *Phys. Rev. Lett.* **70** (1993) 2837–2840, [[hep-th/9301052](#)].
- [33] L. Lehner and F. Pretorius, *Black Strings, Low Viscosity Fluids, and Violation of Cosmic Censorship*, *Phys. Rev. Lett.* **105** (2010) 101102, [[arXiv:1006.5960](#)].
- [34] T. Banks, M. R. Douglas, G. T. Horowitz, and E. J. Martinec, *AdS dynamics from conformal field theory*, [hep-th/9808016](#).
- [35] A. W. Peet and S. F. Ross, *Microcanonical phases of string theory on  $AdS_m \times S^n$* , *JHEP* **12** (1998) 020, [[hep-th/9810200](#)].
- [36] V. E. Hubeny and M. Rangamani, *Unstable horizons*, *JHEP* **05** (2002) 027, [[hep-th/0202189](#)].

- 
- [37] O. J. C. Dias, J. E. Santos, and B. Way, *Lumpy  $AdS_5 \times S^5$  black holes and black belts*, *JHEP* **04** (2015) 060, [[arXiv:1501.06574](#)].
- [38] Y. B. Zeldovich, *Generation of Waves by a Rotating Body*, *JETP Lett.* **14** (1971) 180.
- [39] Y. B. Zeldovich, *Amplification of cylindrical electromagnetic waves reflected from a rotating body*, *Sov. Phys. JETP* **35** (1972) 1085.
- [40] W. H. Press and S. A. Teukolsky, *Floating Orbits, Superradiant Scattering and the Black-hole Bomb*, *Nature* **238** (1972) 211–212.
- [41] A. A. Starobinsky and S. M. Churilov, *Amplification of waves during reflection from a rotating black hole*, *Sov. Phys. JETP* **37** (1973) 28.
- [42] A. A. Starobinsky and S. M. Churilov, *Amplification of electromagnetic and gravitational waves scattered by a rotating black hole*, *Sov. Phys. JETP* **38** (1973) 1.
- [43] S. L. Detweiler and J. R. Ipser, *Stability of scalar perturbations of a Kerr-metric black hole*, *Astrophys. J.* **185** (1973) 675–683.
- [44] T. J. M. Zouros and D. M. Eardley, *Instabilities of Massive Scalar Perturbations of a Rotating Black Hole*, *Annals Phys.* **118** (1979) 139–155.
- [45] S. L. Detweiler, *Klein-Gordon Equation and Rotating Black Holes*, *Phys. Rev.* **D22** (1980) 2323–2326.
- [46] R. Brito, V. Cardoso, and P. Pani, *Superradiance*, *Lect. Notes Phys.* **906** (2015) pp.1–237, [[arXiv:1501.06570](#)].
- [47] H. K. Kunduri, J. Lucietti, and H. S. Reall, *Gravitational perturbations of higher dimensional rotating black holes: Tensor perturbations*, *Phys. Rev.* **D74** (2006) 084021, [[hep-th/0606076](#)].
- [48] Ó. J. C. Dias, G. T. Horowitz, and J. E. Santos, *Black holes with only one Killing field*, *JHEP* **07** (2011) 115, [[arXiv:1105.4167](#)].
- [49] Ó. J. C. Dias and J. E. Santos, *Boundary Conditions for Kerr-AdS Perturbations*, *JHEP* **10** (2013) 156, [[arXiv:1302.1580](#)].

- [50] V. Cardoso, Ó. J. C. Dias, G. S. Hartnett, L. Lehner, and J. E. Santos, *Holographic thermalization, quasinormal modes and superradiance in Kerr-AdS*, *JHEP* **04** (2014) 183, [[arXiv:1312.5323](#)].
- [51] C. A. R. Herdeiro and E. Radu, *Kerr black holes with scalar hair*, *Phys. Rev. Lett.* **112** (2014) 221101, [[arXiv:1403.2757](#)].
- [52] Ó. J. C. Dias, J. E. Santos, and B. Way, *Black holes with a single Killing vector field: black resonators*, *JHEP* **12** (2015) 171, [[arXiv:1505.04793](#)].
- [53] S. R. Green, S. Hollands, A. Ishibashi, and R. M. Wald, *Superradiant instabilities of asymptotically anti-de Sitter black holes*, *Class. Quant. Grav.* **33** (2016), no. 12 125022, [[arXiv:1512.02644](#)].
- [54] B. E. Niehoff, J. E. Santos, and B. Way, *Towards a violation of cosmic censorship*, *Class. Quant. Grav.* **33** (2016), no. 18 185012, [[arXiv:1510.00709](#)].
- [55] G. Denardo and R. Ruffini, *On the energetics of reissner nordstrom geometries*, *Physics Letters B* **45** (1973), no. 3 259 – 262.
- [56] J. D. Bekenstein, *Extraction of energy and charge from a black hole*, *Phys. Rev. D* **7** (Feb, 1973) 949–953.
- [57] S. W. Hawking and H. S. Reall, *Charged and rotating ads black holes and their cft duals*, *Phys. Rev. D* **61** (Dec, 1999) 024014.
- [58] N. Uchikata and S. Yoshida, *Quasinormal modes of a massless charged scalar field on a small Reissner-Nordstrom-anti-de Sitter black hole*, *Phys. Rev.* **D83** (2011) 064020, [[arXiv:1109.6737](#)].
- [59] P. Bosch, S. R. Green, and L. Lehner, *Nonlinear Evolution and Final Fate of Charged Anti de Sitter Black Hole Superradiant Instability*, *Phys. Rev. Lett.* **116** (2016), no. 14 141102, [[arXiv:1601.01384](#)].
- [60] O. J. C. Dias, P. Figueras, S. Minwalla, P. Mitra, R. Monteiro, and J. E. Santos, *Hairy black holes and solitons in global AdS<sub>5</sub>*, *JHEP* **08** (2012) 117, [[arXiv:1112.4447](#)].
- [61] P. Basu, J. Bhattacharya, S. Bhattacharyya, R. Loganayagam, S. Minwalla, et al., *Small Hairy Black Holes in Global AdS Spacetime*, *JHEP* **1010** (2010) 045, [[arXiv:1003.3232](#)].

- [62] S. Bhattacharyya, S. Minwalla, and K. Papadodimas, *Small Hairy Black Holes in  $AdS_5 \times S^5$* , *JHEP* **1111** (2011) 035, [[arXiv:1005.1287](#)].
- [63] S. A. Gentle, M. Rangamani, and B. Withers, *A Soliton Menagerie in AdS*, *JHEP* **05** (2012) 106, [[arXiv:1112.3979](#)].
- [64] O. J. C. Dias and R. Masachs, *Hairy black holes and the endpoint of  $AdS_4$  charged superradiance*, *JHEP* **02** (2017) 128, [[arXiv:1610.03496](#)].
- [65] S. S. Gubser, *Breaking an Abelian gauge symmetry near a black hole horizon*, *Phys. Rev.* **D78** (2008) 065034, [[arXiv:0801.2977](#)].
- [66] S. A. Hartnoll, C. P. Herzog, and G. T. Horowitz, *Holographic Superconductors*, *JHEP* **12** (2008) 015, [[arXiv:0810.1563](#)].
- [67] O. J. C. Dias, R. Monteiro, H. S. Reall, and J. E. Santos, *A Scalar field condensation instability of rotating anti-de Sitter black holes*, *JHEP* **11** (2010) 036, [[arXiv:1007.3745](#)].
- [68] K. Murata, S. Kinoshita, and N. Tanahashi, *Non-equilibrium Condensation Process in a Holographic Superconductor*, *JHEP* **07** (2010) 050, [[arXiv:1005.0633](#)].
- [69] S. A. Hartnoll, C. P. Herzog, and G. T. Horowitz, *Building a Holographic Superconductor*, *Phys. Rev. Lett.* **101** (2008) 031601, [[arXiv:0803.3295](#)].
- [70] J. McGreevy, *Holographic duality with a view toward many-body physics*, *Adv. High Energy Phys.* **2010** (2010) 723105, [[arXiv:0909.0518](#)].
- [71] S. Sachdev, *Condensed Matter and AdS/CFT*, [arXiv:1002.2947](#). [Lect. Notes Phys.828,273(2011)].
- [72] S. A. Hartnoll, *Horizons, holography and condensed matter*, in *Black holes in higher dimensions* (G. T. Horowitz, ed.), pp. 387–419. 2012. [arXiv:1106.4324](#).
- [73] S. A. Hartnoll, A. Lucas, and S. Sachdev, *Holographic quantum matter*, [arXiv:1612.07324](#).
- [74] M. W. Choptuik, *Universality and scaling in gravitational collapse of a massless scalar field*, *Phys. Rev. Lett.* **70** (Jan, 1993) 9–12.

- [75] U. Sperhake, *The numerical relativity breakthrough for binary black holes*, *Class. Quant. Grav.* **32** (2015), no. 12 124011, [[arXiv:1411.3997](#)].
- [76] **Virgo, LIGO Scientific** Collaboration, B. P. Abbott et al., *Observation of Gravitational Waves from a Binary Black Hole Merger*, *Phys. Rev. Lett.* **116** (2016), no. 6 061102, [[arXiv:1602.03837](#)].
- [77] **Virgo, LIGO Scientific** Collaboration, B. P. Abbott et al., *GW151226: Observation of Gravitational Waves from a 22-Solar-Mass Binary Black Hole Coalescence*, *Phys. Rev. Lett.* **116** (2016), no. 24 241103, [[arXiv:1606.04855](#)].
- [78] Y. Fours-Bruhat, *Theoreme d existence pour certains systemes d equations aux derivees partielles non lineaires*, *Acta Math.* **88** (1952) 141–225.
- [79] M. Headrick, S. Kitchen, and T. Wiseman, *A New approach to static numerical relativity, and its application to Kaluza-Klein black holes*, *Class. Quant. Grav.* **27** (2010) 035002, [[arXiv:0905.1822](#)].
- [80] T. Wiseman, *Numerical construction of static and stationary black holes*, in *Black Holes in Higher Dimensions*, ch. 10, pp. 233–279. Cambridge University Press, 2012.
- [81] A. Adam, S. Kitchen, and T. Wiseman, *A numerical approach to finding general stationary vacuum black holes*, *Class. Quant. Grav.* **29** (2012) 165002, [[arXiv:1105.6347](#)].
- [82] S. Hollands, A. Ishibashi, and R. M. Wald, *A Higher dimensional stationary rotating black hole must be axisymmetric*, *Commun. Math. Phys.* **271** (2007) 699–722, [[gr-qc/0605106](#)].
- [83] V. Moncrief and J. Isenberg, *Symmetries of Higher Dimensional Black Holes*, *Class. Quant. Grav.* **25** (2008) 195015, [[arXiv:0805.1451](#)].
- [84] G. T. Horowitz and J. E. Santos, *Geons and the Instability of Anti-de Sitter Spacetime*, *Surveys Diff. Geom.* **20** (2015) 321–335, [[arXiv:1408.5906](#)].
- [85] P. Figueras and T. Wiseman, *Stationary holographic plasma quenches and numerical methods for non-Killing horizons*, *Phys. Rev. Lett.* **110** (2013) 171602, [[arXiv:1212.4498](#)].

- [86] S. Fischetti, D. Marolf, and J. E. Santos, *AdS flowing black funnels: Stationary AdS black holes with non-Killing horizons and heat transport in the dual CFT*, *Class. Quant. Grav.* **30** (2013) 075001, [[arXiv:1212.4820](#)].
- [87] P. Figueras and T. Wiseman, *On the existence of stationary Ricci solitons*, *Class. Quant. Grav.* **34** (2017), no. 14 145007, [[arXiv:1610.06178](#)].
- [88] P. Grandclement and J. Novak, *Spectral methods for numerical relativity*, *Living Rev. Rel.* **12** (2009) 1, [[arXiv:0706.2286](#)].
- [89] A. Q. C. Canuto, M. Y. Hussaini and T. A. Zang, *Spectral methods*, Springer-Verlag (2006).
- [90] L. N. Trefethen, *Spectral methods in matlab*, SIAM, Philadelphia (2000).
- [91] J. P. Boyd, *Chebyshev and fourier spectral methods dover*, Books on Mathematics, (2001).
- [92] J. Markevičiūtė, and J. E. Santos, *Hairy black holes in  $AdS_5 \times S^5$* , *JHEP* **06** (2016) 096, [[arXiv:1602.03893](#)].
- [93] A. Buchel and L. Lehner, *Small black holes in  $AdS_5 \times S^5$* , *Class. Quant. Grav.* **32** (2015), no. 14 145003, [[arXiv:1502.01574](#)].
- [94] B. de Wit and H. Nicolai, *Deformations of gauged  $SO(8)$  supergravity and supergravity in eleven dimensions*, *JHEP* **05** (2013) 077, [[arXiv:1302.6219](#)].
- [95] H. Godazgar, M. Godazgar, and H. Nicolai, *Nonlinear Kaluza-Klein theory for dual fields*, *Phys. Rev.* **D88** (2013), no. 12 125002, [[arXiv:1309.0266](#)].
- [96] H. Godazgar, M. Godazgar, and H. Nicolai, *Testing the non-linear flux ansatz for maximal supergravity*, *Phys. Rev.* **D87** (2013) 085038, [[arXiv:1303.1013](#)].
- [97] H. Godazgar, M. Godazgar, and H. Nicolai, *Generalised geometry from the ground up*, *JHEP* **02** (2014) 075, [[arXiv:1307.8295](#)].
- [98] H. Godazgar, M. Godazgar, and H. Nicolai, *Embedding tensor of Scherk-Schwarz flux compactifications from eleven dimensions*, *Phys. Rev.* **D89** (2014), no. 4 045009, [[arXiv:1312.1061](#)].

- [99] K. Lee, C. Strickland-Constable, and D. Waldram, *Spheres, generalised parallelisability and consistent truncations*, *Fortsch. Phys.* **65** (2017), no. 10-11 1700048, [[arXiv:1401.3360](#)].
- [100] A. Baguet, O. Hohm, and H. Samtleben, *Consistent Type IIB Reductions to Maximal 5D Supergravity*, *Phys. Rev.* **D92** (2015), no. 6 065004, [[arXiv:1506.01385](#)].
- [101] M. Cvetič, H. Lu, C. N. Pope, A. Sadrzadeh, and T. A. Tran, *Consistent  $SO(6)$  reduction of type IIB supergravity on  $S^{*5}$* , *Nucl. Phys.* **B586** (2000) 275–286, [[hep-th/0003103](#)].
- [102] Z. W. Chong, H. Lu, and C. N. Pope, *BPS geometries and AdS bubbles*, *Phys. Lett.* **B614** (2005) 96–103, [[hep-th/0412221](#)].
- [103] J. T. Liu, H. Lu, C. N. Pope, and J. F. Vazquez-Poritz, *New supersymmetric solutions of  $N=2$ ,  $D=5$  gauged supergravity with hyperscalars*, *JHEP* **10** (2007) 093, [[arXiv:0705.2234](#)].
- [104] J. T. Liu, H. Lu, C. N. Pope, and J. F. Vazquez-Poritz, *Bubbling AdS black holes*, *JHEP* **10** (2007) 030, [[hep-th/0703184](#)].
- [105] B. Chen, S. Cremonini, A. Donos, F.-L. Lin, H. Lin, J. T. Liu, D. Vaman, and W.-Y. Wen, *Bubbling AdS and droplet descriptions of BPS geometries in IIB supergravity*, *JHEP* **10** (2007) 003, [[arXiv:0704.2233](#)].
- [106] A. Ashtekar and A. Magnon, *Asymptotically anti-de Sitter space-times*, *Class. Quant. Grav.* **1** (1984) L39–L44.
- [107] M. Henneaux and C. Teitelboim, *Asymptotically anti-De Sitter Spaces*, *Commun. Math. Phys.* **98** (1985) 391–424.
- [108] M. Henningson and K. Skenderis, *The Holographic Weyl anomaly*, *JHEP* **07** (1998) 023, [[hep-th/9806087](#)].
- [109] G. W. Gibbons, H. Lu, D. N. Page, and C. N. Pope, *The General Kerr-de Sitter metrics in all dimensions*, *J. Geom. Phys.* **53** (2005) 49–73, [[hep-th/0404008](#)].
- [110] G. W. Gibbons, M. J. Perry, and C. N. Pope, *The First law of thermodynamics for Kerr-anti-de Sitter black holes*, *Class. Quant. Grav.* **22** (2005) 1503–1526, [[hep-th/0408217](#)].

- [111] M. Cvetič, H. Lu, and C. N. Pope, *Charged rotating black holes in five dimensional  $U(1)^3$  gauged  $N=2$  supergravity*, *Phys. Rev.* **D70** (2004) 081502, [[hep-th/0407058](#)].
- [112] Z. W. Chong, M. Cvetič, H. Lu, and C. N. Pope, *General non-extremal rotating black holes in minimal five-dimensional gauged supergravity*, *Phys. Rev. Lett.* **95** (2005) 161301, [[hep-th/0506029](#)].
- [113] Z. W. Chong, M. Cvetič, H. Lu, and C. N. Pope, *Five-dimensional gauged supergravity black holes with independent rotation parameters*, *Phys. Rev.* **D72** (2005) 041901, [[hep-th/0505112](#)].
- [114] Z. W. Chong, M. Cvetič, H. Lu, and C. N. Pope, *Non-extremal rotating black holes in five-dimensional gauged supergravity*, *Phys. Lett.* **B644** (2007) 192–197, [[hep-th/0606213](#)].
- [115] M. Cvetič, G. W. Gibbons, H. Lu, and C. N. Pope, *Rotating black holes in gauged supergravities: Thermodynamics, supersymmetric limits, topological solitons and time machines*, [hep-th/0504080](#).
- [116] J. B. Gutowski and H. S. Reall, *General supersymmetric  $AdS(5)$  black holes*, *JHEP* **04** (2004) 048, [[hep-th/0401129](#)].
- [117] J. B. Gutowski and H. S. Reall, *Supersymmetric  $AdS(5)$  black holes*, *JHEP* **02** (2004) 006, [[hep-th/0401042](#)].
- [118] H. K. Kunduri, J. Lucietti, and H. S. Reall, *Supersymmetric multi-charge  $AdS(5)$  black holes*, *JHEP* **04** (2006) 036, [[hep-th/0601156](#)].
- [119] S.-Q. Wu, *General Nonextremal Rotating Charged  $AdS$  Black Holes in Five-dimensional  $U(1)^3$  Gauged Supergravity: A Simple Construction Method*, *Phys. Lett.* **B707** (2012) 286–291, [[arXiv:1108.4159](#)].
- [120] A. Ashtekar and S. Das, *Asymptotically Anti-de Sitter space-times: Conserved quantities*, *Class. Quant. Grav.* **17** (2000) L17–L30, [[hep-th/9911230](#)].
- [121] V. Balasubramanian and P. Kraus, *A Stress tensor for Anti-de Sitter gravity*, *Commun. Math. Phys.* **208** (1999) 413–428, [[hep-th/9902121](#)].
- [122] F. Aprile, D. Roest, and J. G. Russo, *Holographic Superconductors from Gauged Supergravity*, *JHEP* **1106** (2011) 040, [[arXiv:1104.4473](#)].

- [123] S. W. Hawking and D. N. Page, *Thermodynamics of Black Holes in anti-De Sitter Space*, *Commun. Math. Phys.* **87** (1983) 577.
- [124] S. L. Cacciatori and D. Klemm, *Supersymmetric AdS(4) black holes and attractors*, *JHEP* **01** (2010) 085, [[arXiv:0911.4926](#)].
- [125] J. Markevičiūtė, *Rotating hairy black holes in  $AdS_5 \times S^5$* , *Journal of High Energy Physics* **2019** (Mar, 2019) 110, [[arXiv:1809.04084](#)].
- [126] J. Markeviciute and J. E. Santos, *Evidence for the existence of a novel class of supersymmetric black holes with  $AdS_5 \times S^5$  asymptotics*, *Class. Quant. Grav.* **36** (2019), no. 2 02LT01, [[arXiv:1806.01849](#)].
- [127] J. Kinney, J. M. Maldacena, S. Minwalla, and S. Raju, *An Index for 4 dimensional super conformal theories*, *Commun. Math. Phys.* **275** (2007) 209–254, [[hep-th/0510251](#)].
- [128] M. Berkooz, D. Reichmann, and J. Simon, *A Fermi Surface Model for Large Supersymmetric AdS(5) Black Holes*, *JHEP* **01** (2007) 048, [[hep-th/0604023](#)].
- [129] H. K. Kunduri and J. Lucietti, *Near-horizon geometries of supersymmetric AdS(5) black holes*, *JHEP* **12** (2007) 015, [[arXiv:0708.3695](#)].
- [130] M. Cvetič, H. Lu, and C. N. Pope, *Charged Kerr-de Sitter black holes in five dimensions*, *Phys. Lett.* **B598** (2004) 273–278, [[hep-th/0406196](#)].
- [131] A. Chamblin, R. Emparan, C. V. Johnson, and R. C. Myers, *Charged AdS black holes and catastrophic holography*, *Phys. Rev.* **D60** (1999) 064018, [[hep-th/9902170](#)].
- [132] J. P. Gauntlett, J. B. Gutowski, and N. V. Suryanarayana, *A Deformation of  $AdS(5) \times S^{**5}$* , *Class. Quant. Grav.* **21** (2004) 5021–5034, [[hep-th/0406188](#)].
- [133] J. M. Maldacena and C. Nunez, *Supergravity description of field theories on curved manifolds and a no go theorem*, *Int. J. Mod. Phys.* **A16** (2001) 822–855, [[hep-th/0007018](#)]. [,182(2000)].
- [134] S. S. Gubser, *Curvature singularities: The Good, the bad, and the naked*, *Adv. Theor. Math. Phys.* **4** (2000) 679–745, [[hep-th/0002160](#)].

- [135] S. W. Hawking, C. J. Hunter, and M. Taylor, *Rotation and the AdS / CFT correspondence*, *Phys. Rev.* **D59** (1999) 064005, [[hep-th/9811056](#)].
- [136] S. W. Hawking and H. S. Reall, *Charged and rotating AdS black holes and their CFT duals*, *Phys. Rev.* **D61** (2000) 024014, [[hep-th/9908109](#)].
- [137] O. Madden and S. F. Ross, *On uniqueness of charged Kerr-AdS black holes in five dimensions*, *Class. Quant. Grav.* **22** (2005) 515–524, [[hep-th/0409188](#)].
- [138] D. Klemm and W. A. Sabra, *General (Anti-)de Sitter black holes in five dimensions*, *Journal of High Energy Physics* **2** (Feb., 2001) 031, [[hep-th/0011016](#)].
- [139] R. C. Myers and M. J. Perry, *Black holes in higher dimensional space-times*, *Annals of Physics* **172** (Dec., 1986) 304–347.
- [140] O. J. C. Dias, J. E. Santos, and B. Way, *Numerical Methods for Finding Stationary Gravitational Solutions*, [arXiv:1510.02804](#).
- [141] J. Markeviciute and J. E. Santos, *Stirring a black hole*, *JHEP* **02** (2018) 060, [[arXiv:1712.07648](#)].
- [142] S. Kachru, X. Liu, and M. Mulligan, *Gravity duals of Lifshitz-like fixed points*, *Phys. Rev.* **D78** (2008) 106005, [[arXiv:0808.1725](#)].
- [143] L. Huijse, S. Sachdev, and B. Swingle, *Hidden Fermi surfaces in compressible states of gauge-gravity duality*, *Phys. Rev.* **B85** (2012) 035121, [[arXiv:1112.0573](#)].
- [144] J. F. Pedraza, W. Sybesma, and M. R. Visser, *Hyperscaling violating black holes with spherical and hyperbolic horizons*, [arXiv:1807.09770](#).
- [145] S. Ferrara, R. Kallosh, and A. Strominger,  *$N=2$  extremal black holes*, *Phys. Rev.* **D52** (1995) R5412–R5416, [[hep-th/9508072](#)].
- [146] A. Strominger, *Macroscopic entropy of  $N=2$  extremal black holes*, *Phys. Lett.* **B383** (1996) 39–43, [[hep-th/9602111](#)].
- [147] S. Ferrara and R. Kallosh, *Supersymmetry and attractors*, *Phys. Rev.* **D54** (1996) 1514–1524, [[hep-th/9602136](#)].

- [148] S. Ferrara and R. Kallosh, *Universality of supersymmetric attractors*, *Phys. Rev.* **D54** (1996) 1525–1534, [[hep-th/9603090](#)].
- [149] A. H. Chamseddine, S. Ferrara, G. W. Gibbons, and R. Kallosh, *Enhancement of supersymmetry near 5-d black hole horizon*, *Phys. Rev.* **D55** (1997) 3647–3653, [[hep-th/9610155](#)].
- [150] R. Kallosh, A. Rajaraman, and W. K. Wong, *Supersymmetric rotating black holes and attractors*, *Phys. Rev.* **D55** (1997) R3246–R3249, [[hep-th/9611094](#)].
- [151] S. Ferrara, G. W. Gibbons, and R. Kallosh, *Black holes and critical points in moduli space*, *Nucl. Phys.* **B500** (1997) 75–93, [[hep-th/9702103](#)].
- [152] S. M. Hosseini, K. Hristov, and A. Zaffaroni, *An extremization principle for the entropy of rotating BPS black holes in  $AdS_5$* , *JHEP* **07** (2017) 106, [[arXiv:1705.05383](#)].
- [153] S. M. Hosseini, K. Hristov, and A. Zaffaroni, *A note on the entropy of rotating BPS  $AdS_7 \times S^4$  black holes*, *JHEP* **05** (2018) 121, [[arXiv:1803.07568](#)].
- [154] S. Kim and K.-M. Lee, *1/16-BPS Black Holes and Giant Gravitons in the  $AdS(5) \times S^{**5}$  Space*, *JHEP* **12** (2006) 077, [[hep-th/0607085](#)].
- [155] G. T. Horowitz and S. F. Ross, *Naked black holes*, *Phys. Rev.* **D56** (1997) 2180–2187, [[hep-th/9704058](#)].
- [156] R. Gueven, *The Conformal penrose limit and the resolution of the pp-curvature singularities*, *Class. Quant. Grav.* **23** (2006) 295–308, [[hep-th/0508160](#)].
- [157] S. Harrison, S. Kachru, and H. Wang, *Resolving Lifshitz Horizons*, *JHEP* **02** (2014) 085, [[arXiv:1202.6635](#)].
- [158] J. Bhattacharya, S. Cremonini, and A. Sinkovics, *On the IR completion of geometries with hyperscaling violation*, *JHEP* **02** (2013) 147, [[arXiv:1208.1752](#)].
- [159] D. Brecher, A. Chamblin, and H. S. Reall,  *$AdS / CFT$  in the infinite momentum frame*, *Nucl. Phys.* **B607** (2001) 155–190, [[hep-th/0012076](#)].
- [160] G. T. Horowitz and S. F. Ross, *Properties of naked black holes*, *Phys. Rev.* **D57** (1998) 1098–1107, [[hep-th/9709050](#)].

- [161] G. T. Horowitz and H.-s. Yang, *Black strings and classical hair*, *Phys. Rev.* **D55** (1997) 7618–7624, [[hep-th/9701077](#)].
- [162] N. Kaloper, R. C. Myers, and H. Roussel, *Wavy strings: Black or bright?*, *Phys. Rev.* **D55** (1997) 7625–7644, [[hep-th/9612248](#)].
- [163] K. Madhu and K. Narayan, *String spectra near some null cosmological singularities*, *Phys. Rev.* **D79** (2009) 126009, [[arXiv:0904.4532](#)].
- [164] L. M. Burko, *Strength of the null singularity inside black holes*, *Phys. Rev.* **D60** (1999) 104033, [[gr-qc/9907061](#)].
- [165] K. Narayan, *Null cosmological singularities and free strings*, *Phys. Rev.* **D81** (2010) 066005, [[arXiv:0909.4731](#)].
- [166] G. F. R. Ellis and B. G. Schmidt, *Singular space-times*, *General Relativity and Gravitation* **8** (Nov, 1977) 915–953.
- [167] F. J. Tipler, *Singularities in conformally flat spacetimes*, *Physics Letters A* **64** (1977), no. 1 8 – 10.
- [168] C. Clarke and A. Królak, *Conditions for the occurrence of strong curvature singularities*, *Journal of Geometry and Physics* **2** (1985), no. 2 127 – 143.
- [169] B. C. Nolan, *Strengths of singularities in spherical symmetry*, *Phys. Rev.* **D60** (1999) 024014, [[gr-qc/9902021](#)].
- [170] A. Ori, *Strength of curvature singularities*, *Phys. Rev. D* **61** (Feb, 2000) 064016.
- [171] B. C. Nolan, *The Central singularity in spherical collapse*, *Phys. Rev.* **D62** (2000) 044015, [[gr-qc/0001026](#)].
- [172] N. Bao, X. Dong, S. Harrison, and E. Silverstein, *The Benefits of Stress: Resolution of the Lifshitz Singularity*, *Phys. Rev.* **D86** (2012) 106008, [[arXiv:1207.0171](#)].
- [173] S. Klainerman, I. Rodnianski, and J. Szeftel, *The Bounded L2 Curvature Conjecture*, [arXiv:1204.1767](#).
- [174] D. Christodoulou, *The Formation of Black Holes in General Relativity*, in *On recent developments in theoretical and experimental general relativity*,

- astrophysics and relativistic field theories. Proceedings, 12th Marcel Grossmann Meeting on General Relativity, Paris, France, July 12-18, 2009. Vol. 1-3*, pp. 24–34, 2008. [arXiv:0805.3880](#).
- [175] M. Cvetič and S. S. Gubser, *Phases of  $R$  charged black holes, spinning branes and strongly coupled gauge theories*, *JHEP* **04** (1999) 024, [[hep-th/9902195](#)].
- [176] M. M. Caldarelli, G. Cognola, and D. Klemm, *Thermodynamics of Kerr-Newman-AdS black holes and conformal field theories*, *Class. Quant. Grav.* **17** (2000) 399–420, [[hep-th/9908022](#)].
- [177] H. K. Kunduri and J. Lucietti, *Notes on non-extremal, charged, rotating black holes in minimal  $d=5$  gauged supergravity*, *Nuclear Physics B* **724** (2005), no. 1 343 – 356.
- [178] B. P. Dolan, *Thermodynamic stability of asymptotically anti-de Sitter rotating black holes in higher dimensions*, *Class. Quant. Grav.* **31** (2014) 165011, [[arXiv:1403.1507](#)].
- [179] H. B. Callen, *Thermodynamics and an Introduction to Thermostatistics, 2nd Edition*. Aug., 1985.
- [180] G. T. Horowitz, *Introduction to Holographic Superconductors*, *Lect. Notes Phys.* **828** (2011) 313–347, [[arXiv:1002.1722](#)].
- [181] J. Sonner and B. Withers, *A gravity derivation of the Tisza-Landau Model in AdS/CFT*, *Phys. Rev.* **D82** (2010) 026001, [[arXiv:1004.2707](#)].
- [182] D. Arean, M. Bertolini, C. Krishnan, and T. Prochazka, *Type IIB Holographic Superfluid Flows*, *JHEP* **03** (2011) 008, [[arXiv:1010.5777](#)].
- [183] A. Buchel and C. Pagnutti, *Exotic Hairy Black Holes*, *Nucl. Phys.* **B824** (2010) 85–94, [[arXiv:0904.1716](#)].
- [184] A. Donos and J. P. Gauntlett, *Superfluid black branes in  $AdS_4 \times S^7$* , *JHEP* **06** (2011) 053, [[arXiv:1104.4478](#)].
- [185] S. A. Gentle and B. Withers, *Superconducting instabilities of  $R$ -charged black branes*, *JHEP* **10** (2012) 006, [[arXiv:1207.3086](#)].

- [186] R.-G. Cai, L. Li, and L.-F. Li, *A Holographic P-wave Superconductor Model*, *JHEP* **01** (2014) 032, [[arXiv:1309.4877](#)].
- [187] E. Banks and J. P. Gauntlett, *A new phase for the anisotropic  $N=4$  super Yang-Mills plasma*, *JHEP* **09** (2015) 126, [[arXiv:1506.07176](#)].
- [188] G. T. Horowitz and M. M. Roberts, *Holographic Superconductors with Various Condensates*, *Phys. Rev.* **D78** (2008) 126008, [[arXiv:0810.1077](#)].
- [189] C. P. Herzog, *An Analytic Holographic Superconductor*, *Phys. Rev.* **D81** (2010) 126009, [[arXiv:1003.3278](#)].
- [190] J. Sonner, *A Rotating Holographic Superconductor*, *Phys. Rev.* **D80** (2009) 084031, [[arXiv:0903.0627](#)].
- [191] O. J. C. Dias and R. Masachs, *Charged black hole bombs in a Minkowski cavity*, [arXiv:1801.10176](#).
- [192] O. J. C. Dias and R. Masachs, *Evading no-hair theorems: hairy black holes in a Minkowski box*, *Phys. Rev.* **D97** (2018), no. 12 124030, [[arXiv:1802.01603](#)].
- [193] J. Fernandez-Gracia and B. Fiol, *A No-hair theorem for extremal black branes*, *JHEP* **11** (2009) 054, [[arXiv:0906.2353](#)].
- [194] Y. Brihaye and B. Hartmann, *A Scalar field instability of rotating and charged black holes in  $(4+1)$ -dimensional Anti-de Sitter space-time*, *JHEP* **03** (2012) 050, [[arXiv:1112.6315](#)].
- [195] F. Aprile, D. Rodriguez-Gomez, and J. G. Russo, *p-wave Holographic Superconductors and five-dimensional gauged Supergravity*, *JHEP* **01** (2011) 056, [[arXiv:1011.2172](#)].
- [196] S. S. Gubser, C. P. Herzog, S. S. Pufu, and T. Tesileanu, *Superconductors from Superstrings*, *Phys. Rev. Lett.* **103** (2009) 141601, [[arXiv:0907.3510](#)].
- [197] S. A. Fulling, *Nonuniqueness of canonical field quantization in riemannian space-time*, *Phys. Rev. D* **7** (May, 1973) 2850–2862.
- [198] S. W. Hawking, *Black hole explosions*, *Nature* **248** (1974) 30–31.
- [199] W. G. Unruh, *Notes on black-hole evaporation*, *Phys. Rev. D* **14** (Aug, 1976) 870–892.

- [200] J. W. York, Jr., *Role of conformal three geometry in the dynamics of gravitation*, *Phys. Rev. Lett.* **28** (1972) 1082–1085.
- [201] G. W. Gibbons and S. W. Hawking, *Action Integrals and Partition Functions in Quantum Gravity*, *Phys. Rev.* **D15** (1977) 2752–2756.
- [202] G. W. Gibbons, C. A. R. Herdeiro, and C. Rebelo, *Global embedding of the Kerr black hole event horizon into hyperbolic 3-space*, *Phys. Rev.* **D80** (2009) 044014, [[arXiv:0906.2768](#)].
- [203] J. D. Brown and J. W. York, Jr., *Quasilocal energy and conserved charges derived from the gravitational action*, *Phys. Rev.* **D47** (1993) 1407–1419, [[gr-qc/9209012](#)].
- [204] V. Iyer and R. M. Wald, *Some properties of Noether charge and a proposal for dynamical black hole entropy*, *Phys. Rev.* **D50** (1994) 846–864, [[gr-qc/9403028](#)].
- [205] I. Papadimitriou and K. Skenderis, *Thermodynamics of asymptotically locally AdS spacetimes*, *JHEP* **08** (2005) 004, [[hep-th/0505190](#)].
- [206] G. Compere, *Note on the First Law with p-form potentials*, *Phys. Rev.* **D75** (2007) 124020, [[hep-th/0703004](#)].
- [207] A. Chamblin, R. Emparan, C. V. Johnson, and R. C. Myers, *Holography, thermodynamics and fluctuations of charged AdS black holes*, *Phys. Rev.* **D60** (1999) 104026, [[hep-th/9904197](#)].
- [208] G. T. Horowitz and V. E. Hubeny, *Quasinormal modes of AdS black holes and the approach to thermal equilibrium*, *Phys. Rev.* **D62** (2000) 024027, [[hep-th/9909056](#)].
- [209] A. Donos and J. P. Gauntlett, *Holographic Q-lattices*, *JHEP* **04** (2014) 040, [[arXiv:1311.3292](#)].
- [210] M. S. Costa, L. Greenspan, M. Oliveira, J. Penedones, and J. E. Santos, *Polarised Black Holes in AdS*, *Class. Quant. Grav.* **33** (2016), no. 11 115011, [[arXiv:1511.08505](#)].
- [211] R. Wald, *Gravitational spin interaction*, *Phys. Rev. D* **6** (Jul, 1972) 406–413.

- [212] J. Natario, *Quasi-Maxwell interpretation of the spin-curvature coupling*, *Gen. Rel. Grav.* **39** (2007) 1477–1487, [[gr-qc/0701067](#)].
- [213] L. F. O. Costa, J. Natário, and M. Zilhão, *Spacetime dynamics of spinning particles: Exact electromagnetic analogies*, *Phys. Rev. D* **93** (May, 2016) 104006.
- [214] M. Mathisson, *Republication of: New mechanics of material systems*, *General Relativity and Gravitation* **42** (2010), no. 4 1011–1048.
- [215] A. Papapetrou, *Spinning test-particles in general relativity.*, *Proceedings of the Royal Society of London A: Mathematical, Physical and Engineering Sciences* **209** (1951), no. 1097 248–258.
- [216] F. A. E. Pirani, *On the Physical significance of the Riemann tensor*, *Acta Phys. Polon.* **15** (1956) 389–405. [[Gen. Rel. Grav.41,1215\(2009\)](#)].
- [217] W. Tulczyjew, *Motion of multipole particles in general relativity theory*, *Acta Phys. Pol.* **18** (1959) 393.
- [218] A. H. Taub, *Motion of test bodies in general relativity*, *Journal of Mathematical Physics* **5** (1964), no. 1 112–119, [<http://dx.doi.org/10.1063/1.1704055>].
- [219] W. G. Dixon, *A covariant multipole formalism for extended test bodies in general relativity*, *Il Nuovo Cimento (1955-1965)* **34** (1964), no. 2 317–339.
- [220] W. G. Dixon, *Dynamics of extended bodies in general relativity*, *Proceedings of the Royal Society of London A: Mathematical, Physical and Engineering Sciences* **314** (1970), no. 1519 499–527.
- [221] O. Semerák, *Spinning test particles in a Kerr field - I*, *MNRAS* **308** (Sept., 1999) 863–875.
- [222] C. Moller, *On the definition of the centre of gravity of an arbitrary closed system in the theory of relativity*, *Commun. Dublin Inst. Adv. Stud.* **5** (1949), no. 42.
- [223] B. Carter, *Hamilton-jacobi and schrodinger separable solutions of einstein's equations*, *Comm. Math. Phys.* **10** (1968), no. 4 280–310.
- [224] M. S. Costa, L. Greenspan, J. Penedones, and J. E. Santos, *Polarised black holes in ABJM*, *Journal of High Energy Physics* **6** (June, 2017) 24, [[arXiv:1702.04353](#)].

- [225] M. S. Costa, L. Greenspan, M. Oliveira, J. Penedones, and J. E. Santos, *Polarised black holes in AdS*, *Classical and Quantum Gravity* **33** (June, 2016) 115011, [[arXiv:1511.08505](#)].
- [226] T. Crisford and J. E. Santos, *Violating the Weak Cosmic Censorship Conjecture in Four-Dimensional Anti-de Sitter Space*, *Phys. Rev. Lett.* **118** (2017), no. 18 181101, [[arXiv:1702.05490](#)].
- [227] T. Crisford, G. T. Horowitz, and J. E. Santos, *Testing the Weak Gravity - Cosmic Censorship Connection*, *ArXiv e-prints* (Sept., 2017) [[arXiv:1709.07880](#)].
- [228] O. Aharony, O. Bergman, D. L. Jafferis, and J. Maldacena,  *$N=6$  superconformal Chern-Simons-matter theories, M2-branes and their gravity duals*, *JHEP* **10** (2008) 091, [[arXiv:0806.1218](#)].
- [229] P. Figueras, M. Kunesch, and S. Tunyasuvunakool, *End Point of Black Ring Instabilities and the Weak Cosmic Censorship Conjecture*, *Phys. Rev. Lett.* **116** (2016), no. 7 071102, [[arXiv:1512.04532](#)].
- [230] P. Figueras, M. Kunesch, L. Lehner, and S. Tunyasuvunakool, *End Point of the Ultraspinning Instability and Violation of Cosmic Censorship*, *Phys. Rev. Lett.* **118** (2017), no. 15 151103, [[arXiv:1702.01755](#)].
- [231] T. Crisford, G. T. Horowitz, and J. E. Santos, *Vacuum Counterexamples to Cosmic Censorship in AdS*, [arXiv:1805.06469](#).
- [232] R. Bartnik, *Einstein equations in the null quasispherical gauge*, *Class. Quant. Grav.* **14** (1997) 2185–2194, [[gr-qc/9611045](#)].
- [233] H. Kodama and A. Ishibashi, *A Master equation for gravitational perturbations of maximally symmetric black holes in higher dimensions*, *Prog. Theor. Phys.* **110** (2003) 701–722, [[hep-th/0305147](#)].

